Time-series analysis of B[e] supergiant stars

Augustus Porter
Pembroke College
University of Oxford

A thesis submitted for the degree of
Doctor of Philosophy

Hilary 2021

Statement of Originality

I carried out the work presented in this thesis between October 2016 and March 2021 under the supervision of Prof. Katherine Blundell. I hereby declare that no part of this thesis has been submitted in support of another degree, diploma or other qualification at the University of Oxford or other higher learning institute. Except where otherwise stated or where reference is made to the work of others, the work in this thesis is entirely my own.

Section 3.3 and Chapter 4 are based on work which has been published in Porter et al. (2021c) (MNRAS, 501, 5554). While I was the lead author and the work is my own, David Grant carried out the `CMFGEN` simulation described in Section 4.3.1.1 and the work was carried out with the regular consultation of Prof. Blundell.

Chapter 5 is based on work which has been published in Porter et al. (2021b) (MNRAS, 503, 4802). While I am the lead author and the work is my own, Prof. Philipp Podsiadlowski was key in suggesting the idea of tidally-modulated pulsations, and the work was carried out with the regular consultation of Prof. Blundell.

Chapter 6 forms the basis of Porter et al. (2021a), which has been submitted to MNRAS. While I am the lead author and the work is my own, the work was carried out with regular consultation of Prof. Blundell.

Acknowledgements

There are a great many people I have to thank, both within Oxford and without, for their support and friendship, without which I would not have been able to complete this DPhil. First and foremost I wish to thank my supervisor, Katherine Blundell. Without her incredible support, guidance and enthusiasm none of this work would have been possible. I also thank Philipp Podsiadlowski for his helpful discussions and help in understanding some of the unusual phenomena presented in this thesis. Many thanks go to David Grant and Dominic McLoughlin as integral parts of the Global Jet Watch team and for their helpful feedback and suggestions for my work.

Outside of academia, I thank my oldest friends Nathaniel, Jack and Harry, for being the three best friends anyone could ask for and for always making me ask the question: "What would Dave Brock do?". To Zana, Simon, Denise, Piers: I am incredibly lucky to have met you guys in Oxford, and I am forever happy to call you my friends. And to everyone in the Pembroke MCR and PCBC communities, which have been huge parts of my life these last four years: there are too many of you all to list, but you have all had an impact on me and made my time at Oxford much the better, whether it be in the bar or the boat house.

And finally, my largest thank you goes to my parents, Laurie and William, for their unwavering love and support. Finishing a DPhil in the midst of a global pandemic and national lockdowns has been less than ideal, but knowing I always had a safe and welcoming place at home was what got me through.

Abstract

B[e] supergiant stars (B[e]SGs) are a rare and unusual class of massive evolved stars which are poorly understood. I demonstrate how studying B[e]SGs by analysing time-series observations reveals key information about this stellar class which may help to build a common picture and determine the origin of their phenomena. I utilise spectroscopic data from the Global Jet Watch, which is able to observe astronomical objects with sustained high time-resolution, and describe my contributions to the data reduction pipeline. I access and analyse high-resolution FEROS spectra, and photometry from the ASAS, ASAS-SN, OMC, and TESS surveys.

I take an in-depth case study of the B[e]SG binary GG Carinae, which has been widely studied but poorly understood. I demonstrate that previous determinations of the binary's orbital solution were incorrect and accurately measure it for the first time, finding that the binary is significantly eccentric ($e = 0.50 \pm 0.03$) and that the system is brightest at periastron. I discovered a pulsation mode in the system from photometric and spectroscopic variability, and analysed it in depth for the first time. The variability has a period of 1.583156 ± 0.0002 days and displays amplitude modulation over the binary's orbital period, such that the amplitude of the detected variability is largest just after periastron. The variability is most likely due to an $l = 2$ f-mode pulsation in the primary which is modulated by the time-varying tidal potential in the eccentric orbit. I study the two atomic circumbinary rings of GG Carinae and find evidence of subtle variability of the line centres and the blue-peak to red-peak ratios of the emission lines arising from the inner circumbinary ring over the FEROS observations. I show these variations may be caused due to the binary exciting the circumbinary rings to higher eccentricities over the observation timescales.

A preliminary study utilising TESS and ASAS-SN data of the Galactic B[e]SG sample reveals signatures of binarity in a further three specimens. This increases the ratio of confirmed or suspected binaries in the Galactic B[e]SG population from 4/9 to 7/9, indicating that binarity may be key in understanding the phenomenon. Pulsations similar to those seen in GG Carinae are also detected in at least two further objects for the first time, demonstrating that pulsations may also be a commonality of the class.

Contents

Chapter 1

Introduction

1.1 Introduction to massive binary stars

A star's defining feature is its mass, M, and massive stars with mass $\gtrsim 15\,M_{\odot}$, play an important role in astrophysics. They are the brightest stars in the night sky with the luminosity, L, of a star having a strong relationship to the mass, $L \propto M^{\alpha}$, with the exponent α somewhere between 3–4 (Griffiths et al. 1988; Demircan & Kahraman 1991; Eker et al. 2015). Their disproportionately high luminosities, which are due to the high temperatures and pressures in their stellar cores which their mass facilitates, lead to massive stars to burn their nuclear fuel more rapidly than their lower-mass counterparts. This rapid burning of their fuel leads to massive stars evolving at a faster rate and having significantly shorter lifetimes than lower mass stars. Massive stars are also comparatively rare; the famous initial mass function of Salpeter (1955) finds that the number density distribution of stars by their initial mass has a steep exponential drop off, such that $N(M)\mathrm{d}M \propto M^{-2.35}$. However, despite their shorter lifetimes and comparative rarity, the intense luminosity of massive stars, often peaking in the ultraviolet (UV), can ionise the interstellar medium and their powerful stellar winds can significantly affect the evolution of their host galaxies (Kennicutt 2005). Massive stars dramatically finish their lives as supernovae and the collective effect of supernova feedback may further affect the host galaxy, affecting its morphology, chemical properties, inducing it to lose mass, and diminishing star formation (Larson 1974; Scannapieco et al. 2008). The supernova remnants of black holes and neutron stars are exotic test beds for new physics from a wide array of topics, from accretion physics in X-ray binaries, gravitational waves from coalescing binary black holes, to testing Einstein's gravitation theories. Massive stars and their evolution, therefore, are a vital part of the astrophysics story.

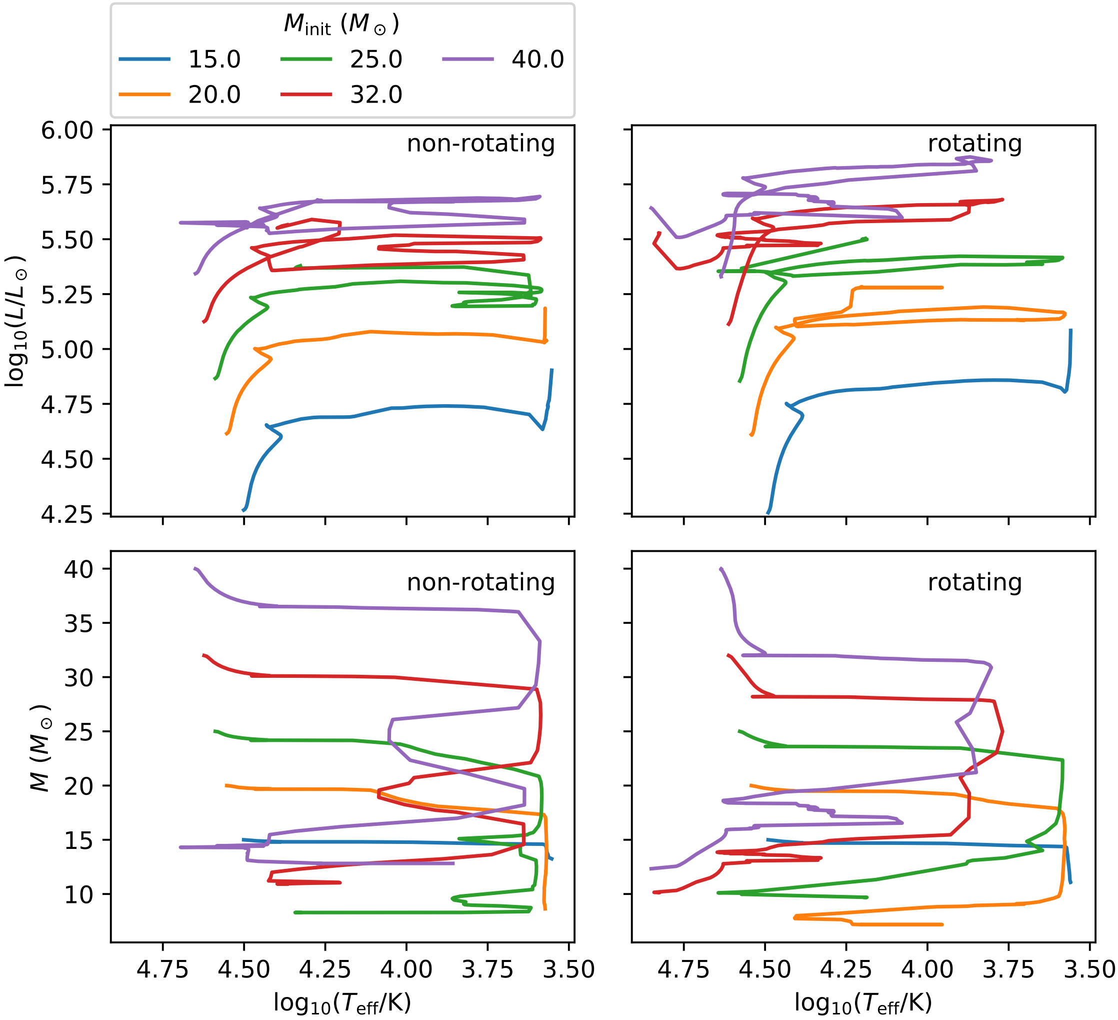

Figure 1.1: Top panels: Evolution of the luminosity, L, against effective temperature, $T_{\rm eff}$, of non-rotating (left) and rotating (right) single massive stars at solar metallicity for a range of initial masses, $M_{\rm init}$. Bottom panels: The evolution of stellar mass, M, and $T_{\rm eff}$ of the same evolutionary models. The $M_{\rm init}$ of the models in all panels are listed in the legend above the top-left panel. The models are taken from Ekström et al. (2012).

A massive star, as with all stars, will begin its life on the main sequence with core hydrogen burning. It will occupy the top-left part of the Hertzsprung-Russell (HR) diagram, indicating its high temperature and luminosity. Figure 1.1, top panels, shows the evolution of stars across the HR diagram with initial mass, $M_{\rm init}$, from 15 $M_\odot$ to 40 $M_\odot$ in the cases with and without initial rotation of $v_{\rm rot} = 0.4\,v_{\rm crit}$, where $v_{\rm crit}$ is the star's critical rotation speed above which the star would lose mass at its equator as its surface gravity would be equal to the centrifugal and radiation pressure forces.

These models were calculated by Ekström et al. (2012) at solar metallicity up until the end of the carbon burning phase in the stellar core. Rotating stars, generally, have higher luminosities than their non-rotating counterparts of the same initial mass due to increased mixing in their stellar cores. During main sequence evolution, the cores of both rotating and non-rotating stars gradually get hotter which leads to higher stellar luminosities over their main sequence lifetimes. As the massive stars near the end of the main sequence, they enter a “blue supergiant” (BSG) phase. As massive stars evolve off the main sequence, having expended their hydrogen fuel in the stellar core, their cores rapidly contract and heat up; concurrently, this heat is transferred to the stellar envelope which causes it to expand and the surface to thereby cool. This process causes the star to appear redder to the observer yet it will stay roughly constant in luminosity. Once the core contracts and heats up even further, helium fusion begins, extending the life of the star. A massive star in this evolutionary state is in a “red supergiant” (RSG) state. Depending on the stellar mass, rotation rate, and mass loss, RSGs may evolve back to the bluewards side of the HR diagram, undertaking what is known as the “blue loop”, to return to a BSG state (Ekström et al. 2012; Saio et al. 2013). It may therefore be a challenge to determine whether a luminous blue star is in a pre- or post-RSG evolutionary state, though observables such as surface chemical abundances or pulsational properties may give us some clues (Saio et al. 2013). Less massive stars, or those which are not rotating, do not evolve back to become BSGs due to the lack of mass-loss whilst they are in the RSG state (Ekström et al. 2012).

The bottom panels of Figure 1.1 show the evolution of the mass for the same stellar models as the top panels. These models show that massive stars exhibit significant mass loss over their lifetimes due to material escaping from their stellar surfaces via winds, thereby enriching their host galaxies with gas and dust. Rotating stars are more readily able to lose mass during their main sequence evolution via decretion from around their stellar equators; they may be observed as classical Be stars which have strong hydrogen Balmer emission (Porter & Rivinius 2003). It is also clear that stars undergoing the blue loop in their evolution lose significant fractions of their mass over their post-main sequence lifetimes.

Whilst stellar evolution models can reasonably, albeit with certain uncertainties and shortcomings, model the evolution of a single, isolated star, most stars are not singles. Moe & Di Stefano (2017) built a very detailed picture of the frequency of binaries and multiplicity and found that solar type primary stars, on average, have 0.5±0.04 companions. For massive, O-type primaries, this frequency increases to 2.1±0.3 companions, on average, per primary. Similarly, Sana et al. (2008) found that three-quarters of massive O-type stars in the cluster NGC 6231 were members of multiple systems. Sana et al. (2012) found that 70% of all massive stars will exchange mass with a companion, drastically affecting the evolution of both stars. The impact of binarity, therefore, adds complexity to the evolution of massive stars. Moe & Di Stefano (2017) found that the companion's mass for massive primary stars in short period binaries is a uniform distribution, favouring massive companions when compared to the Salpeter initial mass function. Moe & Di Stefano (2017) also noted that 10–20% of the primaries in observed OB binaries are in fact the true secondary in a system where the primary has evolved to a neutron star or a black hole via a core-collapse supernova. Binary stars are therefore very common in the universe, especially for massive stars. Binarity, and multiplicity, is believed to be so common in massive stars since it is able to preserve the angular momentum of the proto-stellar gas clouds more readily than a rotating single star of the mass of the multiple components (Larson 2010). The study of massive stars is therefore heavily linked to the study of binaries and multiples.

Binary stars encompass wide ranging fields of physics, from gravitation, to accretion, mass transfer, and gravitational wave progenitors. Interacting binaries are the origin of interesting and diverse observational phenomena including X-ray binaries, cataclysmic variables, and type Ia supernovae. The pair of black holes whose merger led to the first gravitational wave detection GW 150914 would have started their lives as a binary system composed of two massive components.

1.1.1 Binary dynamics

1.1.1.1 Kepler's laws

The orbits of binary stars, like planets, follow Kepler's three laws. These are:

1. The stars orbit around a common centre of mass in two ellipses, with the centre of mass of the system being one of the foci of the ellipses.

2. A line segment joining each star to the centre of mass sweeps equal area in equal time.

3. The period, P, of the orbit squared is proportional to the semi-major axis, a, of the binary system cubed. The square of the period is also inversely proportional to the total mass, $M_{\rm tot}$, of the system, and the full equation form is

$$P^2 = \frac{4\pi^2 a^3}{GM_{\rm tot}}, \tag{1.1}$$

1.1.1.2 Orbital energy, angular momentum, and eccentricity

The orbital energy, E, of a binary consisting of stars of constant mass m_1 and m_2 will be constant throughout their orbit, and is the sum of the gravitational potential energy and the kinetic energy of the stars. It can be shown that the specific orbital energy, ϵ, which is the energy of the binary divided by the reduced mass of the system $\mu = m_1\, m_2/M_{\rm tot}$ is given by

$$\epsilon = \frac{E}{\mu} = \epsilon_{\rm kin} + \epsilon_{\rm pot} = \frac{v^2}{2} - \frac{GM_{\rm tot}}{r}, \tag{1.2}$$

where r is the instantaneous separation of the binary components, v is their instantaneous relative velocity, and $M_{\rm tot} = m_1 + m_2$. An orbit is bound if $E < 0$, and is unbound if $E >= 0$. As gravitation is unable to exert torque on the attracting bodies (under the assumption that they are spherical) the angular momentum of the orbit is conserved, and therefore the orbital energy can be shown to be

$$E = -\frac{Gm_1 m_2}{2a}. \tag{1.3}$$

The energy of a gravitationally bound binary consisting of constant masses m_1 and m_2 is therefore solely dependent on the semi-major axis of the binary, a. The specific orbital angular momentum, $h = L/\mu$, where L is the total angular momentum, is given by

$$h^2 = GM_{\rm tot}a(1 - e^2), \tag{1.4}$$

where e is the eccentricity of the orbit. Eccentricity, which defines the non-circularity of the orbit, is a particularly interesting parameter in the study of binaries. At periastron, when the binary components are closest to one another in their orbit with a separation $r = a(1-e)$, the stronger tidal forces between the components can lead to interactions between them. At apastron, where the binary components are furthest from one another with separation $r = a(1 + e)$, the binary components may have significant interactions with a circumbinary disk. Equation 1.4 may be rearranged

$$e = \sqrt{1 + \frac{2\epsilon h^2}{(GM_{\mathrm{tot}})^2}}, \tag{1.5}$$

demonstrating that it is therefore the interplay between the energy of a binary's orbit and its angular momentum which defines its eccentricity. For a given angular momentum, a circular orbit has a lower orbital energy (i.e. it is more negative). And, vice versa, for a given orbital energy, a circular orbit has higher angular momentum.

Figure 1.2 displays the effect of varying the orbital eccentricity on the orientation of the orbit of a binary component (left panel). The eccentricity vector of the orbit points from the centre of mass to the point of periastron, with magnitude of the orbital eccentricity. The angle that the eccentricity vector, which points from the center of mass to the position of the star at periastron with a magnitude of the orbital eccentricity, makes to the plane of the sky from the point of view of an observer is the argument of periastron, ω. The right panel of Figure 1.2 displays the variance in the orbits' orientation with varying ω.

Binary orbital parameters are constant in the ideal case of two isolated, non-deformable spheres. There are times when this may be broken, such as if there is mass transfer between the components, if one of the stars is losing mass via a wind, interactions with a circumbinary disk or planet, the binary is losing energy due to the emission of gravitational waves, or tidal deformation effects which break the spherical symmetry of one of the stars.

1.1.2 Observation techniques of binary stars

Here I introduce the common techniques to determine the orbits of binary stars.

1.1.2.1 Visual binaries

If the two binary components can be spatially resolved by astronomical instruments and the proper motion of the stars can be measured over time then the binary is classed as a visual binary. I will not expand on these types of binaries further, as this method is not discussed later in this thesis.

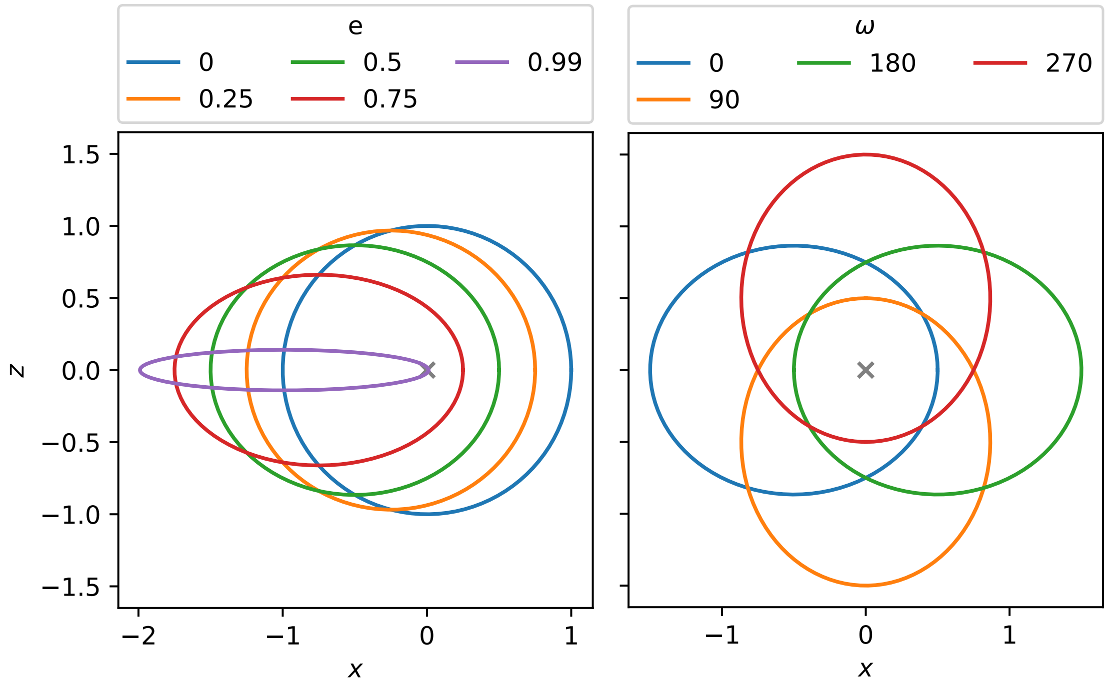

Figure 1.2: Demonstration of how eccentricity, e, and argument of periastron, ω, affect the orientation of a binary star component's orbit in the x-z plane. The observer observes along the z axis, defining the plane of the sky to be the positive x direction. The semi-major axis of the orbit is held constant at 1. A gray $\times$ symbol at $(0, 0)$ indicates the center of mass which the binary orbits about; the companion of this component would likewise orbit the common center of mass, with the same eccentricity and argument of periastron. In the left panel, ω is kept fixed at 0°, in the right panel e is kept fixed at 0.5. The orbit of the companion is not shown.

1.1.2.2 Eclipsing binaries

As the stars move about one another, should their orbit be significantly inclined to the line of sight, the stars may pass in front of each other at some stage during their orbits. This will lead to a drop in the measured light from the system, known as an eclipse. Assuming a simplified picture of a circular orbit, the stars will eclipse if

$$R_1 + R_2 > a \cos i, \tag{1.6}$$

where R_1 is the radius of star 1, R_2 is the radius of star 2, a is the separation of the stars, and i is the inclination of the orbit to the plane of the sky. It shows that stars are more likely to eclipse if they are of large radii, closer together, and the orbit is inclined to the plane of the sky. Whether eccentric binaries have eclipses depends on the orientation of the orbit and its eccentricity, as well as the stellar radii, inclination, and separation. It is possible for eccentric binaries to only display one eclipse.

Eclipses are a powerful tool, as the relative depths of the two eclipses can tell the observer the relative surface brightnesses of each star in the observed wavelength range. The duration of the eclipses and times of ingress and egress tell the observer the relative sizes of the stars in relation to the semi-major axis of the orbit, and give limits on the inclination of the orbit. The placement of the eclipses in the phase of the orbit allows us to observe the eccentricity of the orbit and the argument of periastron.

1.1.2.3 Spectroscopic binaries

The spectroscopic method of observing binary orbits is used extensively in Chapter 4 of this thesis, therefore I expand on the method in this section.

As the stars move through space in their orbits, they will have cyclic radial velocities (RVs) according to an observer if the binary's orbit is inclined to the plane of the sky and therefore there is motion along the line-of-sight. This relative motion between the star and the observer will lead to Doppler shifts of the light of the stars observed, meaning the light shifts to the longer-wavelength "red" end of the spectrum while the star is moving away from the observer, and conversely shifts to the shorter-wavelength "blue" end of the spectrum while the star moves towards the observer. This wavelength shift, also known as redshift, is given by

$$z = \frac{\Delta\lambda}{\lambda} = \sqrt{\frac{1 + \frac{v_r}{c}}{1 - \frac{v_r}{c}}} - 1, \tag{1.7}$$

where z is the redshift, $\Delta\lambda$ is the change in the observed wavelength, λ is the laboratory wavelength presuming no shift, v_r is the relative RV between the observer and the object, and c is the speed of light. v_r is defined to be positive when the star is moving away from the observer, such that the distance between the two is increasing. In the non-relativistic regime Equation 1.7 simplifies to

$$z = \frac{\Delta\lambda}{\lambda} = \frac{v_r}{c}. \tag{1.8}$$

Though the whole stellar spectrum is shifted by the motion of the stars, in practice astronomers measure the shifts of emission or absorption lines in the spectra. These lines, once they have been identified, have known and unique laboratory wavelengths depending on the atom, ion, or molecule in question, allowing for easy measurement of the shift in wavelength. The RV of a binary component along the line of sight, which we can measure with the Doppler shifting of emission lines, is given by

$$v_r = K_n \left(\cos(\omega + \nu) + e \cos(\omega) \right) + \gamma, \tag{1.9}$$

where K_n is the amplitude of the RV variations of star n, e is the eccentricity of the orbit, ω is the argument of periastron, ν the true anomaly, and γ is the systemic velocity of the system (Benacquista 2013, eq.2.79). K_n encodes information about the binary, and is given by

$$K_{1,2} = \frac{2\pi a_{1,2} \sin i}{P\sqrt{1-e^2}} = \frac{m_{2,1}}{m_1 + m_2} \frac{2\pi a \sin i}{P\sqrt{1-e^2}}, \tag{1.10}$$

where i is the inclination of the orbit to the plane of the sky, and the other symbols have the same definitions as in Section 1.1.1 (Benacquista 2013, p.27). ν is given by

$$\nu = 2 \arctan\left(\sqrt{\frac{1+e}{1-e}} \tan\left(\frac{E}{2}\right) \right), \tag{1.11}$$

where E is the eccentric anomaly (Roy 2005, p.75). The eccentric anomaly is defined in the relation

$$M = E - e \sin E, \tag{1.12}$$

where M is the mean anomaly (Roy 2005, p.76). Mean anomaly may be trivially calculated as $M = 2\pi p$, where p is the orbital phase and is given by $p = (t - t_0)/P$, where t is the time of observation and t_0 is a reference time, usually the time of periastron passage. Equation 1.12 must be solved for E iteratively in order to calculate the eccentric anomaly at orbital phase M.

K_n, e, and ω may be directly determined from observing the RVs of the binary system over its orbit. The orbital parameters of the binary can be measured from the RV curve of just one of the binary components; it is often the case that the RVs may only be measured for one of the stars if the second has neither absorption nor emission lines. However, if the RV curves of both components of the binary can be measured then the ratio of the K_n values of the RV curves give the ratio of the masses of the two stars, such that $M_1/M_2 = K_2/K_1$. However, determining the absolute masses of the binary components requires the inclination, i, of the orbit to be known or for one of the star's masses to be known by other means.

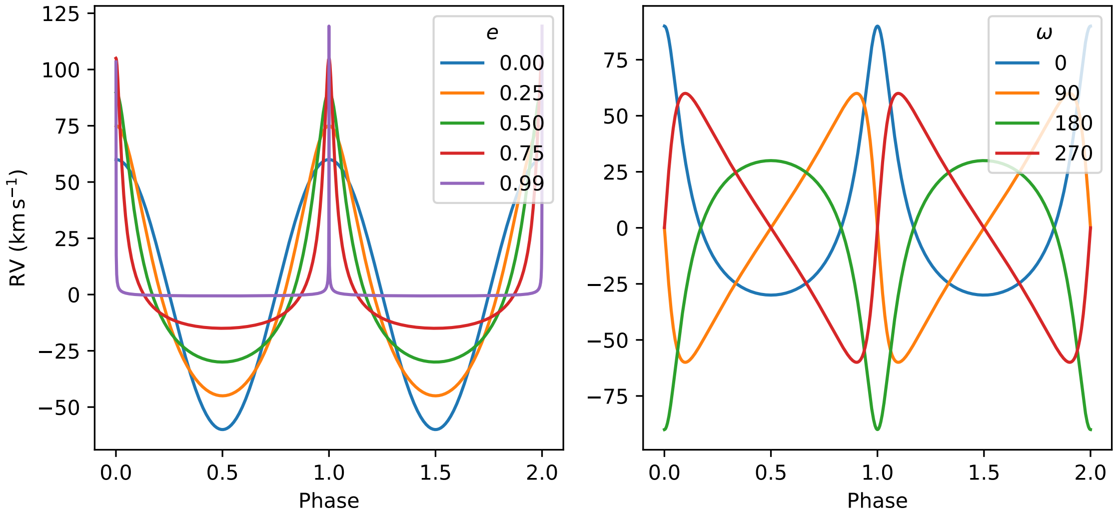

Figure 1.3: Left: effect of eccentricity, e, on the radial velocity curve of a binary component, keeping argument of periastron, ω, fixed at 0°. Right: effect of ω on the RV curve of a binary component, keeping e fixed at 0.5. The RV curves indicate what would be observed for the orbits shown in Figure 1.2 if the observer were observing along the z axis.

Figure 1.3 displays the RV variations of a binary component with a K of 60 km s^{-1}. The left panel shows e varying between 0 and 0.99 with ω fixed at 0°, and the right hand panel shows the RVs calculated with $e = 0.5$ and varying ω. The RV curves match the orbits shown in Figure 1.2, for an observer viewing the system along the positive z axis and assuming an orbital inclination of 90°.

1.2 B[e] supergiant stars

Geisel (1970) first discovered a correlation between stars which host both infrared excess in their continua and narrow, low-excitation emission lines. This was the first observation of the B[e] phenomenon; stars of B spectral type which host strong Balmer line emission, low excitation permitted emission lines of mildly-ionised metals such as Fe II, forbidden emission lines such as [Fe II] or [O I], and infrared excess in their spectra due to hot circumstellar dust. The correlation of narrow emission lines and infrared excess was backed up in many follow up surveys (e.g. Allen 1973; Swings 1974; Allen & Swings 1976). The notation of “B[e]” was suggested by Conti (1975) to differentiate these stars which exhibit narrow forbidden and low-excitation emission lines from the similar Be stars, which also have strong Balmer emission. The B[e] phenomenon arises in a wide range of objects, from pre-main sequence stars, to compact planetary nebulae, to symbiotic B[e] binaries, to B[e] supergiants (B[e]SGs) (Lamers et al. 1998). The physical conditions, common to all B[e] sub-classes, which form the B[e] phenomenon are: Balmer and permitted emission lines form in the stellar atmosphere above the photosphere; the temperature of the singly-ionised emission regions, leading to e.g. Fe II emission, is $\sim 10^4$ K, and is heated by the stellar radiation itself; the presence of forbidden emission lines indicates that the circumstellar gas is of low density; the infrared excess is caused by dust with temperature ∼500–1000 K (Lamers et al. 1998). This thesis concerns itself with the B[e]SGs, which form the most homogeneous grouping of the B[e] stars.

One of the failures of the standard model of massive star evolution is that it fails to predict the existence of the B[e]SGs. B[e]SGs are a classification of luminous stars ($\log(L/L_\odot) > 4$), which occupy the upper-left part of the HR diagram and display the B[e] phenomenon previously described. B[e]SGs are remarkably rare; currently there are only ∼33 confirmed B[e]SGs discovered, and ∼25 further candidates (Kraus et al. 2014; Levato et al. 2014; Kraus 2009, 2017, 2019). The uncertain number is due to the difficulty in accurately determining the distances to the Galactic B[e]SG candidates sample, which therefore have uncertain luminosities. Their positions in the HR diagram imply that they have evolved off the main sequence (Kraus 2019), and the rarity of the B[e]SG stars implies that the phenomenon may be a short-lived transition phase of these massive stars in their post-main sequence lifetimes (Kraus 2009).

1.2.1 Observables and characteristics of B[e] supergiants

Lamers et al. (1998) listed the characteristics which define the B[e]SG class, which are reproduced in Table 1.1.

It is notoriously difficult to determine the true stellar characteristics of B[e]SGs, such as their masses, intrinsic luminosities and effective temperatures, due to the stars being embedded deep in their circumstellar winds and envelopes which cause their displaying of the B[e] phenomenon, leading to pure emission spectra which are formed in the circumstellar environment. This also precludes direct spectroscopic observation of their photospheres, which would otherwise allow us to directly measure observables such as metallicity, surface gravity, and rotation (Kraus 2009). A select few B[e]SGs have been reported to be rotating at significant fractions of their break-up velocities (e.g. Gummersbach & Wolf 1995; Zickgraf 1999, 2006; Kraus et al. 2008). However,

Primary criteria
- Display the B[e] phenomena.
- Luminous supergiants with $\log(L/L_\odot) > 4$.

Secondary criteria
- Indications of mass-loss in the system, such as P-Cygni profiles.
- Hybrid spectra of narrow, low-excitation emission lines and wide, high excitation absorption lines.
- An enhanced abundance of N or an enhanced He/H ratio, showing the star is evolved.
- B[e]SGs usually have high extinction, $A_V > 3\,\mathrm{mag}$, since they are massive stars located at large distances.
- Photometric variability is usually small, and of the order 0.1–0.2 mag.

Table 1.1: Criteria defining the B[e] supergiants, as listed in Lamers et al. (1998).

doubt has been cast on the measurement of these rotation velocities by Kraus et al. (2016a), who found the He I absorption used to determine the rotation velocity of one specimen was polluted by the wind absorption and by variability associated with pulsations. They conclude that this casts doubt on the rotation velocities of the entire sample, and thus it cannot be assumed that B[e]SGs are rapid rotators.

1.2.2 History of the understanding of the B[e] supergiant phenomenon

The "classical" view of B[e]SGs was proposed in Zickgraf et al. (1985), in which the stars host a two-component stellar wind consisting of both a fast, line-driven wind observed in the UV which is typical of supergiant stars, and a slow, cool wind component consisting of Balmer emission and narrow emission lines arising from permitted and forbidden transitions. Zickgraf et al. (1985) proposed that the stars are rotating close to their break-up velocity, with the polar regions forming the fast winds, and the slow wind being a decretion disk from the equator. A density contrast of $\sim$100–1000 was proposed for the two wind components (Zickgraf et al. 1989). As the equatorial wind expands and cools, it condenses to form dust in a disk or ring like structure. Figure 1.4 displays this classical picture of B[e]SGs, taken from Zickgraf et al. (1985). This classical picture was ostensibly supported by the reports of high rotation velocities observed in B[e]SGs. Oudmaijer et al. (1998) extended the classical picture of

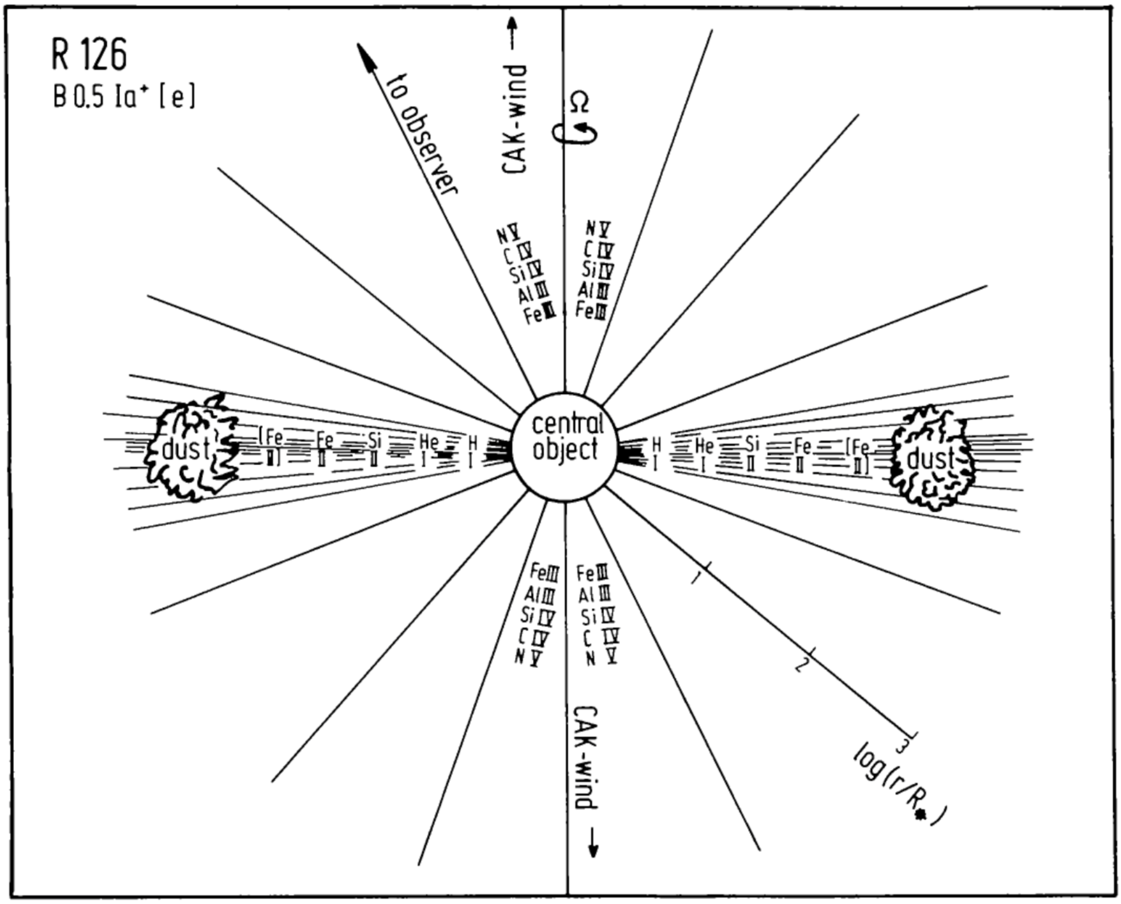

Figure 1.4: Schematic of the classical view of the B[e] supergiants, specifically of the star R126, taken from Zickgraf et al. (1985). This schematic demonstrates the outflowing disk from the star's equator and the fast stellar wind from the poles which is proposed to lead to the phenomena which define the B[e] supergiants.

B[e]SGs, finding that at intermediate latitudes the wind had properties between these two extremes, indicating a less clear cut picture but suggesting that complex wind components could be observed. Molecular emission has been observed in the spectra of B[e]SGs, predominantly in CO but also SiO and TiO in certain objects (Kraus 2019). The temperatures of these molecules are observed to be >2000 K, exceeding the dust sublimation temperature of ∼1500 K, indicating that the molecules arise in a transition region between atomic emission and the dust in the equatorial disk.

In Zickgraf et al. (1985)'s scenario, B[e]SGs closely resemble the rapidly rotating "classical" Be stars, whose strong H-alpha emissions are caused by decretion disks about the stellar equator of the rapidly rotating stars (Porter & Rivinius 2003). Classical Be stars are sometimes thought to be the main-sequence progenitors of B[e]SGs (e.g. Kraus et al. 2013).

Numerous studies have since challenged this classical picture of B[e]SGs. One such challenge is that reevaluation by Kraus et al. (2016a) of the He I absorption in LHA 120-S 73, which Zickgraf (2006) used to determine the star's rotation rate, found that the rotation broadening could not be measured and that the variable absorption more resembles the signal of non-radial pulsations. Therefore the measured rotation of LHA 120-S 73 is unreliable, and casts doubt on the measured rotation rates of the other B[e]SGs. A far more substantial challenge to the classical picture of B[e]SGs are the studies which measure the distribution of material in their circumstellar environments. Recent observations show the disks are in Keplerian rotation around the stars which are detached from the stellar surfaces (De Wit et al. 2014). CO and SiO bandhead emission has been observed in B[e]SGs, indicating molecular emission in their cool outer disks (Morris et al. 1996; Kraus 2009; Kraus et al. 2013; Oksala et al. 2013; Kraus et al. 2015b). The inner edges of the molecular regions are often at a lower temperature than the molecules' dissociation temperature, indicating that the molecules do not extend up to the areas where it is too hot for them to condense (e.g. Kraus et al. 2013). This implies that the disks are not continuous outflows from the stellar equators, unlike the model proposed by Zickgraf et al. (1985).

Additionally, forbidden emission line spectroscopy has shown that B[e]SGs display puzzling features in their atomic disks. [O I] and [Ca II] emission arises from discrete, concentric, sometimes inhomogeneous, gaseous rings in the equatorial disks of B[e]SGs (Kraus et al. 2010; Wheelwright et al. 2012; Aret et al. 2012; Kraus 2016; Torres et al. 2018; Maravelias et al. 2018). For example, Kraus et al. (2016a) studied the forbidden emission lines around LHA 120-S 73 and found that all of these lines had double peaked profiles associated with a disk. However, they found that many lines had profiles that could only be fitted using more than one disk rotational velocity. They conclude that this indicated that the B[e]SG is surrounded by a series of at least four spatially-distinct thin rings of differing densities orbiting the star in Keplerian orbits. Maravelias et al. (2018) found that these concentric rings are a common feature of the B[e]SGs, studying this phenomenon in depth in eight B[e]SGs. They found, however, that each B[e]SG has its own unique ring structure and configuration consisting of different numbers of rings of different elements orbiting at different radii. Kraus (2016) and Kraus et al. (2016b) presented SINFONI and APEX pictures of the spatially resolved disk around MWC 137 imaged in CO band emission which show the ring like structure of the disk very clearly, and which show that there are strong density inhomogeneities even within the rings. The emission-line profiles of the rings in B[e]SGs show that their originating disks have remarkably little radial extent, due to the sharpness of the profiles and steepness of their edges, and Maravelias et al. (2018) showed that these rings are remarkably stable over time. These detached, inhomogeneous rings are inconsistent with the disks in B[e]SGs being continual outflows from the stellar equators. In the B[e]SG systems which are confirmed binaries, these rings are circumbinary (Kraus et al. 2013; Maravelias et al. 2018).

These factors leave the origin of the circumstellar material of B[e]SGs, and therefore the reason they display the B[e] phenomenon, unknown. Given that the progenitors of the B[e]SGs are the hottest O-stars, the circumstellar material cannot be pre-main sequence in origin, since any material would have been cleared by the radiation pressure from the star over its main sequence lifetime. Therefore the disks of B[e]SGs must have been formed by mass loss from the stellar surface and the presence of concentric rings suggest that the mass is lost in discrete episodes. Mass-loss methods invoked to explain the unusual circumstellar environments of B[e]SGs include mass ejection caused by non-radial pulsations on the stellar surface (Kraus et al. 2016a), "shepherd moon"-like planets or massive bodies leading to gaps and rings in the circumstellar disk (Kraus et al. 2016a), binary interactions (Podsiadlowski et al. 2006; Miroshnichenko 2007; Wang et al. 2012; Maravelias et al. 2018), rotational instability (Zickgraf et al. 1985, 1989; Kurfürst et al. 2014, 2018), or the interactions of wind shells from different stages of a star's evolution (Chiţă et al. 2008; Akashi et al. 2015). Kraus (2017) and Kraus (2019) reviewed the different proposed formation mechanisms.

1.2.3 Evolutionary status of the B[e] supergiants

As mentioned, the optically thick stellar atmospheres of B[e]SGs preclude the direct observation of the stellar surfaces, which would have allowed for the age and evolutionary state of the stars to be directly measured. However, evolutionary status of B[e]SGs can be inferred by other means. The location on the HR diagram of the B[e]SGs of the Magellanic Clouds, which have the most accurate luminosity determinations, show that all B[e]SGs have evolved off the main sequence and are in the post-main sequence stage of their lifetimes (see Kraus 2019, figure 1). However, it cannot be determined from their position on the HR diagram alone which evolutionary stage the B[e]SGs are in, such as whether they have yet undergone the blue loop.

Kraus (2009) showed that measurements of the ratio of the ^{12}C and ^{13}C isotopes may help to determine the evolutionary state of B[e]SGs. The initial interstellar value of the ^{12}C/^{13}C ratio is $\sim$70, but over a star's lifetime it manufactures ^{13}C in its stellar core. The ^{13}C is transported to the stellar surface via rotation and mixing, which causes the surface ^{12}C/^{13}C ratio to drop. Therefore, a smaller ratio of ^{12}C/^{13}C indicates a more evolved star. The ratio may drop as low as $\sim$5 for post-red supergiant (RSG) stars. The surface ratio of ^{12}C/^{13}C is not directly measurable in B[e]SGs, but in practice the ratio of ^{12}C/^{13}C in the circumstellar environment may be found from molecular ^{12}CO and ^{13}CO bandhead emission. As the B[e]SG phase is believed to be short-lived, the material constituting the circumstellar CO must have been lost from the stellar surface shortly before our observation of it, making the circumstellar ^{12}CO/^{13}CO ratio a strong proxy for the surface ^{12}C/^{13}C ratio. Using this ratio, estimates of whether the B[e]SGs are in a pre-RSG or post-RSG state may be made. However, the evolution of ^{12}C/^{13}C is also strongly dependent on the initial rotation rate of the stars (Ekström et al. 2012). Therefore, as the rotation of B[e]SGs are mostly unknown and as Kraus et al. (2016a) has cast doubt on the measured rotation rates, whether B[e]SGs are in a pre- or post-RSG phase in their evolution is still an open question. For the B[e]SGs in which it has been measured, ^{12}CO/^{13}CO ranges from between 9 to 20 (Kraus 2019).

The work of Saio et al. (2013) showed that the evolutionary status of BSGs may be determined using asteroseismic methods. They found that late type BSGs, which have undergone the blue loop and had an earlier RSG stage, are expected to have a spectrum of radial and non-radial pulsational modes excited. Pre-RSG stars, on the other hand, will have these pulsations suppressed. Though pulsations are rare in B[e]SGs, this method may give evidence to the specific evolutionary stage of a B[e]SG.

1.2.4 B[e] supergiants in binaries

It has been argued that the B[e]SG phenomenon is intrinsically tied to binarity. Podsiadlowski et al. (2006) proposed that B[e]SGs are formed by massive binary mergers, with the merger being a dramatic event with a strong outburst which leaves an extended stellar envelope. Miroshnichenko (2007) also argued that the B[e]SG phenomenon is coupled to binarity, but there is no requirement for a full merger, and that these objects are binaries which have experienced a period of rapid mass exchange which led to mass loss and dust formation in the circumstellar environment. Out of the 15 candidate Galactic B[e]SGs, 7 are confirmed or suspected binaries, and the binary status has not been determined for any of the extragalactic B[e]SGs (Kraus 2019). It is therefore undetermined whether binarity is the sole origin of the B[e]SG phenomenon. Interestingly, for all of the confirmed B[e]SG binaries but one (HD 87643, Maravelias et al. 2018), the circumstellar rings are found to be circumbinary in origin, such as in GG Car (Kraus et al. 2013), MWC 300 (Wang et al. 2012), HD 62623 (Millour et al. 2011), and HD 327083 (Wheelwright et al. 2012). This indicates that binarity may be intrinsically tied to the displaying of the B[e]SG phenomenon in these objects.

Recent studies have shown that the classical Be phenomenon may be intrinsically caused by binarity and binary interaction (Klement et al. 2019; Bodensteiner et al. 2020; El-Badry & Quataert 2021). In a sample of 57 classical Be stars, Klement et al. (2019) found that 26 showed strong evidence for binarity in their Spectral Energy Distributions (SEDs); for the rest of the sample the data are inconclusive. They concluded that most, if not all, classical Be stars are close binaries.

1.2.5 Unanswered questions

The major unanswered questions about B[e]SGs are: at what stage are they in their evolution? How does the circumstellar material get lifted from the stellar surfaces? Why are they so rare? Are they a short evolutionary stage that most or all massive stars go through? How is their circumstellar material arranged in such a bizarre way? Is binarity required for a star to display the B[e]SG phenomenon? Is there a common picture that emerges for all of the objects?

1.3 Circumbinary disks

A circumbinary disk is material which is orbiting a binary system around both of the binary components in a great orbit outside of their separation distance. This is in contrast to a circumstellar disk which orbits a single star, even though that star may itself be within a binary system. The time-varying gravitational potential disallows stable orbits within ~2–4 binary orbital radii from the centre of mass of the binary, which thus clears out a central cavity in the disk (Lubow & Artymowicz 2000). This variable potential also leads to the disks having unusual dynamics. They may also influence the dynamics of the binary star which they orbit.

1.3.1 Dynamical feedback to the binary

Post-main sequence binaries, such as post-AGB binaries and millisecond pulsar binaries, often have high eccentricities. This is in contrast to expectations, since there should have been efficient circularisation in earlier stages of the binary's life, either through tidal interactions between the stellar components (Zahn 1977), or drag from a common envelope stage (Iben & Livio 1993). Different channels have been invoked to explain the observed range in eccentricities, one of which is interactions between the binaries and their circumbinary disks allowing energy and angular momentum to be transferred between them (Dermine et al. 2013; Antoniadis 2014). Fleming & Quinn (2017) in a numerical study found that the inner binary excites resonances in the circumbinary disk, and these resonances drive dynamical evolution in both the binary and the disk.

1.3.2 Disk precession and eccentricity growth

Theoretical and numerical work has shown that circumbinary orbits are expected to precess due to the time varying gravitational potential. In an analytical study Farago & Laskar (2010) predicted that in three body orbits, if the outer body is massless, there exists a family of stable orbits in which the inner bodies and outer body have high mutual inclination. Doolin & Blundell (2011) tested this result with a suite of 3D N-Body simulations of test particles orbiting binaries, observing precession of the inclination and longitude of ascending node of the circumbinary orbits, and quantified the regions of parameter space in which circumbinary orbits can be stable. In a hydrodynamic study, Martin & Lubow (2017) found that similar precession may also occur in gaseous disks orbiting eccentric binaries, observing that a misaligned disk can oscillate in its orbital orientation. Martin & Lubow (2018) then quantified this precession across a range of parameter spaces relating to the parameters of the inner binary and the conditions of the circumbinary disk. This study found that viscous forces within the disk cause the oscillations to dampen over time, causing the disk to settle, or nearly settle, in an orientation perpendicular to the binary's orbital plane if the initial disk was sufficiently inclined. This was then formalized in an analytical study by Zanazzi & Lai (2018), who generalized this effect in terms of binary eccentricity and initial misalignment.

In addition to precession in inclination and longitude of ascending node, eccentricity growth may be induced in circumbinary disks due to the tidal influence of the binary (Lubow & Artymowicz 2000). Papaloizou et al. (2001), in a simulation of a massive planet embedded in a circumstellar disk, found that the regions of the disk exterior to the planet's orbit become eccentric due to instability caused by the coupling to the planet's tidal potential. A spiral wave is induced which transports angular momentum outwards, leading to disk eccentricity growth. Pierens & Nelson (2013) found a similar effect in simulations of protoplanetary disks around the binary stars Kepler-16, Kepler-34, and Kepler-35. They found that the eccentricity of the disk may oscillate, while the argument of periastron librates around 180° (with 0° being the argument of periastron of the binary). A similar result is reported in Lines et al. (2015) and Lines et al. (2016), which also found that asymmetries in the density of the disks would arise when their eccentricities were pumped, with the highest disk densities at apastron and lowest at periastron. Fleming & Quinn (2017) studied the coevolution of binaries and circumbinary disks, and also found that eccentricities can be induced and caused to oscillate in the circumbinary disk by the binary. Thun et al. (2017) found similar results in a study of numerical effects in circumbinary disk simulations.

1.3.3 Spectroscopic signatures of circumbinary rings

In emission-line spectroscopy, circumbinary disks are defined by double-peaked profiles (Smak 1969, 1981). The peaks are the same intensity and the line profile is symmetric for an axially symmetric disk, but inhomogeneities in the disk may lead to one of the peaks becoming less intense compared to the other.

For the radially thin circumbinary disks of B[e]SGs studied in this thesis, only the projected Keplerian orbital velocity, $v_{\rm kep} \sin i$ where i is the orbital inclination, central velocity, v_0, and instrumental resolution, σ, may be measured from the circumbinary lines. This is in contrast to extended disks where other parameters such as opacity, temperature distributions, or density distributions may be constrained.

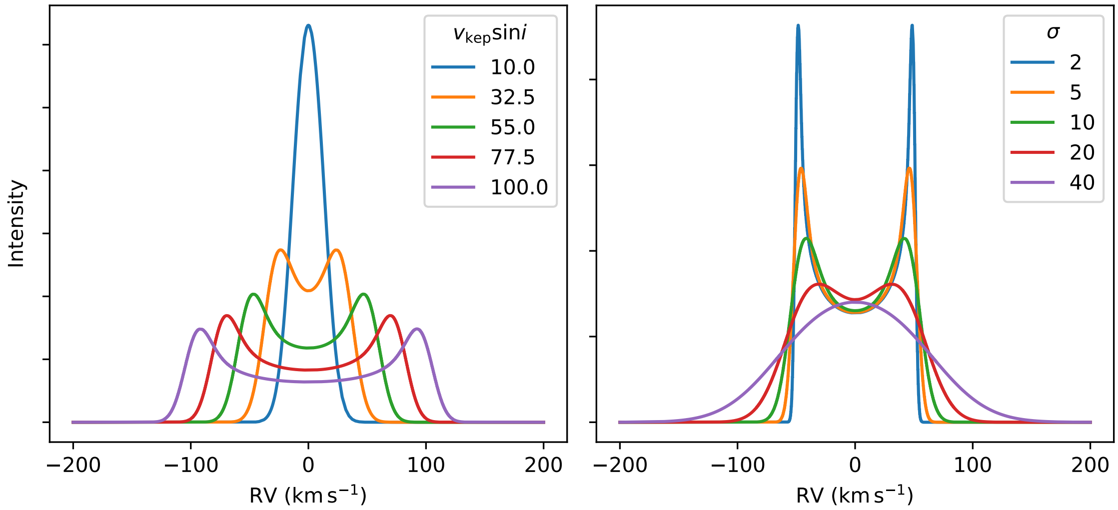

Figure 1.5: Left: effect of varying projected orbital speed, $v_{\rm kep}\sin i$, on the ring line profile, while keeping the resolution, σ, fixed at $10\,{\rm km\,s^{-1}}$. Right: effect of varying σ on the ring line profile, while keeping $v_{\rm kep}\sin i$ fixed at $50\,{\rm km\,s^{-1}}$.

Figure 1.5 demonstrates how a circumbinary ring profile may be observed in spectroscopy for varying orbital velocity (left panel) and varying spectral resolution (right panel). There is a degeneracy with $v_{\rm kep}$ and inclination, since the splitting of the double peaked profile gives a lower limit of the true orbital velocity due to the potential inclination of the circumbinary ring to the line of sight of the observer. The right panel shows, for decreasing spectral resolution (increasing σ), that the double peaked profile becomes less defined, and ends up resembling a Gaussian profile when the values of σ and $v_{\rm kep}\sin i$ become comparable. Therefore high spectral resolutions are required to adequately study these rings.

1.4 Structure of this thesis

This thesis studies the B[e]SG binary GG Carinae (GG Car) in depth, using Global Jet Watch spectroscopy along with publicly available photometry and spectroscopy. In Chapter 2, I describe my contribution to the data reduction pipeline of the Global Jet Watch spectroscopic observing program. In Chapter 3, I introduce GG Car and the previous literature which has been published about the object. I describe the datasets that are used to analyse GG Car, and give a brief description of its spectroscopic properties. In Chapter 4, I study the variability of the system at its ∼31-day orbital period and determine the orbital solution of the binary. Chapter 5 studies the unusual short-period variability of the system. Chapter 6 studies atomic emission which originates in the system's circumbinary disk. Chapter 7 presents the conclusions of this thesis.

Chapter 2

Global Jet Watch data reduction

Abstract

In this chapter, I describe my contributions to the Global Jet Watch (GJW) project's spectroscopic data reduction pipeline. I give a brief overview of the GJW project. I go on to describe the workflow of the reduction pipeline, how calibration frames are utilised and built, how the wavelengths are calibrated and corrected, and how the scientific spectra are extracted. I describe the novel methods which are utilised to minimise noise in the final spectra and maximise the spectroscopic resolution of the output spectra.

2.1 Global Jet Watch overview

The Global Jet Watch (GJW) is a spectroscopic observing program consisting of five telescopes, separated in longitude, which observes a variety of astronomical objects. The telescopes are located in Chile, India, Western Australia, Eastern Australia, and South Africa, and each have identical setups. The observatories are equipped with spectrographs that take optical spectra in the $\sim 5\,800 - 8\,400$ Å wavelength range, chosen to focus on the H-alpha line, which is important for a number of objects. The telescopes have a wavelength resolution $R = \lambda/\Delta\lambda \sim 4\,000$, classing it as a mid-resolution instrument. The telescopes' separation of longitude allows for continual observation of astronomical objects at a very high cadence as the Earth rotates on its axis, allowing for short-term variability in the spectra of the targets to be observed.

The observatories can be run in science mode, when they are observing celestial objects in the night sky, or calibration mode, usually during the day where calibration exposures are taken in order to calibrate the science exposures so that they are scientifically usable and comparable to one another. In science mode, the telescope's dome is opened, and the telescope collects light from the night sky, using a curved primary mirror of 0.5-metre diameter and a smaller secondary mirror, to focus the light into an optic fibre. The photons travel along the optic fibre then are collimated onto a Volume Phase Holographic (VPH) grating, which sits in an enclosure on the floor next to the telescopes. A VPH grating differs from a traditional diffraction grating as it has a pattern in refractive index, rather than transparency. This means that, effectively, no light is lost in the grating, increasing the throughput of the spectrograph and allowing more photons to be collected. The photons, now dispersed according to their wavelength by the VPH grating, are then focused by a camera lens onto a 2504×3326 pixel CCD detector, where their x-y incident position on the CCD is recorded. The CCDs used are the KAF 8300 detector inside a Finger Lakes Instrument (FLI) Microline-8300 camera, which contain a triple stage Peltier cooler which cools the cameras to -30° C to minimise thermal excitation noise. The axis that the photons make on the CCD is the "dispersion axis", with one end of the axis receiving photons of shorter wavelength, and the other end receiving photons of longer wavelength. The exposure time of the CCD can be longer when observing faint targets, in order to observe enough photons at each wavelength as the signal-to-noise ratio (SNR) in Poisson statistics is

$$\mathrm{SNR} = \frac{N}{\sqrt{N}} = N^{\frac{1}{2}} \propto t_{\mathrm{exp}}^{\frac{1}{2}}, \tag{2.1}$$

where N is the number of photons collected, and t_{exp} is the exposure time. Shorter exposure times may be used in order to observe brighter objects, since each pixel becomes saturated when it counts $\sim$65 000 photons.

In calibration mode, the observatories work in much the same way except the telescope dome is closed and instead of collecting photons from objects in the night sky, photons from known sources in the dome are collected, fed through optical fibres, dispersed by the grating, and recorded on the CCDs. There are four types of calibration frames:

1. Thorium krypton (ThKr) frames. These capture emission spectra of a mixture of thorium and krypton gases, which emits peaks at known wavelengths; this allows us to calibrate the wavelength dispersion across the dispersion axis.

2. LED frames. These capture flat-field spectra, smoothly illuminating the red end of the dispersion axis, since they emit reddish light, in order to find efficiency, or "gain", variations pixel-by-pixel.

3. Tungsten frames. These are similar to the LED frames, except they illuminate the blue end of the dispersion axis.

4. Dark frames. These are frames for which no light is exposed on the CCD, but the pixel counts are read out after a certain time, equal to the exposure time of any "light" frames, and matched in CCD temperature. This allows us to subtract any pixel counts which are due to thermal excitation in the CCD.

So, in all, there are four kinds of light frames (science/target, ThKr, LED, Tungsten) alongside dark frames. Figure 2.1 displays the full CCD readings for the four types of light frames. These show how the LED and Tungsten frames smoothly illuminate the red and blue ends of the spectrum respectively, with the dispersion placed diagonally on the CCD. The ThKr frame has only a few, localised points corresponding to the emission lines of known wavelength. The science frame is an example spectrum of GG Carinae which has a very intense H-alpha line, which can be seen around pixel (x = 1250, y = 1600), and a measurable continuum along the whole wavelength range. The data collected by GJW are separated according to which

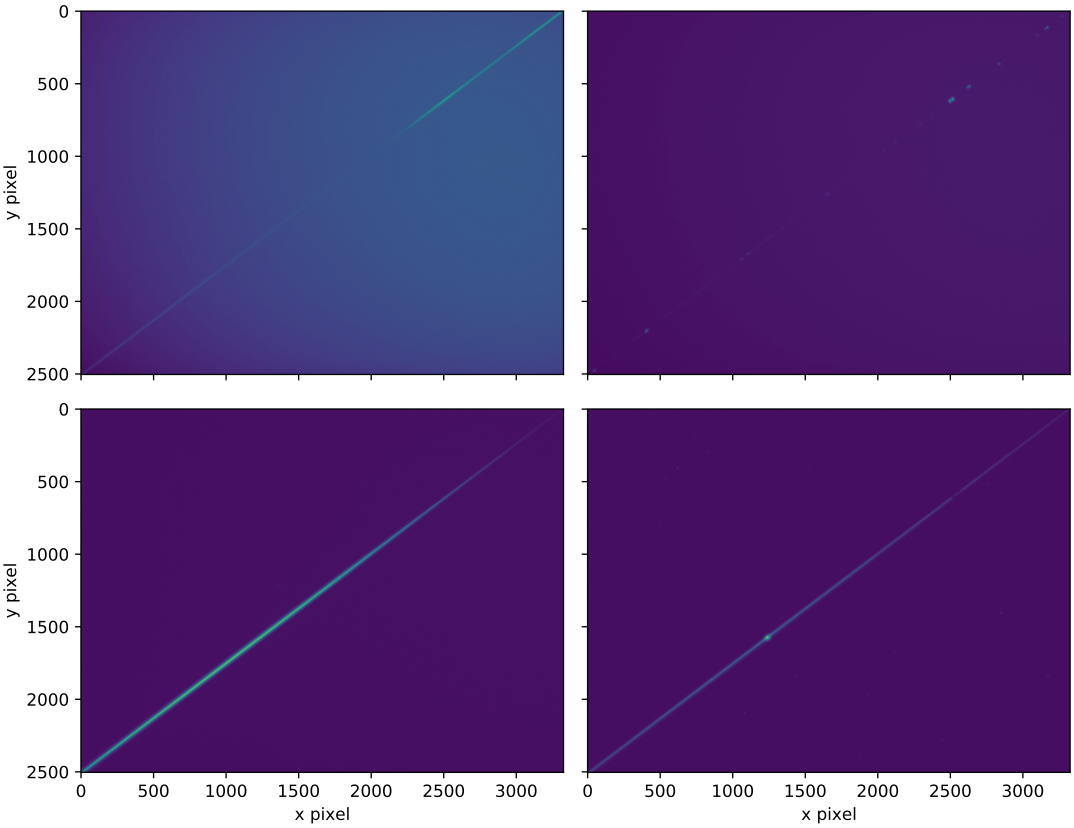

Figure 2.1: Examples of the four different types of "light" frames of GJW. They are Tungsten flat fields (top left), LED flat fields (bottom left), ThKr spectra (top right), and science target frames (bottom right). Yellow corresponds to more counts on the CCD's pixels, and blue to fewer counts.

telescope and which observing night they were taken, and we use science and calibration data from the same observing night in the same observatory in order to reduce the "two-dimensional" spectra, as can be seen in Figure 2.1, into scientifically usable "one-dimensional" spectra. The remainder of this chapter describes my contributions to how that is done in the `Endeavour` software package. `Endeavour` is written in `python3.x` and utilises the standard `numpy`, `scipy`, and `astropy` libraries (Robitaille et al. 2013; Price-Whelan et al. 2018; Virtanen et al. 2020). The GJW data reduction pipeline runs on a series of virtual machines in Oxford, two of which are relevant to the work in this Chapter. These are the data depository machine, GJW-DD, which stores the raw telescope data which has been received from the observatories, and the data processing machine, GJW-DP, which runs the reduction pipeline software.

2.2 Pre-processing

2.2.1 Screening frames

The screening process is run before any reduction takes place to ensure that the frames are valid and are good spectra; this saves computing resources by avoiding reducing invalid frames and avoids any problems arising in the final one-dimensional spectra due to over-saturation of the CCD pixels or other problems. The pipeline recursively trawls through the data directories on GJW-DD, tests each file and saves the result, along with information such as the type of exposure and Julian date of the exposure, into an SQL database on GJW-DP.

First the pipeline ensures that the image file is of the right size, between 16 and 18 MB, with files outside of this range discarded outright because they will not be valid spectrum frames. Then the file is opened and it is confirmed that all of the header parameters are as expected and that the image exposure time is one of a predetermined number of values (0.1, 0.3, 0.5, 1.0, 3.0, 5.0, 10.0, 30.0, 60.0, 100.0, 120.0, 300.0, 600.0, 1000.0, 1200.0, 1800.0, 3000.0, or 3600.0 seconds). A frame with a different exposure time will be erroneous. There are then checks to make sure that Dark frames are properly identified as such in their headers.

For light files, the pipeline checks that the images are neither underexposed or overexposed. For both of these checks, a median-filter of kernel-size three is applied to the image to avoid any false-positive results which may occur due to either cosmic rays or hot pixels, then the CCD is split into ten strips and a straight line is fitted to the ten brightest regions in each frame, one in each strip. These brightest points should be along the dispersion axis, and the value of the brightest pixel in each of these ten bright regions is recorded. To test for underexposure, the correlation parameter, r, of the straight line fit of the x-y values of the ten bright points is used. In a good exposure, the absolute value of r should be approaching 1, since the dispersion axis is nearly a straight line in a diagonal across the CCD; however, if a point outside the dispersion axis was one of these 10 designated brightest points, which may occur if the dispersion axis were not bright enough, then the r value will be less than one. Therefore, any light file with an absolute value of r less than 0.99 is assumed to be uncorrelated, and therefore underexposed, and is marked as invalid. To test for overexposure, the value of the 10 aforementioned bright pixels are checked; if all of these pixels have counts over 60,000 then the image is taken to be overexposed and is marked as invalid.

2.2.2 Finding ThKr emission line centres

In order to calibrate the wavelength along the dispersion axis on the CCD, frames which were illuminated using the aforementioned ThKr bulbs, which have emission lines at known wavelengths, are utilised. These frames can calibrate the wavelength of the observations by allowing us to analytically fit a polynomial function which links x-y position on the CCD with wavelength. Therefore, for each emission line peak in each ThKr frame x, y, and wavelength, λ, need to be determined. These values will then be saved in a database, to later be used to build a mapping between x-y coordinate and λ.

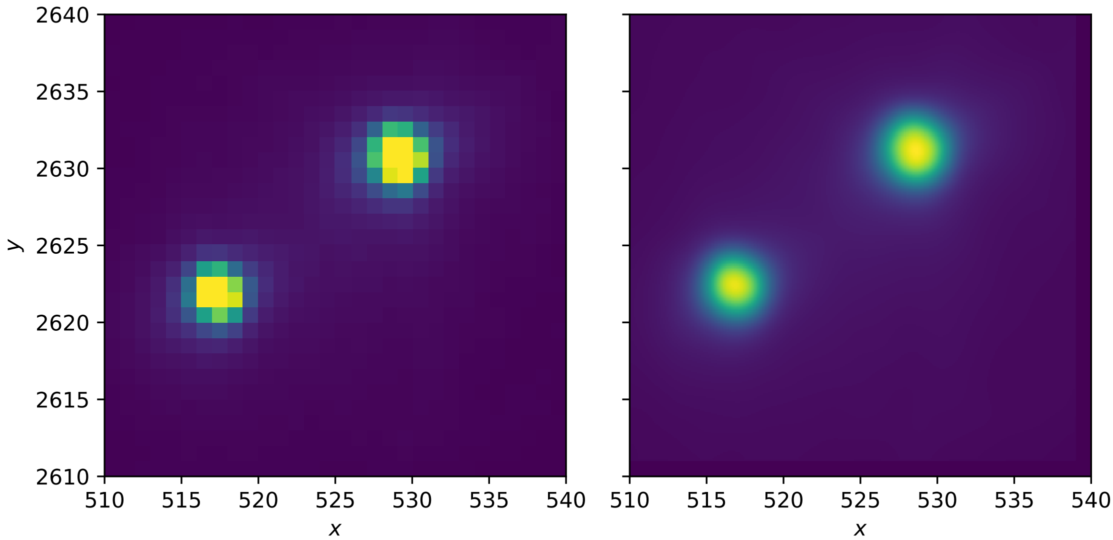

Figure 2.2: Comparison of a subset of a ThKr exposure frame before regridding (left) and after (right).

The centroids of the known emission lines are found by searching for the brightest pixels of the CCD, cutting out a region around the peak, and then creating a 20 times finer mesh to fit by interpolating using a third order two-dimensional spline interpolator. This interpolation is carried out because the emission line peaks can often be just a few pixels wide and therefore difficult to fit without the interpolation. Figure 2.2 displays a cut of an original ThKr frame which contains two intensity peaks from two emission lines, and the same region when it has been regridded to 20× its original resolution.

Once the finer image of the emission line are obtained, the median and standard deviation of the counts in each interpolated pixel are taken, and all pixels with counts less than the median plus double the standard deviation are discarded. However, if this leaves fewer than 100 of the new finer pixels, then the cut is the median plus one standard deviation. This step leaves just the very tip of the emission line peak to fit. The finding of the centroid of the emission line is then done using a "centre-of-mass" approach. This is done since the peaks can often be irregular non-Gaussian shapes. This is especially true for the brighter lines in the ThKr spectrum; the pixels at these peaks may have reached near their saturation limit, and the center-of-mass algorithm can still find the very center of the peak. Figure 2.3 displays the difference between the Centre of Mass finding and the two-dimensional Gaussian fitting methods of finding the x-y positions of the ThKr emission lines.

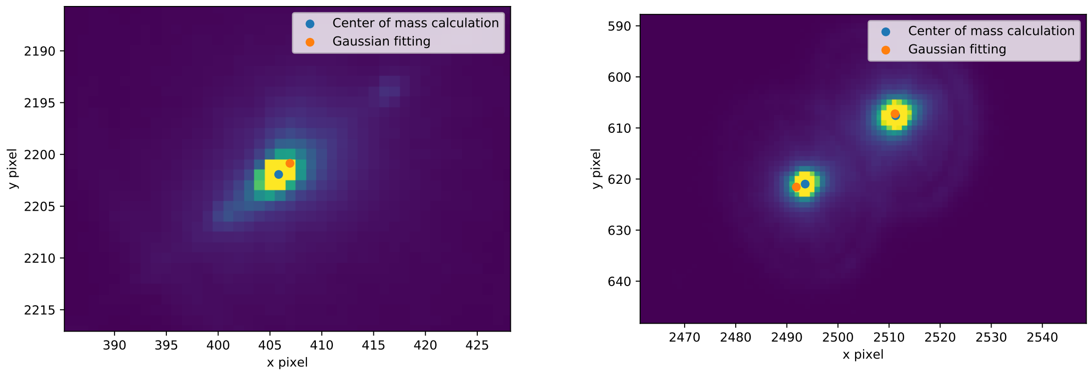

Figure 2.3: Images of two regions of a ThKr wavelength calibration exposure, both with a comparison of the two methods of the determination of the centroids of the emission lines; the Center of Mass determinations are in blue, and the Gaussian Fitting centers are in orange.

Once the x-y positions of the emission lines on the CCDs are found, they are then compared to a manually identified set of emission lines where both the x-y positions on the CCD and the wavelength of the intensity peaks are known. The unknown lines are then identified by using a machine-learning algorithm that compares the distance along the dispersion axis of the peaks in the identified and unidentified frames and their relative heights, and can therefore identify the relevant peaks in the unidentified frame. This algorithm was written by another student of Professor Katherine Blundell, so I will not elaborate further in this thesis.

Once as many peaks as possible are found and identified for all the ThKr frames in that night's directory, then we can use all of the position and wavelength information to take the mean x-y position across all the exposures and assigning the mean as the position of that emission line, and the standard deviation as the uncertainty. This has the benefit of combining the fits found with the longer and shorter exposure times. Longer exposures allow more peaks to be found but the brightest ones will often be saturated, making their centroids less accurate, but including the shorter exposure times means that those wavelength's peaks can still be found accurately. Outlier peaks are discarded. The locations of the emission lines, and the means and standard deviations, are saved in a database.

2.2.3 Choosing files to use for reduction night

The `Endeavour` reduction pipeline reduces a single night's observations from a single observatory at a time. In order for the reduction to go ahead, the following files need to be present in the observing night directory:

1. Astrophysical target observations.
2. LED flat field frames and Tungsten flat field frames.
3. The fitted x-y positions and known wavelengths of emission lines in ThKr wavelength calibration frames.
4. Dark calibration frames. We require at least one Dark frame at each of the exposure times we have in the light frames.
5. Bias calibration frames. These are Dark frames with an exposure time of 0 seconds, therefore measuring readout noise.

If the observation night contains no astrophysical target observations then it is skipped. If the night is missing any of the calibration or dark frames at a given exposure time, then the relevant calibration frames are taken from another observing night, from the same observatory, which is the closest time to the target observations; they are then used for the remainder of the reduction as if they originated from that night. It is important that any missing calibration frames are replaced from a night as close in time as possible to the target exposures so that any stochastic changes in the observatories which may affect the spectra, such as CCD deterioration or drifts in the position of the dispersion axis on the CCD, are kept to a minimum.

Once all the science and calibration frames that will be used for this observing night are collected, they are copied from GJW-DD onto GJW-DP where all of the calculations take place and temporary reduction files are stored.

2.3 Constructing the calibration frames

The ThKr, LED, Tungsten and Dark calibration frames are used in order to calibrate the science spectra and ensure that they are comparable and scientifically usable. This requires processing of these raw calibration frames in order to create different processed calibration frames. This processing for each of the different type of frames is described in this section.

2.3.1 Dark and bias frames

A master bias frame is first constructed for the observing night by taking the median average of each pixel value of all bias frames. This master bias frame is then subtracted from all other dark, target and calibration frames. Then the master dark exposure frames are constructed for each different exposure time required in the observing night by median average. These master darks are then subtracted from all target and light calibration frames.

2.3.2 Wavelength calibration frames

The λ calibration is done using the positions and wavelengths of the emission line peaks found in the ThKr frames earlier in the calibration. The ThKr emission line calibration from the closest (in time) observing night folder which has at least 12 unique peaks identified along the dispersion axis is chosen to build the wavelength calibration frame.

In order to build the calibration frames, a relation between wavelength λ and position (x, y) needs to be found. This is done by fitting polynomials to the x-y and x-λ relationships for the emission line peaks previously identified. This is demonstrated in Figure 2.4, which shows the residuals of the fits for λ and y with respect to x for an example night of ThKr frames for different orders of polynomials.

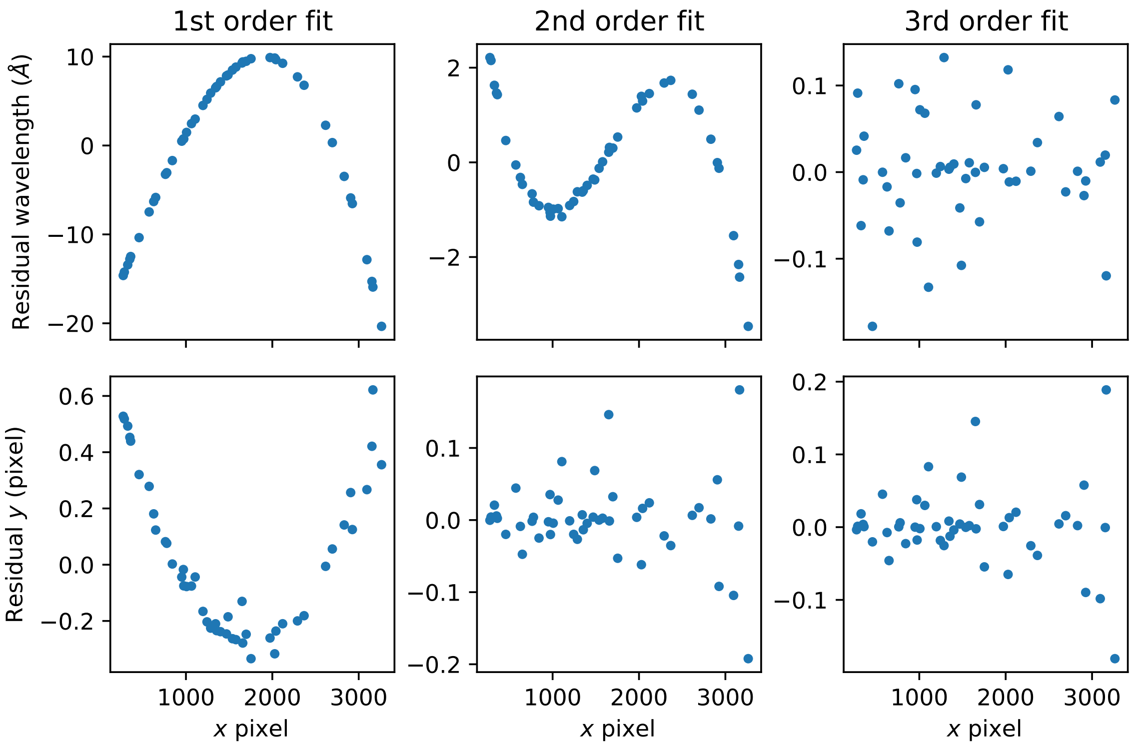

Figure 2.4: The residuals of the fit of differing order polynomials for λ as a function of x (top row) and y as a function of x (bottom row).

Figure 2.4 shows that the x-λ relationship is best described as a cubic, since the structure of the residuals disappears to random noise once a cubic is fit. The x-y relationship is, for similar reasons, best described by a quadratic relationship. These cubic and quadratic polynomial relationships need to be fitted for each observing night, since the orientation of the dispersion axis on the CCD may drift stochastically over time.

Using the relationships of x-λ and x-y, the wavelength, Λ, can be calculated for a pixel with arbitrary location (X, Y) on the CCD. This is found by calculating the intercept position, (x_0, y_0), on the quadratic x-y dispersion axis polynomial fit where

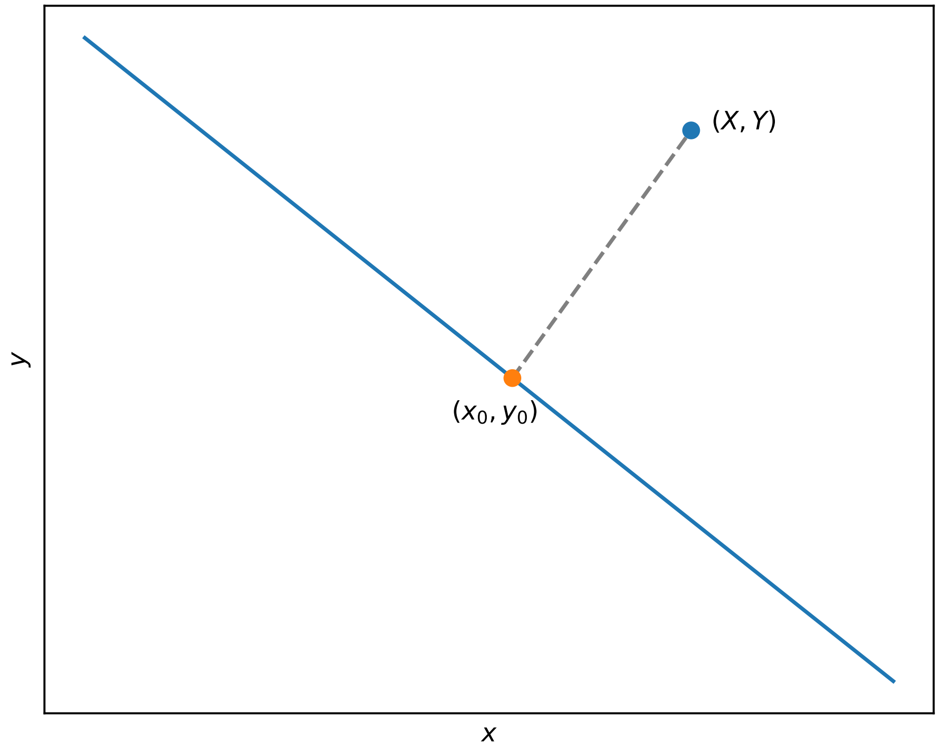

Figure 2.5: Determining the intercept position (x_0, y_0) on the dispersion axis for a point (X, Y) on the CCD. The point (X, Y) is assigned the same wavelength as (x_0, y_0) using the x-λ cubic relationship.

(X, Y) is normal to the curve. This is demonstrated in Figure 2.5. This intercept value of x_0 is used in the cubic x-λ polynomial in order to get the wavelength at that intercept point, so that $\Lambda = \lambda(x_0)$; that wavelength Λ is then assigned to the point (X, Y) on the CCD. This calculation is done for a ribbon with a width of 8 pixels above and below the dispersion axis along the whole CCD, assigning a wavelength to each point along the dispersion axis. A wavelength is therefore assigned to each pixel on the CCD, which is the first step to calculating the one-dimensional spectrum.

2.3.3 Flat field and pixel-by-pixel variation frames

The flat field frame is the illumination calibration frame to which the intensity of the science target frames will be compared in order to create the one-dimensional intensity vs wavelength spectrum, and the pixel-by-pixel variation frame gets divided from the science frames to remove any differences in the response function between the individual pixels; both of these frames are constructed using the Tungsten and

LED calibration frames.

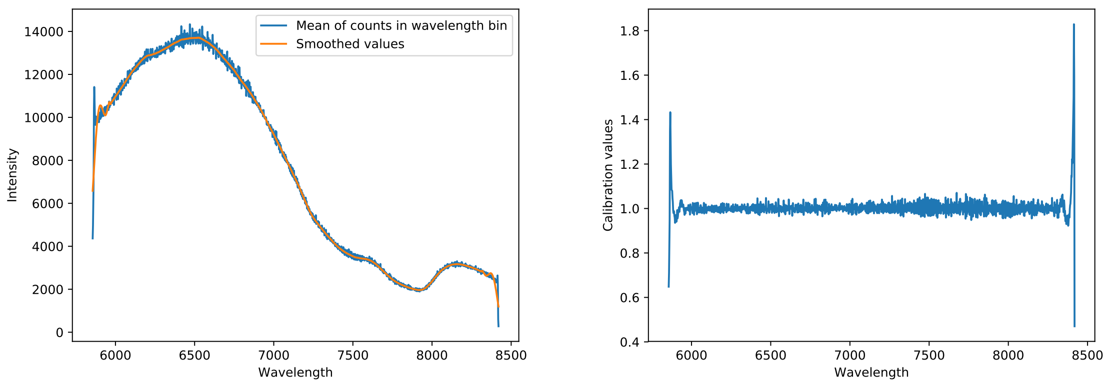

Figure 2.6: Left: The mean counts in the wavelength bins along the dispersion axis in the summed Tungsten and LED flats frame. Right: The wavelength dependence of the "gain" in the calibration frames. This is a multiplication of the illumination of the CCD and the response rate of each individual pixel.

The first step in creating both of these frames is to median-average the Tungsten and LED frames at each unique exposure time; these median frames at the different exposure times are then simply added together to create the summed-flat master frame. Then, a ribbon of 8 pixels vertically above and below the dispersion axis is extracted. 8 pixels is chosen to be suitably large so to contain all of the incident light along the dispersion axis; since the dispersion axis is diagonal across the CCD the width of the ribbon, when measured perpendicular to the dispersion axis, will be $\sim$6.4 pixels. Any under-illuminated pixels get discarded at a later stage. The mean counts of the pixels in the ribbon in 2 Å wavelength bins is calculated; this defines the illumination of the dispersion axis as a function of wavelength. A Savitzky-Golay filter (Savitzky & Golay 1964) is then applied to these illumination values along the dispersion axis in order to get a smooth illumination-wavelength function. This step is visualised in the left panel of Figure 2.6.

An illumination-wavelength value is then calculated for each pixel by interpolating the Savitzky-Golay-smoothed values from the wavelength bins (the orange line in the left panel of Figure 2.6) to the individual pixel's wavelength value. An "illumination-gain" frame of the CCD is then calculated by dividing each pixel's summed-flat frame values by its interpolated "calibration" value. This essentially normalises the counts in each pixel by the average number of counts in each wavelength bin in order to remove the wavelength dependence of the illumination, which is due to the LEDs and Tungsten frames not emitting equally at all visible wavelengths. The normalised "illumination-gain" along the wavelength range is shown in the right panel of Figure 2.6. This "illumination-gain" value is wavelength-independent and is a multiplication of the perpendicular-to-dispersion-axis illumination shape on the CCD in the calibration exposures and pixel-by-pixel gain variations of the CCD. Both of these effects need to be separated.

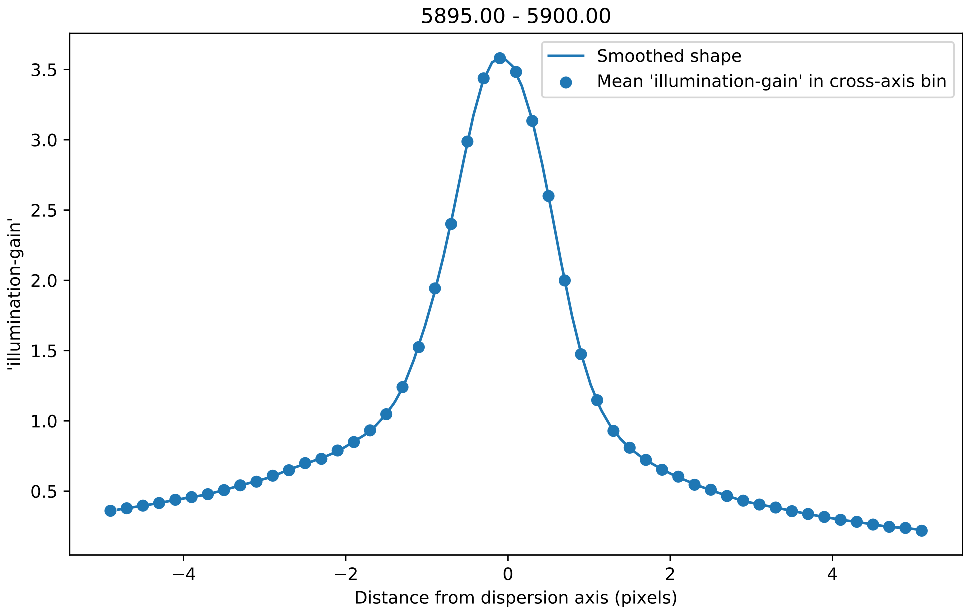

Figure 2.7: The mean "illumination-gain" values in the distance-from-dispersion bins for a typical wavelength bin, and the smoothed shape of the illumination across the dispersion axis in this wavelength bin.

The cross-dispersion shape and pixel gain are separated by splitting the "illumination-gain" frame into 5 Å wavelength bins along the dispersion axis, and then taking a Savitzky-Golay filter perpendicular to the dispersion axis in order to get the smoothed shape of the illumination perpendicular to the dispersion axis. Each pixel in each bin is then assigned an illumination value by interpolating the smoothed value by its perpendicular distance from the dispersion axis. The smoothing of the cross-dispersion shape in a typical wavelength bin is shown in Figure 2.7. These illumination values are then saved in a two-dimensional grid for each pixel to create the flat-field calibration frame, giving us the smoothed shape of the illumination of the CCD as a function of both x-y, and perpendicular distance from the dispersion axis.

The pixel-by-pixel gain variation frame is then calculated by dividing the aforementioned "illumination-gain" values by the smoothed illumination values of each pixel, giving us the different relative response rates of each pixel to illumination. An interpolated frame of three times the resolution of the illumination array is then created, along with a corresponding new wavelength-calibration frame of the same dimensions. The reason for creating these new, higher resolution calibration frames is explained in the next section.

2.4 Reducing the science data

Now all of the processed calibration frames are created, namely the master dark frames, the wavelength calibration map, the illumination map, and the pixel gain map, we can now move onto reducing the two-dimensional science frames to one-dimensional spectra.

2.4.1 Creating the summed science frames

For each observing night, both the individual astrophysical target frames are reduced, along with "Summed" science frames. The summed frames are created by taking a median-average of each pixel value for each target frame of a given object at each unique exposure time. Subsequently the summed frames and single frames are reduced identically. The summed frames are used since they are akin to taking longer exposure times of the objects, thereby increasing the SNR by the relationship in Equation 2.1.

2.4.2 Pre-extraction cleaning and interpolation

The first thing done to these bias-and-dark-subtracted target frames is dividing out the pixel-by-pixel response variations calculated in the previous section. The science frame is then regridded and interpolated in the same manner as the illumination calibration frame before. A resolution of three times the original CCD is chosen as this reaches the maximum signal to noise of the final one-dimensional spectrum - higher resolutions than this do not give any more improvement and cause more strain on computing resources. This regridding is done to minimize the effect of uneven illumination across individual pixels within the dispersion axis arising from the diagonal orientation of the dispersion axis. The two dimensional interpolation is calculated using a fifth-order polynomial in order that all the details of the illumination of the science frame are captured in maximum detail.

2.4.3 Extracting the one dimensional spectrum

Once the final regridded and interpolated science and illumination frames are made, a strip of the science, wavelength and illumination values are extracted up to 8 pixels vertically above and below the dispersion axis. The pixels which have a calibration pixel value less than 0.5 are then cut; this ensures that all of the pixels are illuminated enough in order to extract useful information. Generally this leaves the pixels which are within ∼3.5 pixels of the dispersion axis to be reduced. This corresponds to a little over two pixels on either side perpendicular to the dispersion axis. All of these science and calibration intensity pixels are then split into wavelength bins of 0.3 Å. These will be the final wavelength bins of the one dimensional spectra. To minimize outlying pixel-intensity values in the science frames the mean and standard deviation of the science frame intensities in each wavelength bin are calculated; any pixels which have counts more than two standard deviations away from the mean are then discounted from further analysis.

The paradigm for the extraction method is that the light on the CCD has the same shape perpendicular to the dispersion axis for both the flat-field frames and the science frames, but with varying amplitudes in the science frame. Therefore the intensity of the spectrum in wavelength bin i, I_i, can be given as the ratio of the science frame intensity values, S_i, to the calibration frame intensity values, C_i. This ratio should be constant for all pixels in the wavelength bin, which is a perpendicular slice of the dispersion axis, given the light is dispersed the same way onto the CCD in both the science and calibration frames. Multiple methods which may be used to calculate the ratio of the science pixel values in bin i to the calibration pixel values. They are:

1. The mean of the division of the pixel values by the calibration values:
$$I_i = \frac{1}{N} \sum_{k=0}^{N-1} \frac{S_i^k}{C_i^k}, \tag{2.2}$$
where N is the number of pixels in the wavelength bin, and k denotes the kth pixel in the wavelength bin and runs from 0 to $N-1$.

2. The mean of the science pixel values divided by the mean of the calibration values:
$$I_i = \frac{\sum_{k=0}^{N-1} S_i^k}{\sum_{i=0}^{N-1} C_i^k}, \tag{2.3}$$
where the symbols mean the same as in Equation 2.2.

3. The gradient of a first order polynomial fitted to S_i against C_i. By this paradigm, `Endeavour` calculates the intensity value for a wavelength bin by fitting a first order polynomial to the science target intensity values versus the illumination calibration values in the wavelength bin; the gradient of this straight line fit is then the intensity value. This is akin to the traditional method of taking an average of the science values divided by the calibration values, but reduces the noise induced by lower signal-to-noise pixels further from the dispersion axis. For the fit, each science point is given an uncertainty associated with the $\sqrt{N}$ Poisson-distributed uncertainty in the pixel counts in both the original dark and science target frames. The associated uncertainty in the intensity in that wavelength bin is then the uncertainty in the gradient in the straight-line fit. Figure 2.8 demonstrates how the one-dimensional spectrum is extracted, using the example of the Si II 6347 emission line in GG Car's spectrum. The top-left panel displays the science dispersion axis in x-y space on the CCD around the emission line. The top-right panel shows the illumination calibration frame for the same pixels on the CCD. The pixels are split into wavelength bins 0.3 Å wide. The bottom-left panel displays the science pixel values plotted against the calibration pixel values for some of these bins, which are separated by 2 Å are plotted in the figure, for clarity. The pixel values in each wavelength bin are plotted in a different colour. A straight line is fitted to each of the points in each wavelength bin, and the gradient is extracted. The panel on the bottom-right shows the gradient extracted versus wavelength for these selected

wavelength bins; these therefore correspond to the one-dimensional intensity of the spectrum in these wavelength bins.

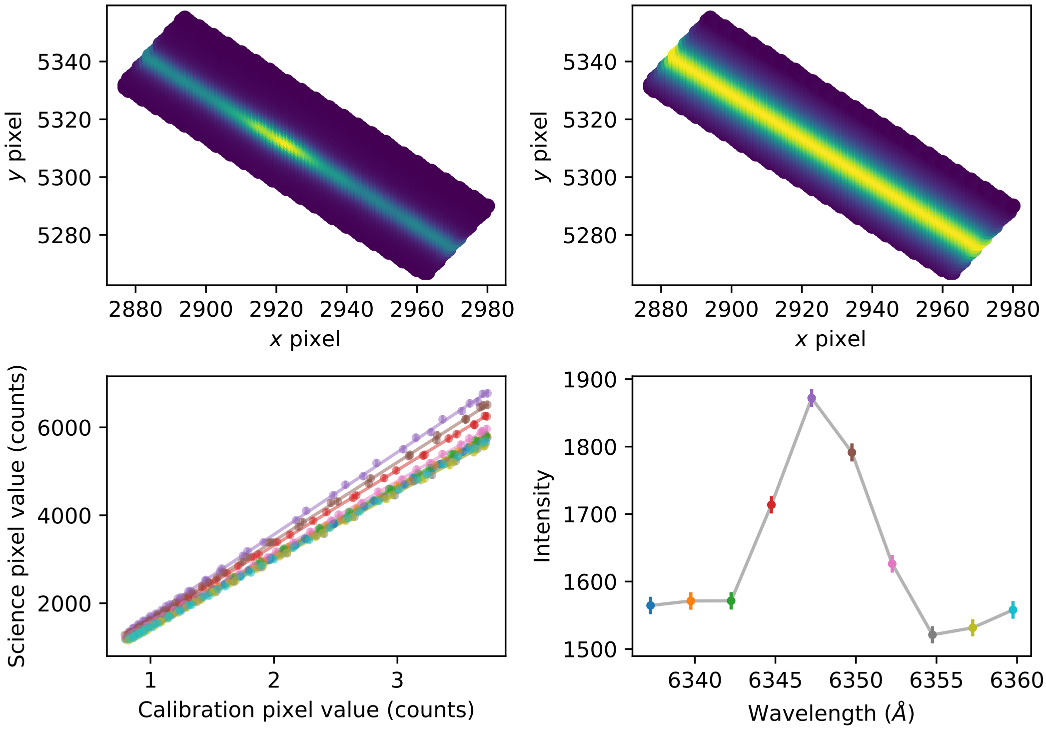

Figure 2.8: Demonstration of how the one-dimensional spectrum is extracted. The top-left panel displays the two dimensional spectrum around the Si II 6347 emission line in an example GG Carinae target spectrum. The top-right panel shows the corresponding calibration values for the same pixels. The pixels are binned according to wavelength with bins 0.3 Å wide. The bottom-left panel shows the science versus calibration pixel values for selected wavelength bins for this demonstrative figure which are separated by 2 Å, along with the linear relationships fitted to the pixel values. The panel on the bottom-right shows the resulting one-dimensional spectrum; the colour of the points corresponds with the colours of the points and lines in the bottom-left panel. In the true final spectrum, the intensity for each wavelength bin is extracted.

Figure 2.9 displays how the different extraction methods compare for two demonstrative sections of the spectrum of GG Carinae (GG Car). The left panel shows how the extraction methods fare on a section of the spectrum which contains three metal lines and is in a low signal-to-noise regimen. The gradient method of extraction is more effective in resolving the metal lines, and there is less noise in this spectrum. The [O I] 6300 line is barely perceptible in methods 1 and 2, but is very clear in method 3.

Similarly the right panel shows how the different extraction methods fare on GG Car's H-alpha complex, which is a very high signal-to-noise part of the spectrum; like the low signal-to-noise region, the gradient method is the most able to resolve the blue shoulder of the emission line. High resolution experiments, such as FEROS which has a very high resolving power $R = \lambda/\Delta\lambda \approx 48\,000$ (Kaufer et al. 1999), show that there is a deep blue-ward absorption in the H-alpha complex of GG Car. Figure 2.10 displays the average H-alpha complex of GG Car, as observed by FEROS, along with the profile convolved with Gaussian profiles to transfer R to 4000, 6000, and 8000 to simulate what the H-alpha complex would appear like for observing programs of those resolving powers.

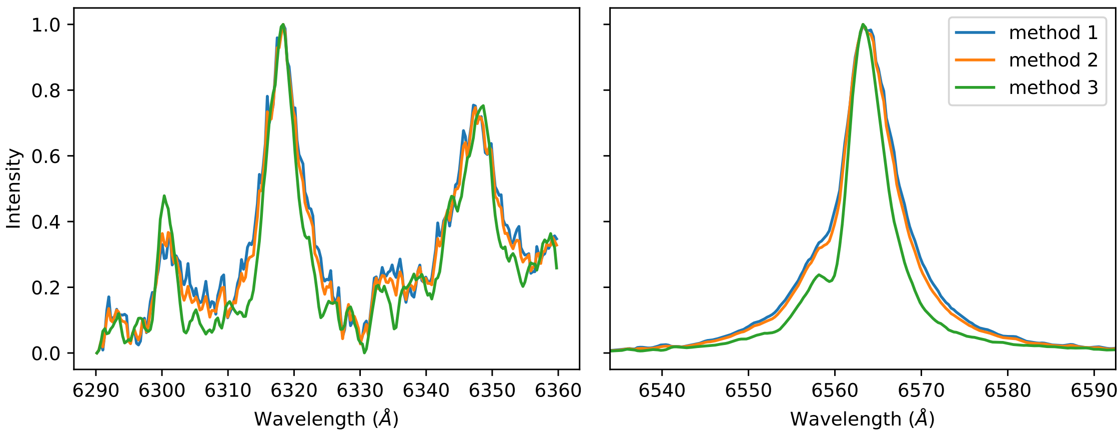

Figure 2.9: Comparison of the different extraction methods of two regions of two GJW GG Car spectra taken on the same observing night. The left panel is taken from a 1000 s exposure, and displays the [O I] 6300, Fe II 6318, and Si II 6347. The right panel displays the H-alpha line from a 100 s exposure. Method 1 corresponds to calculating the intensity in a bin using Equation 2.2; method 2 calculates the intensity using Equation 2.3; and method 3 calculates the intensity by fitting the gradient of the science vs calibration count relationship. The spectra have all been normalised and offset so that the intensity ranges from $0 \to 1$.

Comparing the H-alpha profiles calculated using the different extraction methods in Figure 2.9, right panel, to the convolved H-alpha profiles of Figure 2.10 the profiles calculated using the traditional methods 1 and 2 extract the H-alpha profile with a resolving power of $R \sim 4000$. However method 3, using the gradient extraction method, resolves it to have $R \sim 6000$. Since the gradient method is superior at resolving the spectra, and additionally minimises noise in the spectra, it is the chosen method to reduce spectra in `Endeavour`.

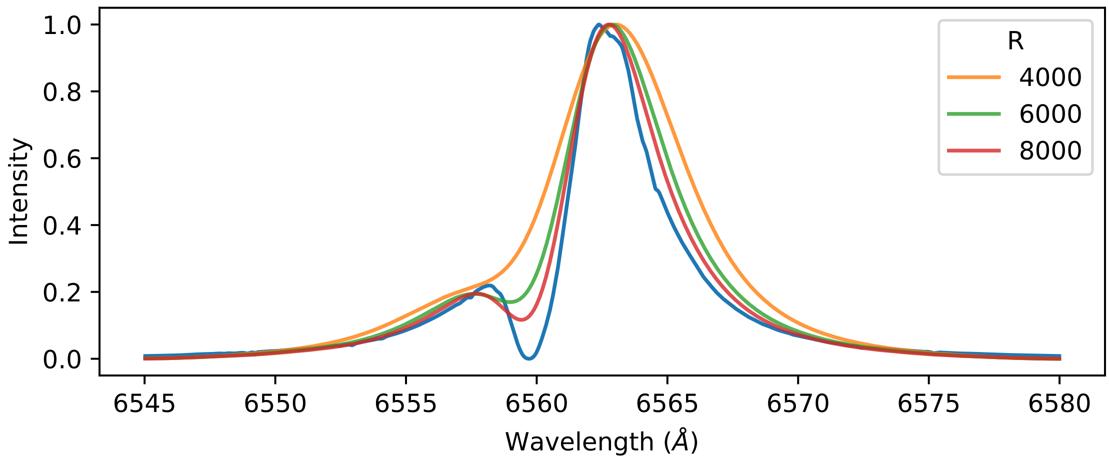

Figure 2.10: The H-alpha complex of GG Car as observed by FEROS (blue line), which has resolving power $R = \lambda/\Delta\lambda \sim 48\,000$. The FEROS line profile is convolved with Gaussians to transfer it to $R = 4000$ (yellow), 6000 (green), and 8000 (red).

Method 3 more effectively resolves the spectra due to the relative lower-weight that is given to the lower signal-to-noise pixels, which are further from the dispersion axis, using this gradient extraction. The lower signal pixels will be more affected by light of wavelengths corresponding to neighbouring wavelength bin's wavelength but which, due to the finite spectral resolution of the spectrograph, land in the wavelength bin of interest. Therefore, reducing the input from these outer pixels reduces the adverse effect of this light from brighter wavelengths on neighbouring wavelength bins, thereby increasing the effective output spectral resolution. These outer pixels are still useful in adding statistics to the intensity calculations, and their removal leading to noise in the final spectra. Therefore, including the outer pixels but minimising their relative weighting using the gradient method maximised the quality and fidelity of the final spectra.

The methods of interpolating the frames to a finer mesh and gradient extraction have lead to improvements in the signal-to-noise and spectral resolution in the final one-dimensional spectrum, respectively. These improvements are displayed in sample GG Car spectra in Figure 2.11. The spectra are the same as in Figure 2.9. There is a regular noise profile in the non-interpolated spectrum which is minimised in the interpolated spectrum. The noise profile is partially due to the diagonal dispersion axis over the CCD, which leads to the most intense center of the dispersion axis grazing some pixels and going through the centers of others. Since the CCD is a grid, and the dispersion axis is a straight line on the order of a few pixels, this leads to a repeating pattern of some wavelength bins receiving counts more efficiently than others. Interpolating the two-dimensional spectrum to a finer mesh, and therefore having smaller pixels and wavelength bins, minimises this effect. It was found that interpolating to a 3× finer grid agreeably minimises the noise profile without unacceptably increasing computational time of calculating the spectra and calibration frames.

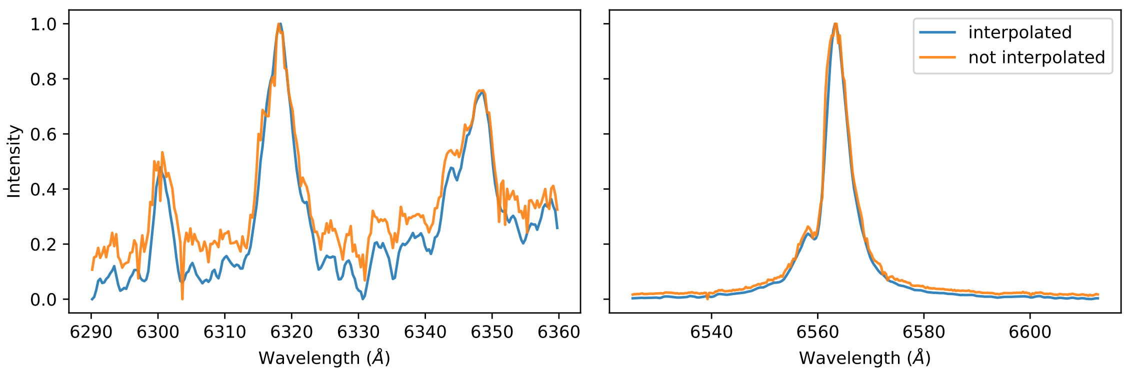

Figure 2.11: Sections of the one-dimensional spectrum of GG Car when it is extracted after interpolating the two-dimensional spectrum to a 3× finer mesh (blue) and when not interpolating (orange). The wavelength ranges and spectra are the same as in Figure 2.9, and the spectra are extracted using the same "gradient" method 3 from that Figure.

Once the intensity is calculated for all of the wavelength bins in the spectrum, the spectrum and its uncertainty are written to file. These files give the fully reduced, one dimensional Global Jet Watch spectra. These finished spectra are then saved onto GJW-DR, and the temporary files that were stored on GJW-DP are deleted.

2.5 Wavelength correction using atmospheric absorption

Since there is often a temperature difference in the observatories between when the wavelength calibration ThKr frames are taken and the target exposures are taken, there may be thermal contraction in the spectrograph and camera architecture which can cause the dispersion axis to slightly drift across the CCD. This can lead to inaccuracies in the wavelength calibrations of the GJW spectra which can be up to 1 Å in magnitude.

In order to correct for this, the atmospheric absorption features in the one-dimensional spectra are used to correct each individual spectrum's wavelength. The shift in wavelength for a spectrum at the Telluric A band region is easy to extract using a cross-correlation method, correlating the spectrum's absorption feature with the average spectrum of all of the Telluric A features for that object. The shift with the maximum correlation is then the shift which is required to get that region to its correct wavelength. This makes the assumption that there are enough one-dimensional spectra of the object reduced such that their average spectrum has a Telluric A features which are at the correct position, otherwise there may be a systemic offset of the wavelengths for the given object.

The cross-correlation of the Telluric A band correction is demonstrated in Figure 2.12. The top panel shows the correlation of a target spectrum's Telluric A band with the average spectrum's Telluric A band; the correlation peaks at 0.7198 Å, which we call $\Delta\lambda$. Therefore $\Delta\lambda$ is the shift in wavelength required to correct the calibration in this region. The bottom panel shows the average Telluric A band in blue, the uncorrected target spectrum in orange, and the corrected target spectrum in green.

This $\Delta\lambda$ correction could be applied to the entire spectrum, however the thermal expansion will not create a zeroth-order shift in wavelength. Instead there may be a translation and a rotation of the dispersion axis will lead to a distortion of the wavelength calibrations which is non-uniform along the spectrum. Therefore, a method to translate the shift at the Telluric A band to the entire spectrum would lead to an even more accurate wavelength calibration. Here I describe the method used to implement the wavelength corrections along the entire target dispersion axis.

From fitting the peaks in the ThKr wavelength calibration frames, we know both their x-y pixel and x-λ polynomials. We will call these $y_{\mathrm{ThKr}}(x)$ and $\lambda_{\mathrm{ThKr}}(x)$ respectively. Then, for the target exposure frame, the y position of the centre of the dispersion axis at every x pixel is determined and a quadratic is fit to the relationship, which gives the x-y polynomial target spectrum, which we will call $y_{\mathrm{target}}(x)$. The aim of this work is to determine the true relationship of wavelength against x-pixel

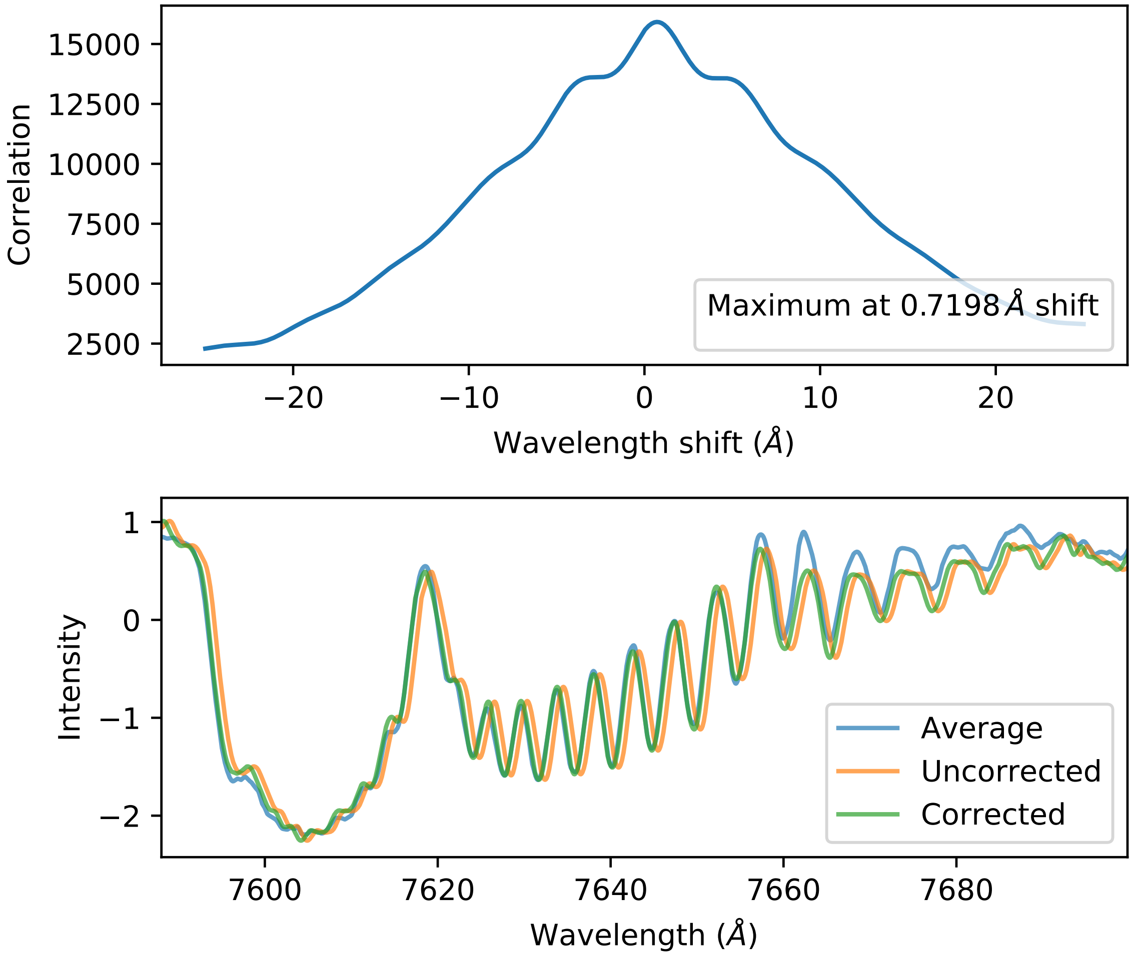

Figure 2.12: Top panel: The correlation of a GG Carinae spectrum's Telluric A band absorption feature with the median Telluric A band absorption, as a function of wavelength shift. Bottom panel: The correction applied to the spectrum in this region (blue is the average spectrum, orange uncorrected, green corrected).

in the target spectrum, which is currently unknown. We will call this relationship $\lambda_{\text{target}}(x)$.

This can be done if it is assumed that rate of change of the wavelength as a function of the distance, D, travelled along the dispersion axis is approximately the same for the ThKr frame and the Target frame, such that

$$\frac{d\lambda_{\text{Thkr}}}{dD} \approx \frac{d\lambda_{\text{target}}}{dD}. \tag{2.4}$$

This can be safely approximated since the changes in the dispersion axes are small, and are a simple rotation and translation of the axis on the CCD. The distance along the dispersion axis is calculated for each frame as a function of x, and is given by the standard path integral

$$D(x) = \int_0^x \sqrt{1 + \left(\frac{dy}{dx}\right)^2}\, dx. \tag{2.5}$$

$\lambda_{\text{ThKr}}(x)$ can be recast into $\lambda_{\text{ThKr}}(D)$ directly for the ThKr frames. $\lambda_{\text{target}}(D)$ is calculated as

$$\int_{D_0}^{D} \frac{d\lambda_{\text{target}}}{dD}\, dD = \int_{D_0}^{D} \frac{d\lambda_{\text{ThKr}}}{dD}\, dD, \tag{2.6}$$

$$\lambda_{\text{target}}(D) - \lambda_{\text{target}}(D_0) = \lambda_{\text{ThKr}}(D) - \lambda_{\text{ThKr}}(D_0), \tag{2.7}$$

and therefore

$$\lambda_{\text{target}}(D) = \lambda_{\text{ThKr}}(D) - \lambda_{\text{ThKr}}(D_0) + \lambda_{\text{target}}(D_0), \tag{2.8}$$

where D_0 is a reference distance along the target dispersion axis which has a known wavelength. If D_0 is chosen such that it corresponds to the mid-point of the Telluric A band, then we know that $\lambda_{\text{target}}(D_0) = \lambda_{\text{true}} = 7638\,\text{Å}$. The corresponding path length on the target dispersion axis, D_0, needs to be determined in order to calculate $\lambda_{\text{ThKr}}(D_0)$. We know that D_0, and its corresponding x value, x_0, is the point at which the true wavelength on the target dispersion axis is equal to λ_{true}. We know that $\lambda_{\text{ThKr}}(x)$ is wrong by a value of $\Delta\lambda$ at x_0 using the Telluric A correlation previously described; therefore, $\lambda_{\text{true}} = \lambda_{\text{ThKr}}(x_0) + \Delta\lambda$. We can therefore solve $\lambda_{\text{ThKr}}(x) + \Delta\lambda - \lambda_{\text{true}} = 0$ for x to give us x_0, and then calculate D_0 using Equation 2.5 by calculating the path integral of $y_{\text{target}}(x)$ from 0 to x_0. This value of D_0 is then used in the $\lambda_{\text{ThKr}}(D)$ polynomial to give us $\lambda_{\text{ThKr}}(D_0)$. Now Equation 2.8 may be used to calculate the corrected wavelengths of the target spectrum, having calculated the path length D associated with each wavelength bin in the target spectrum.

The calculated wavelength correction for a target spectrum against the original uncorrected wavelength is shown in Figure 2.13. This is the correction for the same example spectrum in Figure 2.12; note that at the wavelength of the Telluric A band (7638 Å) the correction matches the maximum correlation shift of the band found earlier (0.7198 Å). Therefore, from using the known x-y relations of the dispersion axes of the Target frame and ThKr frame across the CCD, the x-λ relation of the

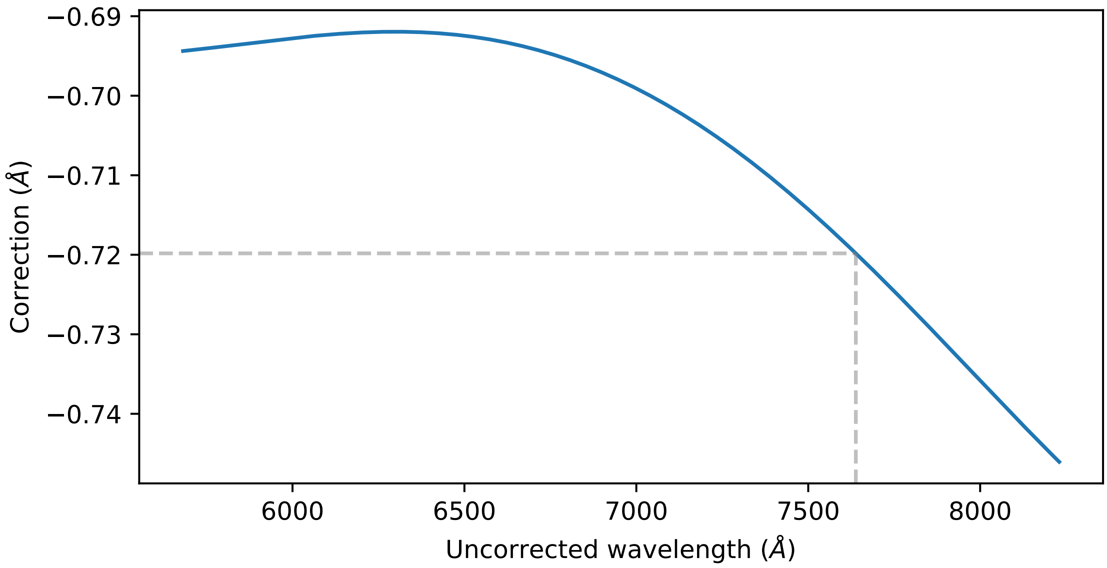

Figure 2.13: Wavelength correction as a function of the uncorrected wavelength for the same example GJW spectrum as shown in Figure 2.12. A horizontal, grey line corresponds to the measured wavelength shift in Figure 2.12, and the vertical line corresponds to the mid-wavelength of the Telluric A band.

dispersion of the ThKr frame, and finding the value by which the wavelength calibration is wrong at a known point, it is possible to correct the wavelength calibrations across the whole target spectrum to a more accurate value.

After this process, the corrected wavelength is then saved in the one-dimensional spectrum data file and we have our fully processed target spectrum.

Chapter 3

The B[e] supergiant binary GG Carinae: an introduction

Abstract

In this chapter, the in-depth case study of the B[e] supergiant binary GG Carinae (GG Car), which forms a large part of this thesis, is introduced. Section 3.1 reviews previous work and the historical understanding of GG Car; Section 3.2.1 introduces the available V-band photometry of GG Car; Section 3.2.2 describes the available TESS photometry of GG Car and how it was obtained; Section 3.2.3 describes both the Global Jet Watch (GJW) and FEROS spectroscopy of GG Car; Section 3.3 determines the luminosity of the primary of GG Car and determines its place in the Hertzprung-Russell diagram, comparing it to stellar evolution models, and estimates the mass of the primary; Section 3.4 and 3.5 briefly describe the mid-resolution and high-resolution spectra of GG Car, respectively.

GG Car's *Gaia* parallax is used to determine a distance to the system of $d = 3.4^{+0.7}_{-0.5}\,\mathrm{kpc}$, and find the luminosity of the primary $L_{\mathrm{pr}} = 1.8^{+1.0}_{-0.7} \times 10^5\,L_\odot$. The mass of the primary is constrained to $M_{\mathrm{pr}} = 24 \pm 4\,M_\odot$. The radius of the primary is found to be $R_{\mathrm{pr}} = 27^{+9}_{-7}\,R_\odot$, and its age in the range 5–10 Myr.

3.1 Introduction

GG Carinae (GG Car, also referred to as HD 94878 and CPD-59 2855) is an enigmatic Galactic binary which has been studied for over a century due to its peculiar spectroscopic and photometric properties. Despite the history of study, satisfying explanations of its variability, binary orbital solution, and circumstellar environment have remained elusive. In this section, I review previous studies of GG Car in the literature, and the evolution of the understanding of this object.

3.1.1 Early work on GG Carinae and the determination of its orbital period

The earliest published mention of GG Car comes from Pickering & Fleming (1896), who simply noted that its spectrum is "Peculiar. Resembles η Carinae". Cannon (1916) then classified GG Car as hosting a P-Cygni-type spectrum, characterised by bright hydrogen and helium lines.

The binarity of the system has long been hinted by its variability. The photometric variability of GG Car was first reported in Kruytbosch (1930), who discovered a periodicity of 31.043 days. They also noted that "occasionally plates from the same night showed noticeable differences in brightness", giving a very early indication of the short-period variability which is discussed in Chapter 5 of this thesis. Kruytbosch (1930) observed that, even in the context of variable stars, GG Car displays unusual behaviour. They concluded "Variations in light of a regular or semi-regular character in a short period, as shown by [GG Car], were not known before in the case of a star with a spectrum of the P Cygni type. The star forming the object of this note is therefore of special interest and deserves further attention". Hoffleit (1933) confirmed the photometric period determination of Kruytbosch (1930) in a study of variable stars exhibiting P-Cygni spectra, but argued that the 31-day photometric period was half the true orbital period of the binary. They argued that GG Car should be understood as an eclipsing binary, with two photometric minima per orbital period. Due to the system only having one photometric minimum every 31 days, it was therefore for long unclear whether the true orbital period of the binary was 31 or 62 days.

Greenstein (1938) determined the periodicity of the photometry of the system to be $\sim$31 days, but agreed with Hoffleit (1933) that this should be half of the orbital period. Greenstein (1938) also observed that at least one of the stars in the binary must be variable, and that the lightcurve is peculiar with the individual photometric cycles being variable.

Hernandez et al. (1981) were the first to study time-series spectroscopic variability of GG Car. They observed radial velocity variations in Balmer P Cygni absorption centers, and Fe II and [Fe II] emission, determining a spectroscopic period of 31.030 days. The measurement of the spectroscopic variability confirmed the binarity of the system, and showed that the orbital period was ∼31 days. They reported that the system is surrounded by an expanding envelope of $\sim$130 km s^{-1}, which precludes the observation of the stars' photospheric lines. They noted that the amplitude of the radial velocity variations are smaller for the Fe lines than for the P Cygni absorption components. They fitted the orbital elements of the binary of GG Car, however, they conceded that these are unlikely to be the true orbits of the binary since the system is surrounded by an optically thick envelope which precludes the detection of the stars' photospheric absorption lines. It would later be known that this observation is typical of B[e]SGs.

Gosset et al. (1984) however also argued that the photometry of the system is best described by a 62-day period based on photometric measurements, despite Fourier analysis indicating a ∼31-day period. In their Fourier analysis of the light curve, they additionally noted a significant periodicity at a frequency of $\sim$0.6356 day^{-1} (1.6 days). However, Gosset et al. (1985) then reassessed the orbital period of GG Car in a spectroscopic study and revised the period to 31.02 days, agreeing with Hernandez et al. (1981). They noted that both the average velocity and the amplitude of variations of the hydrogen "envelope" emission increase as a function of Balmer number, which could be due to an expanding envelope. They noted that the light curve cannot be explained in the traditional eclipsing binary paradigm.

Despite these studies being able to indubitably determine that the binary's orbital period is ∼31 days via spectroscopy, an accurate determination of GG Car's binary orbital solution has remained elusive due to the aforementioned lack of photospheric absorption lines in the system. The confusion as to the photometric period arises from long- and short-period variability in the system, which causes successive orbits' lightcurves to be non-identical (Gosset et al. 1984; van Leeuwen et al. 1998; Krtičková

& Krtička 2018).

Brandi et al. (1987) found that the UV spectrum of GG Car is complex, dominated by Fe II absorption lines but contains absorption by other species and ionisations, and that the width of absorption features increases with ionisation stage. They pointed out some characteristics of GG Car that need to be taken into consideration while constructing a model: the Balmer lines display P-Cygni profiles during the whole light curve, originating in an accelerated envelope; the radial velocities show different amplitudes between lines, and even between emission and absorption components of the same line, implying that the envelope is stratified and not spherically symmetric; absorption lines appear in He I lines at the brightest point in the system's light curve; smaller scale variations are also present, along with the main 31-day period; and that the binary is eccentric. Similarly Krtičková & Krtička (2018) found that there is significantly more absorption than emission in the UV emission lines of GG Car. Additionally, Krtičková & Krtička (2018) were unable to observe any clear periodicities in the UV continuum fluxes, despite the variability in the V-band; however, they noted that the orbital variability may have been obscured by short-period variability of one of the components, and that this component dominates the UV spectrum of GG Car.

A measurement of the binary orbital solution was calculated by Marchiano et al. (2012) by measuring the radial velocities of He I absorption, which they interpreted as photospheric absorption in the stars. They found the binary to have a period of 31.033 ± 0.008 days. However, in Chapter 4 I show that their assumption that these absorption lines originate in the photospheres of the stars is flawed, and that therefore the Marchiano et al. (2012) orbital solution is inaccurate. I then calculate a new, accurate measurement of the orbital solution of the binary.

3.1.2 GG Carinae as a B[e] supergiant

Allen (1973) was the first to observe infrared excess in the the spectrum of GG Car, indicating re-radiation from circumstellar dust as is now known to be typical of B[e]SGs. Swings (1974) first reported observed GG Car's [O I], [Fe II] and Fe II emission lines, and noted splitting in the Fe II emission lines. They suggested a thin equatorial ring rotating at $\sim$30 − 35 km s^{-1} around the star. This was the first indication that the object had a disk-like structure in its circumstellar environment. McGregor et al.

(1988) and Lopes et al. (1992) both showed that the system is very luminous, with $\log(L/L_{\odot}) \gtrsim 4.7$, though these measurements were hampered by inaccurate distance determinations to the system. The studies determined significant mass-loss rates of the star of $\sim 2.5-5.7 \times 10^{-6} M_{\odot}\,\mathrm{yr}^{-1}$. Lamers et al. (1998) classified GG Car as a B[e]SG due to these previous works, noting these studies' observations of the B[e] phenomenon in the object; its high luminosity; indications of mass loss through P Cygni line profiles; and its hosting of a hybrid spectrum of narrow emission lines and broad absorption features.

Both Barbier & Swings (1982) and Gnedin et al. (1992), trying to determine the geometry of the circumstellar envelopes of peculiar stars, found that the light from GG Carinae is significantly polarised and that there are significant differences in the level of polarisation between the two studies' epochs (1979/1980 vs 1989). However, they were not able to discern much information about the conditions leading to this polarisation. Pereyra et al. (2009) found that H-alpha emission is polarised, indicating that the emission originates at least in part from an optically thin rotating disk. The continuum flux around H-alpha does not display significant polarisation. Pereyra et al. (2009) was unable to determine whether the H-alpha originates from a circumstellar or a circumbinary disk.

GG Car exhibits strong molecular CO bandhead emission in the infrared spectrum (McGregor et al. 1988; Morris et al. 1996; Kraus 2009; Oksala et al. 2013; Kraus et al. 2013). Kraus (2009), studying the CO bandhead emission in B[e] supergiants, found a $^{12}\mathrm{C}/^{13}\mathrm{C}$ ratio of $\lesssim 10$ in the circumstellar environment of GG Car. This confirms that GG Car is a post-main sequence object due to the enrichment of the heavier isotope. The authors noted that the $^{13}\mathrm{CO}$ emission is much stronger in GG Car than is expected for their models; they concluded that the star must either be much more luminous (and therefore massive) than found by McGregor et al. (1988) or the star is rotating at a much quicker rate than the $300\,\mathrm{km\,s^{-1}}$ that they assumed in their models. Marchiano et al. (2012) studied GG Car's spectral energy distribution and were able to fit contributions of the B[e]SG primary, a gaseous envelope, and a dusty envelope. They found that the primary in GG Car is more luminous than determined by McGregor et al. (1988). With the new luminosity and temperature determination of the primary of GG Car, the tension noted by Kraus (2009) was resolved. The $^{12}\mathrm{C}/^{13}\mathrm{C}$ ratio measured from CO emission present in the system suggests that the primary is in an early, pre-red supergiant, evolved stage of its post-main sequence evolution (Kraus 2009; Kraus et al. 2013; Oksala et al. 2013). However, their determination assumes that the two binary components have evolved as pseudo-single stars, and it also assumes that the rotational velocity used in the models is accurate (Kraus 2019).

Kraus et al. (2013) determined that the CO bandhead emission in GG Car originates in a thin CO circumbinary ring orbiting at $\sim$80 $\mathrm{km\,s^{-1}}$ projected onto the line of sight, and suggested that the circumbinary disk was formed during a classical Be phase of the primary while the primary was still on the main sequence. Maravelias et al. (2018) studied GG Car's forbidden optical emission lines and found [Ca II] and [O I] emission lines originating from the same region as the CO emission, and another [O I] ring orbiting with a projected velocity of $\sim$30 $\mathrm{km\,s^{-1}}$. They determined the systemic velocity of the system to be $-22\,\mathrm{km\,s^{-1}}$ using these circumbinary lines. Therefore, GG Car hosts a complex circumstellar and circumbinary environment consisting of thin, concentric atomic and molecular rings, and a dusty envelope, typical of B[e]SGs, as described in Section 1.2.

In contrast to the well-identified primary, the class of the secondary component of GG Car is undetermined. The system was observed in the X-ray band by the SWIFT mission, and the data are available in the 1SXPS catalogue (Evans et al. 2013). There was a "poor" detection of X-rays from the system, not significantly above the background level. This indicates that GG Car is not a significant source of X-ray radiation, and it is unlikely the system is an X-ray binary or a highly energetic colliding-wind binary such as η Carinae (Pittard et al. 1998).

Therefore GG Car, with its unexplained photometric and unusual spectroscopic variability at the orbital period, indications of variability at shorter periods, poorly determined orbital solution, and its displaying of the unexplained B[e]SG phenomena, show that it is a poorly understood object, even in the context of the poorly understood B[e] stars. Studying GG Car in detail can help us to understand the B[e]SG phenomenon and its origin, the physics of massive, mass-losing, post-main sequence stars in binary systems and the shaping of the circumstellar environment.

3.2 Observations

In this Section, I introduce and describe the photometric and spectroscopic observations of GG Car that are analysed in this thesis.

3.2.1 V-band photometry

V-band photometric data of GG Car are available from the All Sky Automated Survey (ASAS: Pojmański 2004; Pojmański & Maciejewski 2002)[1]; the Optical Monitoring Camera (OMC: Mas-Hesse et al. 2003) aboard the Integral Satellite[2]; and the All Sky Automated Survey for Supernovae (ASAS-SN: Shappee et al. 2014; Kochanek et al. 2017)[3]. Each of these surveys uses standard Johnson V-filters, centred at 550 nm and with a full width half maximum of 88 nm. Details of the observations used in this study for each survey are given in Table 3.1.

Survey	N_{obs}	Median m_V [mag]	Date range	Median σ_{m_V} [mag]
ASAS	387	8.66	2000-12-08 – 2009-03-28	0.025
OMC	1654	8.62	2003-01-29 – 2019-01-27	0.013
ASAS-SN	632	8.69	2016-02-05 – 2018-07-22	0.010

Table 3.1: The number of observations, median magnitude m_V, date range, mean cadence, and median error σ_{m_V} for the V-band photometric data of GG Car for each survey used in this study.

The ASAS-SN lightcurve for GG Car is calculated using the `Sky Patrol` feature on the ASAS-SN website, where the user can enter any celestial coordinate and return a light curve. Ostensibly the saturation limit for the ASAS-SN cameras is around the 10th magnitude, but it is able to make corrections to the photometry automatically. However, sometimes the automatic correction fails and spurious data need to be removed manually[4].

[1] All Sky Automated Survey (ASAS) information and data accessible from `http://www.astrouw.edu.pl/asas/`.

[2] Optical Monitoring Camera information and data accessible from `http://sdc.cab.inta-csic.es/omc`.

[3] ASAS-SN data of GG Car available from `https://asas-sn.osu.edu/?ra=163.99550&dec=-60.39264`.

[4] For further examples in failures of ASAS-SN flux correction due to saturation, see figure 9 in Kochanek et al. (2017) and example 5 in `http://www.astronomy.ohio-state.edu/~assassin/public/examples.shtml`

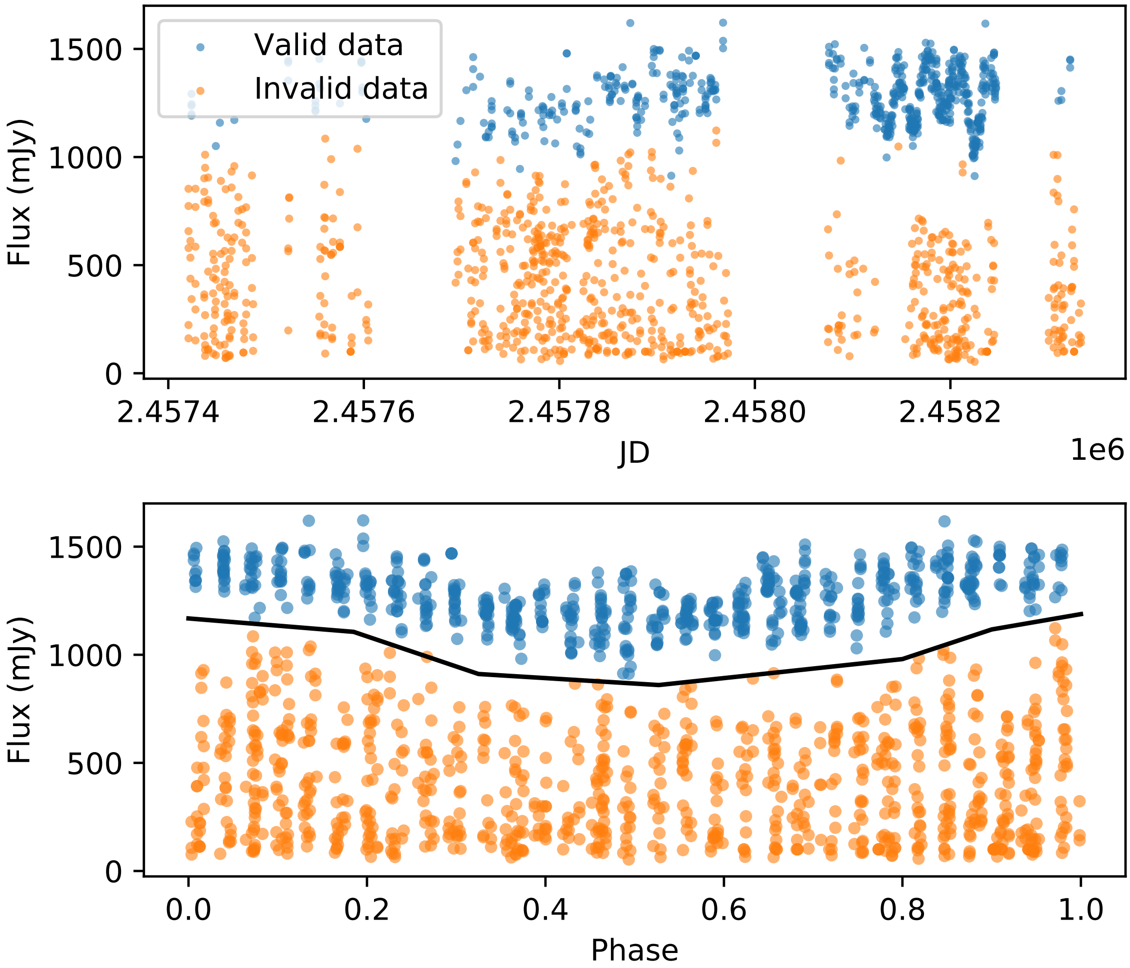

Figure 3.1: The entire ASAS-SN V-band photometry data set of GG Car. The blue points denote the data determined to be valid, and the orange points those are classed as invalid. The top panel is the flux against Julian day, and the bottom panel is flux against orbital phase. The black line in the lower panel indicates the cutoff below which a data point is invalid. The phases are calculated with the ephemeris given in Equation 4.1.

Figure 3.1 displays the entire ASAS-SN dataset on GG Car. There is a very clear break in the data at higher fluxes than at lower fluxes which is clearly unphysical and which does not occur for the ASAS and OMC V-band data. The break becomes more apparent when the data are folded according to the orbital phase of the binary, which is shown in the bottom panel. The break and lower-flux data points are due to failures in ASAS-SN's flux correction methods when the CCDs are past their saturation point, as expected for objects brighter than the 10th magnitude.

Since the break between the valid and invalid data is so clear, the classification of a data point's validity may be done by eye. When the data are ordered by orbital phase, a line is demarcated and if a data point is below the line then it is taken that the flux correction has failed and it is flagged as invalid. Unfortunately for GG Car, the majority of the ASAS-SN data points have invalid correction (632 valid data points versus 883 invalid data points). The valid data points are of very high quality, however, and therefore useful precision photometry is possible using the ASAS-SN data.

3.2.2 TESS photometry

The Transiting Exoplanet Survey Satellite (TESS: Ricker et al. 2014) is a mission geared towards discovering new exoplanet candidates; however, its high-cadence and high-precision photometry of the majority of the sky means that it has proved a valuable resource for stellar astrophysics, in particular asteroseismology. The TESS satellite is in a highly-elliptical, 13.7-day orbit around Earth, and observes the sky in 26 overlapping "Sectors", with each Sector being observed for roughly one month. Two minute cadence data will be released for a pre-selected 400 000 sources, but full-frame image (FFI) data with a cadence of 30 minutes is available for any source which lies within one of TESS's 26 sectors. The brightness limits for TESS observations are approximately Johnson V-magnitudes of 3–12, and the passband filter has an effective wavelength of 7 500 Å and a width of 4 000 Å. This wide bandpass is therefore roughly centred on the Johnson I_c band, but also encompasses the R_c and z bands. The filter therefore transmits to longer wavelengths than the V-band surveys described in Section 3.2.1.

GG Car lies in two of TESS's sectors, meaning that there are nearly two months of TESS photometric data available for the system. The TESS FFI data are reduced

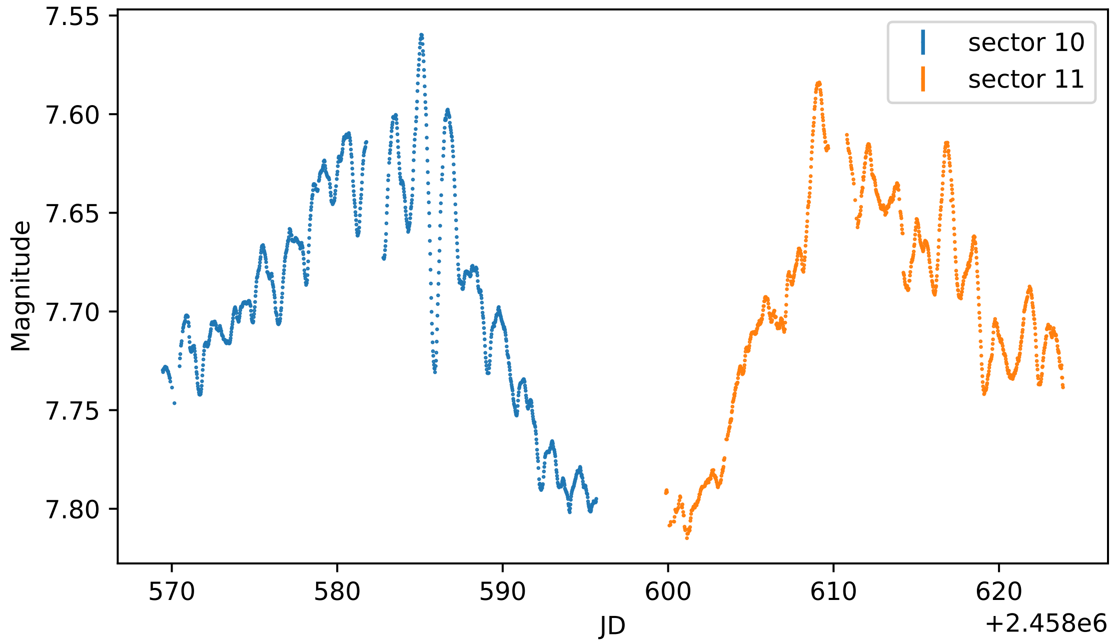

Figure 3.2: TESS light curve of GG Car.

using the `eleanor` code (Feinstein et al. 2019). TESS observed GG Car in sectors 10 and 11 from 26th March 2019 to 21st May 2019, covering almost two full orbital cycles.

The pixel scale of TESS is 21 arcseconds per pixel, with a similar full-width-at-half-maximum point-spread-function (PSF) of the instrument. This presents a problem for GG Car since its nearest neighbour, V413 Car (CPD-59 2857), is only 49 arcseconds away (∼2 pixels). `eleanor` is able to minimise the impact that this may have by choosing optimal apertures and PSF modelling. The FFI data are extracted in 15×15 pixel "postage stamps", and the PSFs of both GG Car and V413 Car are modelled as Moffat profiles. The brightest 20% of pixels away from the target are blocked which effectively masks background stars and aids the background subtraction. The data are converted to TESS magnitudes, using the mean TESS magnitude of 7.696 taken from the TESS Input Catalogue. The uncertainties of the individual data points of the TESS data are very low, of the order 10^{-4} mag.

Figure 3.2 displays the TESS lightcurve of GG Car, obtained using `eleanor`. The TESS data cover nearly two orbital cycles of the binary of GG Car with high precision and cadence. Both the longer-term variation at the orbital period and short period variations along the lightcurve can be clearly seen in the TESS data. It is also clear that the amplitude of the short period variations changes over the duration of observations, with the amplitudes generally being greater when the object is brighter in its orbital cycle. The TESS lightcurve is studied in detail in Chapter 5 to investigate these short-period variations of the system.

To ensure that the features seen in Figure 3.2 are real and not instrumental artefacts, the TESS lightcurves for three similarly bright stars which were observed nearby on the same CCD as GG Car (V413 Car, AG Car, and HD 94961) were extracted using similar methods. The light curves of these other stars do not display the same features as those in GG Car, allowing us to conclude that the signals observed in Figure 3.2 are astrophysical.

3.2.3 Spectroscopy

3.2.3.1 Global Jet Watch

An overview of the Global Jet Watch (GJW) project is given in Chapter 2; here I describe the observations pertaining to GG Car.

Exposure time [seconds]	# of spectra
100	596
1000	305
3000	416

Table 3.2: The number of GJW spectra used in this study.

The GJW observations of GG Car range from February 2015 to December 2018, and have exposure times of either 100, 1000, or 3000 seconds. This range of exposure times is chosen to allow both the observation of the dominant H-alpha line, with the 100 second exposures, and the metal and He I lines, which require longer exposures to observe with acceptable signal-to-noise. The spectra are barycentric corrected using heliocentric velocities calculated with the `barycorrpy` package (Kanodia & Wright 2018). In this study, all spectra are normalised by the local continuum. Table 3.2 lists the number of observations at each exposure time, and Figure 3.3 displays the distribution of these observations over the ~31-day orbital period of the binary.

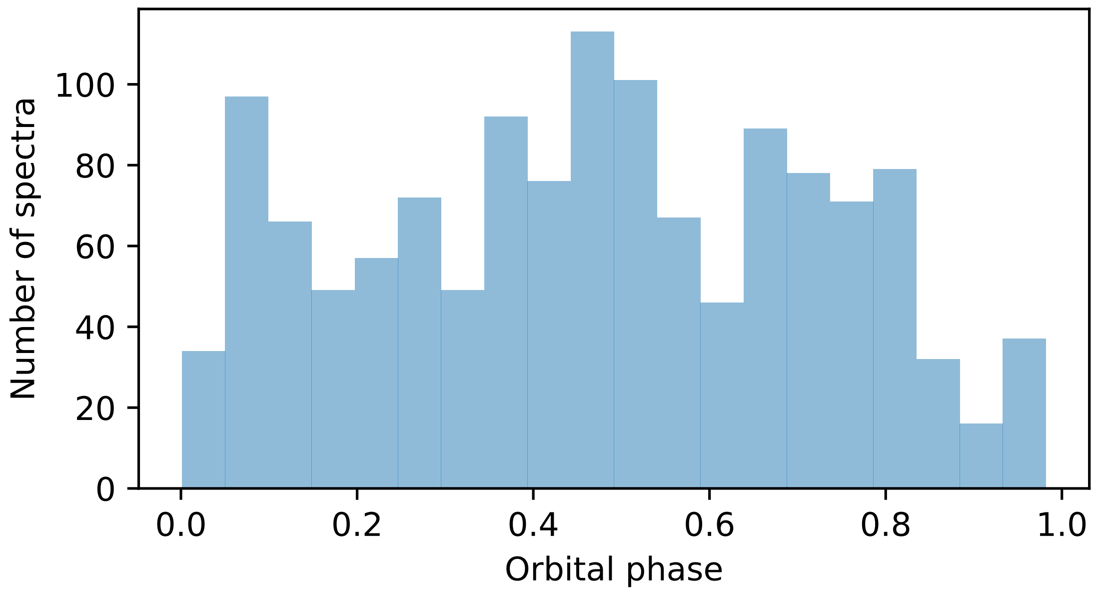

Figure 3.3: The number of GJW spectra, as a function of the orbital phase of GG Car. The phases are calculated using the ephemeris of Equation 4.1.

GJW, being able to undertake sustained observation of a target at nightly and intra-nightly intervals, perfectly suits the observation of GG Car, which has spectroscopic variability at ∼31- and ∼1.6-day periodicities.

3.2.3.2 The Fiber-fed Extended Range Optical Spectrograph (FEROS)

The Fiber-fed Extended Range Optical Spectrograph (FEROS, Kaufer et al. 1999) is a high-resolution echelle spectrograph, located at the European Southern Observatory (ESO) at La Silla, Chile. Before October 2002, the spectrograph was used with the ESO 1.52m telescope; since then it has been used with the 2.2m MPG/ESO telescope. FEROS has a wavelength range of 3600 - 9200 Å and $R = \Delta\lambda/\lambda \sim 48\,000$. The FEROS spectra used in this study have been reduced by ESO using the standard FEROS reduction pipeline.[5] The expected atmospheric transmission in each FEROS spectrum was calculated using `TAPAS` (Bertaux et al. 2014), and is divided from the spectra.

[5]The FEROS spectra used here are available from ESO at `http://archive.eso.org/scienceportal/home` and `http://dc.zah.uni-heidelberg.de/feros/q/web/form`.

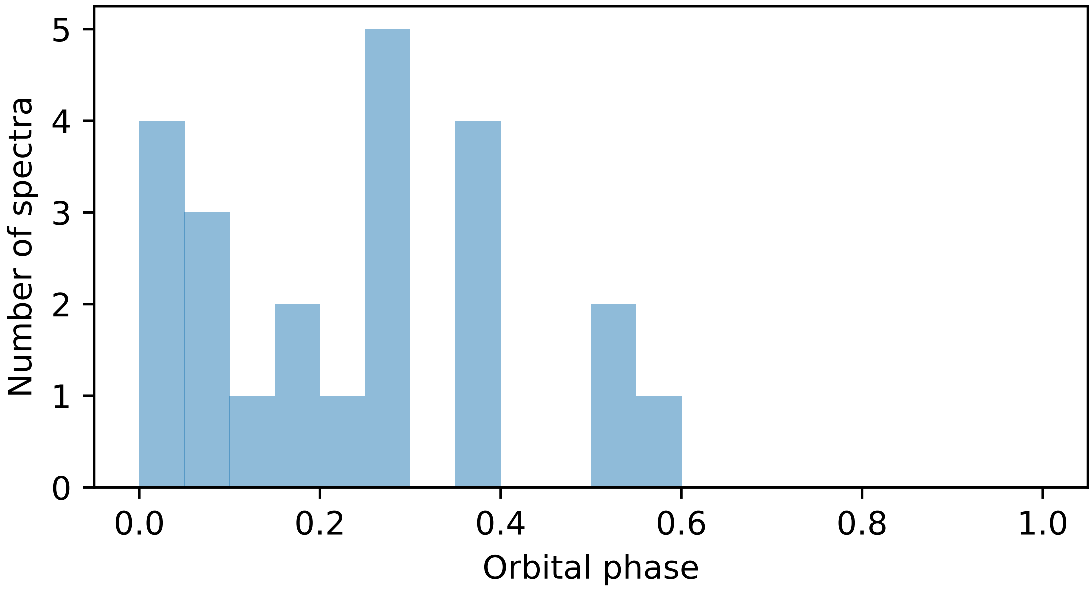

Figure 3.4: Same as Figure 3.3, except for the FEROS spectra available.

FEROS observed GG Car in 1998 (8 spectra), 2009 (1 spectrum), 2011 (2 spectra), and 2015 (12 spectra). Table 3.3 lists the exact dates and times of the observations. Figure 3.4 shows how the observations are distributed along the orbital phase of the binary, and shows that the FEROS data do not have complete enough phase coverage to undertake time-series analysis, unlike the GJW spectra. However, the high-spectral resolution observations may be used to complement the high-temporal resolution GJW data by revealing the fine structure of the emission lines' profiles, and thereby revealing the formation regions of the lines.

3.3 The stellar parameters of the primary of GG Carinae

Previous studies, such as McGregor et al. (1988), Lopes et al. (1992), and Marchiano et al. (2012), have made estimates of the stellar properties of the B[e]SG primary of GG Car. However, these estimates have been hampered and affected by the uncertain distance to the system, which affects the inferred intrinsic luminosity. Here, I determine the luminosity of the primary using the distance to the system inferred from the accurate parallax measured by the *Gaia* mission (Prusti et al. 2016), and use this luminosity to estimate the mass of the primary.

Observation date	Julian Day
1998-12-07	2451154.813
1998-12-08	2451155.857
1998-12-09	2451156.864
1998-12-24	2451171.759
1998-12-25	2451172.809
1998-12-26	2451173.728
1998-12-27	2451174.725
1998-12-28	2451175.729
2009-06-09	2454991.529
2011-02-14	2455606.897
2011-03-23	2455643.756
2015-05-13	2457155.651
2015-05-13	2457155.653
2015-05-13	2457155.655
2015-05-13	2457155.657
2015-11-23	2457349.859
2015-11-23	2457349.861
2015-11-23	2457349.863
2015-11-23	2457349.865
2015-11-26	2457352.849
2015-11-26	2457352.851
2015-11-26	2457352.853
2015-11-26	2457352.855

Table 3.3: The FEROS observations of GG Car.

3.3.1 Determining the luminosity of the B[e]SG primary

Gaia's Data Release 2 (Prusti et al. 2016; Brown et al. 2018) published a parallax to GG Car of 0.2997 ± 0.0303 mas; using the Uniform Distance Prior method of Luri et al. (2018) to convert parallax to a distance indicates a distance to GG Car of $3.4^{+0.7}_{-0.5}$ kpc and a distance modulus of $12.66^{+0.41}_{-0.34}$ mag.

It is shown in Section 4.4.3.3 that the photometric variations at the orbital period are due to luminosity increases at periastron due to mass transfer between the components, and in Section 4.4.2 it is shown that the luminosity of the secondary is expected to be negligible compared to the primary. Therefore, it is assumed that the V-band brightness of the system when it is at photometric minimum, at apastron, is solely dominated by the intrinsic brightness of the B[e]SG primary. Therefore the primary is assigned an intrinsic V-band brightness of $m_V = 8.8 \pm 0.1$ mag (Figure 4.2). The absolute V-band magnitude of the primary, M_V, can be found by

$$M_V = m_V - 5\log\left(\frac{d}{10\,\mathrm{pc}}\right) - A_V = m_V - \mu - A_V, \tag{3.1}$$

where d is the distance to GG Car in parsecs, A_V is the interstellar extinction in the V-band, and μ is the distance modulus.

A_V and the $B-V$ excess, E_{B-V}, are proportional to each other, such that

$$R_V = \frac{A_V}{E_{B-V}}, \tag{3.2}$$

where R_V is the ratio of absolute to relative extinction. It is often assumed that within the Galaxy $R_V \sim 3.2$; however, R_V is highly dependent on the properties of the interstellar medium (ISM) along the line of sight to the target (e.g. Majaess et al. 2016). GG Car's Galactic coordinates (289.133, -00.651) place it within the Galactic plane, where the ISM densities will be greatest. Furthermore, the star-forming Carina nebula has often been found to have an anomalously high R_V (e.g. Feinstein et al. 1973; Herbst 1976; Smith 1987; Tapia et al. 1988; Patriarchi et al. 2003; Hur et al. 2012; Majaess et al. 2016) and extinction which can be significantly more than 5 mag in the V-band (e.g. Preibisch et al. 2014; Damiani et al. 2017). In a study of the dependence of R_V on the Galactic longitude, l, for O-stars, Majaess et al. (2016) found a sharp peak in R_V at $l \sim 290°$, almost exactly at the Galactic longitude of GG Car. The cited studies find R_V in the range $4.4-4.8$ toward the Carina region, therefore $R_V = 4.6 \pm 0.2$ is adopted for the ISM along the line of sight to GG Car for the calculation of its primary's luminosity. Brandi et al. (1987) and Marchiano et al. (2012) found E_{B-V} to be 0.52 ± 0.04 mag and 0.51 ± 0.15 mag, respectively; therefore, a total visible extinction $A_V = 2.35 \pm 0.21$ mag is adopted and it is found $M_V = -6.21 \pm 0.44$ mag.

The bolometric correction, BC_V, of GG Car is calculated to be -2.21 ± 0.20 mag, using the Flower (1996) regime for a star of $\log(T_{\text{eff}}) > 3.90$, which was corrected in Torres (2010), assuming an effective temperature $T_{\text{eff}} = 23000 \pm 2000$ K (Marchiano et al. 2012). Therefore, the bolometric magnitude of the primary $M_{\text{bol}} = M_V + BC_V = -8.42 \pm 0.49$ mag. The luminosity of the primary can then be calculated using the relation

$$M_{\text{bol}} - M_{\text{bol},\odot} = -2.5 \log\left(\frac{L}{L_\odot}\right), \tag{3.3}$$

where $M_{\text{bol},\odot}$ is the solar bolometric magnitude, and $L_\odot$ is the solar luminosity. To be consistent with the BC_V calculated using Flower (1996) and Torres (2010), $M_{\text{bol},\odot} = 4.73$ mag is adopted. Therefore the luminosity of the primary of GG Car is $\log(L_{\text{pr}}/L_\odot) = 5.26 \pm 0.19$. This corresponds to $L_{\text{pr}} = 1.8^{+1.0}_{-0.7} \times 10^5\, L_\odot$. The effective temperature and updated luminosity imply a stellar radius $R_{\text{pr}} = 27^{+9}_{-7}\, R_\odot$. This determination of L_{pr} agrees well with Krtičková & Krtička (2018), who found that the B[e]SGs of the LMC and the SMC, with their well-defined distances, had remarkably uniform luminosities of $\sim (1.9 \pm 0.4) \times 10^5\, L_\odot$.

3.3.2 The place of the B[e] supergiant primary in the Hertzsprung-Russell diagram

The properties of the B[e]SG primary of GG Car, such as its mass and age, need to be estimated via stellar evolution models since the direct observation of its photosphere is precluded by its thick circumstellar environment. If this was not the case, then observation of the star's surface gravity from photospheric absorption lines, and the previous determination of R_{pr}, would allow a direct measure of its mass. Using this method of comparing the observables to stellar evolutionary models to estimate parameters introduces systematic uncertainties, as the resulting parameter estimations will be dependent on the stellar evolution model chosen (see e.g. Gallart et al. 2005).

Therefore, to estimate the mass of GG Car's primary, its position on the Hertzsprung-Russell (H-R) diagram must be compared to stellar evolution models. Its measured

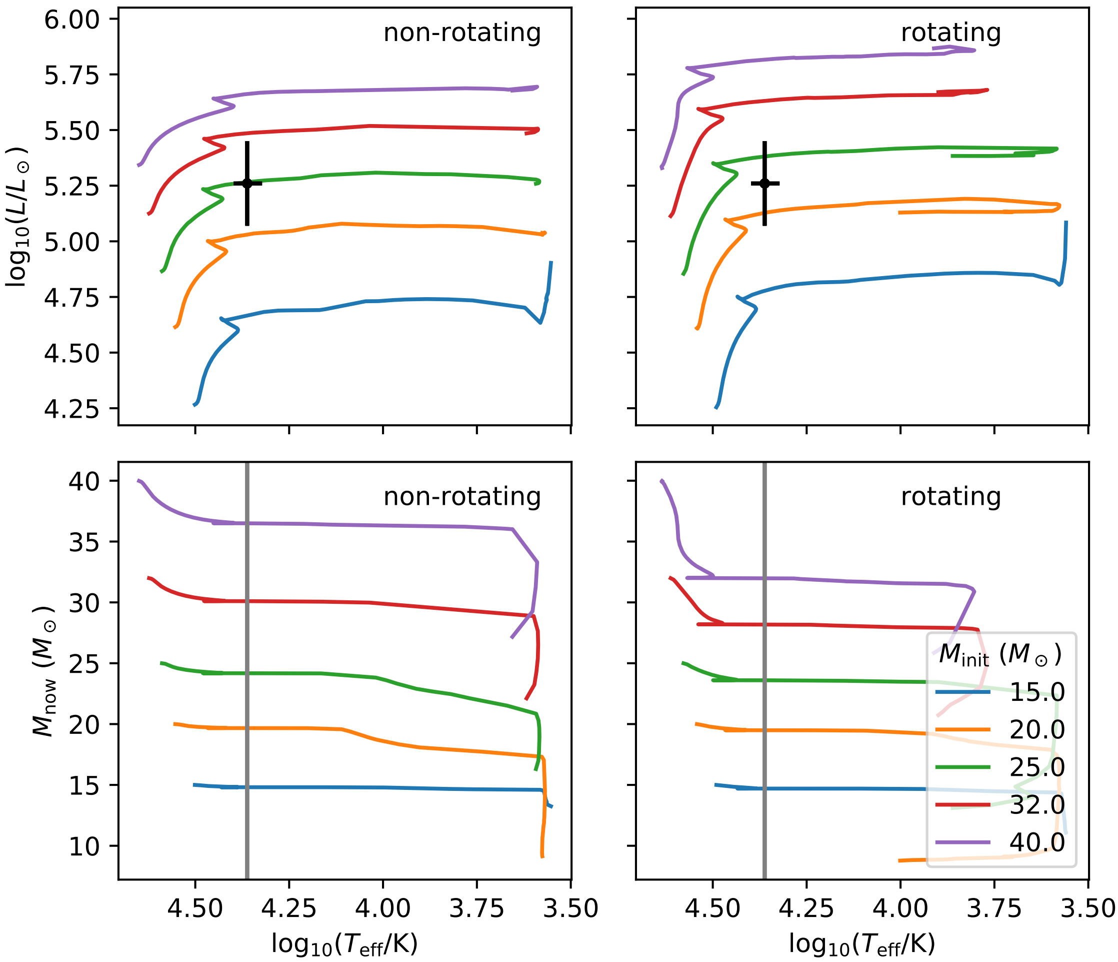

Figure 3.5: Stellar evolutionary models of luminosity, L, (top panels) and stellar mass, $M_{\rm now}$, (bottom panels) against effective temperature, $T_{\rm eff}$, of Ekström et al. (2012) for varying initial stellar mass, $M_{\rm init}$. The left panels show the tracks for the non-rotating cases, and the right panels show the rotating cases. The position of GG Car on the H-R diagram is denoted by a black point. The $T_{\rm eff}$ of the primary of GG Car is denoted by the grey, vertical line in the $M_{\rm now}$ panels. Only data where the ratio of the abundances of the Carbon isotopes $^{12}{\rm C}/^{13}{\rm C} > 5$ are plotted. The legend in the bottom-right panel gives $M_{\rm init}$ for the tracks in all panels.

luminosity and effective temperature are compared to the grid of stellar evolution models of Ekström et al. (2012), who calculated stellar evolution tracks for stars with initial masses from 0.8 to 120 $M_\odot$ at a solar metallicity of $Z = 0.014$; this is similar to the observed metallicity towards the Carina region (Spina et al. 2017). Using the [Fe/H] to Z relation from Bertelli et al. (1994), $\log Z \approx 0.977[\mathrm{Fe/H}] - 1.699$, this gives $Z_{\mathrm{Carina}} = 0.0187 \pm 0.0007$. The models were calculated for both initially rotating and non-rotating stellar models, with the rotating stellar models having an initial rotational velocity $\sim 0.4\, v_{\mathrm{crit}}$, where v_{crit} is the critical break up velocity of the star. Due to GG Car's lack of photospheric absorption lines, the rotational velocity of the star is unknown. Huang et al. (2010) found the peak distribution of rotation rates for young B-type stars to be $0.4\, v_{\mathrm{crit}}$. However, for the more massive young, B-type stars, they found that they generally had lower rotational velocities than low mass stars. This may be due to angular momentum being deposited as orbital motion as opposed to stellar rotation during the formation of these systems (Larson 2010); this holds as most massive stars are observed in binaries (Sana et al. 2008). The strong stellar winds can also efficiently remove angular momentum from the massive stars (Meynet & Maeder 2000). However, previous binary interactions can cause the spin up of a star. With all of these factors, it is not entirely certain whether or not GG Car is a rapid rotator, therefore it is prudent to compare it to models of both rotating and non-rotating stars.

Figure 3.5, top two panels, displays the position of GG Car's primary in the Hertzsprung-Russell (H-R) diagram, along with the Ekström et al. (2012) evolutionary tracks for stars of a range of initial masses along the H-R diagram at solar metallicity, in the rotating (right panel) and non-rotating (left panel) cases. From its position on the H-R diagram relative to the evolutionary tracks, the initial mass of the primary can be estimated to be $20\, M_\odot < M_{\mathrm{init}} < 32\, M_\odot$, where M_{init} is the initial mass of the primary of GG Car. The bottom two panels of Figure 3.5 display the evolution of the mass of the stars in the Ekström et al. (2012) models, and the current T_{eff} of the primary of GG Car; from the initial mass estimate from the top two panels and the evolution of the mass together, it can be deduced that $20\, M_\odot < M_{\mathrm{now}} < 28\, M_\odot$, where M_{now} is the current mass of the primary in GG Car. Therefore, a primary mass $M_{\mathrm{pr}} = 24 \pm 4\, M_\odot$ is assigned. It must be noted that this deduced mass is model dependent using the single-star evolution models of Ekström et al. (2012), and that if there has been significant binary interaction in GG Car's history that the primary has regained thermal equilibrium (see Section 4.4.4).

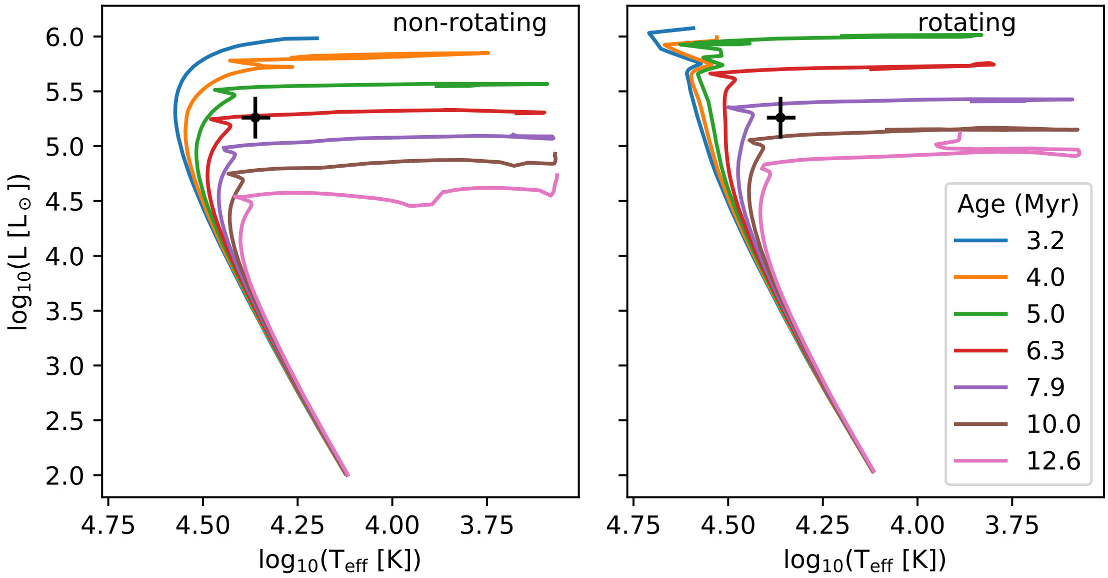

Figure 3.6: HR diagram of the isochrones of Ekström et al. (2012) in the non-rotating (left) and rotating (right) models. The position of GG Car and its uncertainty is indicated by the black point. The legend indicates the age of the isochrone in Myr. Only data for $^{12}C/^{13}C > 5$ are plotted.

Figure 3.6 displays the isochrones calculated by Ekström et al. (2012) at solar metallicity for the non-rotating case (left) and the rotating case (right). Isochrones display the contours on the H-R diagram that are expected for a set of stars with different zero-age main sequence (ZAMS) masses at the same age. Massive stars are brighter and evolve off the main sequence faster than the low-mass stars. In taking account of the rotating and non-rotating isochrones, GG Car's age may be estimated to be in the 5-10 Myr range.

Table 3.4 lists the updated stellar parameters of the primary of GG Car, using the updated *Gaia* distances.

d	$3.4^{+0.7}_{-0.5}$ kpc
$M_{\rm pr}$	$24 \pm 4\, M_\odot$
$T_{\rm eff}$	$23\,000 \pm 2000$ K
$L_{\rm pr}$	$1.8^{+1.0}_{-0.7} \times 10^5\, L_\odot$
$R_{\rm pr}$	$27^{+9}_{-7}\, R_\odot$
Age	5–10 Myr

Table 3.4: *Gaia* distance, d, and stellar parameters of the primary in GG Car, where $M_{\rm pr}$ is the mass of the primary, $T_{\rm eff}$ is the effective temperature of the primary, $L_{\rm pr}$ is the luminosity of the primary, and $R_{\rm pr}$ is the radius of the primary. $T_{\rm eff}$ is taken from Marchiano et al. (2012).

3.4 The Global Jet Watch spectrum of GG Carinae

In this Section, I introduce the mid-resolution spectrum of GG Car as observed by GJW. Whereas Chapters 4 and 5 investigate the variability which is exhibited in GG Car's emission lines in detail, in this section I identify the emission lines that are observed in GG Car's GJW spectrum.

Figure 3.7 displays the average GJW spectrum of GG Car, summed with all 1317 spectra of the object. As noted by other authors (e.g. Hernandez et al. 1981; Gosset et al. 1985; Marchiano et al. 2012), GG Car's visible spectrum is dominated by its strong H-alpha line, and also hosts He I complexes, [O I] emission, and low-ionisation Fe II and Si II lines. The large absorption features between ∼6850–7700 Å in the spectrum are Telluric absorption due to the Earth's atmosphere.

3.4.1 H-alpha and He I lines

The left panel of Figure 3.8 displays the average H-alpha profile in GG Car. H-alpha dominates the visible spectrum, with a peak intensity ∼25 times larger than the continuum, and an average equivalent width (EW) of −278 Å. In the GJW spectra, the H-alpha profile is mostly constant, with a blue shifted absorption component around 6560 Å. The shape is well described by a Beals' P-Cygni Type III profile (Beals 1953), with two emission maxima separated by a dip to the blue of the rest wavelength of the system, and the maximum to the red of the rest wavelength.

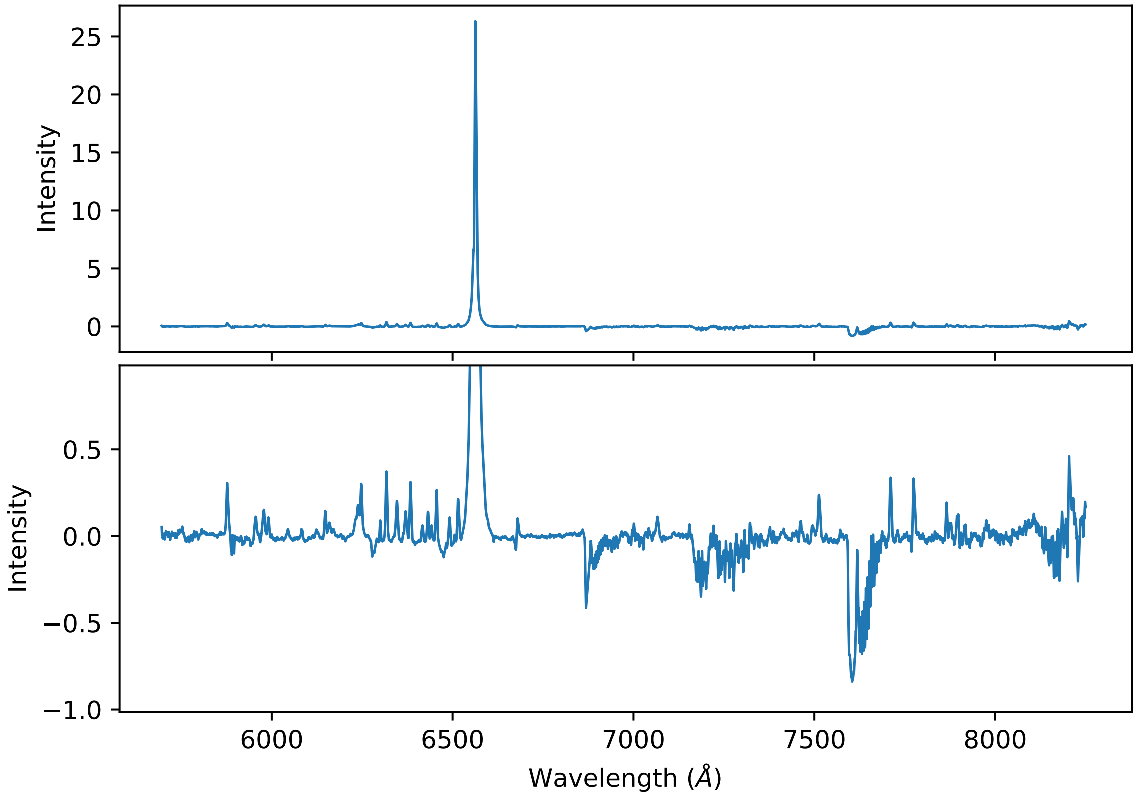

Figure 3.7: The full average GJW spectrum of GG Car. Both panels show the same spectrum, but the bottom panel clips the system's H-alpha complex. The intensity is in local continuum units, and has the continuum subtracted.

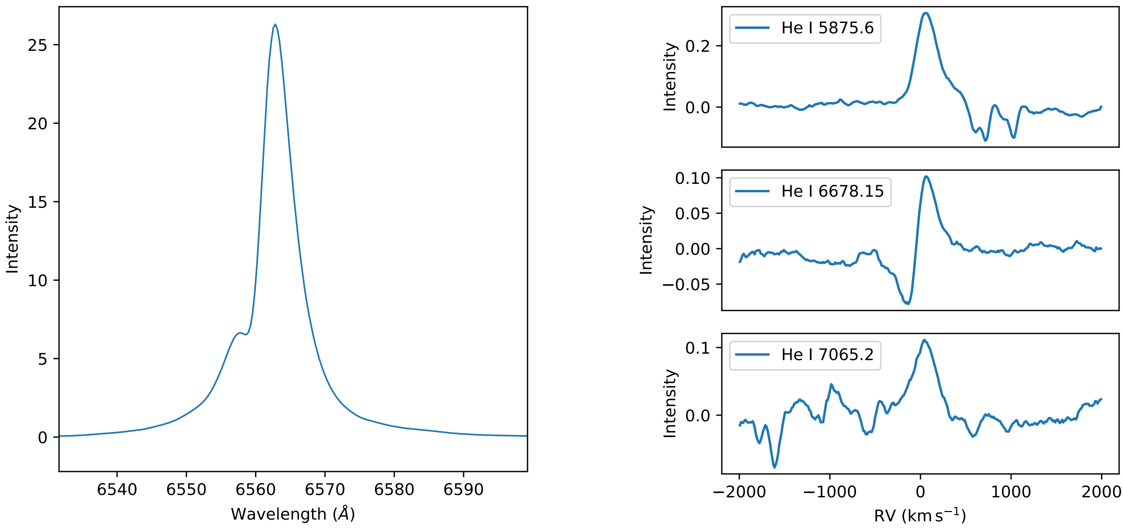

Figure 3.8: The average H-alpha profile (left) and He I profiles (right).

The He I lines, on the other hand, are much weaker than the H-alpha line and much more variable. The average profiles of He I in the GJW observations are shown in Figure 3.8, right panel. To the red of the He I 5875 line are the interstellar Na I D absorption lines, and to the blue of the He I 7065 line is some Telluric absorption. The lines all have blue-shifted absorptions, indicative of significant mass loss in a stellar wind, which are variable on the ~31-day period of the binary. The variability of the profiles at the orbital period are presented and discussed in detail in Chapter 4. In the classical picture of Zickgraf et al. (1986), both the He I and the H-alpha lines are formed in the equatorial regions of B[e]SGs.

3.4.2 Metal emission lines

As can be seen in Figure 3.7, there are plenty of emission lines throughout GG Car's spectrum as observed by GJW, besides the He I and H-alpha. These metal lines are primarily Fe II, however there are also Si II lines, O I and [O I] lines. As with the H-alpha and He I lines, these lines are expected to form in the equatorial regions of the B[e]SG primary, as opposed to the higher ionisation lines which form in the hot polar wind.

Figure 3.9 displays the line identifications for the majority of the metal lines in GG Car's GJW spectrum. There are four Si II lines identified, two [O I] lines, and the O I triplet around 7775 Å. The rest of the lines are Fe II lines; due to the overabundance of Fe II lines in this wavelength range (there are 93 Fe II lines in the 6300-6550 Å wavelength range alone, according to the NIST database), care needs to be taken in order to make the correct species identification. Therefore, to identify the Fe II lines, the higher-resolution FEROS spectra are used alongside the GJW spectra.

3.5 The high-resolution spectrum of GG Carinae

In this section, I introduce aspects of the high-resolution spectrum of GG Car as observed by FEROS.

3.5.1 Hydrogen Balmer series

The hydrogen Balmer series, of which H-alpha is the first member, is the series of emission lines which occur when the electron in neutral hydrogen transitions from the

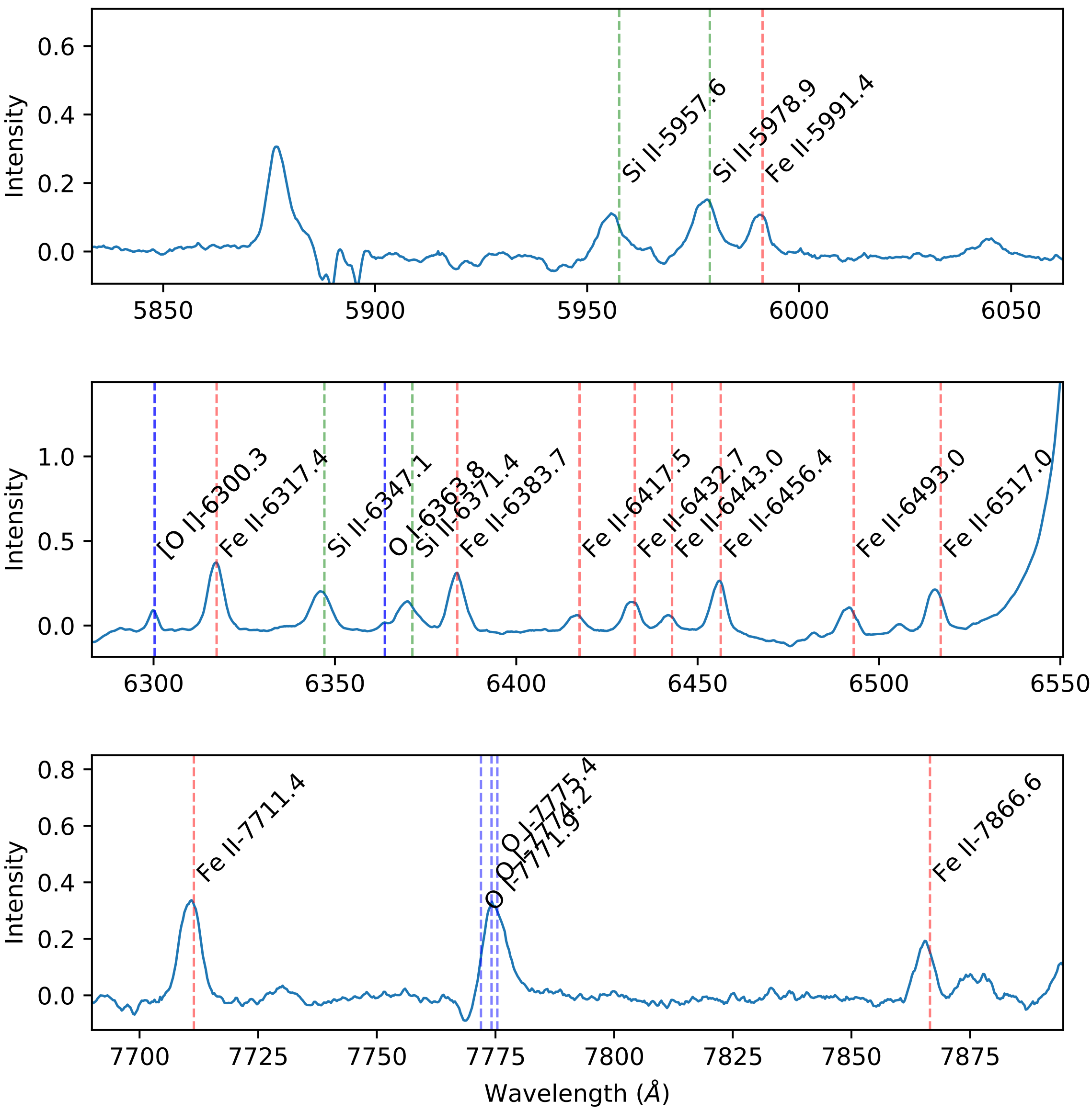

Figure 3.9: Line identifications of the metal lines in the visible spectrum of GG Car used in this study. Green lines indicate Si II lines, blue lines O I, and red lines indicate Fe II.

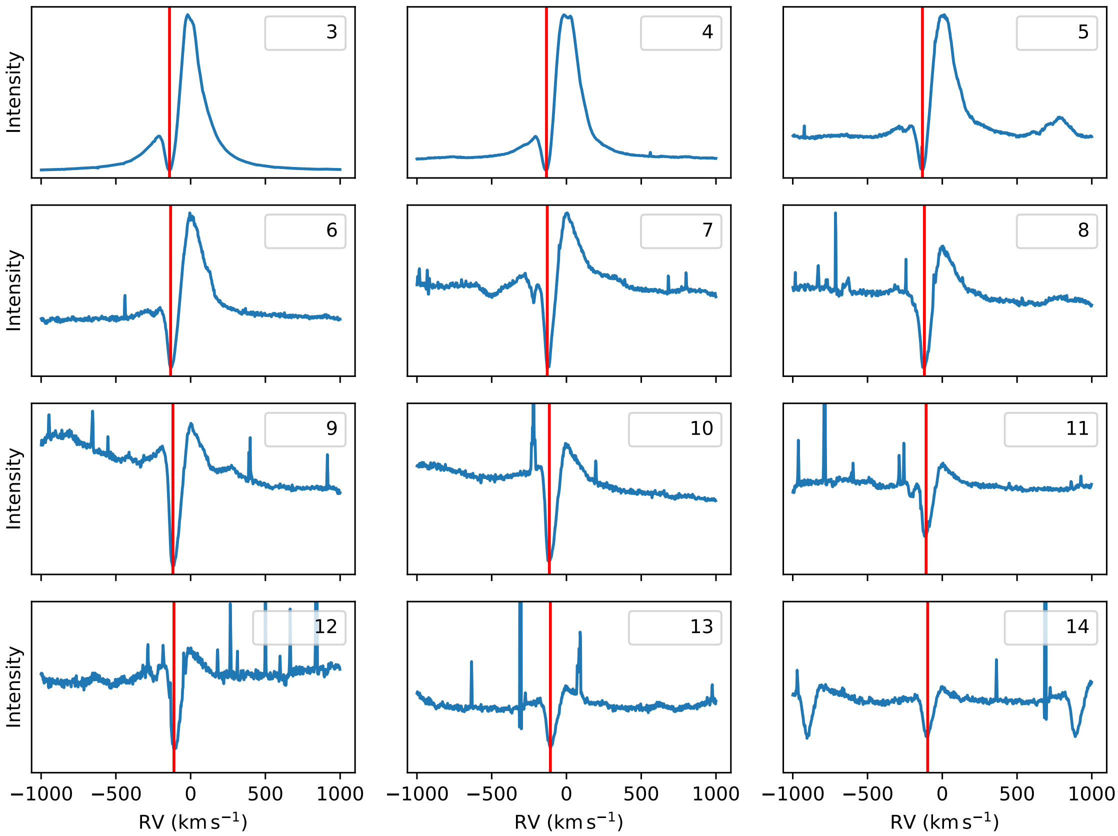

Figure 3.10: The Balmer series in GG Car up to n=14. The n of the initial energy level for the series member is given in the legend. The thin vertical lines are artefacts in the FEROS spectra, and not astrophysical. The radial velocity of deepest absorption is denoted by a vertical red line.

nth energy level to the 2nd, where $n = 3, 4, 5..., \infty$. The central wavelength of each member of the series can be calculated by

$$\frac{1}{\lambda_n} = R_{\mathrm{H}}\left(\frac{1}{2^2} - \frac{1}{n^2}\right), \tag{3.4}$$

where $R_{\mathrm{H}} = 1.09678 \times 10^{-7}\,\mathrm{m}^{-1}$ is the Rydberg constant for hydrogen. The H-alpha line is the only member of the Balmer series that falls in the GJW wavelength range; however, all members of the Balmer series are in the FEROS wavelength range.

Figure 3.10 displays the Balmer series from n=3–14 of GG Car as observed by FEROS. The spectra shown are summed spectra of all the observations listed in Table 3.3. Each of the Balmer lines exhibits blue-shifted absorption. The lower members of the Balmer series are mostly in emission, with H-alpha and H-beta (n=3 and 4)

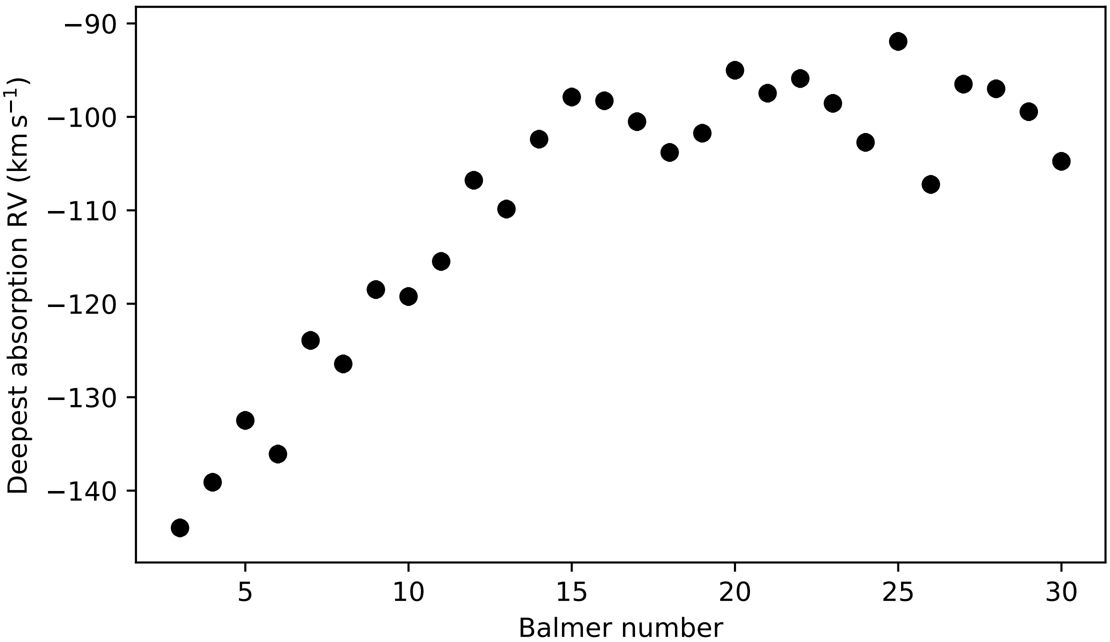

Figure 3.11: Radial velocity of the location of deepest absorption of the H I Balmer series, against n.

exhibiting double peaked profiles, described by Beals Type III. However, this emission gradually becomes weaker along the series, until the absorption dominates. For $14 < n \leq 30$ the profiles are almost pure absorption, and for $n > 30$ there are no further discernible Balmer lines.

Figure 3.11 displays the radial velocity of the location of the deepest absorption in the Balmer series. There is a clear trend for the deepest absorption to become less blueshifted as you travel up the series while $n \leq 14$. However, for $n > 14$, the trend slows down, and the RV of deepest absorption oscillates around $\sim -100\,\mathrm{km\,s^{-1}}$. Gosset et al. (1985) also noted the same relationship of deepest absorption with Balmer number, and ascribed the effect to an outwardly accelerating envelope. However, given that the trend dissipates when $n \gtrsim 15$ when the emission becomes negligible, this implies that the absorption component is at a constant radial velocity for all lines, but the effect of the emission components for the lower n Balmer members pushes the absorption trough blueward. This effect is demonstrated in Figure 3.12; the left plot shows the profiles for one Gaussian emission and one Gaussian absorption component, where all of the Gaussian parameters are kept constant except for the amplitude of the emission componenent, which varies from 45 to 0 arbitrary units. The right plot shows the position of minimum intensity against emission amplitude. Decreasing the

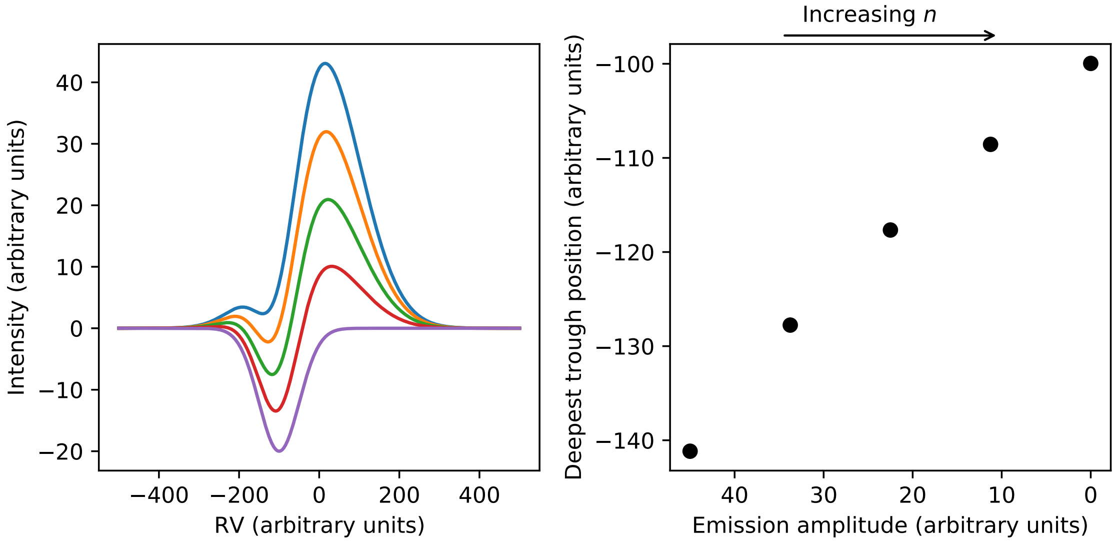

Figure 3.12: Left: Profiles of the addition of two Gaussians, one positive and one negative corresponding to "emission" and "absorption" respectively, with varying emission intensity and constant absorption intensity. All Gaussian parameters (mean, width, and amplitude) are kept constant, except for the amplitude of the emission Gaussian, which varies from 45 to 0 in arbitrary units. Right: The RV position of minimum intensity, for varying amplitude of the emission Gaussian. Decreasing the emission amplitude simulates increasing Balmer number, n.

emission amplitude simulates increasing the Balmer number, n, as Figure 3.10 shows that the emission decreases with increasing n.

The trend in this illustrative figure follows that of both Figure 3.11 and Gosset et al. (1985), in that the blueshift of the deepest absorption decreases for increasing n, up until $n = 14$. Both Gosset et al. (1985) and the FEROS data show that for $n > 14$, the blueshift plateaus, corresponding to when there is negligible emission in the Balmer line. It follows that the position of deepest absorption remains constant for all n. Therefore this absorption originates in an outflow of $\sim -100\,\mathrm{km\,s^{-1}}$, integrated along the line of sight. As at least some of the H-alpha was found to originate in a disk (Pereyra et al. 2009), this absorption could originate in the disk which also has a radial outflow component of this velocity. Alternatively, this absorption may be a component of the stellar wind of the B[e]SG primary, separate from the disk of the system.

Figure 3.13 displays sections of the FEROS spectra containing the Balmer lines

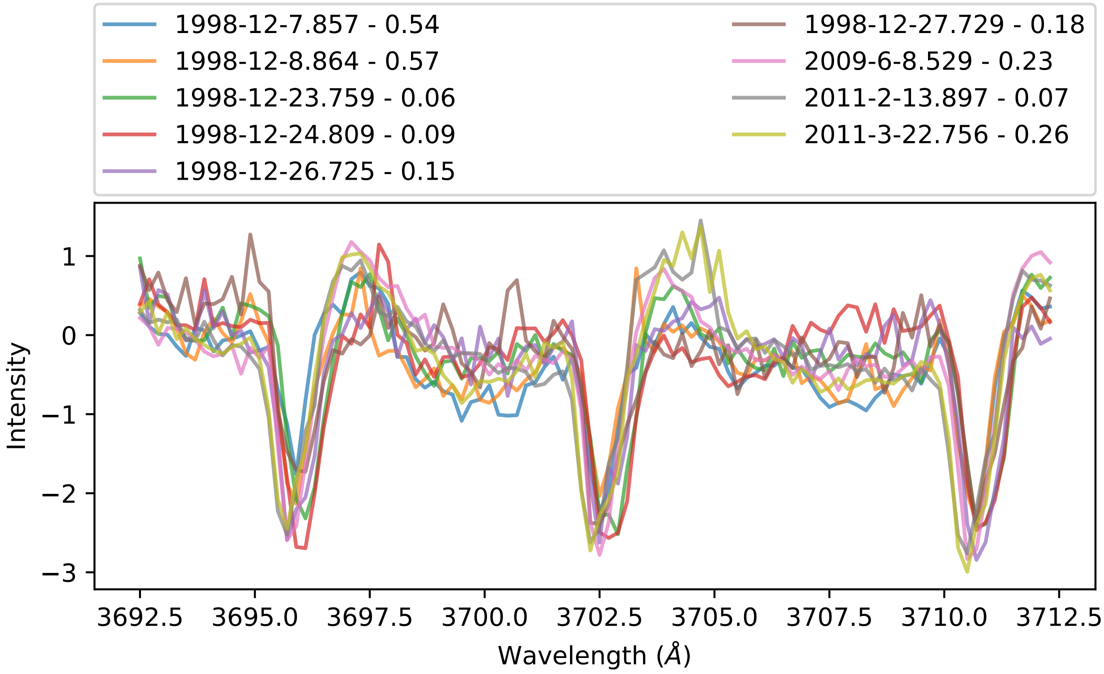

Figure 3.13: The absorption of the Balmer series, from n=15 to 17 as observed by FEROS. The spectra have been sampled at 0.2 Å wavelength bins to reduce noise. The dates of the observations and the corresponding orbital phases are given in the legend. The intensity of the spectra are normalised by the standard deviation of the data.

for n=15 to 17. The spectra are resampled at 0.2 Å to maximise signal to noise. The 2015 spectra do not have acceptable signal to noise in this wavelength region, so they are not included. The centroids of the absorption for these lines, and all the other Balmer lines, do not vary significantly within a given observation year. This rules out the absorption occurring in the photosphere of the primary itself, since no evidence of Keplerian motion is observed. However, the relatively stationary absorption lends evidence that the Balmer absorption may arise in outflowing circumbinary hydrogen. The blushifted edge of the absorption does become slightly more blueshifted between 1998 and 2011, indicating that there may be slight variations in the wind over longer timescales.

3.5.2 The multiple H I and He I absorption components

As can be seen for the Balmer H I lines in Figure 3.10, there is often more than one blueshifted absorption component in the average line complexes, with up to three different absorption components for some lines. This is especially clear for the n=5, 7, 11, and 12 complexes. The He I lines similarly may have up to three absorption components in the high-resolution spectra; however they are very variable, with different numbers of absorptions at different phases. The variability of the He I profiles and absorptions is studied in more detail in Chapters 4, but here we consider what the presence of multiple absorption components indicates.

Figure 3.14 highlights the absorptions for the average FEROS spectra for Balmer H I from n=3–8, and for the three He I lines. When focused in this way, the three absorption regimes in most of the lines becomes clearer. There is only one noticeable absorption in H-alpha (n=3) and none in He I 7065 (for the average line profile). The most blueshifted absorption occurs between $\sim -730 - -335\,\mathrm{km\,s^{-1}}$. The middle absorption region ranges from $\sim -280 - -185\,\mathrm{km\,s^{-1}}$; this absorption can be seen in all lines, except H-alpha and He I 7065. The final regime ranges from $\sim -160 - 0\,\mathrm{km\,s^{-1}}$, and is visible in all of the average profiles, with the exception of He I 7065. Not every line has each absorption component visible.

The presence of three absorption components of different blueshifts in the H I and He I complexes is reminiscient of the results of Oudmaijer et al. (1998), who found three distinct wind velocities in the B[e] star HD 87643, as opposed to the expected two wind velocities for B[e]SGs. Oudmaijer et al. (1998) additionally modelled a B[e]

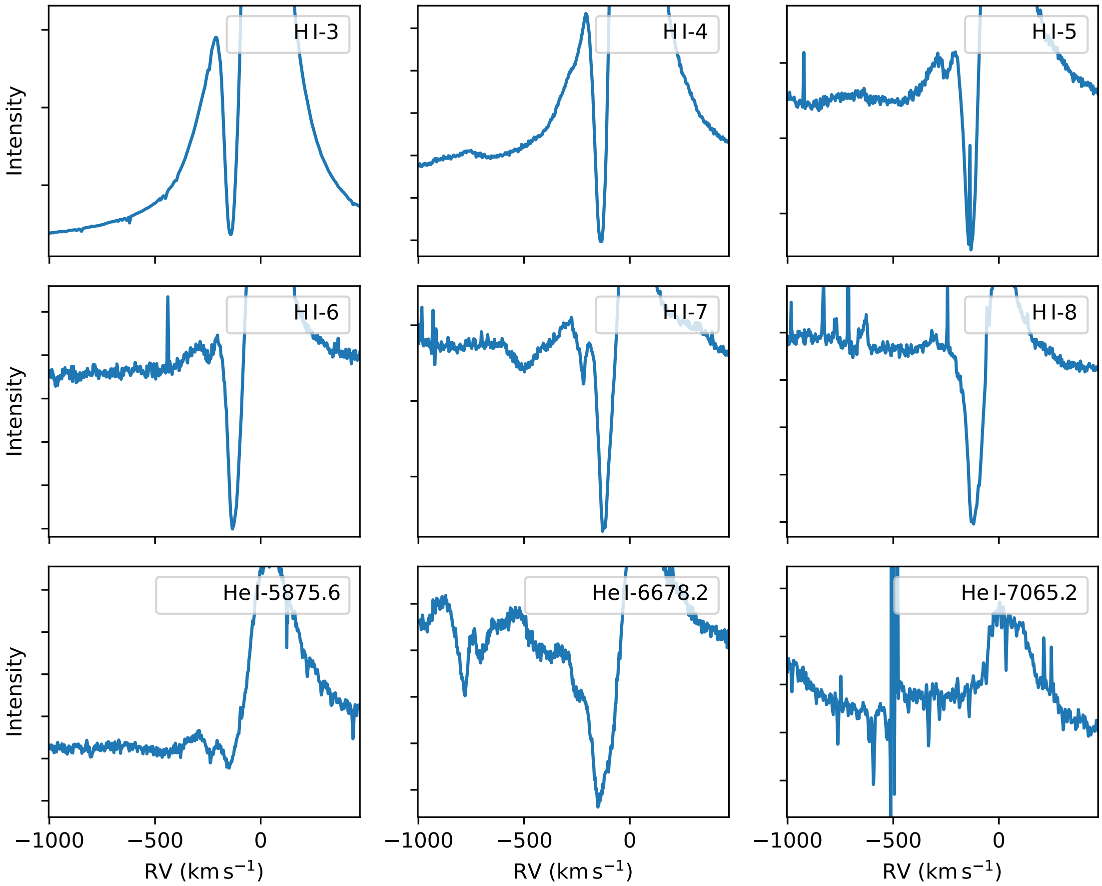

Figure 3.14: The absorption components of the average Balmer H I lines from n=3–8, and the visible He I lines. Up to three distinct blushifted absorption components can be spotted in the lines.

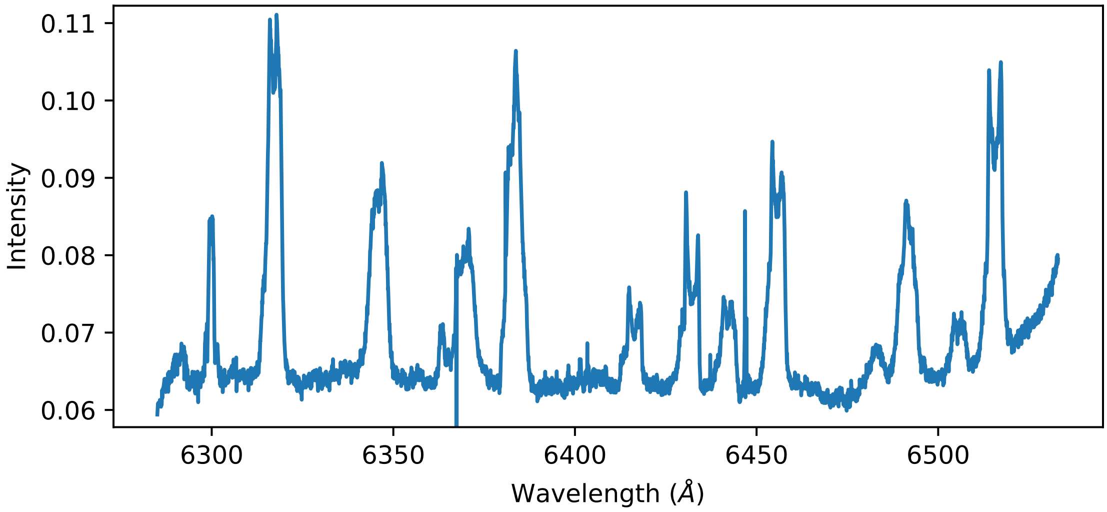

Figure 3.15: Metal lines in the 6300–6525 Å region of GG Car, as observed by FEROS, on 1998-12-07.

star, with a preexisting optically thick Keplerian disk, and were able to recreate three distinct wind regimes, which occur at different polar angles. This indicates that a similar multi-component wind structure may be occurring in GG Car. The multiple absorption components in the H I and He I lines are an indication of the complex circumstellar environment of GG Car.

3.5.3 Metal lines

Figure 3.15 displays the metal emission lines in the 6300–6525 Å wavelength range in GG Car, observed by FEROS on 1998-12-07. It is clear to see in the high-resolution spectrum that the metal lines in this region have heterogeneous structures, indicating that they are formed in different regions and have different behaviours. There are lines exhibiting double-peaked disk profiles, and others having Gaussian-like profiles more associated with winds. In contrast to the H I and He I lines, all of these metal lines are in pure emission, with no discernible absorption, even in the high resolution spectra.

In comparison to the He I lines, there is relatively little variability in the metal lines over the orbital period, with the line profiles on the whole remaining constant in the observations. However, there is significant variability in the central wavelength in some of the metal lines; this variability and its implications are studied in detail in

Chapters 4 and 5. The lines whose centroids are constant in wavelength and which bear double-peaked line profiles arise from the system's circumbinary disk, and are studied in more detail in Chapter 6.

Chapter 4

The orbital variability of GG Carinae

Abstract

This chapter investigates GG Car's time dependent behaviour to understand its variability at its orbital period, which has so far remained unsatisfactorily explained. There is one photometric minimum per orbital period and, in the emission line spectroscopy, there is a correlation between the amplitude of radial velocity variations and the initial energy of the line species. The spectral behaviour is consistent with the emission lines forming in the primary's wind, with the variable amplitudes between line species being caused by the less energetic lines forming at larger radii on average. By modelling the atmosphere of the primary, the radial velocity variations of the wind lines are modelled in order to accurately constrain the orbit of the binary for the first time. I find that the binary is even more eccentric than previously believed ($e = 0.5 \pm 0.03$). Using this orbital solution, the system is brightest at periastron and dimmest at apastron, however the profile of the photometric variability is stochastic and changes for successive orbital cycles. The average shape of the photometric variations at the orbital period can be well described by the variable accretion by the secondary of the primary's wind. With the signs of accretion, and the primary likely having been a classical Be star in its history, I suggest that the evolutionary history of GG Car needs to be reevaluated in a binary context.

4.1 Introduction

While the 31-day orbital period of the B[e]SG binary GG Carinae has been known for a long time due to photometric and spectroscopic variability at this period (Kruytbosch 1930; Hernandez et al. 1981; Gosset et al. 1985), an exact orbital solution has remained elusive due to the lack of photospheric absorption lines in the object. As introduced in Chapter 1, this is typical for the B[e]SG class since the objects are enshrouded in their optically thick circumstellar environments. Without a well-defined binary orbital solution, both the photometric and spectroscopic variability of the system at its 31-day orbital period has remained inadequately explained. Whilst orbital solutions have been calculated, the observed radial velocities and inferred orbital solutions depended on the specific emission line species being observed which, without proper physical elucidation, undermines confidence in the calculated solutions (Hernandez et al. 1981; Gosset et al. 1985).

Gosset et al. (1985) noted that there were multiple blue shifted absorption components in the H I Balmer and He I emission lines of GG Car, with the number of components depending on orbital phase. Marchiano et al. (2012) interpreted the He I absorption components in GG Car as photospheric absorption from both of the binary components, and from this determined a measurement of GG Car's orbital parameters. This interpretation of the He I absorption would be unusual for B[e]SGs, and that interpretation is highly suspect when the He I line profiles include both emission and absorption from the complex wind of the primary. With their interpretation of the He I absorption, Marchiano et al. (2012) inferred a systemic velocity of GG Car of $V_r = -162\,\mathrm{km\,s^{-1}}$. This systemic velocity is incompatible with the $-22\,\mathrm{km\,s^{-1}}$ determined in Maravelias et al. (2018) which was inferred from the system's circumbinary emission lines. Additionally, Hanes et al. (2018) measured that the average systemic velocity $\langle V_r \rangle = -7.14 \pm 13.10\,\mathrm{km\,s^{-1}}$ for the stars composing the Carina nebula, meaning a V_r of $-162\,\mathrm{km\,s^{-1}}$ would be highly anomalous. Both of these factors indicate that the He I absorption of GG Car measured in Marchiano et al. (2012) were systematically more blueshifted than the true systemic velocity of the system, and therefore these absorptions are most likely in fact due to absorption in the complex wind of the system. This casts doubt on the accuracy of the orbital solution of the binary that they measured.

In this chapter, I study the variability of GG Car at its $\sim$31-day orbital period, using high time-resolution spectroscopic data from the Global Jet Watch (GJW) and time-series photometric data from ASAS, ASAS-SN, and OMC. I aim to uncover the true binary orbital solution in the system using alternate methods, and to explain the system's photometric and spectroscopic variability over its orbit. Section 4.2 analyses the variability of the system's photometry and emission lines' radial velocities at the $\sim$31 day orbital period. In Section 4.3, I constrain the orbital solution of the binary by properly calculating the time-dependent emissivity of GG Car's emission lines in its atmosphere and using them to fit the RV variations of the emission lines. The found orbital ephemeris is

$$p = \frac{T - 2452069.36}{31.011}, \tag{4.1}$$

where p is the phase and T is the time in JD. Therefore, phase 0/1 corresponds with periastron of the binary, and phase 0.5 corresponds to apastron. All phases presented in figures in this Chapter are therefore calculated using Equation 4.1. Section 4.4 constrains the mass of the secondary component, and then discuss some models which may cause the photometric variability seen in GG Car, and Section 4.5 presents the conclusions of this chapter and summarises the orbital properties of GG Car found.

4.2 The variability of GG Carinae at its orbital period

4.2.1 Photometric variability

Figure 4.1 displays the V-band photometry of GG Car from ASAS, ASAS-SN, and OMC. The variability is dominated by the $\sim$31-day period of the binary, as can be seen in the bottom panel. There is also some longer term variability present in the data, and noticeable scatter along the lightcurve. As these are mostly ground-based experiments within much larger monitoring programmes, these data have, at best, only a few observations per day.

Figure 4.2 displays the V-band photometry of GG Car folded by the orbital period using the orbital ephemeris of Equation 4.1, which is determined in Section 4.3. The black line shows the average magnitude in 15 phase bins, and the errorbars show the standard deviation of the magnitudes in the bin. There is a lot of scatter in the system's light curve, as is shown by the errorbars, with the average standard deviations

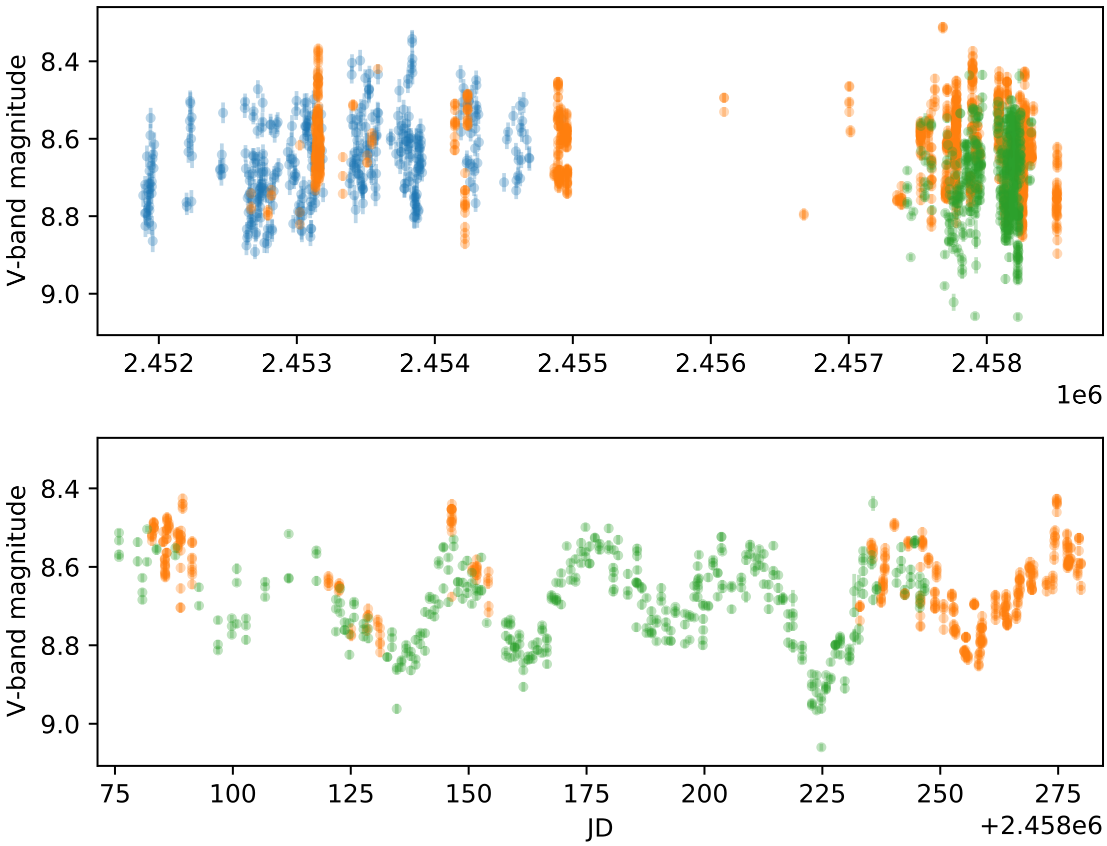

Figure 4.1: V-band photometry of GG Car from ASAS (blue), OMC (orange), and ASAS-SN (green). The top panel displays all available data, and the bottom panel displays a few finely-sampled orbital periods within the ASAS-SN and OMC data sets.

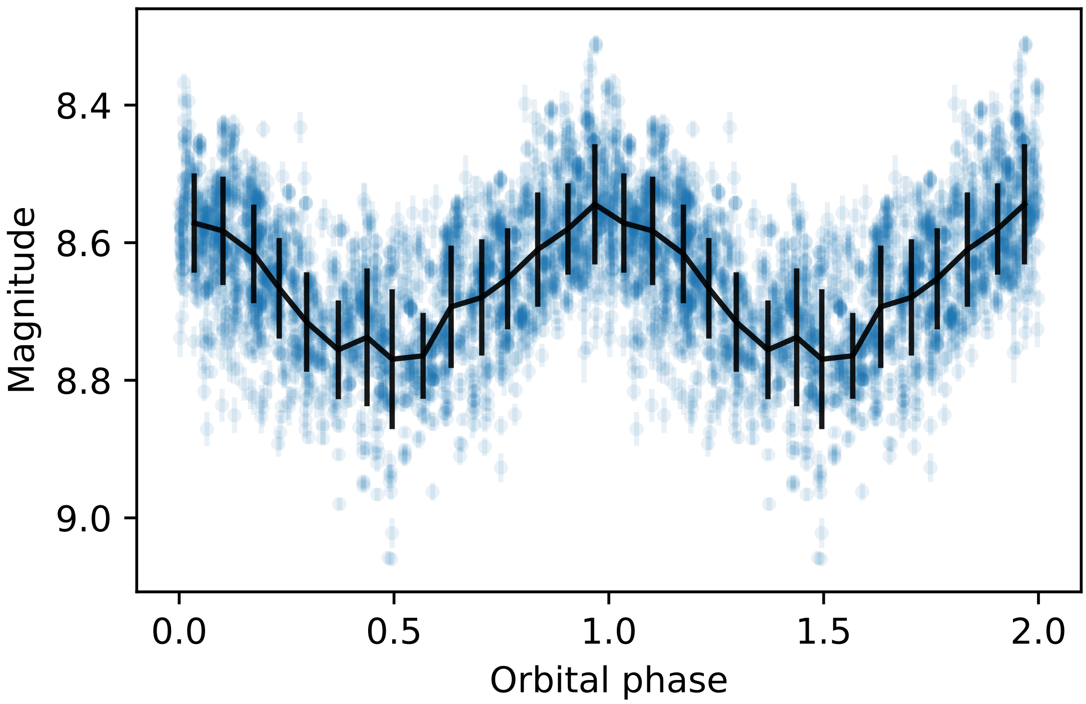

Figure 4.2: V-band photometry of GG Car, folded by the orbital phase of the binary using the ephemeris of Equation 4.1. The black line indicates the mean magnitude in 15 phase bins, and the error bar shows the standard deviation in the bin. The data are repeated for two orbital cycles.

in the bins of 0.078 mag. The mean brightness is continuous, with only one photometric minimum per orbital period and no sign of eclipses. At photometric minimum the standard deviation of the brightness is slightly higher than at other phases.

A cause of the large amount of scatter is that, as can be seen in Figure 4.1, the photometric variations for each 31-day orbital cycle are clearly not identical, but the profiles are stochastic and vary in shape and depth. In addition, a shorter-period and very long-term non-periodic variations are present in the system which are not subtracted from the data; the shorter-period variations are discussed in detail in an upcoming study. Fitting the long-period variations with polynomials and subtracting them from the data only minimally affects the scatter observed, and therefore is not implemented in this analysis.

The black, sliding average, magnitude in Figure 4.2 ranges from 8.55–8.77 magnitudes, indicating an average V-band magnitude change of 0.22 over the orbital period; this corresponds to a flux change of 21.9% over the binary's orbit. As mentioned, the V-band variability over the orbital period is stochastic, so this value is the average brightness change in an orbital period, but this value may vary for successive orbits. The presence of one photometric maximum and one minimum per orbital period matches previous photometric studies. However, there is no clear evidence of the "glitch" observed by Gosset et al. (1985) at photometric maximum.

4.2.2 Spectroscopic variability

In the GJW spectra, the most notably variable emission lines along the orbital period are He I 5875, 6678, and 7065, which usually exhibit P-Cygni profiles, indicating mass loss. However, these He I profiles are highly dynamic and may vary between pure emission and pure absorption. In these mid-resolution spectra, there is usually only one (or no) discernible absorption feature in the He I lines, which I interpret as a blend of the multiple wind features expected for B[e]SGs (Zickgraf et al. 1985; Oudmaijer et al. 1998). Figure 4.3 displays trailed spectra of the He I lines, ordered by the orbital phase of the binary. The blueshifted absorption is deepest around phase 0 and shallowest and often non-existent around phase 0.5. For He I 5875 and 6678, the emission follows a simple continuous variation where it is most redshifted around phase 0.15, and most blueshifted at phase 0.78. He I 7065, on the other hand, hosts similar variations to 5875 and 6678, but gains a blueshifted emission component

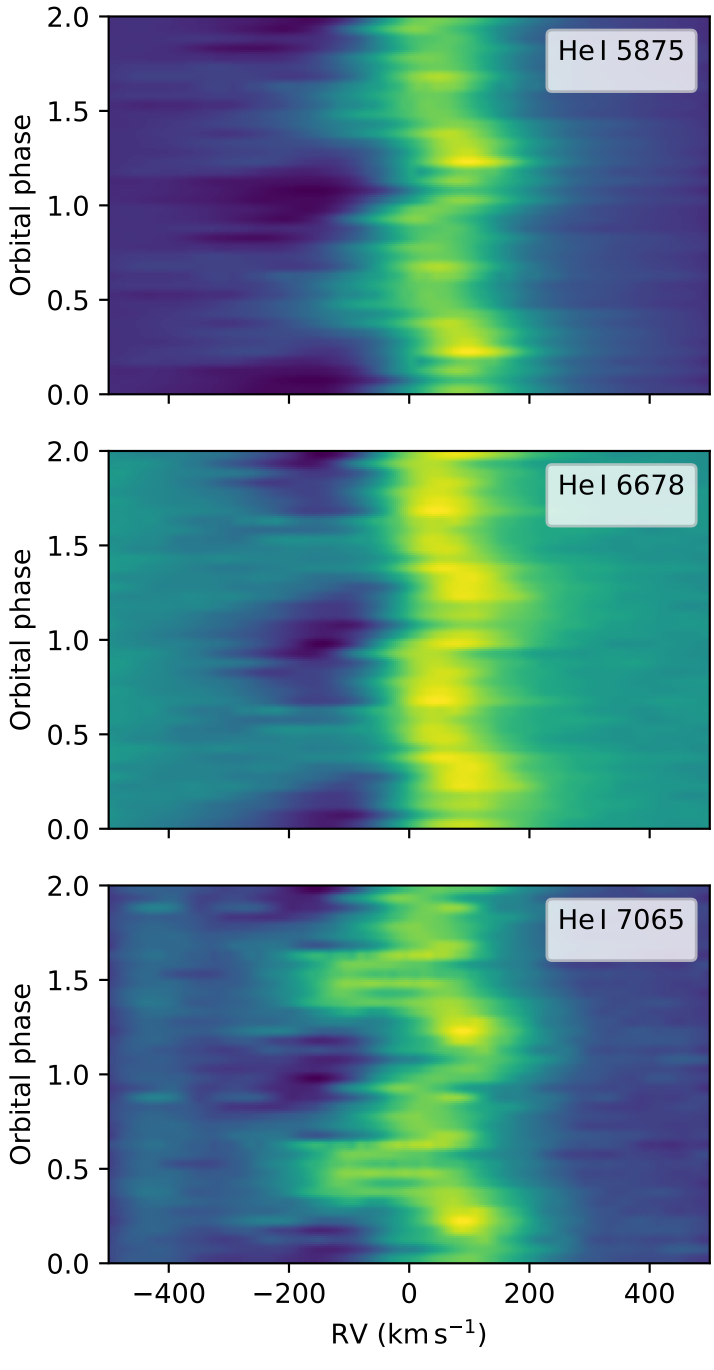

Figure 4.3: Trailed spectra of GG Car's visible He I lines, as observed by GJW. The spectra are split into 20 bins by orbital phase, and the average spectrum of the continuum-normalised spectra in each bin is displayed. Yellow is higher intensity, blue is lower intensity.

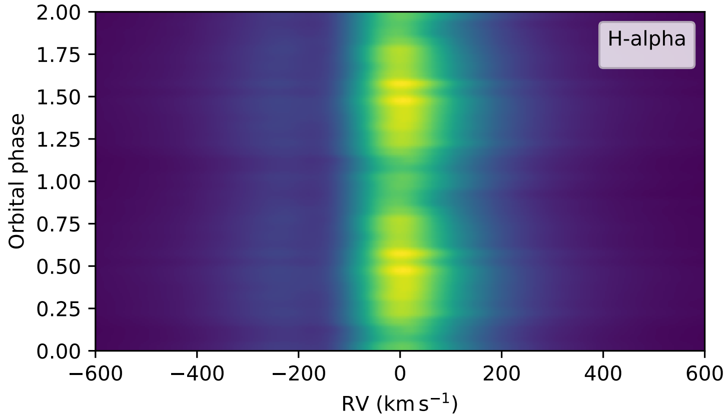

Figure 4.4: Same as Figure 4.3, except for GG Car's H-alpha complex.

between phase 0.3 to 0.6, at around $-120\,\mathrm{km\,s^{-1}}$. This extra component is unclear in individual spectra, but becomes apparent when successive spectra are taken in aggregate in the trailed spectra.

Here the radial velocity (RV) variability of the centres of the He I emission is quantified. It has been shown that Gaussian fitting is a robust and simple method of identifying the centres of emission lines that originate in winds (e.g. Blundell et al. 2007; Grant et al. 2020). Therefore, I fit the He I 5875 and 6678 lines in each GJW spectrum using a model consisting of one positive Gaussian and one negative Gaussian component, via a least-squares optimisation method implemented in `scipy` (Virtanen et al. 2020). The centroid of the positive Gaussian component is taken as the RV of the emission. He I 7065 is fitted in a similar manner, except two positive and one negative Gaussians are used; the centroid of the more redshifted positive Gaussian is then taken as the RV of the emission.

In comparison to the He I lines, the H-alpha complex in GG Car is remarkably constant over the orbital period, as is shown in Figure 4.4. There are no large RV changes and the blueshifted absorption persists at the same RV of around $-160\,\mathrm{km\,s^{-1}}$ for all phases without any measurable RV variability. In Figure 4.4, it appears as the intensity of the peak changes as a function of the orbital phase; however, this is due to the brightness variations along the orbital period. Since the spectra are normalised by the local continuum, around phase 0, when the system is brightest, the continuum is stronger which makes the H-alpha line appear dimmer in comparison. Conversely, at phase 0.5 the continuum is less bright, meaning the H-alpha complex appears brighter

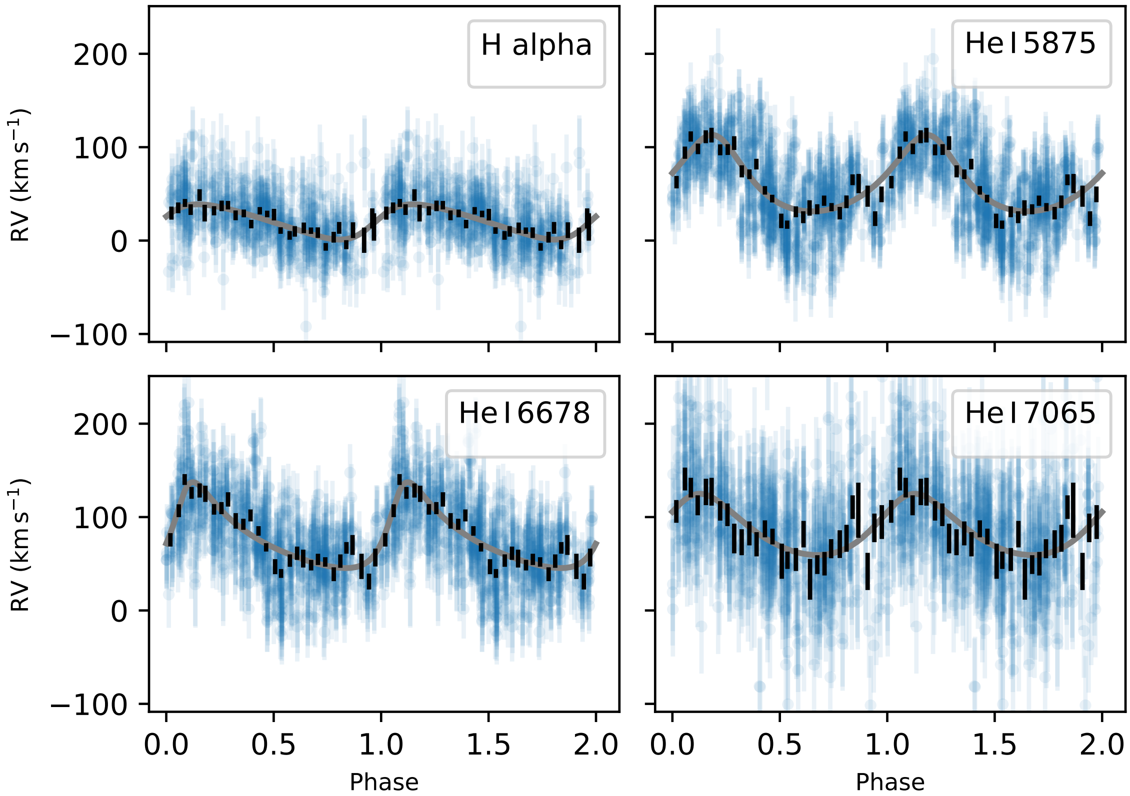

Figure 4.5: Radial velocity variations of the emission components of the visible He I lines at the 31-day orbital period, as observed by the GJW. Orbital solution fits are plotted as solid grey lines. The orbital models from the short-period variations are subtracted from the data, for clarity. The data are split into 30 phase bins for each line species and black error bars indicate the weighted mean and standard error of the weighted mean for the radial velocities in each bin. The error bars are both the errors from the Gaussian fitting routine and the fitted jitter, added in quadrature.

in comparison. This effect makes the equivalent widths of all emission lines a product of the continuum level rather than the emission line strengths. The wings of the H-alpha line, unlike the absorption or peak, do noticeably vary in radial velocity over the orbital period. Therefore, to extract the RV variations of the wings, the H-alpha complex is fit with multiple Gaussian components, including a negative Gaussian to account for the blueshifted absorption. The widest Gaussian component is then taken to be the wings of the H-alpha line.

Orbital RV solutions are fitted to the RV data for each line separately at both the orbital- and 1.583-day periods simultaneously, since the amplitude of the short-period variations are non-negligible for the He I lines. Although the origin of the 1.583-day variability is not Keplerian motion (Chapter 5 shows that it is most likely due to pulsations), a Keplerian model is useful and convenient method to fit a repeating signal in noisy data without adding many parameters. A Keplerian model, therefore, allows for the 1.583-day signal to be concurrently fitted so that the signal does not adversely affect the fitting of the variability at the orbital period by introducing additional noise and scatter. The amplitude K, the eccentricity e, the argument of periastron ω, and the phase of periastron M_0 are fitted for each period. I also fit for jitter, j, which models the width of Gaussian-distributed scatter of the data over the orbital period which may be underestimated by the measurement uncertainties. The systemic velocity v_0 is fitted separately for each line. The RV variations for each emission line are fitted separately by sampling the posterior probability distributions of the fit parameters using the Markov Chain Monte Carlo (MCMC) algorithm `emcee` (Foreman-Mackey et al. 2012). The log-likelihood for a set of parameters, θ, given N RV data points, D, with uncertainty σ is given by

$$\ln P(\theta \mid D, \sigma) = -\frac{1}{2}\sum_{i=0}^{N}\left[\frac{\left(D_i - v_{\mathrm{kep}}(\theta_{\mathrm{orb}}) - v_{\mathrm{kep}}(\theta_{1.583}) - v_0\right)^2}{\sigma_i^2 + j^2} + \ln\left(2\pi(\sigma_i^2 + j^2)\right)\right], \tag{4.2}$$

where θ_{orb} and $\theta_{1.583}$ are the orbital parameters for the long- and the short- period respectively, and v_{kep} is the Keplerian velocity calculated for a set of orbital parameters. The fitted parameters, θ, encodes θ_{orb}, $\theta_{1.583}$, v_0, and j. The uncertainties, σ, are taken from the least-squares fitting algorithm of the Gaussian fitting routines. Equation 4.2 assumes that the measurements are independent and that they have Gaussian-distributed uncertainties, and Section A.1 in the appendix gives further explanation of the form of Equation 4.2. The MCMC was run for 2000 burn iterations, then 2000 sampling iterations with 128 walkers. The fitted parameters are taken to be the median value of the Monte Carlo samples, and the uncertainty of the fitted parameters is taken as the difference of the median with the 16th and 84th percentiles. Table A.1 in the appendix list the fitted orbital parameters of the 31-day variations for to the He I and H-alpha emission lines. Chapter 5 discusses the 1.583-day variations in detail.

Figure 4.5 displays the RV variations of the H-alpha wings and the He I emission components at the orbital period, and the resulting fits for each period are plotted over the data. The data are binned by phase into 30 bins, and the weighted mean and standard error on the weighted mean in each bin are given by the black error

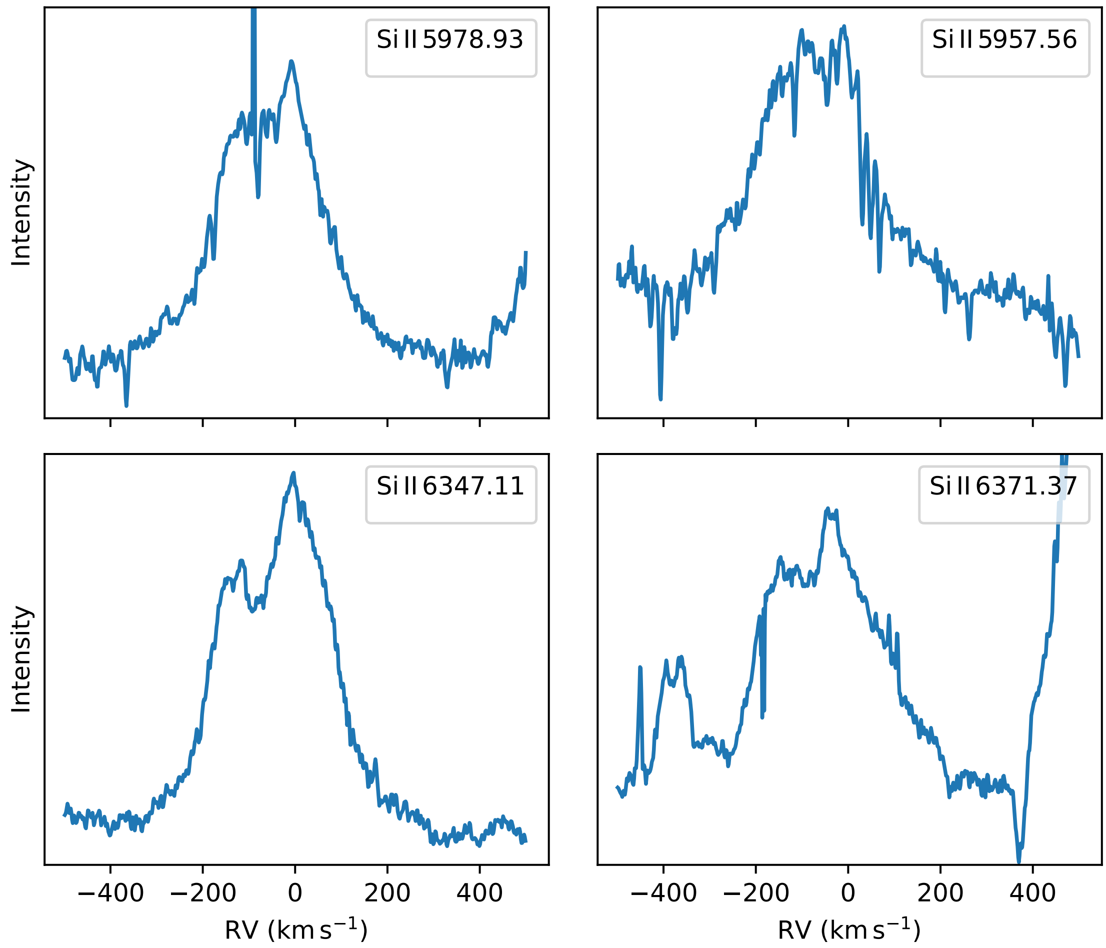

Figure 4.6: Average profiles of the Si II lines used in this study, as observed by FEROS.

bars. The RV variations have different amplitudes and profiles for each line species, with H-alpha having the subtlest variations. The RV variations of He I 6678 and 7065 have very similar profiles, with He I 5875 deviating slightly around phase 0.5, becoming more blueshifted. This is due to a second component arising in this line at that phase, similar to He I 7065; it can be seen very faintly in the trailed spectra in Figure 4.3, top panel. However, the second component is not as overwhelming in the 5875 line as the 7065 line, therefore attempting to fit this intermittent component in He I 5875 generally adds error to the fitting routine as the line becomes over-fit in these mid-resolution spectra.

Several Si II lines and Fe II lines also display RV variability at the orbital period. Due to the wealth of Fe II lines in the visible wavelength range, care is taken to investigate lines which are unblended. The choosing of lines is done with the aid of the

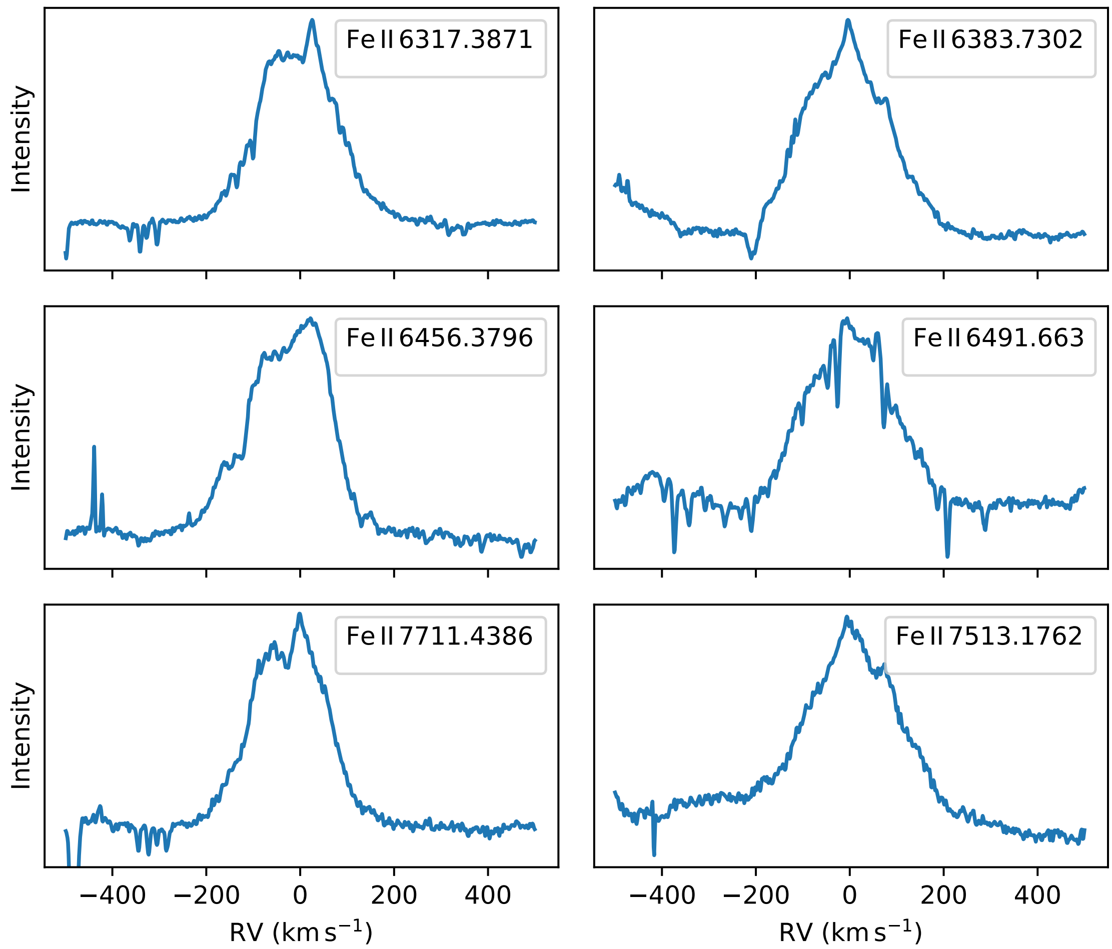

Figure 4.7: Average profiles of the Fe II lines used in this study, as observed by FEROS.

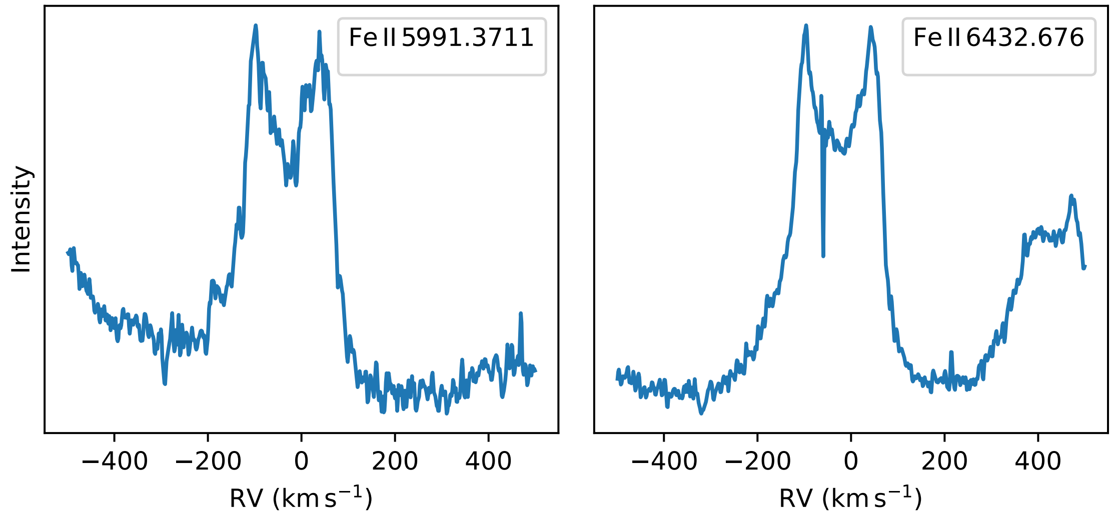

Figure 4.8: Same as Figure 4.6, except for the Fe II lines which do not exhibit variability at the orbital period.

FEROS data, as the high resolution data allow us to clearly discriminate between emission lines. Figure 4.6 displays the average profiles of the Si II lines chosen for this study. Likewise, Figure 4.7 displays the average profiles of the chosen Fe II lines which display 31-day variability.

Certain Fe II lines showed no RV variability in their centroids; two such lines were Fe II 5991.4 and 6432.7 Å. Figure 4.8 displays the FEROS observations of these two Fe II lines. Their line profiles clearly resemble double-peaked disk or ring profiles with a peak-to-peak splitting of $\sim$160 km s^{-1} and a central RV of ~ -20 km s^{-1}. Kraus et al. (2013) and Maravelias et al. (2018) discovered circumbinary material orbiting from $\sim$26 to $\sim$80 km s^{-1}, projected along the line of sight, placing these Fe II lines in those regions. Therefore, due to their disk profiles, splitting, and lack of RV variability, these lines are ascribed as forming in the circumbinary disk of the system. These two lines are both semi-forbidden and have low values of E_k (5.2 eV and 4.8 eV for Fe II 5991 and 6432, respectively) which may explain why they are only formed in the system's circumbinary disk. These circumbinary emission lines are studied in more detail in Chapter 6.

The RVs of the Si II and Fe II lines were calculated by fitting single positive Gaussian profiles to them in the GJW data, since they do not suffer significant absorption and the structure of each line is unresolved. The centroid of the Gaussian is then

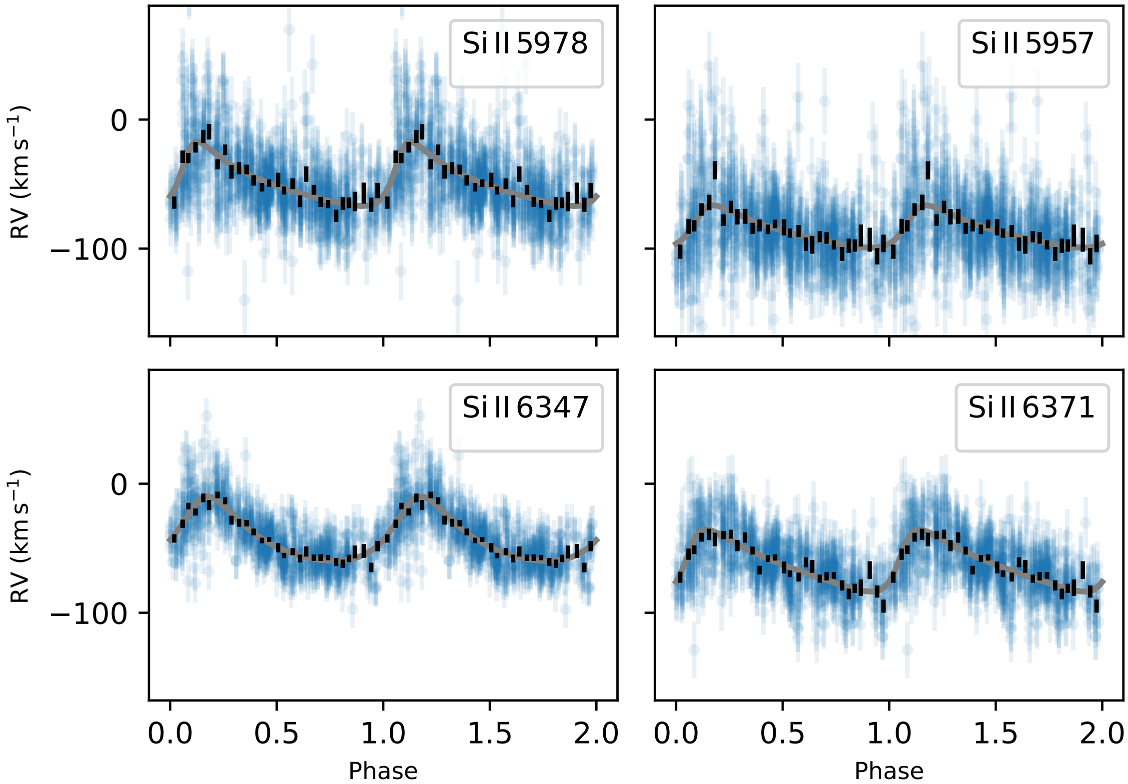

Figure 4.9: Same as Figure 4.5, except for the four Si II lines.

taken as the RV. Figures 4.9 and 4.10 display the RV variations for the Si II and Fe II lines, respectively. Orbital solution models were fitted using the same method as for the He I and H-alpha emission lines, and the resulting fits are also presented in Table A.1. The Si II lines tend to be more blueshifted than the systemic velocity of the system, and have smaller RV variations than the He I lines. The systemic velocities of the Si II lines vary for the different species. The Fe II lines, on the other hand, have much more consistent systemic velocities. In these lines, there appear to be two families of systemic velocities, those around $\sim 0\,\mathrm{km\,s^{-1}}$, and those around $-25\,\mathrm{km\,s^{-1}}$. This matches Gosset et al. (1985), who also found that the systemic velocities interpreted from Fe II lines depended on the multiplet observed.

As can be seen in Figures 4.5, 4.9 and 4.10, the amplitudes and profiles of the RV variations are highly variable across different line species. The He I lines display the largest RV variations, the Si II emission then follows, and the Fe II lines display the smallest RV variations. Since the amplitudes of variations appear to be related to the species of emission line, this raises questions as to the origin of these variations.

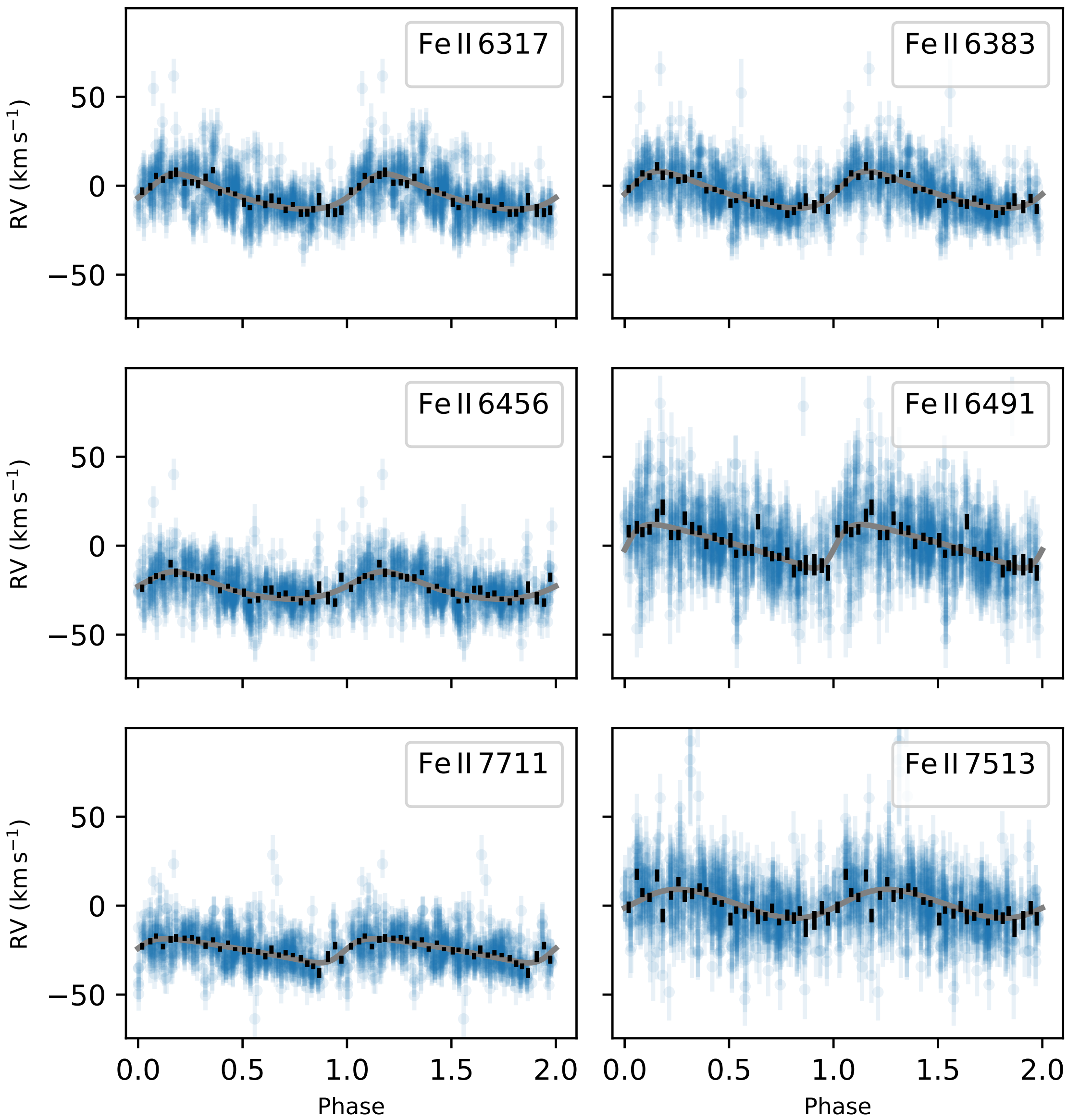

Figure 4.10: Same as Figure 4.5, except for the Fe II lines.

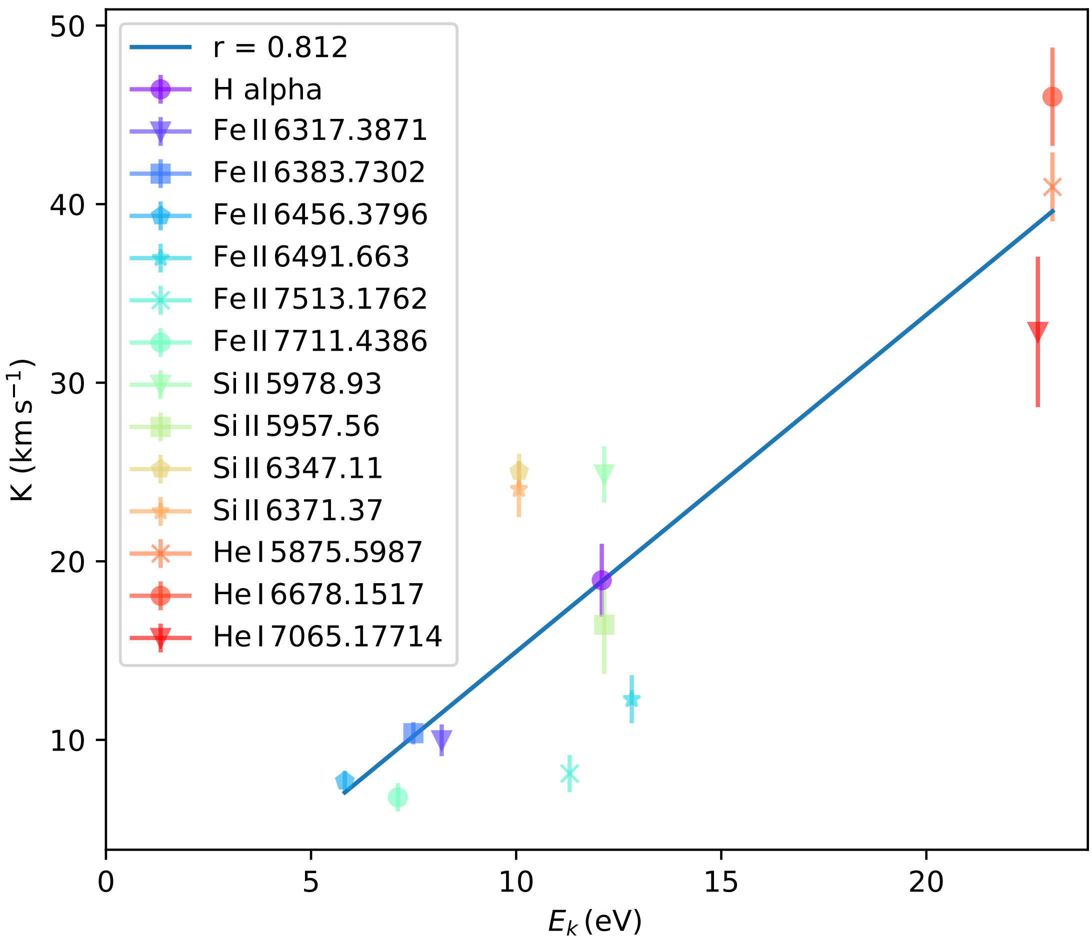

Figure 4.11: Amplitude, K, of the RV variations of the emission lines at the orbital period against E_k, the energy of the initial excited state leading to the lines. The correlation coefficient, r, weighted by the inverse of the square of the error, is quoted in the legend.

They cannot simply reflect the Keplerian motion of one of the binary components. To investigate, Figure 4.11 displays K, the amplitude of the RV fits, against E_k, the energy of the upper atomic state of the transition associated with the emission line. Figure 4.11 shows a strong positive correlation between E_k and K: the higher energy emission lines have larger observed changes in their radial velocities.

Since the emission lines also have differing v_0 by species, whether these are also correlated to E_k is investigated. Figure 4.12 displays the relationship of systemic velocity, v_0, of the emission lines which exhibit RV variability versus E_k, the energy of the upper atomic state. The top panel shows the relationship for all lines, and the bottom panel shows the relationship for all lines except for the Si II species. In the top panel, there is no statistically significant relationship between the two parameters. In the bottom panel, once Si II has been excluded, there is a very strong correlation between the parameters with higher E_k being correlated with more redshifted v_0. The minimal v_0 values, of the Fe II 6456 and 7711 Å lines, closely match the systemtic velocity of the system reported by Maravelias et al. (2018).

Despite being an interesting result, it cannot currently be said further whether the correlation between v_0 and E_k is true and the Si II lines are outliers which are more blueshifted than they should be, or whether there is no real relationship at all between v_0 and E_k.

Figure 4.13 displays the relationship of jitter against E_k. There is a very clear relationship between these two parameters, with higher E_k leading to higher jitter values in the fitting routine. This indicates that higher E_k is related to more scatter in the RV variations of the emission lines over the orbital period. He I 7065 is excluded from this analysis since the jitter for this line He I 7065 is anomalously larger than the other He I lines. This is due to the more complex fitting routine that is required to extract the RV of the He I 7065 emission; this introduces scatter in the RV curve due to fitting inaccuracies which inflates the measured jitter.

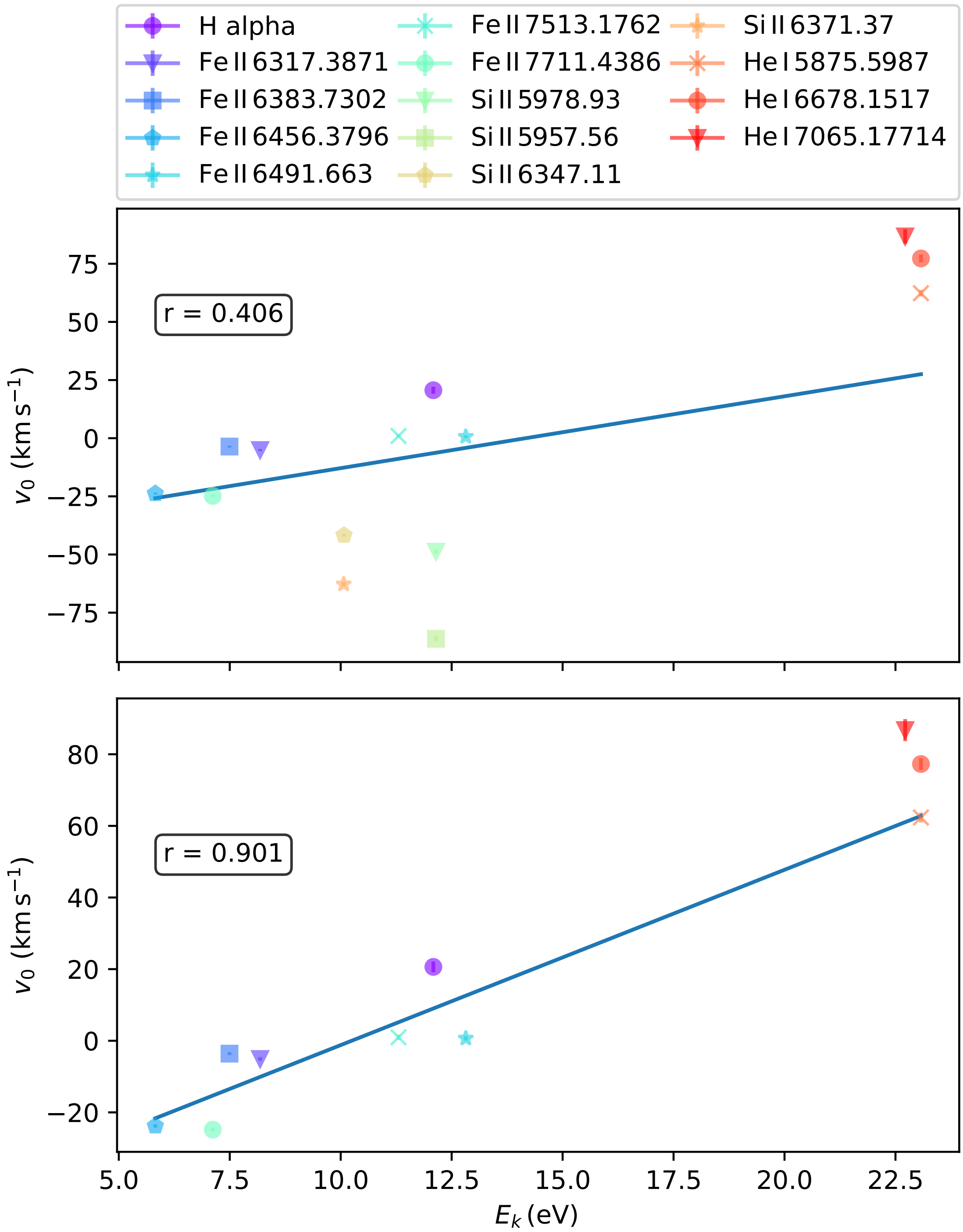

Figure 4.12: The relationship of v_0 with E_k for all lines investigated in this study (top panel) and for all lines except Si II (bottom panel). The correlation parameter, r, is given in the panel for both of these cases.

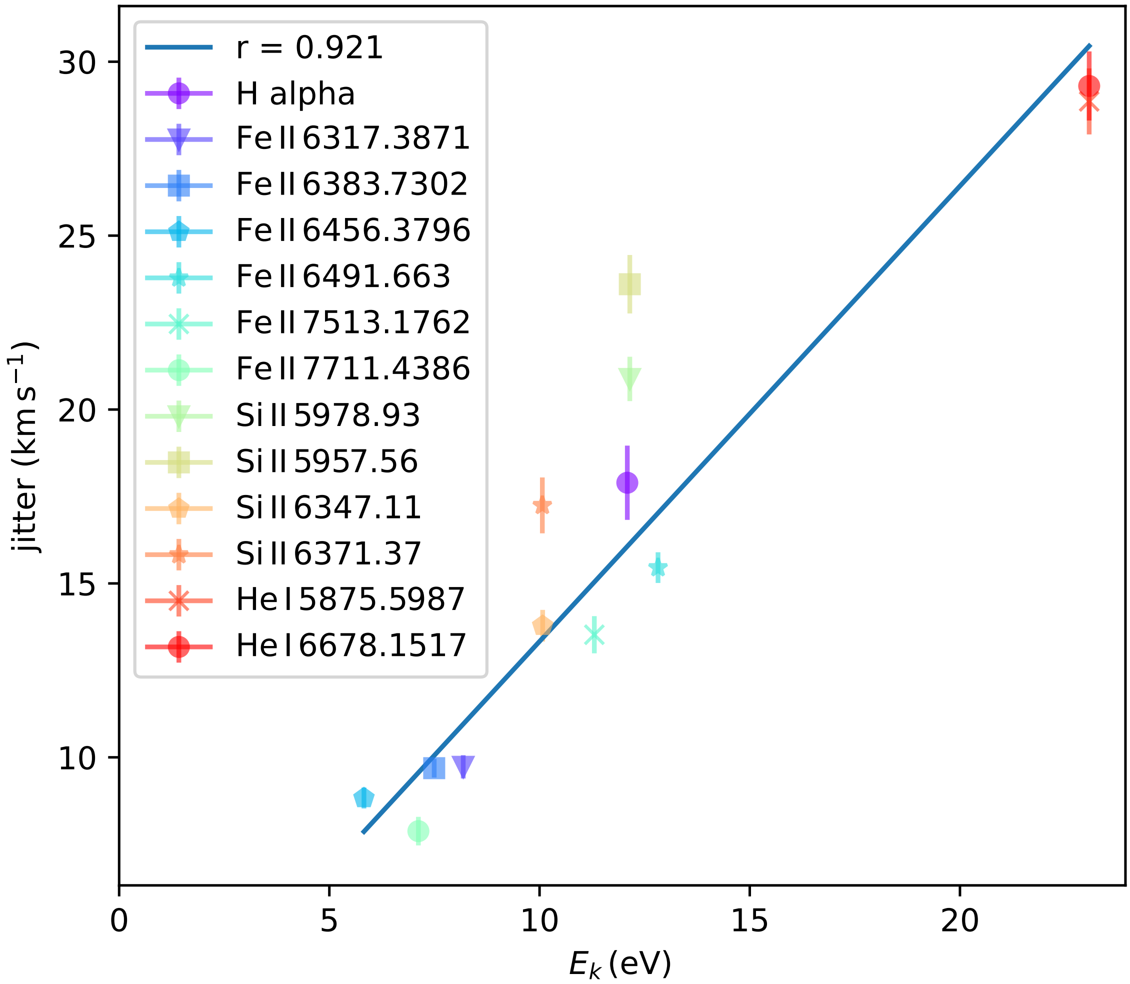

Figure 4.13: The relationship of jitter with E_k for all lines investigated in this study, except He I 7065 which is excluded because its jitter is anomalously large due to the more complex fitting routine that must be used to extract the line's RVs. The correlation parameter, r, is given in the legend.

4.3 Determining the orbital solution of GG Carinae using wind emission lines

The orbital solution of the binary in GG Car has been as-of-yet inadequately determined. Marchiano et al. (2012) ascribed He I absorption as being due to photospheric absorption and they find a systemic velocity $v_0 = -162\,\mathrm{km\,s^{-1}}$ using this assumption. However, adopting this v_0 would mean that all emission lines in the system are significantly redshifted, implying that this v_0 is too negative (see the systemic velocity column of Table A.1 and Figure 4.12). Inspection of FEROS and GJW spectra leads me to agree with Maravelias et al. (2018) that $v_0 \approx -22\,\mathrm{km\,s^{-1}}$ is more consistent with the radial velocities of the system's emission lines. Furthermore, the observation of photospheric absorption lines is rare in B[e]SGs, and even in cases where they are observable they tend to be heavily polluted (Kraus et al. 2016a; Kraus 2019). The He I absorption being blueshifted absorption components originating in the strong stellar wind of the system is more consistent with the data, the B[e]SG paradigm of opaque stellar atmospheres, the findings of Maravelias et al. (2018), and Hanes et al. (2018)'s measurement of the average radial velocities of the stars in the Carina nebula. Therefore, a correct determination of the orbital parameters necessitates an alternative method to uncover the underlying Keplerian motion of the binary components.

The emission lines studied that express RV variability at the orbital period of the binary must be formed in the circumstellar environment and therefore must be formed one of two ways, either in the circumstellar disk of one of the binary components, or in the stellar wind originating from one of the components. They can be ascribed to originating in the stellar wind rather than in a circumstellar disk for three reasons: the amplitudes of the RV variations are different for each line species, as shown in Figure 4.11, whereas they would be identical if they were formed in a disk which followed the Keplerian velocity of one of the stellar components; the primary, which would host the circumstellar disk, is almost filling its Roche lobe (Kraus et al. 2013; Section 4.4.3.3, this study), making a circumstellar disk unstable; and the profiles of the lines which exhibit RV variability do not resemble the double-peaked profiles of Keplerian disks, as shown in the high-resolution FEROS spectra in Figures 4.6 and 4.7. The Fe II 6383.7 line even hosts a slight P-Cygni profile, with blueshifted absorption. The lines which do display disk profiles have no RV variability, indicating

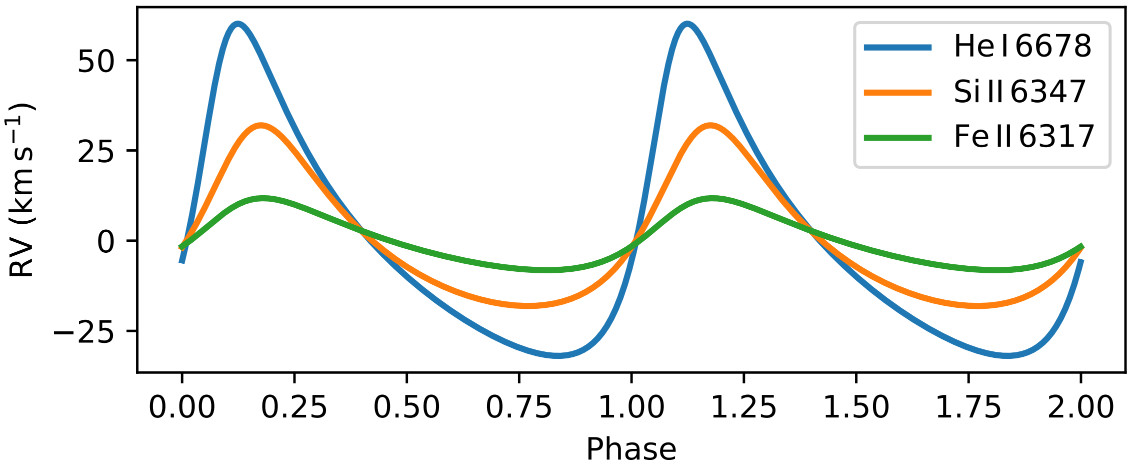

Figure 4.14: Comparison of the fitted RV models at the orbital period to representative He I, Si II, and Fe II emission lines. The systemic velocity has been subtracted from the models to highlight the synchronicity, but varying amplitudes, of the RV variations between the species.

their formation in the circumbinary disk (Fe II 5991 and 6432, Figure 4.8).

The interpretation of the RV variations of the emission lines at the orbital period as originating in the stellar wind of the B[e]SG primary explains the relationship of K with E_k, as is shown in Figure 4.11. As is investigated in Grant et al. (2020) using the example of the Hydrogen Balmer series in η Carinae, the measured velocities and therefore Keplerian orbital solutions from wind emission lines are dependent on the energetics of the emission lines (see their figure 8). Lines which have a higher E_k are formed deep in the wind, closer to the star; conversely the lower E_k lines are formed at larger radii and at later flow times on average than the higher energy lines. The lines are then formed for a finite time before the wind cools down below the temperature required to excite to the line's energy level. This smearing of the Keplerian velocity of the binary component leads to the higher energy lines tracing the Keplerian velocity of the star more closely than the lower energy lines. This smearing is demonstrated in Figure 4.14: the He I, Si II and Fe II RV variations are largely in phase, but the lower energy lines have their variations smeared out compared to the highest energy He I line.

Grant et al. (2020), using the examples of the luminous blue variable in η Carinae and the Wolf-Rayet in RMC 140, showed that the underlying orbital parameters of massive stars obscured in thick circumstellar envelopes can be probed by observing the radial velocity variations of the emission components of lines formed in the stellar wind, despite the smearing. They show that the underlying orbital motion can be found by fitting a Keplerian orbital solution which has been convolved with line emissivity kernels, which are calculated using stellar atmosphere codes to simulate the stellar winds, that quantify the luminosity of the emission lines as a function of the wind-flow time. Therefore, I follow the methodology of Grant et al. (2020) to properly model the time-dependent emissivity of the individual wind lines in GG Car, and use these to fit the orbital parameters of the binary orbit.

4.3.1 Methods

The method of determining the Keplerian orbital solution using wind emission lines and line-formation kernels is described in exquisite detail in section 3 of Grant et al. (2020); here I outline the method in the context of determining the orbital solution of GG Car.

4.3.1.1 CMFGEN simulations

The modelling method of Grant et al. (2020) encapsulates both the star's orbital motion and the propagation of the wind, to reconcile differences in emission line variability with a consistent orbital solution. The method requires knowledge of the luminosity of each emission line as a function of wind-flow time outwards from the star, known as the line-formation kernels.

In order to calculate the line-formation kernels in GG Car emission the atmosphere of the primary is simulated using the non-local thermodynamic equilibrium, fully line-blanketed stellar atmosphere code, `CMFGEN` (Hillier & Miller 1998; Hillier & Lanz 2001). `CMFGEN` allows us to calculate the luminosity of emission lines as a function of radius, r; this is then translated into wind-flow time, $t_{\rm flow}$, by recasting the radius using the analytic β-velocity law of Castor et al. (1975):

$$v_{\rm wind}(r) = v_0 + (v_\infty - v_0)\left(1 - \frac{R_*}{r}\right)^\beta , \tag{4.3}$$

M_*	$24\,M_\odot$
$T_{\rm eff}$	$23\,000\,{\rm K}$
L_*	$1.8 \times 10^5\,L_\odot$
R_*	$27\,R_\odot$
$\dot{M}$	$2.2 \times 10^{-6}\,M_\odot\,{\rm yr}^{-1}$
v_∞	$265\,{\rm km\,s^{-1}}$
β	1
$f_{\rm v}$	0.1
$v_{\rm cl}$	$100\,{\rm km\,s^{-1}}$

Table 4.1: Parameters used in the CMFGEN simulation of the atomsphere of the B[e]SG primary in GG Car. M_* is the mass of the star, $T_{\rm eff}$ is the effective temperature, L_* is the luminosity, R_* is the photospheric radius, $\dot{M}$ is the mass-loss rate, v_∞ is the terminal velocity, β is the velocity law exponent, $f_{\rm v}$ is the clumping volume filling factor, and $v_{\rm cl}$ is the wind velocity where clumping becomes important.

where v_∞ is the terminal velocity of the wind, v_0 is the initial velocity, and R_* is the stellar radius, and integrating from the sonic point r_s to r:

$$t_{\rm flow} = \int_{r_s}^{r} \frac{dr}{v_{\rm wind}(r)}. \tag{4.4}$$

Table 4.1 displays the important parameters used in the CMFGEN simulation of the atmosphere of GG Car. The stellar mass, luminosity, and radius are taken from Section 3.3.1, and the effective temperature is taken from the SED analysis of Marchiano et al. (2012). The value of the terminal velocity, $v_\infty = 265\,{\rm km\,s^{-1}}$, was chosen after inspection of the high-resolution FEROS spectra which show it is both the average half-width at zero intensity of the Si II emission, He I emission and H I Balmer emission from n=3–8, and the radial velocity of the blue-most edge of the middle-absorption component in the absorption complexes of the H I Balmer and He I lines. Appendix A.3 describes the determination of v_∞ in further detail. The mass-loss rate, $\dot{M} = 2.2 \times 10^{-6}\,M_\odot\,{\rm yr}^{-1}$, was estimated using the wind momentum-luminosity relation for early B I-type supergiant stars (Kudritzki & Puls 2000). This mass loss rate is similar to the measurement of McGregor et al. (1988).

β is chosen to be 1, as this has been shown to be a typical value for supergiants in dense winds (Puls et al. 1996). The clumping parameters of the filling factor, $f_{\rm v}$, and the representative wind clumping velocity, $v_{\rm cl}$, having no previous determination

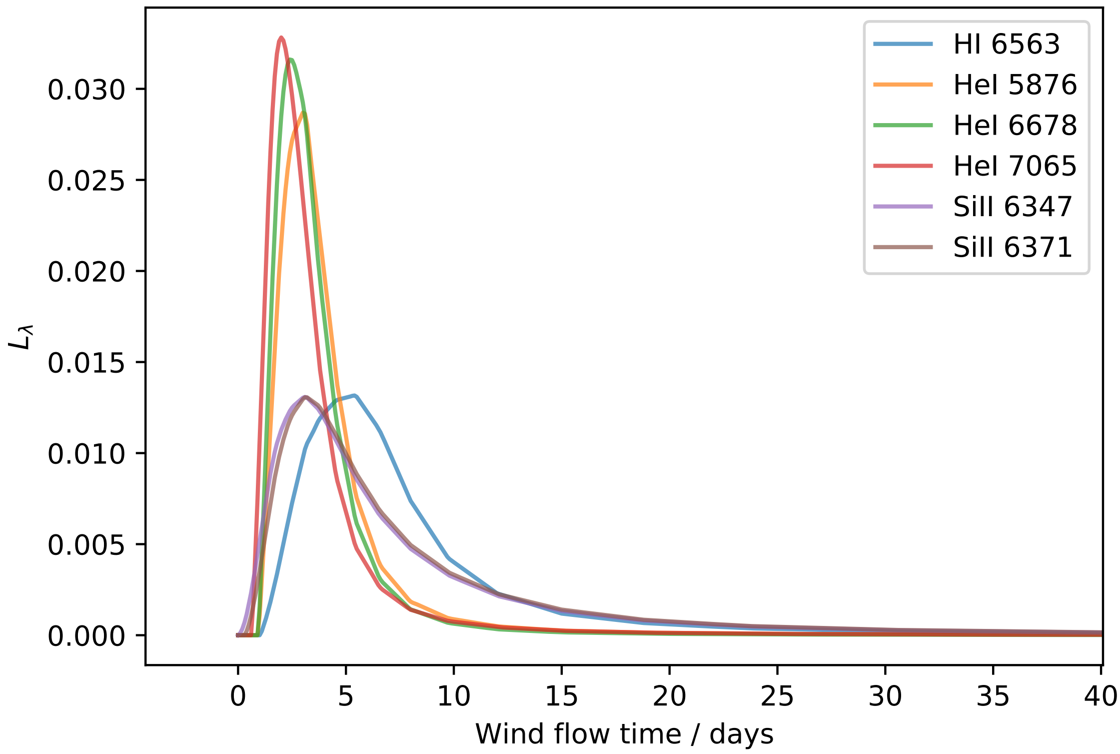

Figure 4.15: Emission line emissivity, L_λ, against wind-flow time for the wind emission lines used in this study.

in the literature on GG Car and being indeterminate from the few high-resolution FEROS spectra available, were chosen to be standard values for massive stars at 0.1 and $100\,\mathrm{km\,s^{-1}}$ respectively.

The resulting line luminosities as a function of wind-flow time are shown in Figure 4.15. The calculated line luminosities against wind-flow time shown in Figure 4.15 reflect that the He I lines are formed shortly after the wind passes the sonic point, whereas the Si II and H-alpha emission form later on average. Table 4.2 lists the peak and median emission times of the calculated line luminosities. The peak and median times of the line luminosities for all lines are less than the ∼31-day period of the binary. It was not possible to extract line-emissivity kernels of Si II 5957 and 5978 or any Fe II lines from the CMFGEN simulation, so these lines are excluded from this analysis.

Figure 4.16 briefly demonstrates how these line emissivities will be used in order to calculate the apparent RV variations of the emission lines in GG Car. The top

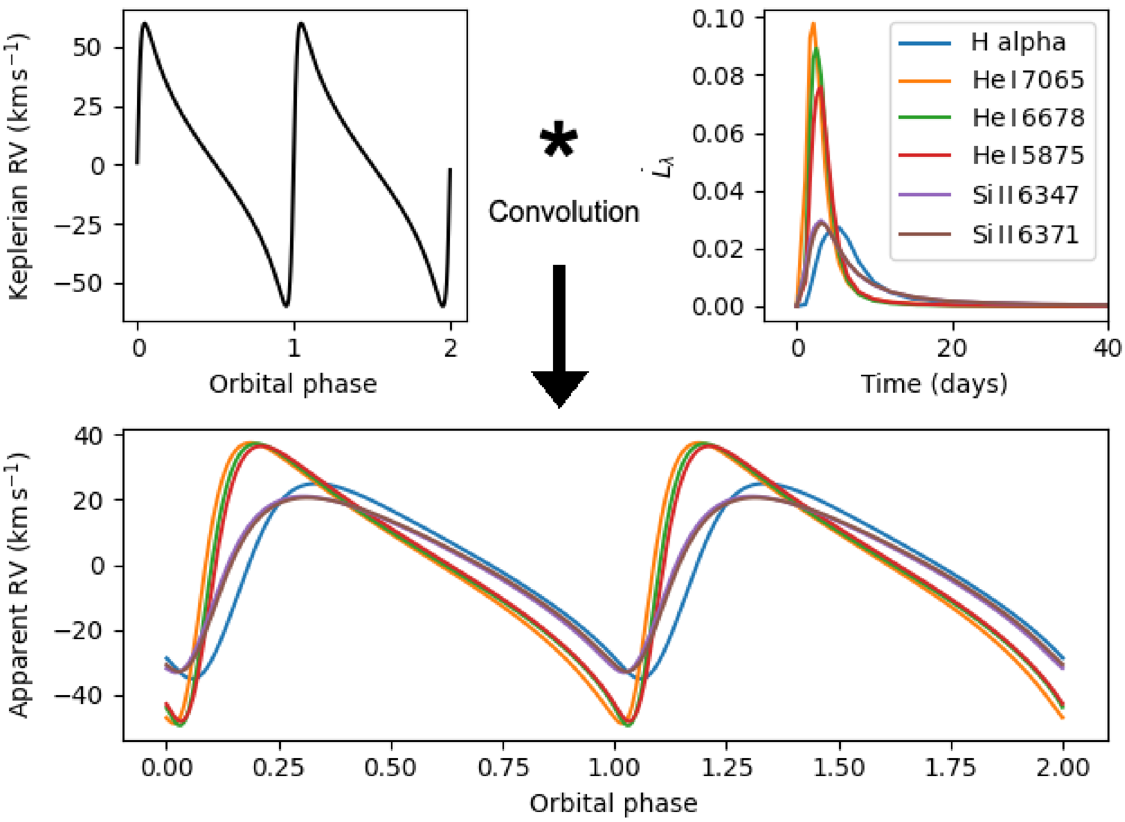

Figure 4.16: Demonstration of how the line-emissivity kernels are used in order to determine the apparent RV curves of the emission lines in GG Car. The top left panel shows an example arbitrary Keplerian RV curve of a binary component, assuming a 31-day orbital period. The top right panel displays the line-emissivity kernels of GG Car calculated using `CMFGEN`, with the relevant line identifications given in the legend. The Keplerian RV curve is convolved with the emissivity kernels of each line in order to calculate the apparent RV variations of each of the emission lines over the orbital period. The would-be apparent RV curves of each emission are shown in the bottom panel. The legend in the top right panel also gives the line identifications for the apparent RV curves. It is these convolved RV curves which are compared to the spectroscopic data, fitting for the Keplerian orbital parameters.

Line	Peak [days]	Median [days]
H-alpha	5.4	$6.4^{+6.0}_{-2.7}$
He I 5876	3.0	$3.5^{+2.3}_{-1.2}$
He I 6678	2.4	$3.2^{+2.0}_{-1.1}$
He I 7065	2.0	$2.9^{+2.3}_{-1.1}$
Si II 6347	3.1	$5.5^{+8.5}_{-3.0}$
Si II 6371	3.1	$5.8^{+8.8}_{-3.0}$

Table 4.2: Time to the peak and median emission of the lines' emissivity kernels, calculated with `CMFGEN`. The difference of the median time with the 84th and 16th percentiles of the emission are quoted by the superscript and subscript respectively.

left panel displays an arbitrary Keplerian RV curve, which represents the true RV of a binary component along its orbit, assuming a 31-day orbit. The top right panel of Figure 4.16 shows the emissivities of the emission lines of interest as a function of wind-flow time, and are the same emissivities as in Figure 4.15. The Keplerian RV is convolved with each of these line emissivities in order to get the apparent RVs of each of the emission lines. Note that the effect of convolving the Keplerian RV curve with the emissivity kernels is to delay the apparent RV curve and to wash out the features of the curve, with varying degrees depending on the shape of the line emissivity kernel. In order for the RV of an emission line to perfectly follow the Keplerian velocity of the binary component, its line emissivity would need to be a delta function at wind-flow time $t = 0$. When fitting the orbital solution of the binary, the RV data of the emission lines are compared to the calculated apparent RV curves while varying the binary's orbital parameters.

4.3.1.2 Fitting the orbital solution

Section 4.2.2 describes how orbital solutions were fitted for the individual emission lines; from these fits the jitter, j, and systemic velocity, v_0, are extracted for each individual line. j and v_0 for each line are listed within Table A.1.

One Keplerian orbital solution is then fit to the RV data of all emission lines simultaneously using the wind line emissivities and the method described in Section 4.3.1.1. The orbital solution is fitted by determining the posterior probability distributions of the orbital parameters with the log-likelihood function, again using the MCMC algorithm `emcee`. In the first instance, the v_0 calculated in the single line-fitting routines is subtracted from the data for each emission line. Then for each

MCMC iteration the Keplerian solution, $v_{\rm kep}$, for the given input parameters, θ, is convolved with the line formation kernel, λ_k, of each line and the log-likelihood is calculated using the convolved Keplerian velocities. The log-likelihood function for the convolution model is thereby given as

$$\ln P(\theta \mid D, \sigma) = -\frac{1}{2}\sum_k \sum_{i=0}^{N} \left[\frac{(D_{k,i} - \lambda_k * v_{\rm kep}(\theta) - v_0)^2}{\sigma_{k,i}^2 + j_k^2} + \ln\left(2\pi(\sigma_{k,i}^2 + j_k^2)\right)\right], \quad (4.5)$$

where $D_{k,i}$ is the ith data point for line k, $\sigma_{i,k}$ is the ith uncertainty for line k taken from the Gaussian fitting routine, λ_k is the line formation kernel for line k, and j_k is the jitter for line k. j_k for each line is taken from the single line fitting routine, described in Section 4.2.2, to account for scatter in the data.

Therefore this method fits for one unified set of the primary's orbital parameters, θ, encoding its semi-amplitude, K, argument of periastron, ω, eccentricity, e, phase of periastron, M_0, and the orbital period, P, using all emission lines simultaneously. M_0 is the phase of periastron relative to a reference time T_0; T_0 is chosen to be JD 2452051.93, which is the time of periastron found by Marchiano et al. (2012). I also fit for v_0 to aid the fitting routine, though this will not be the true systemic velocity of the system, but instead should be near zero since the data for each line has had its individual systemic velocity subtracted.

256 MCMC walkers are run for 10 000 burn iterations then 10 000 walk iterations. The fitted parameters are taken as the median of the Monte Carlo samples of the parameters, and the errors the difference of the median with the 16th and 84th percentiles.

4.3.2 Orbital solution fit results

Table 4.3 presents the results for the underlying Keplerian orbital solution, using all emission lines simultaneously, and Figure 4.17 displays the posterior probability distribution for the fitted orbital parameters. The binary has a period of 31.011 ± 0.01 days, and is very eccentric. The phase of periastron M_0, compared to the reference time T_0 = JD 2452051.93 is 202.35°, meaning that the "phase" of periastron is significantly different to Marchiano et al. (2012). The time of periastron calculated is $T_{\rm peri}$ = JD 2452069.4 $\pm$ 1.3, which therefore gives us the binary orbital ephemeris of

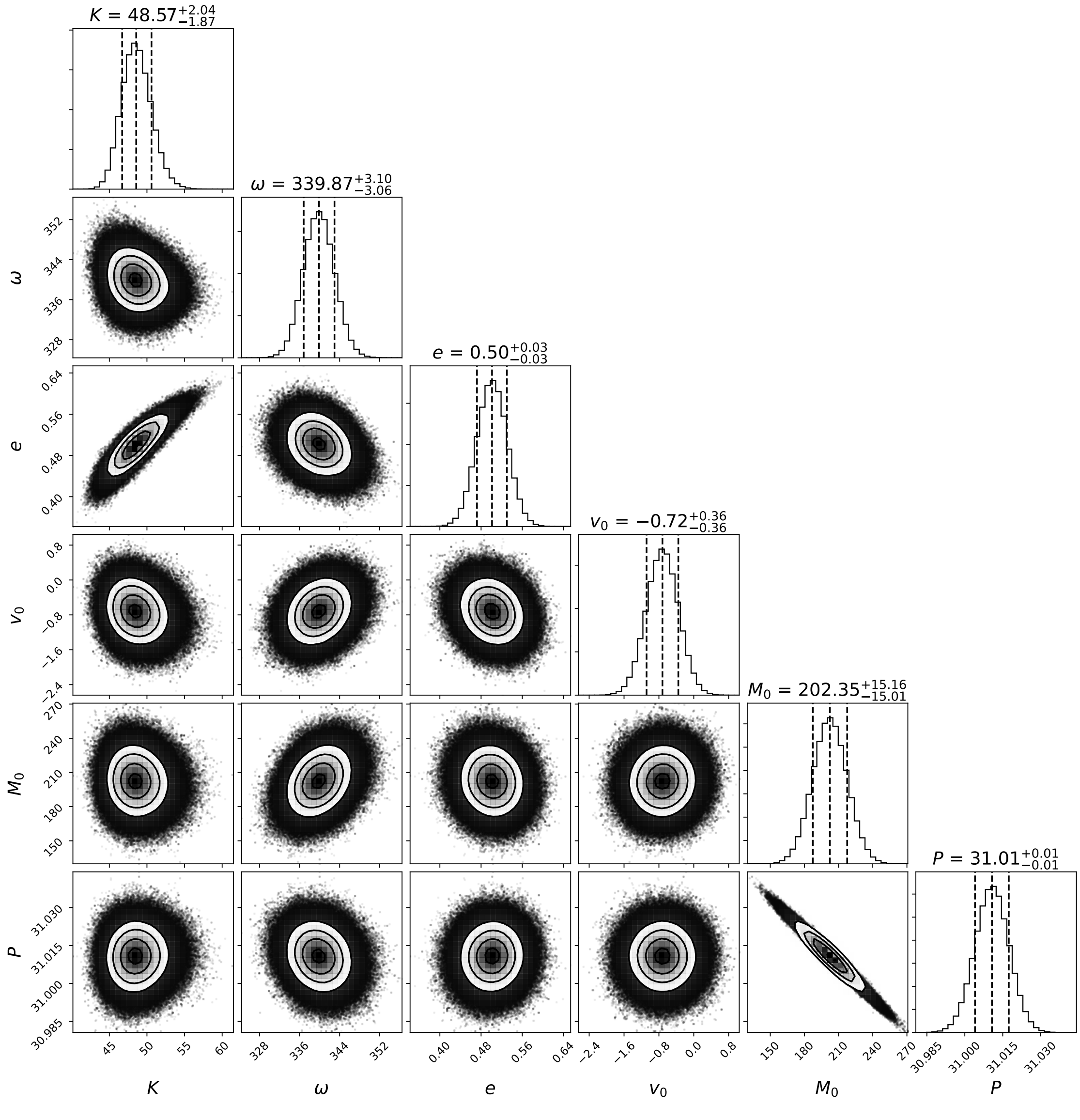

Figure 4.17: The posterior probability distribution for the parameters in the fits of the Keplerian orbital solution. Dashed vertical lines denote the 16th, 50th, and 84th percentiles. K is the orbit amplitude, ω is the argument of periastron, e is orbital eccentricity, v_0 is the velocity offset without physical significance, M_0 is the phase offset of the reference time $T_0 = \mathrm{JD}\,2452051.93$, and P is the orbital period.

K	$48.6^{+2.0}_{-1.9}\,\mathrm{km\,s^{-1}}$
ω	$339.9^{+3.1}_{-3.1}\,^{\circ}$
e	$0.50^{+0.03}_{-0.03}$
v_0	$-0.7^{+0.4}_{-0.4}\,\mathrm{km\,s^{-1}}$
M_0	$202^{+15}_{-15}\,^{\circ}$
P	$31.01^{+0.01}_{-0.01}$ days
T_{peri}	JD 2452069.4 ± 1.3

Table 4.3: The fitted values for the underlying Keplerian motion of the B[e]SG primary using all emission lines in aggregate and their line formation kernels, λ_k. K is the orbit amplitude, ω is the argument of periastron, e is orbital eccentricity, v_0 is the velocity offset without physical significance, M_0 is the phase offset of the reference time $T_0 =$ JD 2452051.93, P is the orbital period, and T_{peri} is the epoch of periastron.

Equation 4.1.

Figure 4.18 displays the data for the RV of each emission line in this study, along with the fitted underlying Keplerian motion in orange, and the Keplerian motion convolved with the line's formation kernel, λ_k, as a black line. Black points denote the average value of the RV data in 10 phase bins. The convolved Keplerian velocities match the phase averaged RV data exceptionally well for all emission lines studied, indicating that this orbital solution along with the calculated λ_ks for each line can recreate the measured RV variability.

Therefore, though `CMFGEN` assumes spherical symmetry and the winds of B[e]SGs are inherently non-symmetric, it is found that simulating the mid-velocity wind speed gives line-formation kernels which are consistent with the relative RV variations of the emission lines in GG Car. The present study, therefore, marks a significant improvement in the determination of the orbital solution of the binary. Further studies may simulate the line formation kernels expected in an inhomogeneous wind, in order to extract an even more accurate orbital solution.

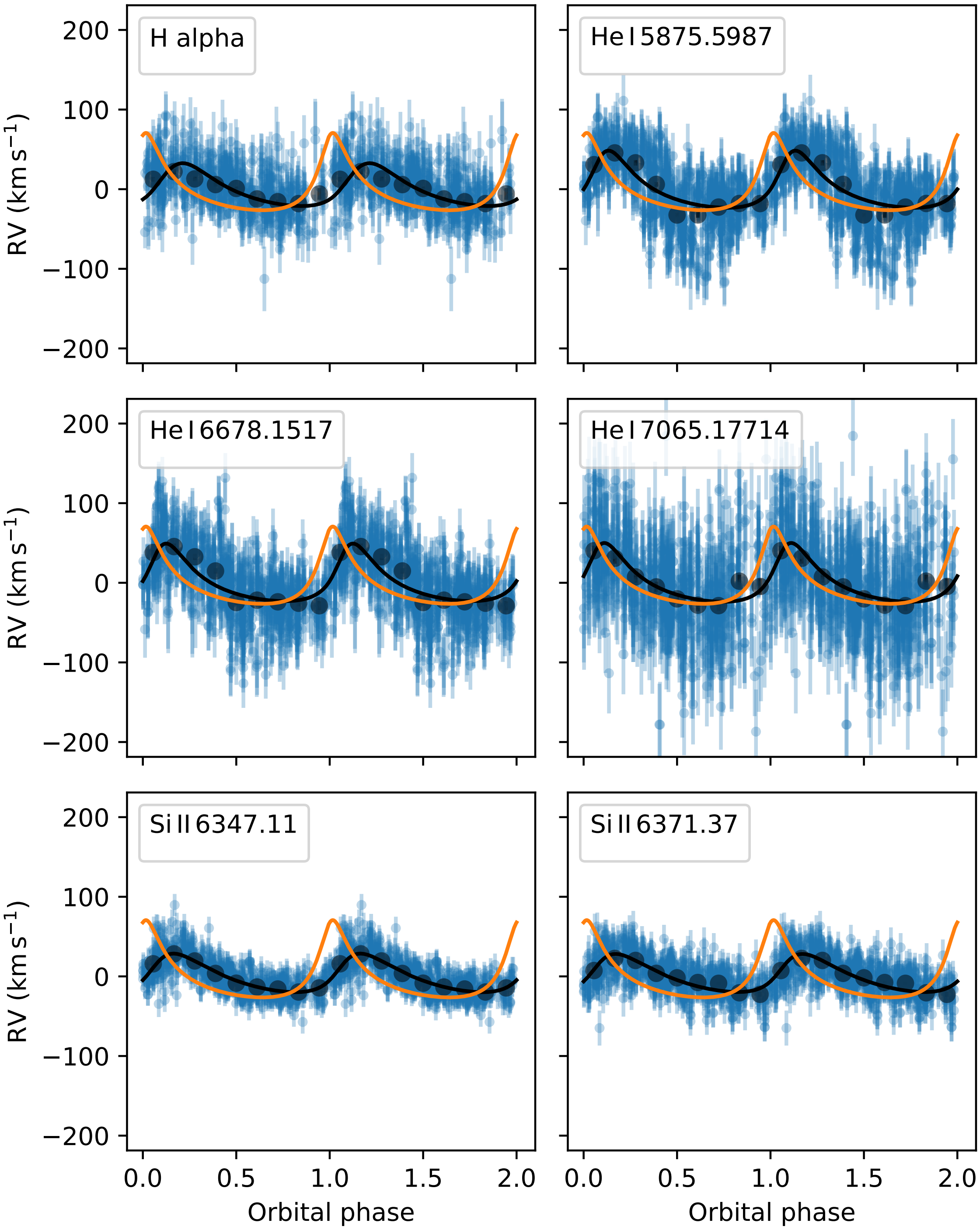

Figure 4.18: Results of the fitted Keplerian solution convolved with the line formation kernel λ_k for each line. The underlying Keplerian velocity, which is the same for each emission line's panel, is plotted in orange. The Keplerian velocity convolved with the line formation kernel is plotted as a black line. Black points show the average RV of the data in 10 phase bins. The data for each line has had its systemic velocity listed in Table 4.3 subtracted.

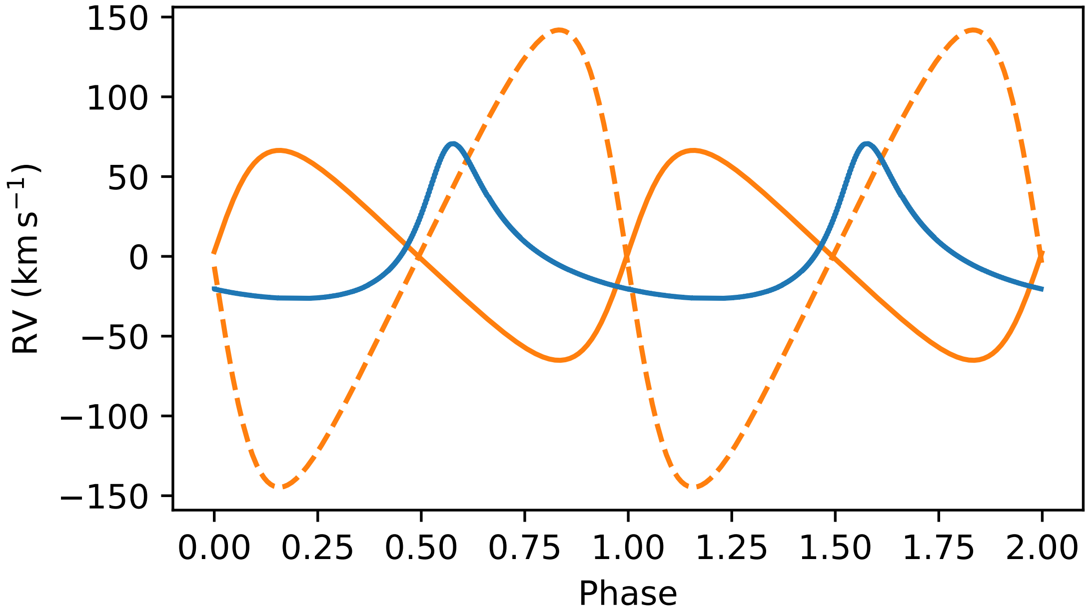

Figure 4.19: Radial velocity of the B[e]SG primary calculated in this work (blue, solid line) along its orbit, compared to the orbital solution of Marchiano et al. (2012) (orange, solid and dashed line for the primary and secondary respectively). Systemic velocities have been subtracted, to allow direct comparison.

4.4 Discussion

4.4.1 Discrepancy with the orbital solution of Marchiano et al. (2012)

Figure 4.19 directly compares the orbital solution determined in Section 4.3.1.2 against the orbital solution of Marchiano et al. (2012). Compared to the Marchiano et al. (2012) solution, I find that the binary is considerably more eccentric, and the argument of periastron is $\sim 20°$ into the plane of the sky, as opposed to nearly along the line of sight. The amplitude, K, of the primary's orbit is significantly less than previously found, which will have repercussions for the mass of the secondary and the orbital separation; this is discussed in Section 4.4.2.

Further evidence for rejecting the orbital solution of Marchiano et al. (2012) comes from their measured systemic velocity, v_0, of $-162 \pm 4.3\,\mathrm{km\,s^{-1}}$; this systemic velocity is far more blueshifted than any of the measured v_0 values listed in Table A.1. In addition, Maravelias et al. (2018) independently found the systemic velocity to be $-22\,\mathrm{km\,s^{-1}}$ by centring the circumbinary [O I] 6300 line, and by using a similar

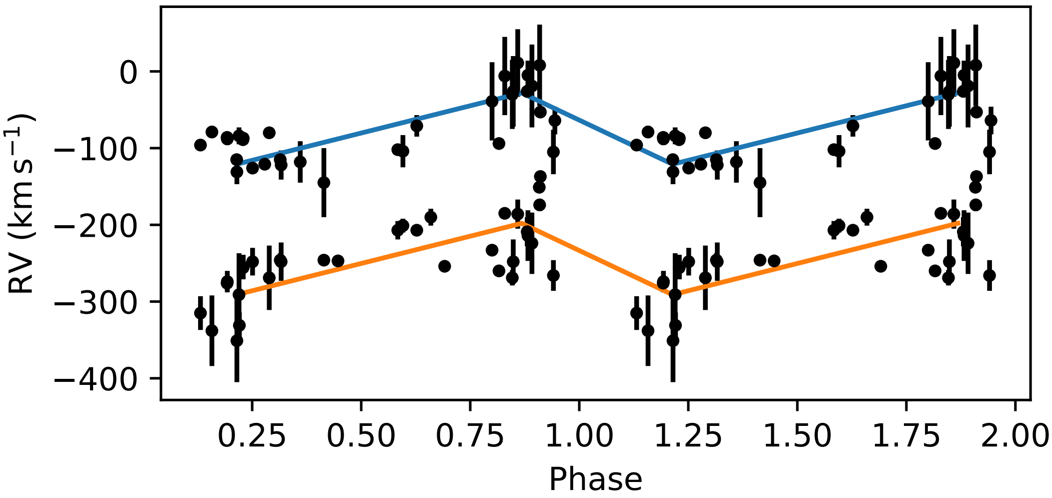

Figure 4.20: The RV data from Marchiano et al. (2012) used in that study to determine the orbital solution of the binary, with the assignment of the absorption components to the primary/secondary removed. Plotted lines roughly indicate what are proposed as two wind components varying together in RV.

method with GJW spectra a consistent systemic velocity of $-12 \pm 14\,\mathrm{km\,s^{-1}}$ is found. As the systemic velocity derived from the He I absorptions is far more blueshifted than all emission lines, it is highly unlikely that these absorptions are due to photospheric absorption in the binary components.

The H I and He I absorption is therefore reinterpreted as self-absorption in the multiple wind components of the B[e]SG primary, leading us to conclude that the orbital solution of Marchiano et al. (2012) is incorrect. I propose that the absorption RV data presented in figure 2 of Marchiano et al. (2012) is consistent with two blushifted wind components, whose RV separation from each other is mostly constant, and whose RV variations are mostly in phase with each other along the binary orbit. Figure 4.20 plots the RV data quoted in table 1 of Marchiano et al. (2012) without their attribution of the RV data to the primary or the secondary, to highlight the inadequacy of their orbital solution. Furthermore, their data supports the finding of this study that there are two absorption components centred around ~ -280 and $-130\,\mathrm{km\,s^{-1}}$.

4.4.2 Constraints on the mass of the secondary

Since no spectral lines from the secondary are detectable, no direct inferences about its mass can be made; however, constraints on its mass can be made using the orbital solution of the primary. The binary mass function for a single-lined binary, f, is given by

$$f = \frac{M_2^3 \sin^3 i}{(M_1 + M_2)^2} = \frac{PK^3}{2\pi G}(1 - e^2)^{3/2} \tag{4.6}$$

where M_1 is the mass of the binary component whose radial velocities have been measured, M_2 is the mass of the unseen companion, i is the inclination of the orbit, P is the orbital period, K is the amplitude of the binary orbit, e the eccentricity of the orbit, and G the gravitational constant. f gives the lower limit of M_2 as

$$M_2 > \max(f, f^{1/3} M_1^{2/3}). \tag{4.7}$$

Using the new orbital parameters in Table 4.3 gives a mass function of $f = 0.24 \pm 0.03\, M_\odot$. Using the primary mass, $M_1 = M_{\rm pr} = 24 \pm 4 M_\odot$, it can inferred that $M_2 > 5.2 \pm 0.6\, M_\odot$.

However, there is also the indication from Borges Fernandes (2010) and Kraus et al. (2013) that the circumbinary disk in GG Car has an inclination of $\sim 60°$. Assuming that the orbit of the binary and circumbinary disk are roughly co-planar, then the circumbinary disk inclination may be used as an estimate for the inclination of the binary orbit. Therefore, a value of $i = 60 \pm 20°$ is adopted, allowing a large uncertainty to acknowledge both the uncertainty from these studies and any precession of the circumbinary disk in relation to the binary orbit (Doolin & Blundell 2011). With an estimate for the binary inclination Equation 4.6 can be solved for M_2. This gives $M_2 = 7.2^{+3.0}_{-1.3}\, M_\odot$, using Monte Carlo means to calculate the uncertainties. For this secondary mass the semi-major axis of the orbit is $a = 0.61 \pm 0.03\,$AU. This makes the mass ratio $q = M_1/M_2 = 3.3^{+0.6}_{-1.0}$.

Here I question whether the secondary of GG Car could significantly contribute to the V-band brightness of the system, and therefore affect the determination of the luminosity of the primary in Section 3.3.1. If the binary components have evolved as pseudo-single stars, it can be inferred that the secondary is still on the main sequence since the primary is expected to have only recently evolved off the main sequence (Kraus 2009; Kraus et al. 2013). With its mass, the luminosity of the secondary would be $\sim 700 - 4800\, L_\odot$, which is between 0.4–2.7% of the luminosity of the primary. In the case that there has been binary interaction in GG Car's past, Farrell et al. (2019) finds that the secondary components of blue supergiants in binaries should have negligible contributions on the V-band photometry, except in cases where the mass ratio is near unity. In a scenario of full mass inversion, where the current secondary is a stripped object, the stripped companion would be expected to be less luminous than the primary and would also emit most strongly in the UV (Wellstein et al. 2001). Even in extreme cases of very bright stripped companions, they are expected to be outshone at visible wavelengths by their primaries (Götberg et al. 2018). It can therefore be concluded that, in all evolutionary cases, the secondary's contribution to the V-band brightness of GG Car is negligible and the luminosity determination of the primary in Section 3.3.1 remains valid.

4.4.3 Photometric variations along the binary orbit

The photometric variation of GG Car along the orbit of the binary is continuous with one minimum and one maximum. The average peak-to-trough magnitude change over the binary orbit is around 0.2 mag in the V-band, corresponding to a brightness contrast of around 20%. In the literature, GG Car has occasionally been referred to as an eclipsing binary; however, there are no signs of eclipses in the lightcurve which survive the scatter in the data and, furthermore, eclipses are not expected to occur for the measured semi-major axis of the orbit, primary radius, and the reported orbital inclination.

Figure 4.21 shows how the photometric variations correspond to the orbital solution determined in Section 4.3, with pertinent stages of the binary orbit noted. The phase at which the system is brightest corresponds near exactly with periastron, peak brightness occurring just slightly before, and correspondingly the system is dimmest at apastron. There is no perceptible dimming at either superior or inferior conjunction, further showing that the binary is not eclipsing. Figure 4.21 also marks phases where the primary is closest and furthest from the observer in its orbit.

In the following sections I explore some causes of continuous photometric variations at the orbital period. In Section 4.4.3.1 I rule out reflection between the binary components and in Section 4.4.3.2 I rule out extinction or reflection by circumbinary material as causes of the brightness changes observed in GG Car. In Section 4.4.3.3, I show that enhanced mass transfer between the binary components and accretion

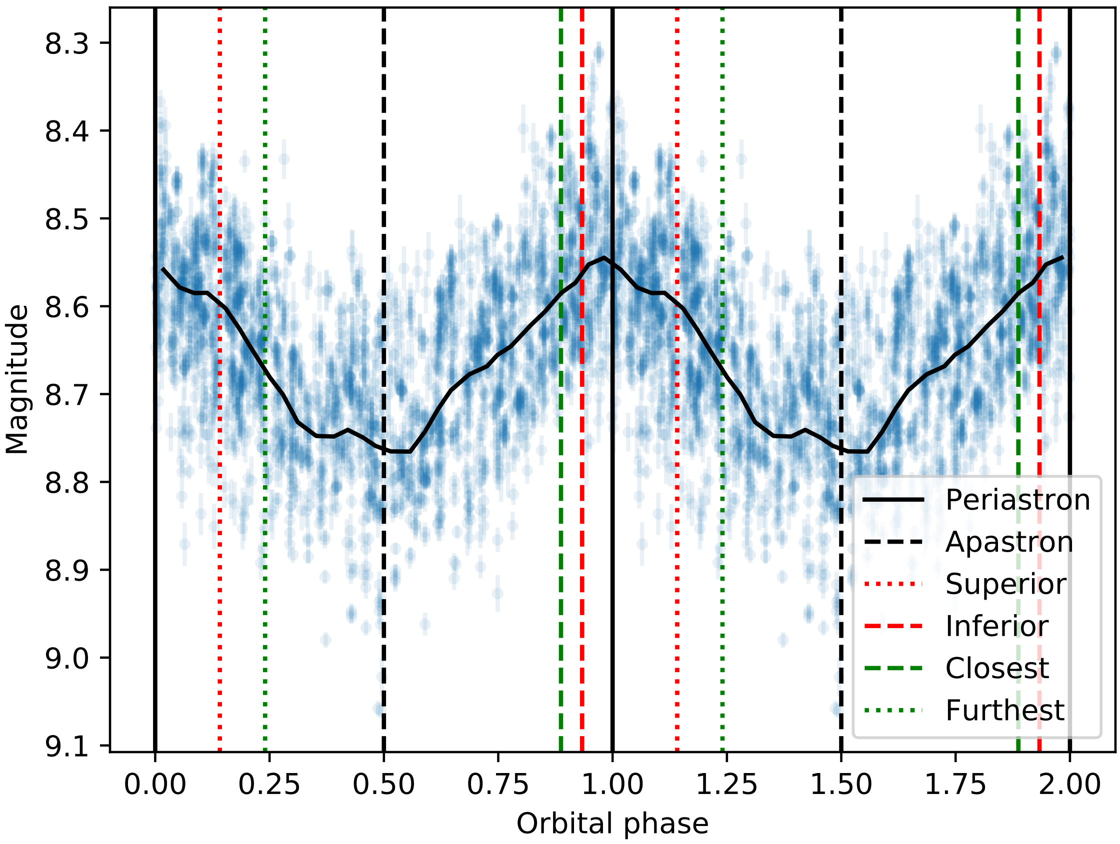

Figure 4.21: The same as Figure 4.2, except important phases in the Black vertical line indicates phases of periastron and apastron, vertical red lines phases of superior and inferior conjunction of the B[e]SG primary, and green lines indicate when the B[e]SG primary is closest or furthest from the observer in its orbit. The Keplerian radial velocity of the B[e]SG primary is overplotted as a gray line, on the right hand axes.

at periastron is very likely to occur given the orbital parameters, and that these can reproduce the photometric variability observed assuming a simple model.

4.4.3.1 Reflection

A possible explanation of the peculiar lightcurve of GG Car is reprocessing and reemission of the radiation incident on each stellar component (Wilson 1990). If the variations were dominated by the reflection of one component's radiation by its companion, the system's lightcurve would have one maximum and one minimum per orbital period as the hemisphere of the companion which is illuminated orbits in and out of the line of sight. As is shown in Figure 4.21, the photometric maximum occurs near inferior conjunction, when the primary and the secondary line-up along the line-of-sight, with the primary being closer to the observer than the secondary.

Entertaining a scenario where the primary heats the secondary, or a disk around the secondary, and the luminosity intercepted is re-radiated it can be presumed that, in the best case scenario, the fractional change in luminosity would be given by

$$\frac{\Delta L}{L} \approx \frac{\Delta L}{L_{\mathrm{pr}}} = \frac{\pi R_{\mathrm{sec}}^2}{4\pi((1-e)a)^2}, \tag{4.8}$$

where R_{sec} is the radius of the secondary, e is the eccentricity of the orbit, a is the semi-major axis of the orbit, L is the total luminosity of the primary and the secondary, and L_{pr} is the luminosity of the primary. In this best case scenario, the intrinsic luminosity of the secondary is approximated $L_{\mathrm{sec}} \approx 0$. Since the brightness contrast is $\sim$20%, in order for reflection to account for the photometric variation, with $e = 0.5$ and $a = 0.61\,\mathrm{AU}$, R_{sec} would have to be $0.27\,\mathrm{AU}$. Using the approximation Eggleton (1983), the radius of the secondary's Roche lobe at periastron can be calculated within 1% accuracy by

$$r_{\mathrm{sec}} = \frac{0.49q^{2/3}}{0.6q^{2/3} + \ln\left(1 + q^{1/3}\right)}\left(1 - e\right)a, \tag{4.9}$$

where q is the mass ratio $M_{\mathrm{sec}}/M_{\mathrm{pr}}$. Given a mass ratio of 7.2/24, the size of the secondary's Roche lobe at periastron is $0.09\,\mathrm{AU}$; therefore, the secondary cannot both be dynamically stable and have a large enough size to reflect enough of the primary's light in order to account for the observed variability. If the secondary filled its Roche lobe, it would lead to a maximum luminosity contrast of $\sim$2.0%; therefore, reflection of the primary's light off the secondary would only provide an insignificant amount of the observed flux change. This is also a best case scenario, which assumes that at maximum light the full illuminated hemisphere of the secondary is facing the observer and at minimum light the illuminated hemisphere is facing away from the observer; given that the system is at $\sim 60°$ inclination and its argument of periastron is almost in the plane of the sky, neither statement is true, and this would diminish the luminosity contrast due to reflection further.

Should the secondary's luminosity be non-negligible and heat the primary, we can estimate the luminosity of the secondary required to heat the primary in order to facilitate the observed contrast, $\Delta L/L = 0.2$, where $L = L_{\mathrm{pr}} + L_{\mathrm{sec}}$. The luminosity of the secondary L_{sec} can be expressed as

$$L_{\mathrm{sec}} = (0.2 L_{\mathrm{pr}}) \;/\; \left(\frac{\pi R_{\mathrm{pr}}^2}{4\pi((1-e)a)^2} - 0.2 \right). \tag{4.10}$$

Entering the orbital parameters and $R_{\mathrm{pr}} = 27\,R_{\odot}$, L_{sec} would have to be negative in order to account for the change. This is clearly unphysical. Additionally, the brightness of the system is falling around superior conjunction, which is incompatible with the brightness changes being caused by reflection of the secondary's flux by the primary.

Therefore, given the stellar and binary orbital parameters of GG Car, it can concluded that reflection is not a significant source of the photometric variability over the orbital period.

4.4.3.2 Extinction, scattering, and reflection by circumbinary material

Circumbinary orbiting material has been invoked to explain photometric variability of binaries at their orbital periods, attributing this to variable extinction, scattering and reflection of starlight by the circumbinary material (e.g. Waelkens et al. 1991, 1996; Khokhlov et al. 2018; Ertel et al. 2019). Given its thick, probably near opaque, circumbinary envelope, could similar processes be causing the photometric variability in GG Car?

Should scattering or reflection of the primary's light by the circumbinary disk be occuring, the brightest times of the system would be when the primary is closest to the far side of the circumbinary disk, which is when the primary is furthest from the observer. Figure 4.21 notes at which point along the light curve that the primary is furthest from the observer, which is when the system is at roughly its mean brightness, indicating that variable scattering and reflection of the primary's light by the far edge of the circumbinary is most likely not the source of the photometric variations at the orbital period. Conversely, if there were considerable variation in the extinction of the primary's flux by the circumstellar envelope over the binary period (as was proposed in GG Car by Gosset et al. (1985)), then the system should be brightest when the primary is closest to the observer. Again, this is not observed, therefore I rule out these possibilities.

4.4.3.3 Enhanced mass transfer and accretion at periastron

Given that the brightness of GG Car is maximal remarkably near to periastron, might the brightness variations be due to enhanced mass loss and mass transfer between the binary components at periastron? This behaviour is widely seen in "Type I" outbursts in Be/neutron star X-ray binaries (see Reig 2011 for a review). At periastron, the neutron star travels through the decretion disk of the Be star, leading to an increase in luminosity.

Figure 4.22 demonstrates the relative sizes of the primary and its Roche lobe against mass ratio at periastron and apastron. With a binary mass ratio of $q = 3.3^{+0.6}_{-1.0}$, separation of $0.61 \pm 0.03\,\mathrm{AU}$, eccentricity 0.50 ± 0.03 and $R = 27\,R_{\odot}$, the primary radius extends to $85 \pm 28\,\%$ of its Roche lobe's radius at periastron. Conversely, at apastron the primary radius extends to $28 \pm 9\,\%$ of the Roche radius. This indicates that the wind of the primary would have to travel significantly further at apastron than periastron before it encounters the secondary. Moreno et al. (2011), calculating the rate of energy dissipation of tidal flows in the surfaces of stars in binaries, calculates that stellar mass-loss may be enhanced around periastron in eccentric orbits due to the increased rate of energy dissipation at periastron. They additionally show that this mass-loss would be expected to be focused in the equator of the star in the orbital plane, such as is expected in B[e]SGs. The trailed spectra of the He I lines shown in Figure 4.3 show that the blueshifted absorption component becomes deeper around phase 0; this likely indicates that more mass is being lost around periastron in the primary's wind. This all indicates that the rate of mass-loss of the primary and the rate of mass being captured by the secondary will be strongly dependent on the phase of the binary given the orbit's eccentricity, and therefore it can be expected that there will be changes in the brightness due to varying rates of mass transfer

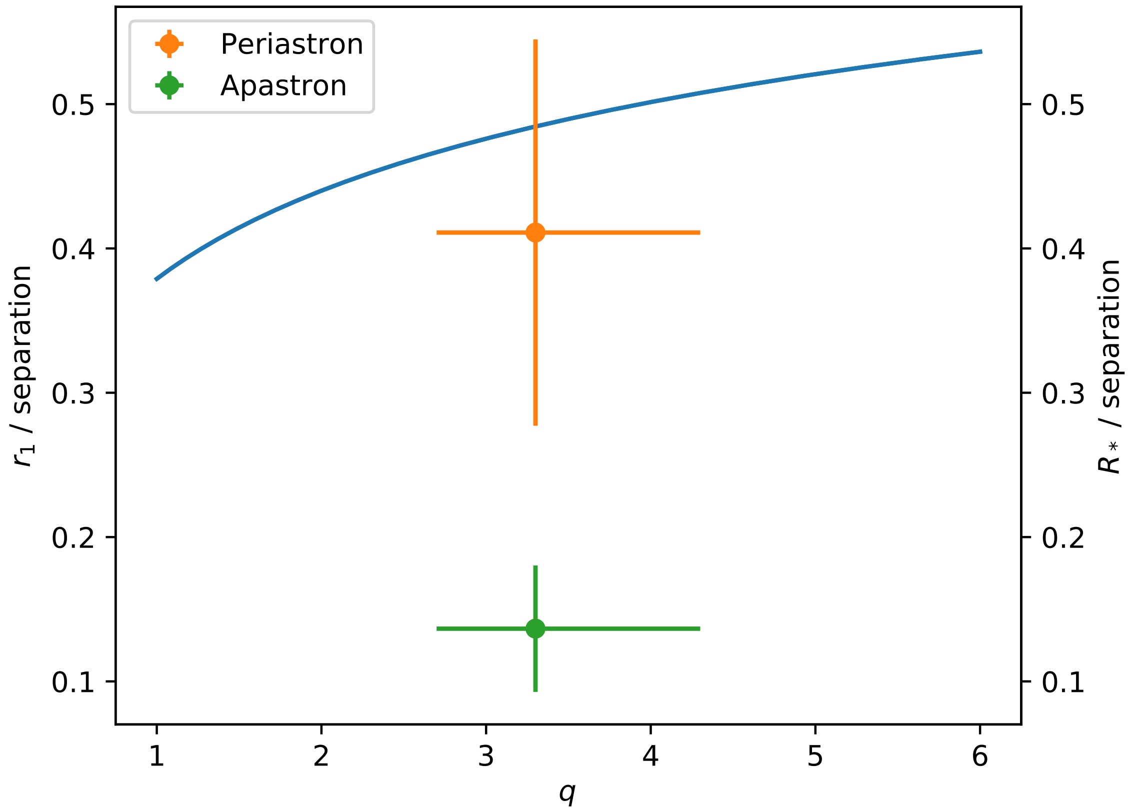

Figure 4.22: Size of the primary's Roche lobe as a function of binary mass ratio, q, in units of the binary separation (blue line), and the radius of the primary, R_*, in units of the binary separation at periastron (orange point) and apastron (green point).

and accretion in GG Car. Any rotation of the primary would additionally shrink its effective Roche lobe, aiding mass loss at the stellar equator.

To investigate whether accretion of the primary's equatorial wind by the secondary may cause the observed V-band flux changes over the orbital period, I construct a two dimensional model of the binary with the primary's equatorial wind modelled as a series of equal-mass rings emitted every time-step from its equator with wind speed $v_{\rm wind}$, whose bulk velocity travels at the velocity of the binary at emission. $v_{\rm wind}$ is assumed to be constant for this simple calculation, that the mass loss rate is also constant, and that the wind is confined to near the equator and is concentrated in the orbital plane. A ring is counted as being accreted when it crosses into the Roche lobe of the secondary. When a ring is accreted in the simulation, the amount of mass accreted from it is set to

$$\Delta M_{\rm ring} = \frac{K}{r_{\rm ring}\, v_{\rm diff}}, \tag{4.11}$$

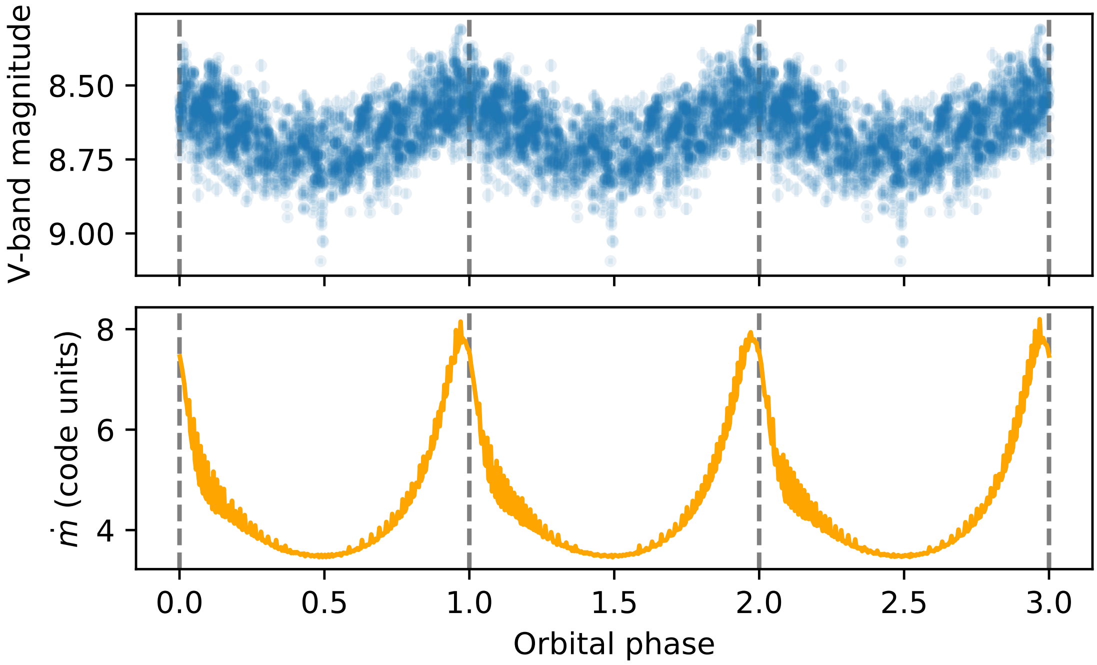

Figure 4.23: Top panel: The V-band photometry of GG Car by orbital phase. Bottom panel: The simulated mass accretion rate of the secondary $\dot{m}$, in arbitrary code units. Grey dashed lines indicate phases of periastron. The simulated luminosity change is calculated using Equation 4.12. The very short term variability in the simulated $\dot{m}$ is numerical noise from the calculation. The simulated shape of the mass accretion rate is strongly correlated with the changes in the V-band photometry over the binary orbit.

where r_{ring} is the radius of the ring, v_{diff} is the differential speed between the secondary and the part of the ring being accreted, and K is an unimportant constant. Once a part of a ring has been accreted, the rest of the material in the ring is assumed to carry on expanding unimpeded away from the binary and is ignored. In the model, the mass accretion rate in a timestep is calculated

$$\dot{m} = \sum_{i=0}^{N_{\text{acc}}} \Delta M_{\text{ring},\,i}, \tag{4.12}$$

where i runs from 0 to N_{acc}, the number of rings accreted in the timestep. Appendix A.4 describes this simple two-dimensional model, and the reasoning behind the weighting of Equation 4.11, in more detail.

Using the GG Car orbital parameters of $e = 0.50$, $a = 0.61\,\text{AU}$, $M_{\text{pr}} = 24\,M_{\odot}$, $M_{\text{sec}} = 7.2\,M_{\odot}$, $R_{*} = 27\,R_{\odot}$, $v_{\text{wind}} = 265\,\text{km}\,\text{s}^{-1}$, the expected changes in accretion rate of GG Car over four orbital periods are calculated. The results of this calculation compared with GG Car's V-band photometry are shown in Figure 4.23. The simulation takes around one orbital period to reach a steady state, the data from the first orbit are excised from Figure 4.23 to avoid misleading edge effects. The simulation results in Figure 4.23 have not been folded by orbital phase, but the simulation has reached a steady state for each orbit.

The shape of the simulated mass accretion rate in this two-dimensional model and the observed V-band photometry are remarkably correlated over the orbital period; the peaks of the expected accretion rate match the peak V-band photometry closely, with the peak brightness occurring just before periastron and minimum brightness at apastron. Appendix A.4 investigates how changing the eccentricity and the wind speed affects the calculation results and finds that the resulting accretion rate variability is similar for higher wind speeds, but that the eccentricity should be between $\sim 0.2-0.7$ to match the observed V-band variability. This, and the peak brightness occurring at periastron, lends supporting evidence for the orbital solution and the time of periastron passage found in Section 4.3.2, which found $e = 0.50 \pm 0.03$. A wind accretion model may also explain the stochastic variances of the lightcurve's profile over successive orbital cycles: since the luminosity changes will be heavily dependent on the conditions of the equatorial wind, any fluctuations or changes in the wind will affect how the brightness changes over an orbital period.

I therefore propose that two-dimensional accretion is powering the V-band photometric variability of GG Car over its orbital period, with the secondary accreting the equatorial wind of the primary. The increase in V-band luminosity in this scenario will be due to heating from the wind falling into the gravitational well of the secondary; however, whether this heating is of the secondary's surface or of an accretion disk around the secondary cannot be yet determined. Furthermore, any accretion luminosity which occurs in the secondary is likely to be reprocessed by the thick circumstellar envelope of the system. Concurrent photometric surveys in the UBV bands, along with high time- and spectral-resolution spectroscopy focused around periastron to search for accretion signatures, would help to determine the correctness of this scenario.

This calculation aims to provide a first-order, proof-of-concept calculation of the variable accretion rate of the primary's equatorial wind by the secondary through the eccentric orbit of the binary components. I make no attempt to fully quantify the absolute value of the accretion rates, nor the full calculation of the expected changes in magnitude in the V-band, which are beyond the scope of the present study. The assumption is made that the rate of mass accretion by the secondary is proportional to the accretion luminosity in the V-band. In addition, I do not attempt to model time-varying mass-loss rates of the primary, which would be expected in the varying gravitational influence of the secondary during the eccentric orbit; however, this effect would be expected to increase the mass-loss rate, and therefore also increase the accretion rate of the secondary, at periastron (Lajoie & Sills 2011a,b; Moreno et al. 2011; Davis et al. 2013).

A scenario of mass-loss and mass-transfer focused at periastron could account for the large eccentricity of GG Car. Eccentric orbits are expected to rapidly circularise due to tidal interaction (Zahn 1977); however, both Soker (2000) and Bonačić Marinović et al. (2008) showed that high eccentricities can be sustained by enhanced mass-loss focused around periastron passages in tidally interacting systems where the mass-losing star is an evolved giant. Similarly, Sepinsky et al. (2007, 2009, 2010) have also shown that mass transfer focused around periastron can reverse the circularisation of binary orbits and pump up the eccentricity. Interaction of the binary with the system's circumbinary disk may also aid in sustaining the eccentricity of the binary orbit (e.g. Dermine et al. 2013; Antoniadis 2014).

4.4.4 Binary evolutionary scenario for GG Carinae

Kraus et al. (2013) pointed to GG Car's circumbinary $^{12}C/^{13}C$ ratio, orbital eccentricity, the observation of Thackeray (1950) of a lack of nebulosity, and the primary's theoretical age assuming a single star's evolutionary history as evidence that the primary evolved as a single star, and was a classical Be star previously in its main-sequence lifetime.

However, recent studies have suggested that Be stars are overwhelmingly formed via binary interactions (e.g. Shao & Li 2014; Klement et al. 2019; El-Badry & Quataert 2021). Furthermore, Bodensteiner et al. (2020) recently found a dearth of main sequence companions to classical Be stars, suggesting that mass transfer from the current secondaries and the associated spin-up of the current primaries dominates the Be star formation channel. Such interaction inverts the mass ratio of the binary, with the Be star being the initially less massive component. Therefore, assuming a

Be progenitor of the primary of GG Car, these studies imply that mass is likely to have needed to have been transferred from the current secondary to the primary in the system's evolutionary history.

In this scenario, the ^{13}C could have been formed in the now-secondary component during its evolution, allowing its surface to be enriched by the isotope; this then allows for the ^{13}C to enrich the circumbinary disk, as non-conservative Roche lobe overflow provides a mechanism for the ^{13}C enriched material to transcend from the secondary's surface to the circumbinary disk. Such non-conservative Roche lobe overflow is widely theorised to give rise to the circumbinary disks of B[e]SGs (e.g. Langer & Heger 1997). Farrell et al. (2019) notes that the high mass transfer rates during this interaction can both lead to dense circumstellar media that obscure the central stars, such as is observed in B[e]SGs, and allow the spin up of the mass gainer. The spin up caused by this mass transfer may then allow decretion about the equator of the primary, thereby allowing the system to display the B[e] phenomenon described by Zickgraf et al. (1985).

Such a binary evolutionary scenario leaves the originally more massive binary component less massive than its companion (e.g. Wellstein et al. 2001). This evolutionary sequence has been well established in the study of high-mass X-ray binaries (HMXRBs; van den Heuvel 1976, 2018) where it is expected the original primary would be a stripped He star before undergoing supernova to become a compact object. In this scenario, the now-primary would have been thrown out of thermal equilibrium by the mass transfer, and would have had a higher luminosity than expected for a single star of its mass; however, it would regain thermal equilibrium on its thermal timescale, $\tau_{\rm therm} = GM^2/(RL) \sim 4000\,$years. It is therefore unlikely that we are observing the system in this short-lived phase.

In the previous section, I suggest that ongoing mass transfer focused at periastron may account for the high eccentricity seen in GG Car. However, HMXRBs have been observed to have high eccentricities (Raguzova & Popov 2005; Walter et al. 2015). Supernova kicks are suggested to account for the significant eccentricities in such systems (Verbunt & van den Heuvel 1995). Such a scenario is not out of the realms of possibility for GG Car, if the current secondary were a supernova remnant. The mass of the secondary in the GG Car system is far larger than the maximum mass of a neutron star (Rezzolla et al. 2018), so if the secondary were a supernova remnant it would need to be a black hole. The lack of X-rays observed in the system argues against this hypothesis, though it is possible that any X-rays produced by accretion would be obscured by GG Car's thick circumstellar environment and wind (Koljonen & Tomsick 2020).

More cannot currently be definitely said about the exact evolutionary history of GG Car, since this would require the species of the secondary component in the system to be determined. This determination is precluded by the thick circumstellar environment, but a search in the UV detecting the presence of a stripped He star would prove that mass transfer and mass inversion had occurred (Götberg et al. 2018). Overall, the evidence presented of ongoing of mass transfer from the primary to the secondary, the recent studies on the potential binary origin of the Be phenomenon, and studies that orbital eccentricity can survive binary interaction, demonstrate that the conclusion that the stars in GG Car evolved as single stars may not be accurate, and that the role of binarity should not be neglected when determining the evolution of systems such as GG Car.

I therefore argue that the evolution of GG Car should be reevaluated in a binary context, in order to further understand the origin of its B[e]SG phenomenon.

4.5 Conclusions

I have presented photometric and spectroscopic data of the B[e]SG binary GG Car and studied its variability through the $\sim$31-day binary orbit of the system.

A distance to GG Car of $d = 3.4^{+0.7}_{-0.5}\,\mathrm{kpc}$ has been inferred using its parallax measured by *Gaia* in DR2. I have determined the luminosity of the primary component, $L_{\mathrm{pr}} = 1.8^{+1.0}_{-0.7} \times 10^5\, L_\odot$, and the radius of the primary, $R_{\mathrm{pr}} = 27^{+9}_{-7}\, R_\odot$, assuming the Marchiano et al. (2012) effective temperature $T_{\mathrm{eff}} = 23\,000 \pm 2000\,\mathrm{K}$. Using the rotating and non-rotating stellar evolution models of Ekström et al. (2012), the mass of the primary is estimated as $M_{\mathrm{pr}} = 24 \pm 4\, M_\odot$.

H-alpha, He I, Si II and Fe II emission lines have been shown to display radial velocity (RV) variability at the orbital period, and it is shown that the amplitudes of the emission lines' RV variations are correlated with the energy of the upper level of the line transition. This implies that the variations are correlated with the temperatures of the line forming regions. This is consistent with these emission lines being formed in the wind of the B[e]SG primary. The wind traces the Keplerian motion of the primary, however lower energy lines form at larger radii in the wind on average, once it has been able to cool, than the higher energy lines, which form closer to the star where it is hotter. Hence there is a delay in emission of the different species according to the energies of the transitions in question. This effect thereby causes a smearing of the observed RV curves, with the lower energy lines smeared more than the higher energy lines.

The atmosphere of the B[e]SG primary component of the binary GG Car was simulated using `CMFGEN` in order to calculate the emissivity of its H-alpha, He I, and Si II lines as a function of wind-flow time. It is found that, in the simulation, these lines are formed in the wind of the primary, and that He I lines form closest into the stellar surface, on average, followed by H-alpha and then Si II lines which also form over a more extended region. This supports the assertion in this study these lines form in the primary's wind, after finding the He I emission has the largest RV variations in GG Car, followed by H-alpha and Si II.

Using the simulated emissivity of these lines as a function of wind-flow time after passing the sonic point, I have been able to accurately measure the Keplerian motion of the primary component of the binary for the first time. The system's orbit is found to be considerably more eccentric ($e = 0.50 \pm 0.03$) than previously thought. A new orbital ephemeris of the binary is defined and given in Equation 4.1. The newly determined orbital solution, convolved with the calculated line-formation kernels, is able to accurately reproduce the observed RV variations of the system's emission lines. Using limits of the circumbinary disk inclination of $60 \pm 20°$ (Borges Fernandes 2010; Kraus et al. 2013) and assuming the disk is roughly coplanar with the binary, the mass of the secondary can be constrained to $7.2^{+3.0}_{-1.3}\,M_\odot$ and the semi-major axis of the orbit to $a = 0.61 \pm 0.03\,\mathrm{AU}$. Therefore the mass ratio of the binary $q = M_1/M_2 = 3.3^{+0.6}_{-1.0}$. Table 4.4 summarises all of the stellar and binary parameters of GG Car which have been determined in this study.

The V-band photometry has been shown to vary smoothly with one maximum and one minimum per orbital period with stochastic variations in amplitude superimposed upon these, such that the profiles of the lightcurve in successive orbits are

Primary stellar parameters	
d	$3.4^{+0.7}_{-0.5}\,\mathrm{kpc}$
T_{eff}	$23\,000 \pm 2000\,\mathrm{K}$
L_{pr}	$1.8^{+1.0}_{-0.7} \times 10^5\,L_\odot$
R_{pr}	$27^{+9}_{-7}\,R_\odot$
M_{pr}	$24 \pm 4\,M_\odot$
Secondary parameters	
M_{sec}	$7.2^{+3.0}_{-1.3}\,M_\odot$
Orbital solution	
K	$48.6^{+2.0}_{-1.9}\,\mathrm{km\,s^{-1}}$
ω	$339.9^{+3.1\,\circ}_{-3.1}$
e	$0.50^{+0.03}_{-0.03}$
v_0	$-0.7^{+0.4}_{-0.4}\,\mathrm{km\,s^{-1}}$
M_0	$202^{+15\,\circ}_{-15}$
P	$31.01^{+0.01}_{-0.01}$ days
T_{peri}	JD 2452069.4 $\pm$ 1.3
a	$0.61 \pm 0.03\,\mathrm{AU}$

Table 4.4: Summary of the stellar and orbital parameters of GG Car determined in this study. *Gaia* distance, d, and stellar parameters of the primary in GG Car, where M_{pr} is the mass of the primary, T_{eff} is the effective temperature of the primary, L_{pr} is the luminosity of the primary, and R_{pr} is the radius of the primary. T_{eff} is taken from Marchiano et al. (2012). M_{sec} is the mass of the secondary. K is the orbit amplitude, ω is the argument of periastron, e is orbital eccentricity, v_0 is the velocity offset without physical significance, M_0 is the phase offset of the reference time $T_0 = \mathrm{JD}\,2452051.93$, P is the orbital period, T_{peri} is the epoch of periastron, and a is the semi-major axis of the binary orbit.

non-identical. With the new orbital solution of the binary, the phases of photometric maxima in GG Car occur just before periastron, and photometric minima occurring at apastron. Having discounted other sources of variability at the orbital period, it is found that the shape of the V-band photometric variations of the system along the binary orbit can be reproduced using a model of enhanced mass transfer between the binary components at periastron and accretion of the primary's equatorial wind by the secondary. I therefore argue that the accretion of the primary's wind by the secondary is the cause of the photometric variations at the orbital period in GG Car. The stochastic nature of the shape of the V-band brightness variations can then be explained by variability in the wind of the B[e]SG primary. Mass-loss and mass-transfer from the primary focused at periastron would help explain the large eccentricity of the binary's orbit, which may otherwise be expected to have been circularised by tidal interaction.

I go on to show that the assumptions used to argue a single star evolutionary scenario for the primary in GG Car are flawed, and suggest that the evolution of the system ought to be reassessed in a binary paradigm.

Chapter 5

Discovery of orbital phase dependent 1.583-day periodicities in GG Carinae

Abstract

This chapter investigates the short-period variations which are exhibited in GG Carinae, using photometric data from TESS, ASAS, OMC, and ASAS-SN, and spectroscopic data from the Global Jet Watch to study visible He I, Fe II and Si II emission lines. I find a hitherto neglected periodicity of 1.583156 ± 0.0002 days that is present in both its photometry and the radial velocities of its emission lines, alongside the system's variability at its orbital period. I find that the amplitudes of the shorter-period variations in both photometry and some of the emission lines are modulated by the orbital phase of the binary, such that the short-period variations have largest amplitudes when the binary is at periastron. This is surprising since the orbital period and the short period are non-commensurate. There are no significant changes in the phases of the short-period variations over the orbital period. Potential causes of the 1.583-day variability are investigated, and it is found that the observed period agrees well with the expected period of the $l = 2$ f-mode of the primary given its mass and radius. It is proposed that the primary is periodically pulled out of hydrostatic equilibrium by the quadrupolar tidal forces when the components are near periastron in the binary's eccentric orbit and the primary almost fills its Roche lobe. This causes an oscillation at the $l = 2$ f-mode frequency which is damped as the distance between the components increases. The detection of such pulsations will have a significant effect on the understanding of the B[e] supergiant phenomenon.

5.1 Introduction

Upon inspection of the time-series data of GG Carinae (GG Car), it became clear that the system was not only variable at its 31-day orbital period. The TESS data, which I accessed and presented in Figure 3.2, clearly shows significant variability at much shorter timescales alongside the systems variability at its orbital period. I also found that the same variability was present in both the Global Jet Watch (GJW) spectroscopy and the V-band photometry of the system.

Although B[e]SGs have usually not been considered to be significantly photometrically variable (Lamers et al. 1998), with the advent of high-precision space photometry such as TESS and Kepler, the related blue supergiant stars (BSGs) have been found to display variability due to pulsations (Aerts et al. 2017; Bowman et al. 2019). Pulsations have been proposed as a potential mechanism for the ejection of material from the stellar surfaces leading to the B[e]SG phenomenon (Kraus et al. 2015a; Kraus 2017; Torres et al. 2018). Therefore the discovery and study of stellar variability in the B[e]SGs, which may be indicative of stellar pulsations, may reveal whether pulsations directly lead to these systems exhibiting the B[e] phenomenon.

There have been some earlier indications of significant variability in GG Car. Early time-series photometry studies noticed that GG Car displays significant intra-night variability, separate from its variability over its $\sim$31 day orbital period (Kruytbosch 1930; Greenstein 1938). Gosset et al. (1984), through Fourier analysis, found an indication of a periodicity at $\sim$1.6 days in the system's photometry. This led them to state that one of the GG Car components is a variable. Krtičková & Krtička (2018) were unable to determine a clear UV lightcurve of GG Car over its orbital period, presumably due to variability in the system; they conclude that the binary component that is brightest in the UV is the variable, but do not find a period. However, despite these indications, there have been no detailed studies of this variability and its cause has remained mysterious.

In this chapter, I investigate this short-period variability of GG Car in detail, in both time-series photometry and GJW spectroscopy. The structure of this chapter is as follows: Section 5.2 identifies and quantifies the period of the short-term variability of the system's photometry and emission lines' radial velocities; Section 5.2.3 investigates the unusual relationship between the amplitude of the short-period variability in the system and the orbital phase of the binary; Section 5.3 presents this chapter's discussion; and Section 5.4 presents this chapter's conclusions.

5.2 The short-period variability of GG Carinae

5.2.1 Photometric variability

Figure 3.2 displays the TESS lightcurve of GG Car. The TESS data cover nearly two orbital cycles of the binary of GG Car with high precision and cadence. Both the longer-term variation at the orbital period and the shorter period variations along the lightcurve are apparent. It is also clear that the amplitude of the short period variation changes over the epoch of observation, with the amplitudes being correlated with the brightness of the system.

Figure 5.1, top panel, displays the Fourier power spectrum of the ASAS, ASAS-SN, and OMC V-band photometry of GG Car calculated using the CLEAN algorithm of Roberts et al. (1987). Figure 5.1, middle panel, shows the power spectrum of the V-band data calculated using the Lomb-Scargle algorithm (Lomb 1976; Scargle 1982). The bottom panel of Figure 5.1 shows the power spectrum of the TESS photometry calculated using the CLEAN algorithm. All subsequent power spectra in this study are calculated using the CLEAN algorithm. The CLEAN algorithm deconvolves the Fourier transform of the data from the Fourier transform of the observational aperture function, thereby overcoming the artefacts that inevitably arise from transforming irregularly sampled data. Appendix B.1 describes the CLEAN algorithm in detail.

The photometric periodograms are dominated by the $\sim$31-day orbital period of the binary, however there are other periods present in the power spectrum. Most notable is the significant peak at a higher frequency of $\sim$0.632 days^{-1}, corresponding to a $\sim$1.583-day period, which arises in all three power spectra. This is the same higher-frequency period noted in Gosset et al. (1984). The V-band data were all taken from ground-based surveys, with the exception of OMC, so there is a peak complex in their power spectra around $1\,\mathrm{days}^{-1}$ due to aliasing effects arising from the Earth's rotation period. There is no such complex in the TESS periodogram, since it is a space-based mission.

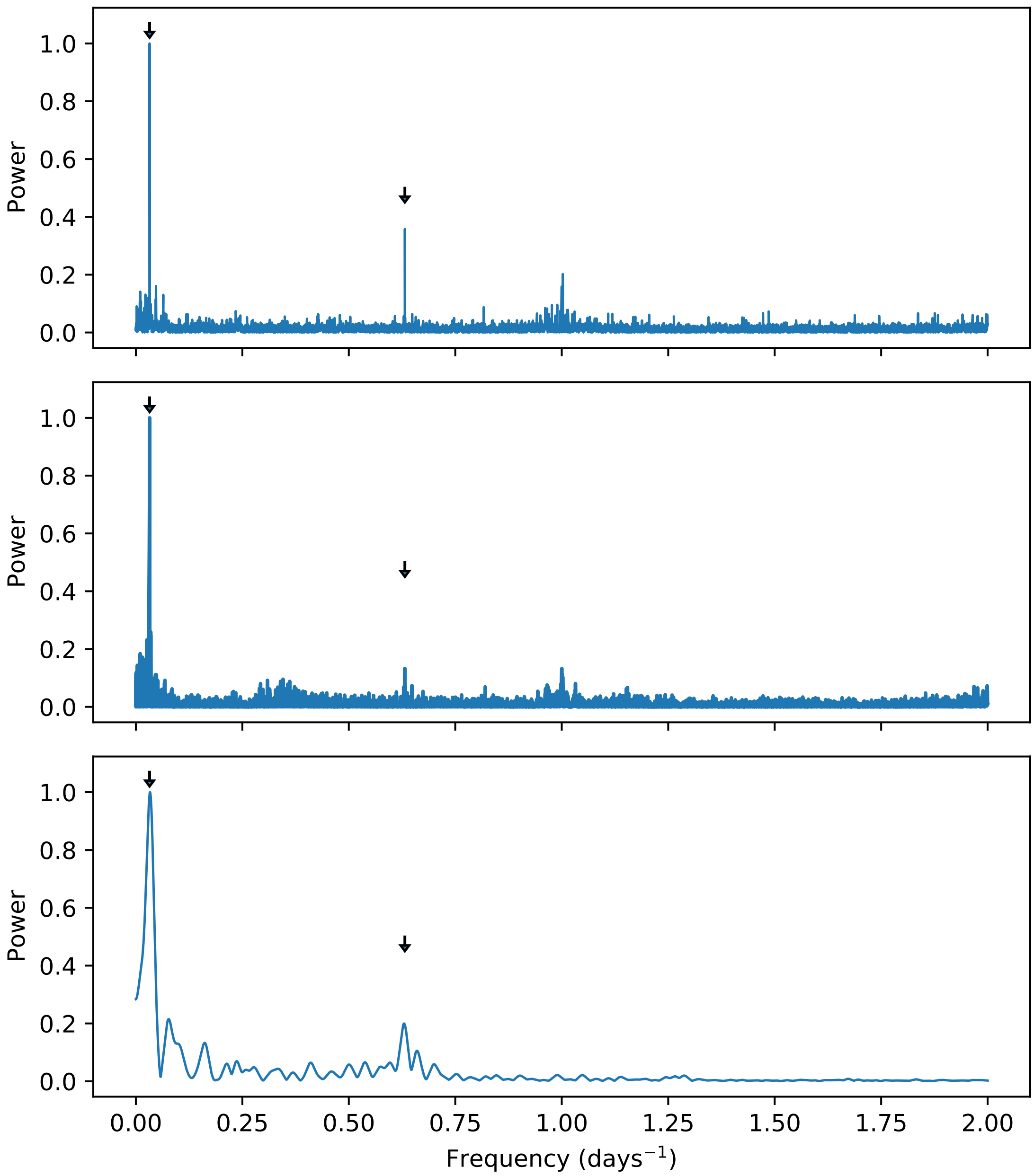

Figure 5.1: Power spectrum of the V-band photometry of GG Car calculated using the CLEAN algorithm (top panel), the power spectrum of the same V-band photometry data calculated using the Lomb-Scargle algorithm (middle panel), and the power spectrum of the TESS photometric data calculated using the CLEAN algorithm (bottom panel). The frequencies corresponding to the orbital period and the short period are denoted by small arrows and presented in Table 5.1. The periodograms are normalised by the peak power.

Data source	Periodicities
V-band photometry (CLEAN)	31.028 ± 0.07 days 1.583156 ± 0.0002 days
TESS photometry	30.2 ± 6.3 days 1.588 ± 0.025 days

Table 5.1: The periodicities found in the power spectra of the photometric data of GG Car, calculated using the CLEAN algorithm.

The frequency and the uncertainty of the peaks in the power spectra are calculated by fitting Gaussians to them, and thereby utilising the centroids and the standard deviations of the peaks as the frequencies and their uncertainties, respectively. However, it may be noted that utilising the widths of periodogram peaks may underestimate the error in the periodicity determinations (VanderPlas 2018). Table 5.1 presents the periodicities found from the photometric data. The $\sim$31-day orbital period derived from the photometry is consistent with the spectroscopic period presented in Chapter 4 within their respective uncertainties. Therefore for the rest of this chapter orbital phases are calculated using the spectroscopic period and ephemeris of Chapter 4, which is more precise at 31.01 ± 0.01 days, to match the orbital phase of the binary. The values of the short period used in this study is the 1.583156 ± 0.0002 day value from the V-band photometry, as it is more precise than the TESS determination, and this period is used for both photometry and spectroscopy. The phases of the short period are calculated by

$$\text{phase} = \frac{T - T_{\text{peri}}}{1.583156}, \tag{5.1}$$

where T is the JD of observation. The phases are calculated relative to T_{peri}, though the choice of this reference time is arbitrary for the short period and without physical significance.

Figure 5.2 displays the V-band and TESS photometry data folded according to Equation 5.1, once the variations at the orbital period are subtracted. Black points average values by phase bin. The short period is very clear to see in both the V-band and the TESS data and the averages show that the variations agree in phase indicating an accurate and persistent period, as the two datasets cover nearly 19 years of observation. There is, however, considerable scatter in the folded data. A cause of this scatter is, as discussed in Chapter 4, because the photometric variations for each

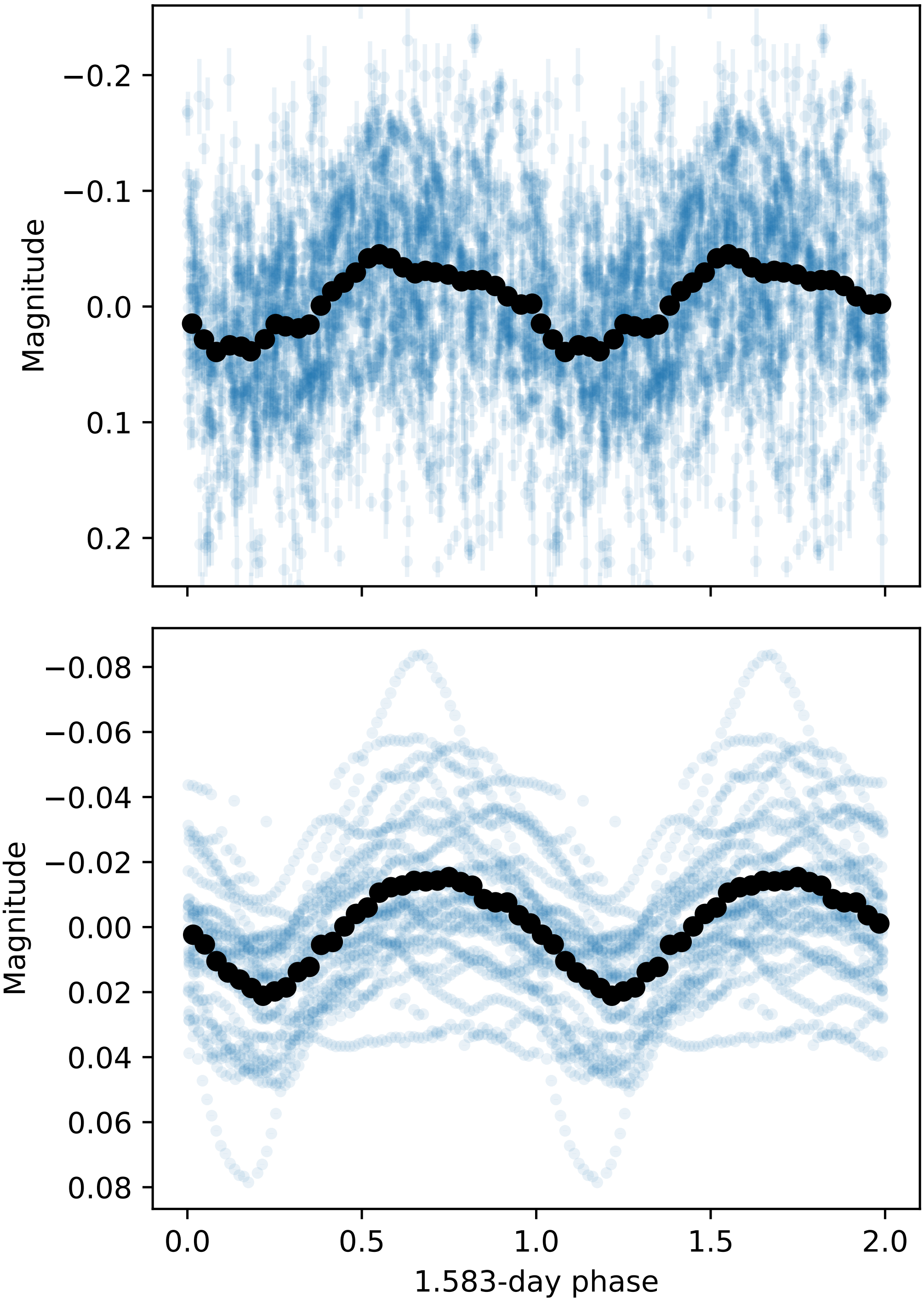

Figure 5.2: Top panel: V-band photometry of GG Car, folded by the short 1.583-day period using Equation 5.1. The data have had variations at the 31-day orbital period subtracted before folding. Black points indicate the average value in 30 bins by phase. Bottom panel: same as the top panel, except for the TESS photometric data, and the black points denote the average in 35 bins by phase.

31-day orbital cycle are not identical, but they vary in shape and depth. This can also be seen in the TESS photometric data in Figure 3.2; the middle minimum is deeper than the minima at the start and end of the observational period. Another cause of the scatter is the variable amplitude of the 1.583-day variations, which is very clear in the TESS data. This amplitude modulation is further discussed in Section 5.2.3.

5.2.2 Spectroscopic variability

We now turn to spectroscopic variability, as observed by the Global Jet Watch. The variability in this section focuses on the radial velocities (RVs) of emission lines in the visible spectrum of GG Car. The same spectra and Gaussian fitting methods are used to extract the RVs of the emission lines as Chapter 4. Chapter 4 has shown that Gaussian fitting is a robust method to extract emission lines centers, amongst other studies (e.g. Blundell et al. 2007; Grant et al. 2020). The 1.583-day periodicity is detected in the RVs of the He I emission lines, and in some Si II and Fe II emission lines.

Figure 5.3 displays the Fourier power spectra for the RVs of the emission of the three visible He I emission lines. The bottom panel displays the geometric mean of the three power spectra to detect common periodicities across the line species. Taking the geometric mean leads to spurious peaks in the individual periodograms being suppressed, and common periodicities which exist across all line species to be promoted. This allows us to observe whether real periodicities exist in noisy periodograms. As with the photometric power spectra in Figure 5.1, the He I variability is dominated by the orbital period, and each of the lines also has a peak at the short-period 1.583-day frequency. There are no common significant peaks at other periods, as shown in the geometric mean of the power spectra.

Periodograms were similarly calculated for the RVs extracted from Fe II and Si II lines. The majority of these lines are also dominated by variations at the orbital period, and a minority show indications of the 1.583-day variations. The metal lines which show an indication of RV variability at the short period frequency are the Fe II 6317.4, 6456.4, 7712.4 and Si II 6347.1, 6371.4 lines, and their periodograms are displayed in Figure 5.4. Even though some of the individual periodograms in Figure 5.4 do not have a significant peak at the short-period compared to the noise of the periodogram, a significant peak survives at this frequency in the geometric mean of the power spectra. Lines studied in Chapter 4 which show no indication of variability at

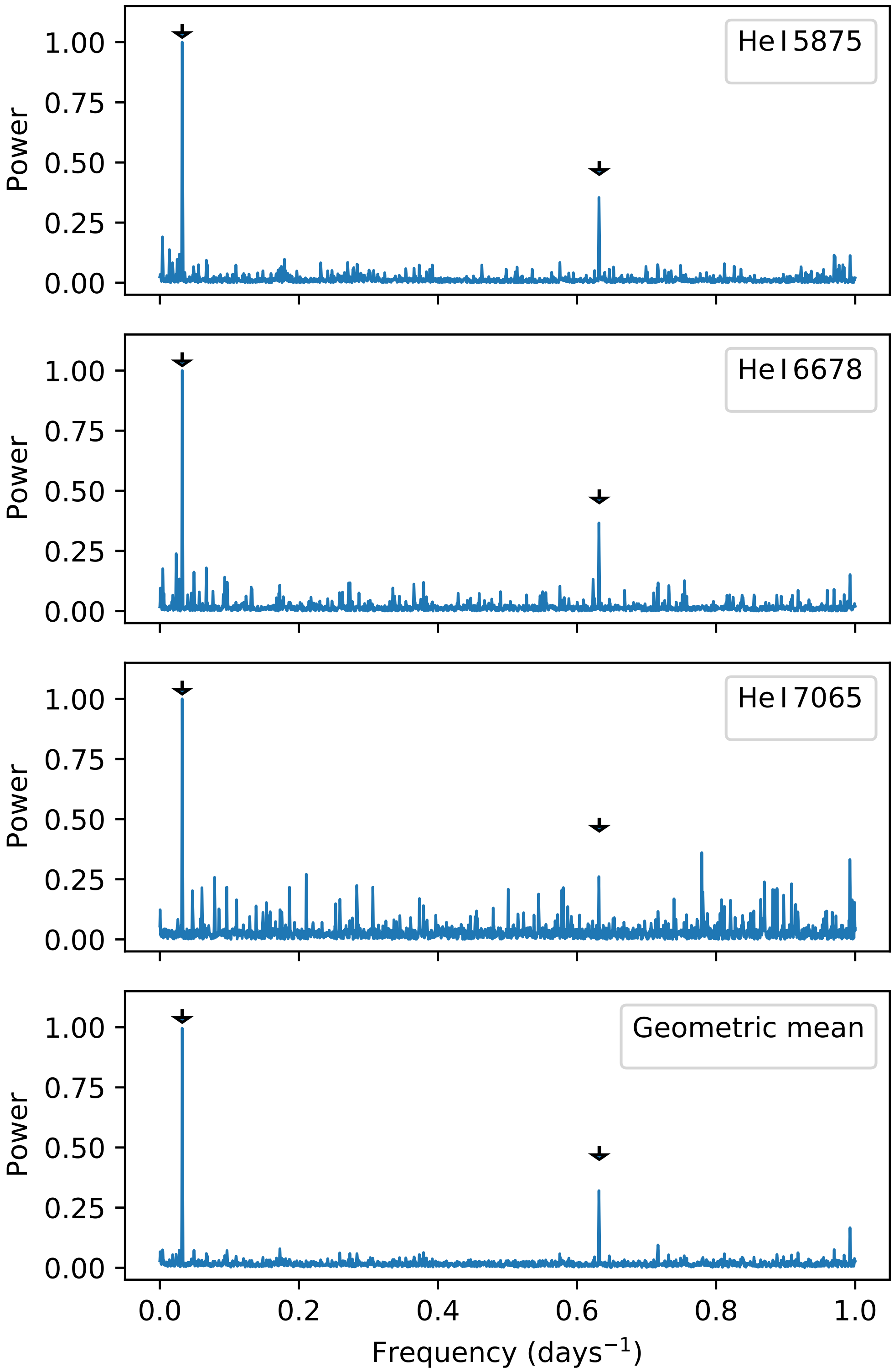

Figure 5.3: Periodograms of the radial velocities of the emission components of the He I lines. The bottom panel displays the geometric mean of the three periodograms. Arrows indicate the frequencies of the orbital period and the new 1.583-day short period. The periodograms are normalised by the peak power, which for these lines are all at the orbital period.

1.583 days in their power spectra are H-alpha, Fe II 5991.3711, 6383.7302, 6432.676, 6491.663, 7513.1762, and Si II 5957.56, 5978.93. Their periodograms are not included in this study as they do not enlighten, and these lines without the short-period variability are not investigated further in this study.

Figure 5.5 displays the RV variations of the emission lines which display variability at the 1.583-day period. The data are binned into 30 bins by phase, and the weighted mean and standard error on the weighted mean in each bin are given by the black error bars. The RV variations have different amplitudes and profiles for each line species, similar to what was found in Chapter 4 with the RV variations at the orbital period. It is unclear why certain lines display the short-period variations whilst others do not, even lines which arise from the same ionisation species. For the He I lines, which display the short-period variations, comparing their RV curves to the photometric variations the phase of the maximal blueshift of the 1.583-day variations roughly corresponds with the phase of minimal brightness at this period.

Similar to the findings in Chapter 4 at the orbital period, the amplitude of the short-period RV variations varies according to line species, with He I having the largest variations and Fe II the smallest. Figure 5.6 plots the amplitude, K, of the RV data against the energy of the upper atomic state of the transition, E_k. A clear correlation of K and E_k is evident, even with the small number of lines available. The method of determining K for the RV variations in described in Appendix B.2.

5.2.3 Orbital-phase dependence of short-period variability

Figure 3.2 shows that, in the TESS observations of GG Car, both the orbital and 1.583-day photometric variations are not uniform, but they vary in both amplitude and profile. Figure 5.7 shows the TESS photometric data once they have had the orbital period variations subtracted, leaving only the short-period variability, and then folded by orbital phase. The largest variations in both observed orbital cycles occurs at around phase 0.12, with those variations being zoomed in the bottom panel. The variations are smallest around phase 0.6, though there is a data gap between phase 1.45–1.55.

Figure 5.8 clearly shows how the amplitude of the short 1.583-day variations is modulated throughout the orbital period of GG Car in the photometric data. For

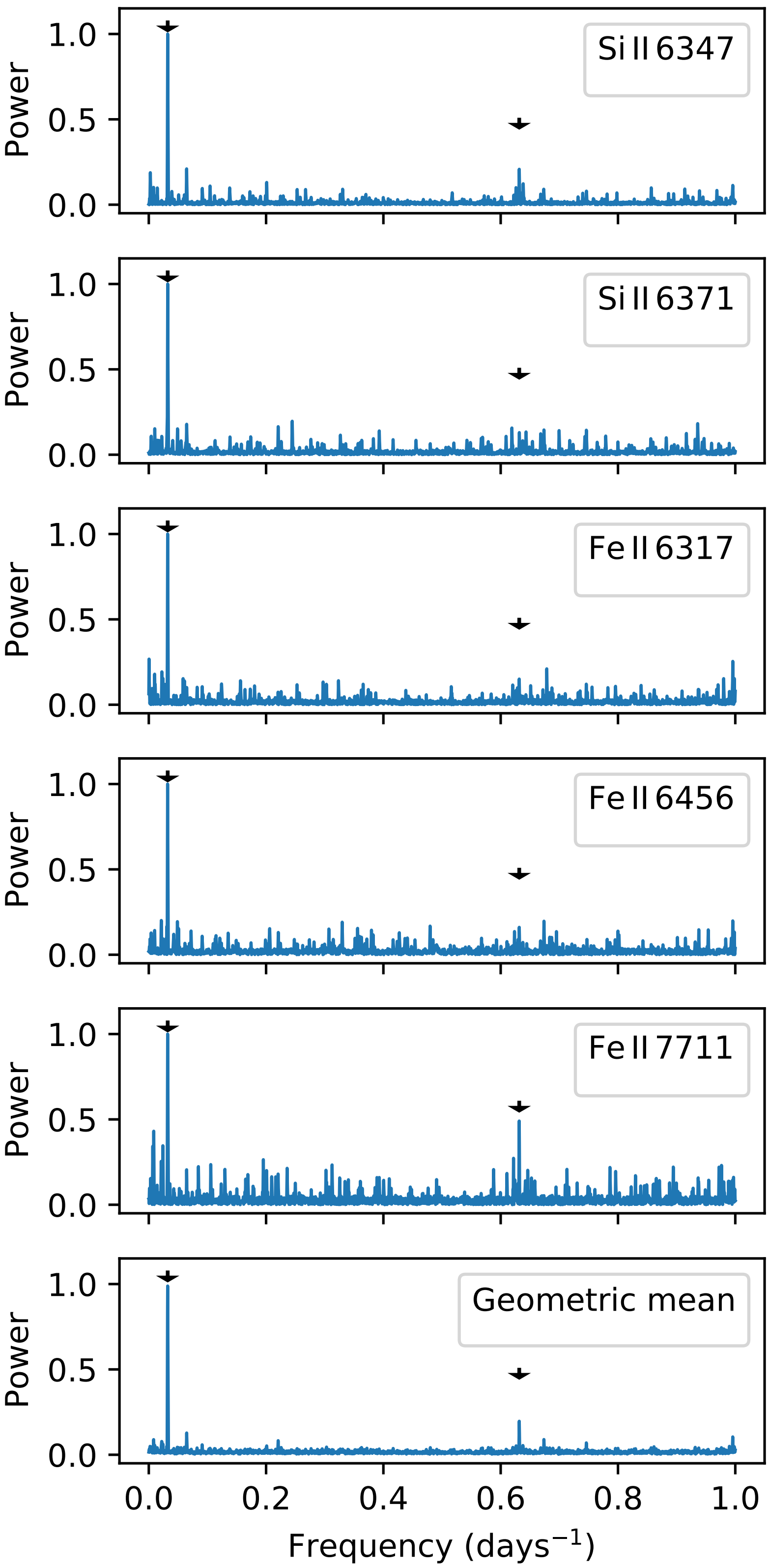

Figure 5.4: Same as Figure 5.3, except for the Si II and Fe II emission lines which display the 1.583-day variation.

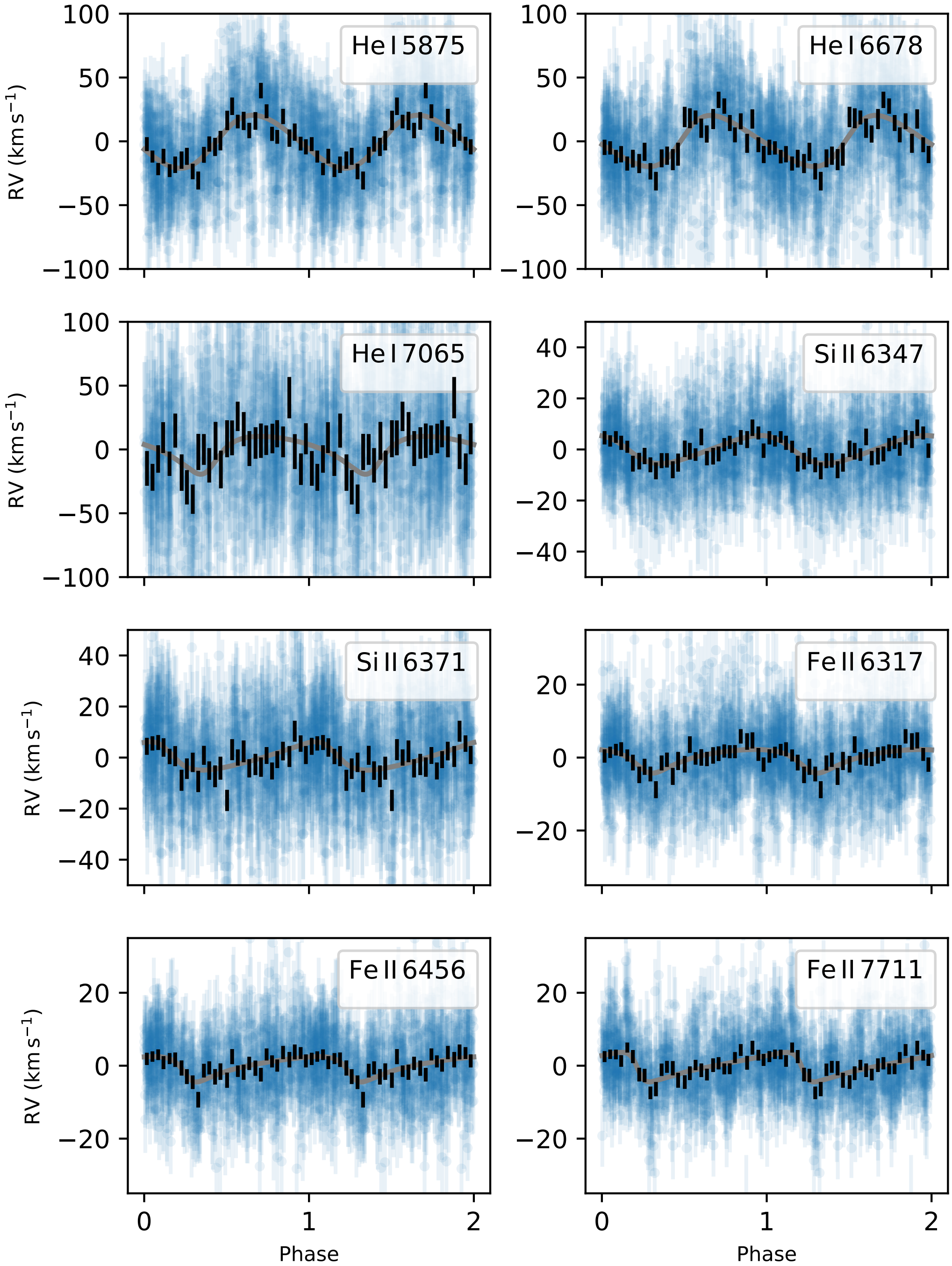

Figure 5.5: Radial velocity variations of the emission lines at the 1.583-day short period. Phases are calculated using Equation 5.1. The variations at the 31-day orbital period have been subtracted from the data of each line, to remove scatter. The data are split into 30 phase bins for each line species and black error bars indicate the weighted mean and standard error of the weighted mean for the radial velocities in each bin. The error bars of the data are both the uncertainties from the Gaussian fitting routine and the jitter, added in quadrature.

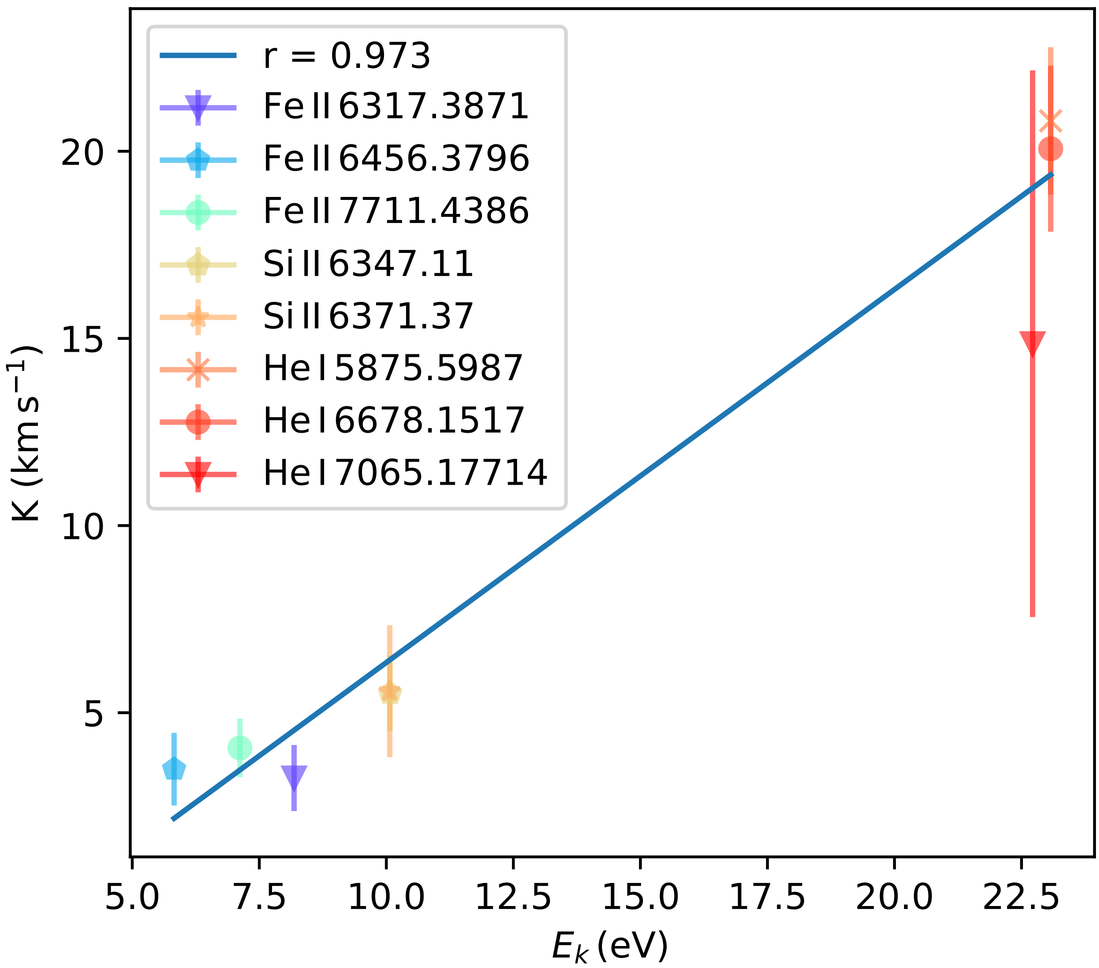

Figure 5.6: Amplitude, K, of the RV variations of the emission lines at the 1.583-day period against E_k, the energy of the initial excited state leading to the lines. The correlation coefficient, r, weighted by the inverse of the square of the error, is quoted in the legend.

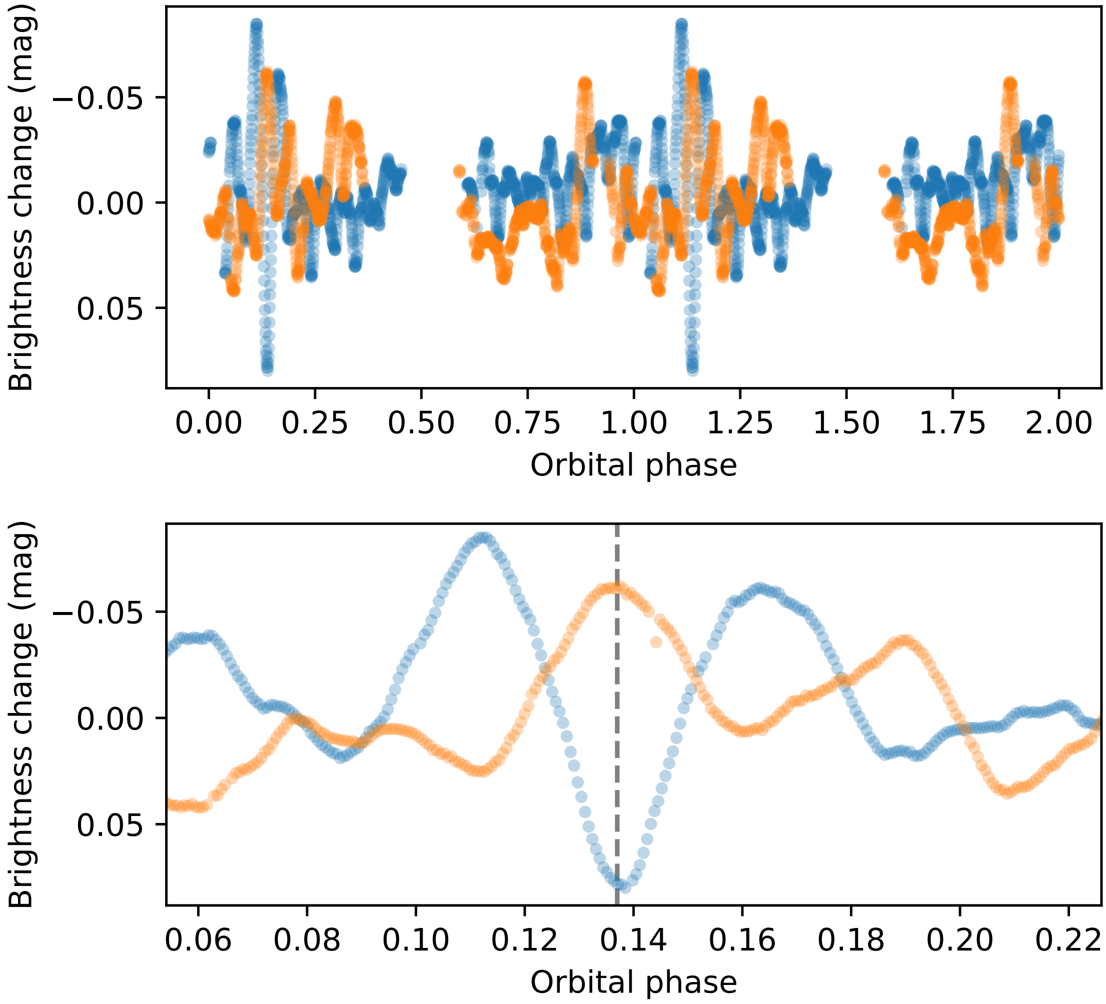

Figure 5.7: TESS photometric data of GG Car with the orbital period variations subtracted leaving only the short-period variations, then folded over the orbital period. Sector 10 data are in blue, and sector 11 in orange. The bottom panel zooms in on the largest variations around phase 0.137, where a dashed vertical line is drawn.

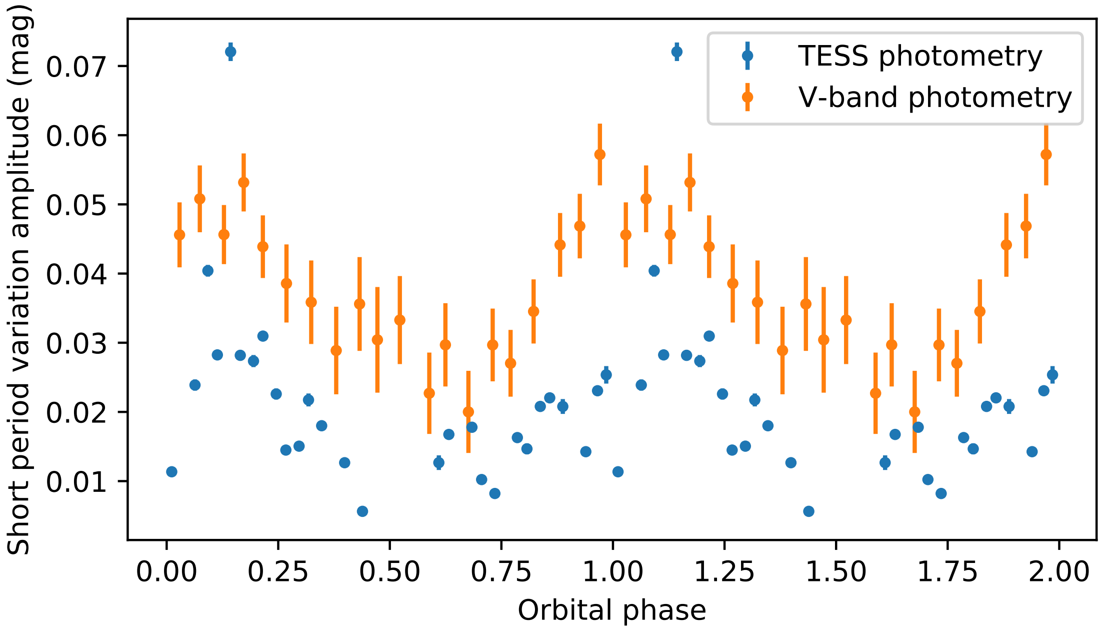

Figure 5.8: Amplitudes of the photometric 1.583-day period as a function of the orbital phase of the binary for both TESS and V-band data. Figure B.1 demonstrates how the data for the V-band photometry variations were calculated.

the TESS data a sinusoid is fitted to each 1.583-day slice within the dataset, with the amplitude and phase kept as free parameters. The amplitudes of the 1.583-day variations are then folded over the 31-day orbital period. It is clear that, in the TESS observational interval, the amplitude of the short-period variation is strongly tied to orbital phase, with the largest variations occurring around phase $\sim$0.1. This is shortly after the binary is at periastron, as per the ephemeris of Chapter 4, and when the system is brightest (both of which occur at phase 0).

For the V-band photometry, since there is not the fine time-sampling of the TESS data, different techniques need to be used to study the amplitude modulations of the short-period variations. To do this, the ASAS, ASAS-SN, and OMC data had the mean 31-day orbital variations subtracted, then a sliding window of orbital phase width 0.15 is used to calculate the short-period amplitudes in the orbital phase intervals. The data in each window were folded by the 1.583-day period and then fitted by a sinusoid, with amplitude, phase, and offset as free parameters. Figure B.1 in the Appendix demonstrates how the amplitude modulation of the V-band photometry along the binary orbit was calculated in each orbital phase window.

Figure 5.8 shows that the amplitude of the short-period variations in the V-band data is also modulated across the orbital phase of the binary. The amplitude-phase signal closely matches that shown by the TESS data in phase and shape, demonstrating that this orbital dependence of the 1.583-day period is long-lived and persistent across all data, and is not a curiosity of the TESS observing epoch. It is also noteworthy that the sharp rise in the TESS amplitude is matched as the phase where the amplitude is largest in the V-band photometry, suggesting that the large spike in amplitude that is seen in the TESS data around phase 0.1 persists throughout the observations of GG Car. The phases of the 1.583-day variations have no significant variability across the orbital period; this can be seen in the fitted sinusoids to the V-band data in Figure B.1, which are all in phase.

In Figure 5.7, it is clear that the variability in the TESS data is not uniform, but it does follow the general trend of having larger amplitudes shortly after periastron. The V-band data, since it is taking the average short-period amplitude of many orbital cycles simultaneously with a sliding window in orbital phase, gives us the average amplitude change over a long period of time. Therefore, it cannot be concluded whether this relationship holds for each orbital cycle, but that, in aggregate, over all orbital cycles there is a general trend for the amplitude of the photometric variability at the 1.583-period to be largest shortly after periastron.

It is then investigated whether this amplitude modulation also exists in the spectroscopic data. Figure 5.9 displays the amplitude modulation along the binary orbit of the 1.583-day RV variations of the He I emission, as observed by the GJW. The amplitude modulations for the spectroscopy were calculated similarly to those of the V-band photometry. It is clear, for all three He I lines, that the amplitude of the spectroscopic RV variations are modulated in a similar manner to the photometric variations. He I 7065, however, has an offset to the other He I lines and the photometry with peak amplitude occurring around phase 0.9.

Figures 5.10 and 5.11 show the same for the short-period presenting Si II and Fe II lines respectively. The Si II 6347 line shows a clear signal, with the amplitude of the short-period variations modulating across the orbital phase in the same manner as the photometry and the He I, whereas Si II 6371's signal of amplitude modulation is less clear. The Fe II shows some indication of amplitude modulation over the binary orbit, however their signals are not very clear due to the smaller amplitudes of the

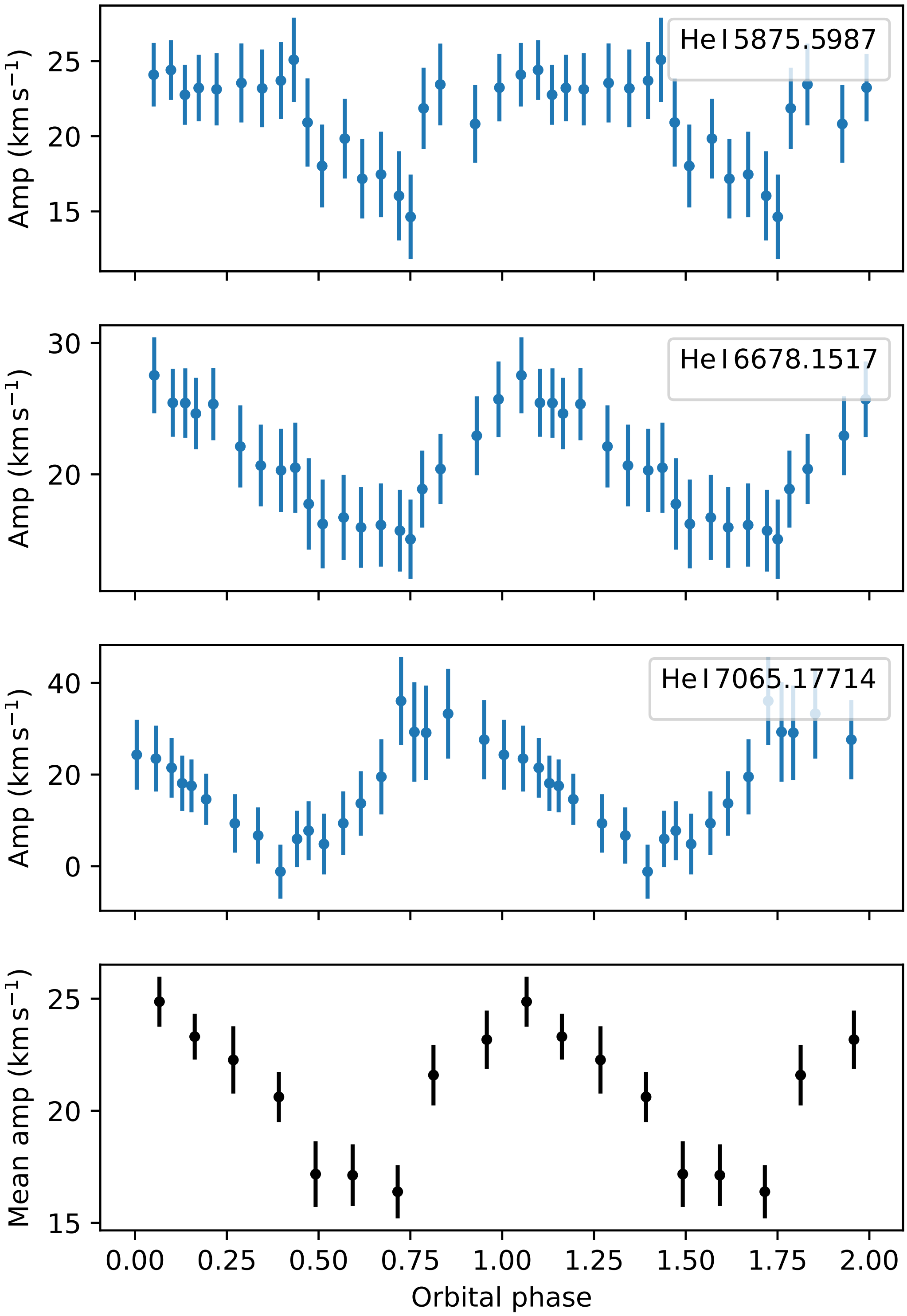

Figure 5.9: The amplitude of the short-period RV variations for the He I lines against orbital phase. The data were calculated in the same manner as the V-band data in Figure 5.8. The bottom panel shows the mean of the short-period amplitude in each phase bin, with the error-bar corresponding to the standard deviation in that bin.

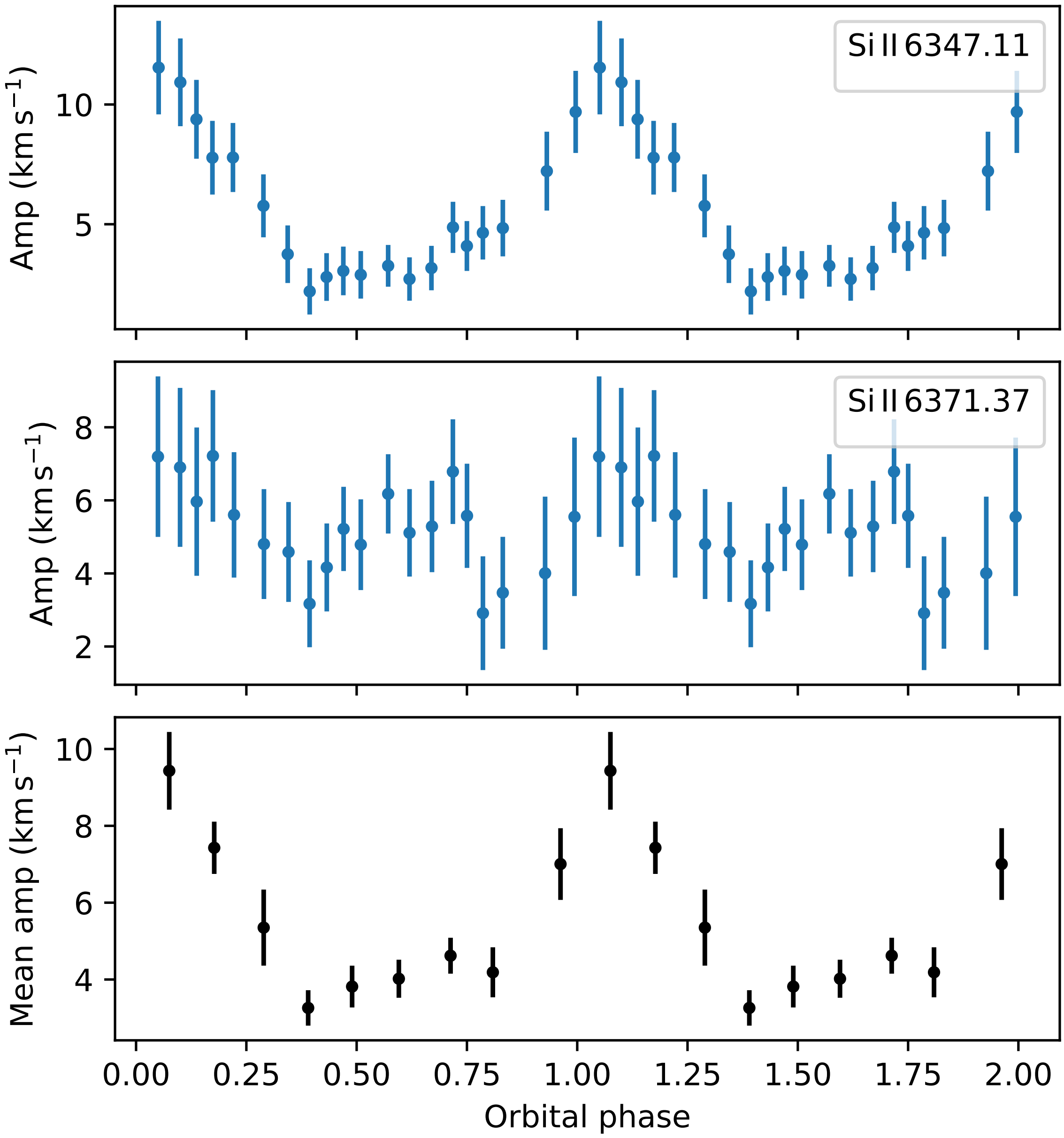

Figure 5.10: Same as Figure 5.9, except for the Si II 6347 and 6371 lines.

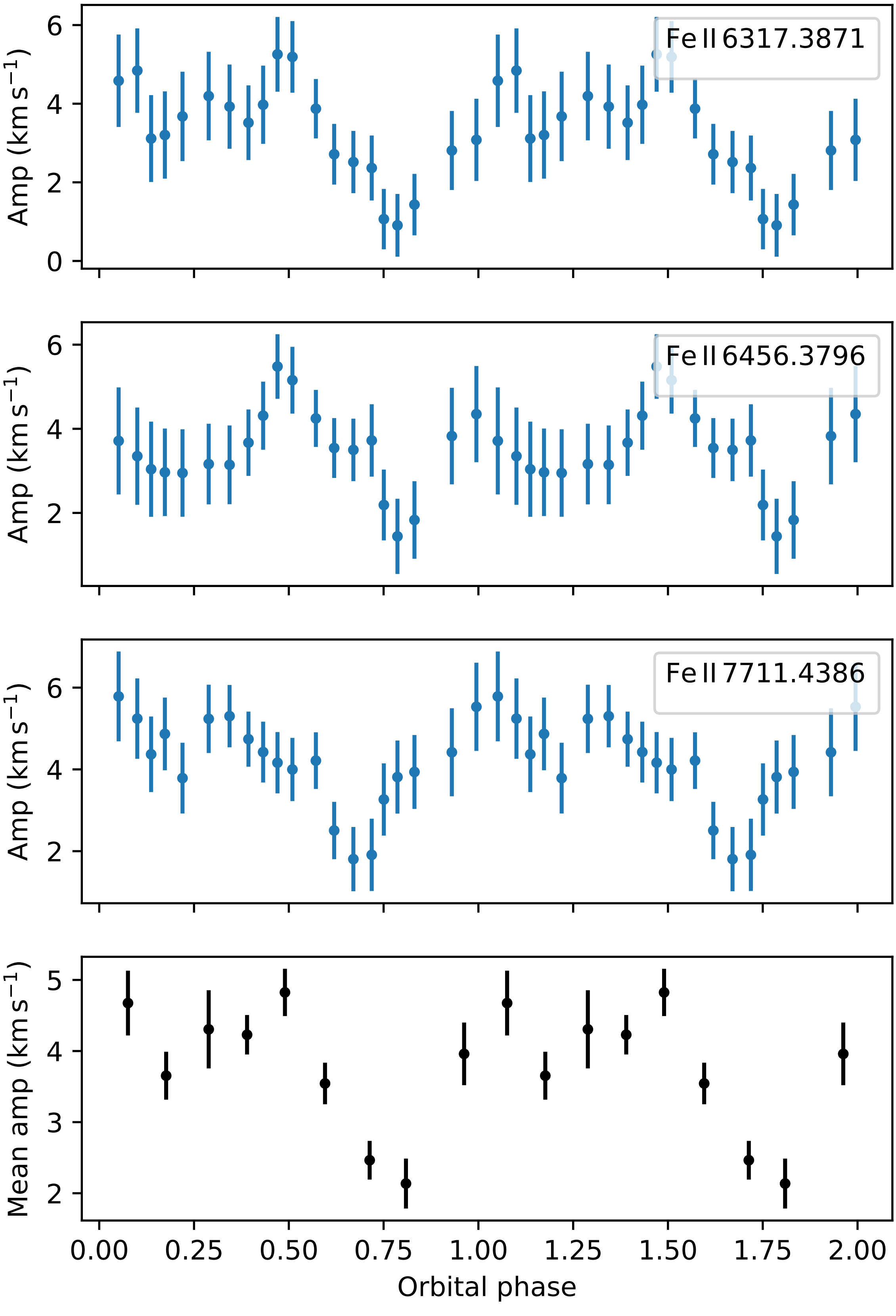

Figure 5.11: Same as Figure 5.9, except for the Fe II lines which display the short period variability.

Fe II lines. The amount of amplitude modulation is largest for the He I lines, followed by the Si II lines, followed by the Fe II lines.

5.3 Discussion

5.3.1 Origin of the 1.583-day variability

Stellar variability is variously explained by rotations, multiplicity, or pulsations. As evidenced by the TESS data, the amplitude of the photometric variability at 1.583 days can reach up to 0.07 mag. This implies a peak-to-trough brightness change of $\sim$14 %; since the secondary of GG Car is predicted to contribute $< 3\%$ of the flux of the system assuming it is a main sequence star of $7.2\,M_{\odot}$ (Chapter 4), then the flux from the secondary alone cannot be the origin of this variability. Here, we investigate whether rotation of the primary, a hidden third body, or pulsations in the primary can cause the 1.583-day variability observed in GG Car.

As shown in Zickgraf et al. (1996) the critical rotation velocity at the equator of a star, above which it cannot rotate without breaking up, can be estimated by

$$v_{\text{crit}} = \sqrt{\frac{G(1-\Gamma_{\text{rad}})M}{R}}, \tag{5.2}$$

where G is the gravitational constant, M is the mass of the star, R is the radius of the star, and Γ_{rad} is the correction to the effective gravity due to radiation pressure by electron scattering. Γ_{rad} is given by

$$\Gamma_{\text{rad}} = \frac{\sigma_e L}{4\pi G M c}, \tag{5.3}$$

where L is the stellar luminosity, c is the speed of light, and σ_e is the electron mass scattering coefficient. For σ_e, a value of $0.308\,\text{cm}^2\,\text{g}^{-1}$ is adopted, which is taken from Lamers (1986); it should be noted that this value of σ_e is calculated for the composition of the circumstellar environment of P Cygni. Entering the stellar parameters of GG Car given in Table 3.4 gives $v_{\text{crit}} = 370 \pm 70\,\text{km}\,\text{s}^{-1}$. Should the 1.583-day period be interpreted as the rotation period of the B[e]SG primary, the surface rotation velocity would be $v_{\text{rot}} = 860 \pm 260\,\text{km}\,\text{s}^{-1}$at the equator, far exceeding the critical rotation velocity of the star. Clearly the 1.583-day period cannot be the stellar rotation period of the B[e]SG primary component of GG Car.

Might there be a hidden close companion of the B[e]SG primary, or circumstellar material which orbits the primary every 1.583 days, causing the short-period variability of the system? Kepler's third law states

$$P^2 = \frac{4\pi^2 a^3}{GM}, \tag{5.4}$$

where P is the orbital period, a is the semi-major axis of the orbit, and M is the total mass of this inner system. Entering $P = 1.58315 \pm 0.0002$ days, and the primary's mass of $M = 24 \pm 4\,M_\odot$ gives $a = 16.5 \pm 0.9\,R_\odot$. Given that GG Car's primary has a radius of $27\,R_\odot$, this implies that a hidden companion would be completely engulfed in the primary star. Whilst it is theorised that B[e]SGs may be post-merger objects (Podsiadlowski et al. 2006), the variable period would not be as stable as it is observed to be if GG Car were a recently-merged object, given that an indication of a ~1.6-day period was first reported by Gosset et al. (1984) and the periodicity continues to the present day.

This leaves pulsations as the likely cause of the short-period variability in GG Car. Pulsations have been observed in B[e] stars at a similar timescale to the one observed in GG Car, though they are rare. Krtičková & Krtička (2018) detects a pulsation period of 1.194 ± 0.06 days in the unclassified B[e] star HD 50138 (V743 Mon). Pulsations with periods at this timescale are often observed in blue supergiants (e.g. Haucke et al. 2018). Saio et al. (2013) reports that radial pulsations and a spectrum of non-radial pulsations may be excited in evolved blue supergiants (BSGs) which have already undertaken the blue loop in their post-main sequence evolution, having been in a prior red supergiant (RSG) state. Conversely, they find that most of these pulsations were suppressed in BSGs which had not yet undergone the blue loop. Since only one significant frequency is observed, other than the orbital frequency, in the periodograms of the photometry and spectroscopy of GG Car this likely indicates that the primary GG Car is in a pre-RSG state, according to the conclusion of Saio et al. (2013). This supports the findings of Kraus (2009) and Kraus et al. (2013), which concluded that GG Car is in a pre-RSG state based on ^{13}CO abundances.

Given that the variability is coupled to the orbit of the binary, this may indicate that the tidal potential is exciting pulsations in the B[e]SG primary (this amplitude modulation is discussed in further detail in Section 5.3.2). As the tidal potential is quadrupolar, the most likely oscillation mode observed is an l=2 mode, where l is the degree of the mode and indicates the number of surface nodes. Gough (1993) shows that f-modes of stars, which act as surface gravity waves with $n = 0$ (where n is the number of radial nodes of the oscillation mode), have angular frequencies which may be determined as

$$\omega^2 = \frac{Lg_s}{R}\left(1 - \epsilon(L)\right), \tag{5.5}$$

where $\omega = 2\pi/P$ is the angular frequency of the mode, $g_s = GM/R^2$ is the surface gravity of the star, R is the stellar radius, $L = \sqrt{l(l+1)}$, and $\epsilon(L)$ is a term to correct for the sphericity of the star. $\epsilon(L)$ is calculated

$$\epsilon(L) = 2L^{-1} + \frac{3\int_0^R (r/R - 1)\rho \exp\left(2Lr/R\right)\,\mathrm{d}r}{\int_0^R \rho \exp\left(2Lr/R\right)\,\mathrm{d}r}, \tag{5.6}$$

where $\rho = \rho(r)$ is the density of the star. Entering the stellar parameters of GG Car into Equation 5.5, and utilising simple distributions of $\rho(r)$, yields values of the $l = 2$ f-mode frequency which are consistent with the measured variability. Assuming a constant density gives $P = 2.4^{+1.2}_{-1.0}$ days. While a constant density is highly unrealistic, we may use simple prescriptions to give higher densities in the stellar centre, such as $\rho(r) \propto 1 - A\,(r/R)^B$, where A and B are constants, that also yield consistent periods. Computing a grid of allowed periods for the $l = 2$ mode using this simple prescription of $\rho(r)$ returns periods which are consistent with the observed periodicity for all values of A and B where $0 \leq A \leq 1$ and $B > 0$. While detailed modelling is beyond the scope of this study, this shows that the observed pulsation frequency is consistent with and likely to be the $l = 2$ f-mode. It must also be noted that, per Equation 5.5, higher values of l up to $\sim$8 may also yield periods which are consistent with the observed variability; however, the $l = 2$ mode would be expected to be excited more strongly than the higher modes by the tidal potential. The mode observed may not be radial, since tidal modulation is only allowed for pulsation modes with $l \neq 0$ (Polfliet & Smeyers 1990).

The RV variability that detected in GG Car's emission lines would then be related to that pulsations in the primary affecting the structure of the wind at its 1.583-day periodicity. Pulsations have been theorised and shown to affect the wind and mass-loss of properties of blue supergiant stars (Aerts et al. 2010; Kraus et al. 2015a; Yadav & Glatzel 2016, 2017; Haucke et al. 2018). Structures in stellar winds caused by pulsations have been proposed to explain variability in certain X-ray binaries (Finley et al. 1992; Koenigsberger et al. 2006).

5.3.2 1.583-day amplitude modulation

In Section 5.2.3, it is shown that the amplitude of the 1.583-day variations is modulated by the orbital phase of the binary, most clearly in the photometry. The amplitudes are largest when the binary is at periastron in its eccentric ($e = 0.5 \pm 0.03$) orbit. This linking between the 31-day orbital period and the 1.583-day short period is unusual, since the ratio between the two periods is $31.01/1.583 = 19.589$, i.e. they are non-commensurate.

GG Car's lightcurve bears a resemblance to the "heartbeat stars" which have resonant, tidally driven, stellar oscillations that have variable amplitudes over the orbital period (see e.g. Fuller 2017). Most heartbeat stars yet discovered are lower mass A and F stars, but the phenomenon has also been observed in massive O and B stars (Pablo et al. 2017; Jayasinghe et al. 2019). These heartbeat stars are eccentric binaries which have orbital periods that are exact integer multiples of the star's g-mode pulsation periods, which lead to coherent and resonant pulsations due to the tidal excitation of the oscillation modes (see also Kumar et al. 1995; De Cat et al. 2000; Willems & Aerts 2002). However, the short-period variability observed in GG Car is clearly non-resonant with the orbital period, as the bottom panel of Figure 5.7 and the non-integer relation between the short-period and orbital period clearly show. Therefore, the periodicity and amplitude modulation reported cannot arise due to resonance. However, there are indications that tidal effects can affect non-resonant free oscillations, and here that possibility is explored.

Chapter 4 showed that, at periastron, the radius of the primary of GG Car extends to $85 \pm 28\,\%$ of its Roche lobe radius, whereas at apastron it only extends to $28 \pm 9\,\%$; therefore, the tidal perturbation at periastron will be significant and a dynamical tide will be raised. Chapter 4 also presents evidence that the primary's mass-loss is focused around periastron. In GG Car, the timescale of the varying gravitational potential will be short given that the orbit is significantly eccentric, with the timescale of periastron passage $T_{\mathrm{peri}} \sim \sqrt{a^3(1-e)^3/GM_{\mathrm{tot}}} \sim 1.7\,\mathrm{days}$, where M_{tot} is the combined mass of the primary and the secondary. A similar determination of the timescale of intense gravitational interaction is the half-width-at-half-maximum (HWHM) of the tidal force, i.e. the time taken for the tidal force of the secondary on the primary to increase from mid-point value to its peak value at periastron. The HWHM of the tidal force is $\sim$1.9 days (since $F_{\text{tidal}} \propto r^{-3}$, where r is the instantaneous separation of the binary components). Therefore, around periastron, the timescale of the change of the tidal force is of the same order as the observed periodicity and dynamical timescale of the primary; the star will be unable to adjust to the changing tidal force in a quasi-static way. Conversely, for the tidal force to go from its minimum at apastron to the mid-point value takes 13.6 days, i.e. an order of magnitude longer than the pulsation period and the dynamical timescale.

It therefore follows that the varying proximity of the two binary components will affect the conditions of the primary, and the rapid change of the tidal forces and enhanced mass loss at periastron will draw the primary out of hydrostatic equilibrium at a timescale of the same order as its dynamical timescale. The primary, attempting to regain equilibrium, oscillates at the observed period of 1.583 days, which has been shown in Section 5.3.1 is likely to be the $l = 2$ f-mode. As the binary components separate after periastron passage, the tidal force becomes increasingly less important, and the star will continue to oscillate at the observed period and ultimately try to regain hydrostatic equilibrium. The timescale for the damping of the oscillations depends on the dominant source of viscosity, but, in the case of the large tidally induced distortion observed in GG Car, could be as fast as the dynamical timescale of the primary's envelope ($\tau_{\text{dyn}} \sim 1$ day). Quantifying mode damping timescales in the envelopes of massive OB stars is an uncertain problem, and is beyond the scope of this study.

Figure 5.12 displays both how the short-period variation amplitude and mean brightness in the V-band compares with the instantaneous separation of the binary components along the orbital period: the mean brightness is near perfectly anti-correlated with the separation of the components. On the other hand, the short-period amplitude of the V-band data increases more rapidly than it decays, and peaks somewhere between orbital phases 0.0 and 0.14, corresponding to $\sim 0-4$ days after periastron. This delay can also be clearly seen in the folded TESS data in Figure 5.7.

There are examples in the literature which support this hypothesis of tidally modulated free oscillations. Moreno et al. (2011) calculated that increased stellar activity can be expected on stellar surfaces around periastron in eccentric binaries due to the

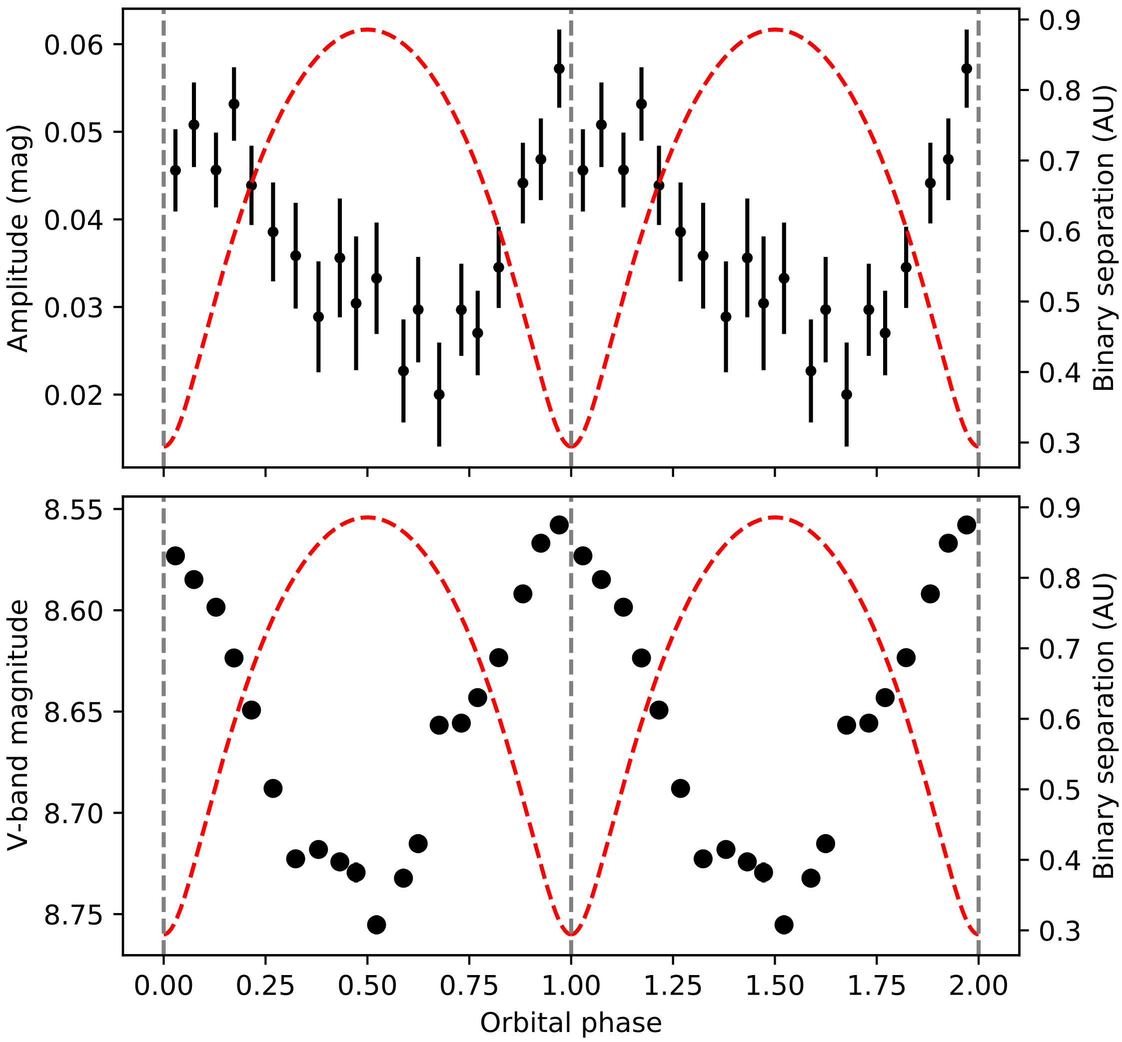

Figure 5.12: Top: Amplitude of the 1.583-day variations in V-band photometry against orbital phase (black points, left hand axis), with the instantaneous separation of the binary components over-plotted (red dashed line, right hand axis). Phases of periastron are denoted by vertical dashed lines. Bottom: same as top, except with the mean V-band magnitude in the phase bin replacing the short-period amplitudes.

raising of dynamical tides and the associated changes in timescale of dissipation of the tidal energy, and this can lead to oscillations. The interaction of free oscillations with tidal interaction was theoretically studied by Polfliet & Smeyers (1990), who show that a tidally distorted star may display free non-radial oscillations with periods of the order of its dynamical timescale. They find that the free oscillations' amplitudes are modulated at a frequency which is an integer multiple of the orbital frequency. Tidal modulation of pulsation amplitudes in this manner have been reported in the β Cephei variables β Cep (Fitch 1969), CC And (Fitch 1967), σ Scorpii (Fitch 1967; Goossens et al. 1984; Chapellier & Valtier 1992), α Vir (Dukes 1974), and 16 Lacertae (Fitch 1969; Chapellier et al. 1995); in these objects, the pulsation periods and the orbital periods are non-resonant, but the pulsational amplitudes undergo an integer number of cycles per orbital period. Chapellier et al. (1995) reports that the amplitude of an $l = 1$ pulsation mode of the system 16 Lacertae undergoes exactly one cycle over the orbital period where the pulsation period and the orbital period are non-commensurate, similar to what is observed in GG Car.

It is worth noting that this amplitude modulation also bears resemblance to binaries which have been recently discovered to have pulsations that are tidally trapped on one hemisphere of the variable component. Handler et al. (2020) discovered a tidally-trapped pulsation mode in the binary star HD 74423, in the form of amplitude modulation of the observed pulsations as a function of orbital phase. Similarly to what is observed in GG Car, the pulsation frequency and orbital frequency in HD 74423 are non-commensurate. Kurtz et al. (2020) find a similar result in CO Cam, finding that four modes are trapped by the tidal potential of the companion. Fuller et al. (2020) presents evidence of a similar process occurring in TIC 63328020. The authors explain the amplitude modulation in these systems as being due to the pulsation axis of the variable component to be aligned with the line of apsis of the binary which cause the pulsations to have a larger amplitude on one hemisphere of the star, either the hemisphere facing towards or away from the companion. A larger, or smaller, photometric variability amplitude is then observed at times of conjunction depending on which hemisphere is facing the observer. According to the orbital geometry of GG Car ($e = 0.50$, $\omega = 339.87°$), superior conjunction occurs at phase 0.14 and inferior conjunction occurs at 0.93. Superior conjunction, therefore, does occur at a remarkably similar phase as the oscillation amplitude's maximum, most clearly shown in Figure 5.7. However, in the scenario of tidally trapped pulsations, the phase of inferior conjunction would then be expected to have the lowest oscillation amplitude.

This is clearly not the case, as the oscillation amplitudes are still very large around phase 0.93. Therefore it is unlikely that the amplitude modulation observed in GG Car is due to tidal trapping of the pulsation mode, though geometrical effects may perhaps be accentuating the observed amplitude of the non-radial pulsation mode at superior conjunction.

Further TESS-quality observations of GG Car observing more orbital periods would be needed to fully confirm such an argument of orbital-phase modulated free oscillations. Alternatively, phase-resolved studies of the spectral energy distribution (SED) of the system could allow the varying contribution of the primary to the SED to be measured. Should the primary's contribution vary with the orbit and the 1.583-day period, this would lock down the variability as being due to pulsations of the primary, and therefore the amplitude modulation would be due to proximity effects of the primary to the secondary.

5.4 Conclusions

It is shown that the B[e]SG binary GG Car is significantly variable in both photometry and spectroscopy at 1.583156 ± 0.0002 days, and this variability has been studied in detail for the first time. This period is much shorter than the well-known 31-day orbital period of the binary. It is shown that the short-period variability cannot be caused by the rotation of the B[e]SG primary, the presence of a hidden third body, or intrinsic variability of the secondary's flux. A 1.583-day variability is consistent with the period of the lower-order f-modes ($l \lessapprox 8$) of GG Car's primary given its mass and radius, and I ascribe the variability as most likely being due to the $l = 2$ f-mode such that it couples to the quadrupolar tidal potential. I therefore argue that pulsations of this mode are the most likely cause of its variability.

In spectroscopy, it is found that the short period manifests itself in the RVs of the He I, Si II and Fe II emission lines; however, not all of GG Car's emission lines display the periodicity. The amplitudes of the spectroscopic RV variations at the 1.583-day period are correlated with the upper energy levels of the transitions causing the line emission, implying that the variations are related to the temperature of the line forming regions.

The amplitudes of the short-period variations are dependent on the orbital phase of the binary, most notably for the V-band and TESS photometry, with the largest variations occurring around or just after periastron, where the system is also at its brightest. This is striking as the ratio between the orbital period and the shorter period is 19.596. This non-integer ratio of the two periods means the shorter period cannot be a tidally-resonant excited oscillation mode in one of the stars.

Chapter 4 shows that the primary's radius extends to $\sim$85% of its Roche radius at periastron, compared to only $\sim$28% at apastron. It is shown in Section 5.3.2 that the timescale of the change of the tidal forces on the primary at periastron are of the same order as its dynamical timescale. Therefore, it is suggested that the primary is being pulled out of hydrostatic equilibrium by the secondary every orbit due to the strong tidal effects at periastron faster than the primary can regain equilibrium. This loss of equilibrium causes pulsations at the $l = 2$ f-mode, which can couple to the quarupolar tidal potential and which is consistent with the 1.583-day period observed, with a larger amplitude when the stars are close in proximity and the primary is being pulled further from equilibrium. These oscillations are damped at a timescale which may be as fast as the dynamical timescale as the separation between the binary components increases and the primary can return to equilibrium.

The unusual behaviour of GG Car's short-period variability reported in this chapter has not been reported in other B[e]SGs as of yet. Further TESS-quality observations and phase-resolved SED observations of GG Car would be required to pin down the cause of its short-period variability and amplitude modulation, and similar phenomena in other B[e]SGs in binaries should be searched for.

Chapter 6

The circumbinary emission of GG Carinae

Abstract

This chapter studies atomic emission lines arising from GG Carinae's circumbinary disk in FEROS spectra collected between 1998 and 2015. Semi-forbidden Fe II] and permitted Ca II emission are formed in the same thin circumbinary ring previously reported to have forbidden [O I] and [Ca II] emission. There are two circumbinary rings orbiting with projected velocities of $84.6 \pm 1.0\,\mathrm{km\,s^{-1}}$ and $27.3 \pm 0.6\,\mathrm{km\,s^{-1}}$. Deprojecting these velocities from the line-of-sight, and using updated binary masses presented in Chapter 4, the inferred radii of the circumbinary rings are $2.8^{+0.9}_{-1.1}\,\mathrm{AU}$ and $27^{+9}_{-10}\,\mathrm{AU}$ for the inner ring and outer ring respectively. There is evidence of subtle dynamical change in the inner circumbinary ring over the 17 years of FEROS data, manifesting in variability in the ratio of the intensity of the blueshifted peak to the redshifted peak of its emission lines and the central velocity becoming more blueshifted. Smoothed-particle hydrodynamic simulations of the system are run which suggest that these observed changes are consistent with eccentricity being pumped in a radially thin circumbinary ring by the binary. A systemic velocity of the GG Carinae system of $-23.2 \pm 0.4\,\mathrm{km\,s^{-1}}$ is found.

6.1 Introduction

As discussed in Section 1.2, B[e]SGs are often surrounded by concentric and radially thin atomic rings orbiting at Keplerian velocities. As the origin of the forbidden emission, the atomic rings are therefore integral to these systems' displaying of the B[e]SG phenomenon. Despite this importance, how these rings come to form and become arranged in such unusual distributions is still unclear.

As introduced in Section 3, GG Car hosts such a complex circumstellar environment typical for B[e]SGs. It has been shown to have a dusty envelope (Allen 1973; Marchiano et al. 2012), Fe II and [Fe II] orbiting in a ring (Swings 1974; Allen & Swings 1976) and CO emission arising from a circumbinary disk (Kraus et al. 2013). Forbidden [O I] and [Ca II] emission have been reported from at least two concentric circumbinary rings (Maravelias et al. 2018). Kraus et al. (2013) argues against the circumbinary disk being formed by Roche Lobe overflow, instead arguing that it is formed of material that was decreted from the primary in a former classical Be progenitor.

In this Chapter, I analyse GG Car's circumbinary atomic emission lines in high resolution FEROS spectra introduced in Section 3.2.3.2. I update the characteristics of the circumbinary rings in the context of the updated orbital parameters and stellar masses determined in Chapter 4, and search for variability in the circumbinary emission lines over the $\sim$17 years of FEROS observations. Section 6.2 presents the detected circumbinary atomic emission lines; Section 6.3 describes the thin-ring model that is used to fit the circumbinary emission lines assuming circular Keplerian orbits; Section 6.4 presents the results of the fitting and the variability detected in the emission lines; Section 6.5 discusses these results in the context of the new orbital solution of Chapter 4 and describes smoothed-particle hydrodynamic simulations of the system which may recreate the observed variability; and Section 6.6 presents this chapter's conclusions.

6.2 Atomic circumbinary emission lines

The steep-sided, double-peaked line profiles associated with thin rings are found in a number of emission lines. Each of these atomic species and their line profiles are

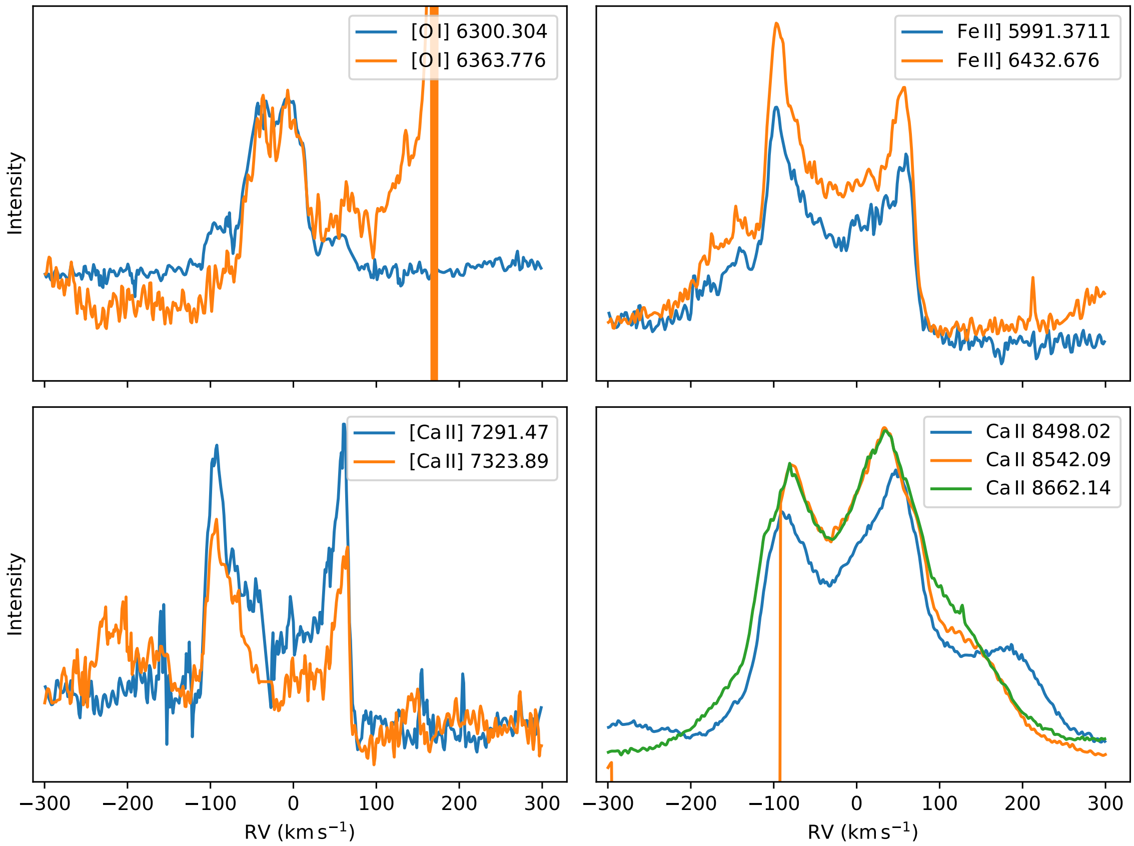

Figure 6.1: Atomic circumbinary ring profiles of GG Car, in radial velocity (RV) space, as observed by FEROS on 1998-12-06. Top left: [O I] emission. The [O I] 6364 line has Si II 6371 to its redward side. Bottom left: [Ca II] emission. Top right: Semi-forbidden Fe II] emission. Bottom right: Permitted Ca II emission. Every Ca II line in GG Car's spectrum is blended by a member of the H I Paschen series, which are to the redward side of Ca II. There is a data gap in the FEROS spectra for RV $< -95\,\mathrm{km\,s^{-1}}$ for the 8542 Å line.

described in this section.

6.2.1 [O I] emission

[O I] 6300 and 6364 Å are present in the spectra of GG Car, but unlike some other B[e]SGs there is no [O I] 5577 Å emission present. Figure 6.1, top left panel, displays the [O I] emission, as observed by FEROS. In the [O I] 6300 line, there are two visible ring profiles superposed over one another: one with a splitting $\sim 80\,\mathrm{km\,s^{-1}}$ and the other with splitting $\sim 25\,\mathrm{km\,s^{-1}}$. This is indicative of two concentric rings giving rise to this emission. The [O I] 6364 line only exhibits a single ring profile, with a splitting similar to that of the lower-splitting 6300 profile. Since the 6364 line is slightly blended, and has low signal-to-noise, only the [O I] 6300 line is analysed since it contains all of the relevant information from the 6364 line.

6.2.2 [Ca II] emission

In the FEROS spectra, [Ca II] 7291 and 7323 Å are present and display a single thin-ring profile. Figure 6.1, bottom left panel, displays the [Ca II] profiles observed by FEROS. Since both lines are of comparable quality and have similar profiles, both [Ca II] of the lines are analysed, summing the lines in velocity space to improve signal-to-noise.

6.2.3 Fe II] emission

I report semi-forbidden Fe II] emission lines which are formed in the higher-velocity circumbinary ring of GG Car. Fe II] 5991 and 6432 Å display clear double-peaked profiles consistent with arising from rings. Other Fe II lines, such as Fe II 6416.9, also host some indication of double-peaked ring profiles; however, they are unacceptably blended with emission from the primary's wind and therefore they are not analysed in this study.

Figure 6.1, top right panel, displays the profiles of the circumbinary Fe II] emission, observed by FEROS. There is a small emission component to the blueward side of the disk profile which causes an asymmetry in the profile; this component is likely to arise in the wind of the B[e]SG primary. In this analysis, this pollution component in fitted and its contribution removed in order to focus on the disk profile. Similarly to the [Ca II] lines, the Fe II] lines are summed in velocity space in the upcoming analysis to maximise signal-to-noise.

6.2.4 Permitted Ca II emission

I also report the discovery of permitted Ca II emission originating in GG Car's circumbinary disk; these are Ca II 8498.02, 8542.09, and 8662.14 Å. Coincidentally, each of these Ca II lines is blended with a different member of the H I Paschen series on their redward sides which are bright and of complex profiles. The Paschen series are associated with H I transitions from the nth to the third energy level, where $n > 3$. The polluting members are the $n = 16$ ($\lambda = 8502$ Å), $n = 15$ ($\lambda = 8545$ Å), and $n = 13$ ($\lambda = 8665$ Å) transitions.

Figure 6.1, bottom right panel, presents the permitted Ca II emission, clearly displaying double-peaked disk profiles at similar splitting to the [Ca II] emission. The asymmetry and redward shoulder in the profiles is caused by the H I Paschen emission, which are ∼3 Å to the red of the Ca II lines. There is a data gap in the FEROS spectra to the blueward side of the Ca II 8542 Å line; therefore, I do not study this line further in this analysis.

In the November 2015 spectra, the double peaked profiles of the Ca II lines are too heavily polluted by the Paschen lines to successfully analyse.

6.3 Thin ring model

For the purpose of fitting the orbital motion of the circumbinary rings to the emission lines, it is assumed that the material constituting the rings are on circular, quasi-Keplerian orbits about the binary. While in Section 6.5.3 I show that circular symmetry may in fact be broken in the later spectra, this assumption allows an expeditious method to extract physically relevant parameters from the data without introducing the danger of over-fitting the data.

The Keplerian orbital speed, $v_{\rm kep}$, of a particle orbiting enclosed mass M at radius R is given by

$$v_{\rm kep} = \sqrt{\frac{GM}{R}}, \tag{6.1}$$

where G is the gravitational constant. The radial velocity of this particle towards the observer, v_r, is

$$v_r = v_{\rm kep} \sin i \sin\theta + v_0, \tag{6.2}$$

where θ is the true anomaly of the particle in its orbit (with 0° defined as conjunction of the particle in front of the centre of mass), i is the inclination of the orbit, and v_0 is the systemic radial velocity of the system. It is assumed that the ring is infinitesimally thin in the radial direction, and the terminology "thin ring" is used to mean radially thin for the remainder of this study. For a thin, circumbinary ring model, there are an infinite number of particles in orbit about M with orbital speed $v_{\rm kep}$ distributed uniformly in θ from $0^\circ \rightarrow 360^\circ$. It is assumed that each particle emits an equal amount of radiation making up the emission line profile, and that none of the emission is occulted. Therefore, the intensity of an emission line as a function of radial velocity $I(v_r) \propto P(v_r) \propto d\theta/dv_r$, where $P(v_r)$ is the distribution of v_r given the uniform distribution of θ. Therefore, from Equation 6.2, $I(v_r)$ can be analytically shown to be

$$I(v_r) \propto \begin{cases} \frac{1}{\sqrt{1-\left(\dfrac{v_r - v_0}{v_{\rm kep}\sin i}\right)^2}}, & \text{if } |v_r - v_0| < v_{\rm kep}\sin i \\ 0, & \text{otherwise.} \end{cases} \tag{6.3}$$

Equation 6.3 assumes perfect spectral resolution and an infinitesimally thin Keplerian-orbiting ring with no turbulence or thermal broadening, none of which will be strictly true. In order to get a real line profile from the theoretical disk profile defined in Equation 6.3, $I(v_r)$ needs to be convolved with a Gaussian of standard deviation σ; σ encodes the resolution of the observing instrument, turbulent velocity in the ring, thermal velocities in the ring, and any finite radial width of the emission region. The line profiles are constructed by convolving Equation 6.3 with a Gaussian of width σ numerically.

Ring profiles are fitted to the [O I], Fe II], [Ca II], and Ca II emission lines by utilising the log-likelihood function, using the Monte Carlo Markov Chain algorithm `emcee` (Foreman-Mackey et al. 2012), to determine the posterior probability distributions of the ring parameters. The physically relevant parameters $v_{\rm kep}\sin i$, v_0, and σ are determined, along with the base continuum level, local continuum gradient, and peak intensity, which are physically insignificant parameters in this study and are therefore excluded from further analysis. The line intensities are a reflection of the continuum brightness which is variable at both the orbital period and 1.583-day period (Chapters 4 and 5), and therefore have little physical significance when considered on their own in GG Car.

As the [O I] 6300 line is formed in two separate circumbinary rings, this line is fit as a superposition of two ring profiles in the FEROS data, fitting for the parameters of both rings concurrently. Figure 6.2, top left panel, displays an example of

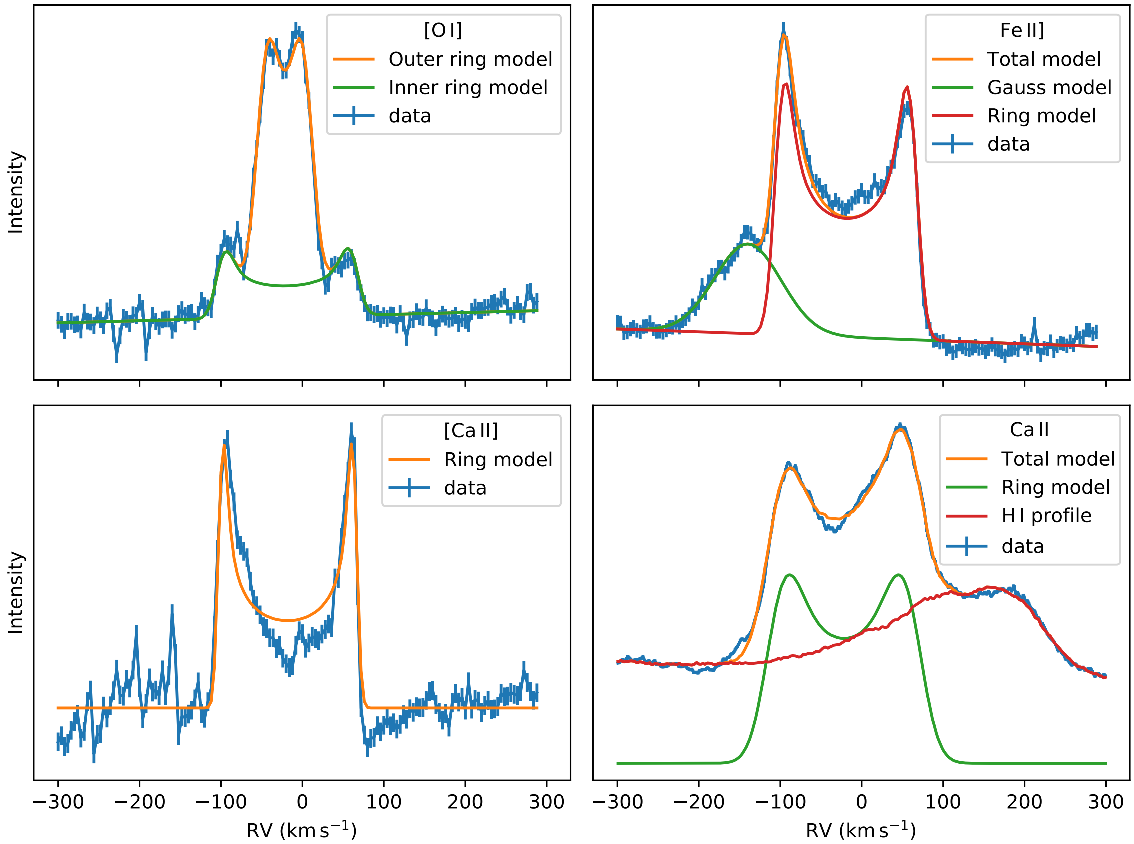

Figure 6.2: Example fits to the circumbinary ring lines. All profiles were observed by FEROS on 1998-12-07. Top left: Double circumbinary ring fit to the [O I] 6300 line. Top right: ring and Gaussian fit to the summed Fe II] 5991.4 and 6432.7 Å lines. Bottom left: single ring fit to the summed [Ca II] 7291.5 and 7323.9 Å lines. Bottom right: circumbinary ring and combined H I Paschen profile fit to the Ca II 8498.0 Å line.

the [O I] 6300 line as observed by FEROS, and the double-ring profile fitted to the line.

The Fe II] 5991 and 6432 lines are mildly blended with another component likely to be formed in the wind of the primary. This polluting component is modelled as a Gaussian in the fitting routine, and the fitted Gaussian model is then subtracted from the data before further analysis is undertaken. Figure 6.2, top right panel, displays a fit to an example FEROS spectrum's Fe II] lines.

As the [Ca II] lines are unpolluted by any components, they are fitted with a single ring profile. An example fit is shown in Figure 6.2, bottom left panel. The Telluric correction routine does not fully remove the atmospheric absorption from the [Ca II] lines in the 1998-12-23 and 1998-12-24 spectra (see Figure 6.4, top row, rightmost two panels). It is still possible to extract acceptable fits from these lines which are consistent with the spectra from near-in-time spectra, therefore these fits are retained for further analysis.

The permitted Ca II lines are polluted by the H I Paschen series. To account for this, for each spectrum an average Paschen line profile is built in RV space using the unpolluted and strong Paschen lines in the FEROS wavelength range. These are the $n = 12$, 14, and 17 lines. The circumbinary ring profile is then fit with the Paschen profile at its appropriate RV offset, with the intensity of the Paschen profile as a free parameter. Figure 6.2, bottom right panel, shows an example fit to the Ca II 8498.0 Å line.

6.4 Results

Figure 6.3 displays the fitted parameters of the FEROS emission lines against time of observation. Note that the x axis skips periods of time without observations. The FEROS fits during 2015 are included, for comparison. With the exception of the fitted v_0 parameters, there is little significant variability of the fitted ring parameters. The variability of the v_0 parameters are presented in Section 6.4.2. The other fitted parameters show no significant changes over the FEROS dataset. The measured σ of the Ca II lines is consistently larger than the other emission lines; this is discussed in Section 6.5.

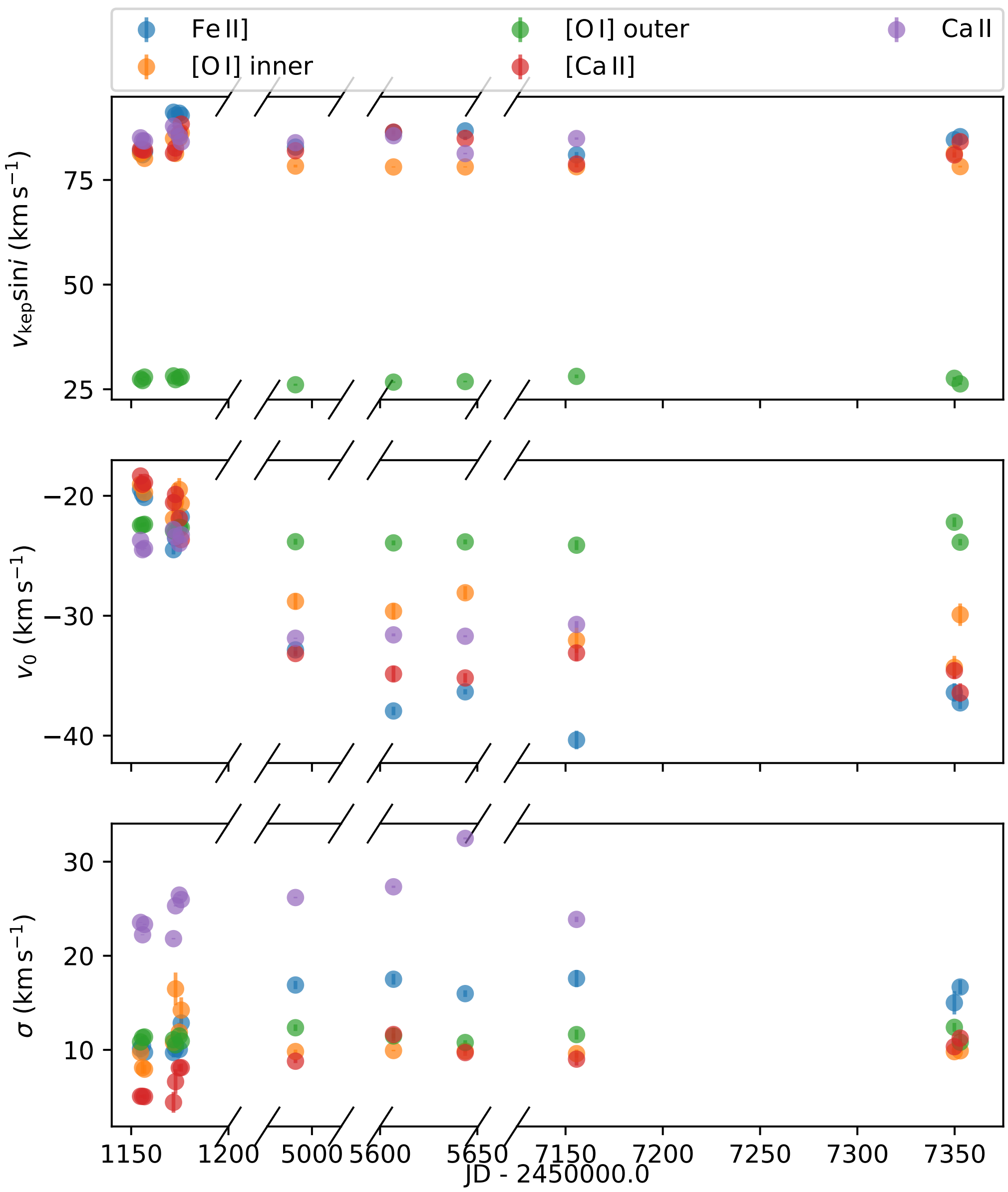

Figure 6.3: Fitted projected Keplerian velocity, $v_{\mathrm{kep}} \sin i$, central velocity, v_0, and convolution width, σ, against time for [O I] 6300, [Ca II], Ca II, and Fe II] lines in the FEROS spectra against time of observation. Note the breaks in the x axis, which split the spectra by year of observation (1998, 2009, 2011 and 2015).

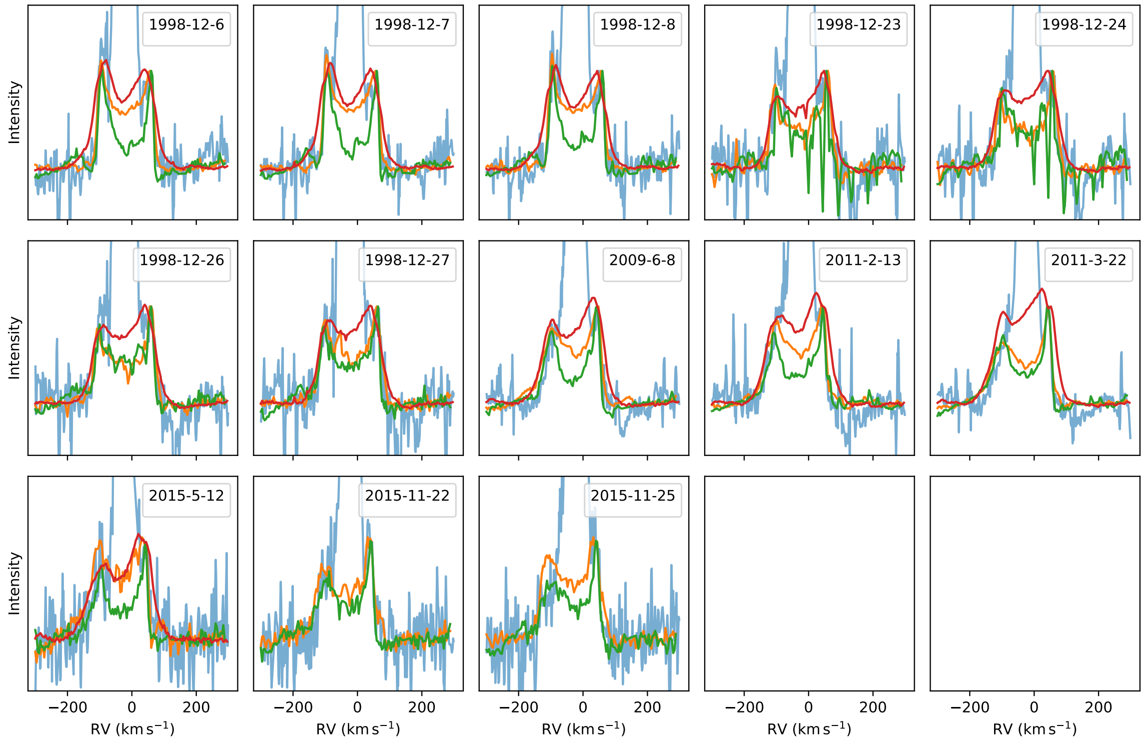

Figure 6.4: Overlay of the circumbinary emission lines in each of the FEROS spectra. [O I] 6300 Å is plotted in blue, Fe II] in orange, [Ca II] in green, and Ca II in red. The Fe II] lines have had the polluting Gaussians subtracted, and the Ca II have had the polluting H I profiles subtracted. The profiles have been normalised by the intensity of the blueshifted peak of the profiles, and are zoomed to focus on the inner circumbinary ring profiles.

It is clear from Figure 6.3 that there are two families of $v_{\rm kep} \sin i$ values. This indicates that there are two circumbinary rings; an inner ring, which is manifested in all studied emission lines, and an outer ring, which is only manifested in [O I]. This is in agreement with Maravelias et al. (2018). The measured $v_{\rm kep} \sin i$ values of the Fe II] and permitted Ca II emission are consistent with those of the inner ring of the [O I] and [Ca II] emission, and also the CO emission presented in Kraus et al. (2013). This indicates that these line components originate in the same circumbinary region.

Figure 6.4 displays the circumbinary emission profiles for each of the studied lines in each FEROS spectrum. The profiles have been processed such that the polluting Gaussian has been subtracted from the Fe II] emission lines, and the H I Paschen profiles have been subtracted from the Ca II lines. The emission line profiles have all been normalised by the red peak of the higher $v_{\rm kep}$ ring profile in Figure 6.4. The emission line profiles are remarkably similar and display the same evolution for all of the emission lines in the FEROS spectra, further indicating that these lines form in the same thin circumbinary region. The emission lines have slight evolution of V/R over the FEROS observations.

6.4.1 Average of fitted parameters

Table 6.1 lists the average values of the fitted ring parameters of all the line species for the inner and outer circumbinary rings. In Table 6.1 the average values of the fit parameters of the inner ring are quoted. The average $v_{\text{kep}} \sin i$ is calculated using all of the ring profiles arising in the inner ring. The average v_0 also takes into account the v_0 of the [O I] from the outer ring, such that it indicates the systemic velocity of the system using all circumbinary lines. The average σ only takes into account the inner ring's [O I], [Ca II], and Fe II], since the σ of the Ca II is considerably larger. Therefore the σ values of the [O I], [Ca II] and Fe II] lines observed by FEROS give the most representative σ of the inner ring.

From these circumbinary lines it is determined that the systemic velocity of the system is $-23.2 \pm 0.4\,\text{km}\,\text{s}^{-1}$.

6.4.2 Central velocity changes of the inner ring

The only fitted parameter to significantly change during observations is the v_0 of the inner ring's emission lines in the FEROS spectra. Figure 6.5 displays the average v_0 of each line from each year of observation separately, and also displays the average v_0 for all of the lines consisting of the inner circumbinary ring as a black point. The average v_0 for the inner ring in 1998 is $-21.2 \pm 0.1\,\text{km}\,\text{s}^{-1}$, whereas it is $-32.0 \pm 0.1\,\text{km}\,\text{s}^{-1}$ and $-34.5 \pm 0.1\,\text{km}\,\text{s}^{-1}$ in 2009 and 2011, and $-33.4 \pm 0.2\,\text{km}\,\text{s}^{-1}$ in 2015. The v_0 of the outer [O I] ring, on the other hand, is not significantly different throughout the observations, with a value of $-22.6 \pm 0.1\,\text{km}\,\text{s}^{-1}$ in 1998, $-23.8 \pm 0.3\,\text{km}\,\text{s}^{-1}$ in 2009, $-23.9 \pm 0.14\,\text{km}\,\text{s}^{-1}$ in 2011, and $-23.5 \pm 0.2\,\text{km}\,\text{s}^{-1}$ in 2015. The variability of the inner rings' v_0, and constancy of the outer ring's v_0, is reflected in the standard deviations of their constituent emission lines' v_0 values in Table 6.1; this leads to the outer [O I] ring making the strongest contribution to the average v_0 quoted in the bottom line of Table 6.1. Figure C.1, in the appendix, shows that the $v_{\text{kep}} \sin i$

Line	$v_{\rm kep}\sin i$ (km s^{-1})	v_0 (km s^{-1})	σ (km s^{-1})
Outer ring			
[O I]	27.3 ± 0.6	-23.0 ± 0.7	11.2 ± 0.4
Inner ring			
Fe II]	84.6 ± 3.5	-25.0 ± 7.2	11.7 ± 2.8
[O I]	82.6 ± 2.6	-23.0 ± 5.0	9.9 ± 0.4
[Ca II]	82.9 ± 1.9	-22.7 ± 6.3	6.6 ± 2.0
Ca II	85.1 ± 0.8	-24.0 ± 1.4	24.2 ± 2.1
Average	84.6 ± 1.0	-23.2 ± 0.4*	9.8 ± 0.7 **

Table 6.1: Average ring profile fit parameters to the different line species. $v_{\rm kep}\sin i$ is the fitted Keplerian velocity which has not yet been deprojected from the line of sight, v_0 the centre velocity, and σ the convolution Gaussian width. The values are the means of all the fit parameters in the different spectral observations weighted by the inverse fit uncertainties, and the errors are the standard deviations of the fitted parameters weighted by the inverse fit uncertainties. The average values of the inner ring's line species are shown. *The v_0 average takes into account the v_0 of the outer ring [O I]. ** The σ average of the inner ring does not take into account Ca II.

determined from the inner ring between 1998 and 2015 remains constant.

This pattern of the inner ring becoming more blueshifted over the FEROS observations is clear when circumbinary ring profiles of each line are averaged over all observations in a year. Figure 6.6 shows the circumbinary emission line profiles as observed by FEROS, with all spectra from the same year summed. In the $\sim$17 year time span of these observations, the higher velocity ring profile has become more blueshifted in each emission line. Correspondingly, there is some development in the shapes of the profiles, with the red peaks having higher intensity than the blue peak causing a decreasing V/R ratio. The bluemost edge of the profiles also become less steep over the observations. For the lower velocity ring of [O I] 6300, however, the profile and central radial velocity are unchanged between 1998 and 2015. It is verified that the v_0 shift of the inner ring is real, and not due to inconsistent wavelength calibrations, by removing the heliocentric velocity correction of the FEROS spectra and confirming that the telluric absorption features are at consistent wavelength. The relative drift between the central velocities of the [O I] and [Ca II] lines was also noted in Maravelias et al. (2018).

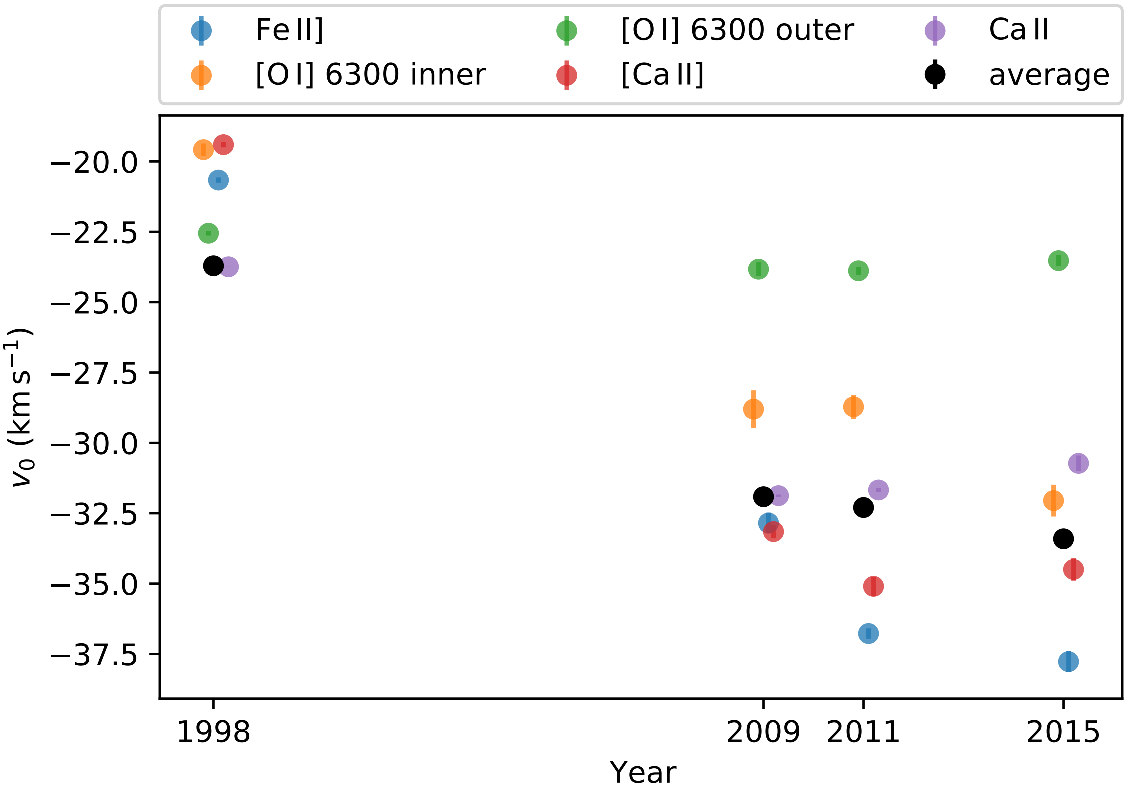

Figure 6.5: The changes in v_0 of the circumbinary rings as observed by FEROS. The fitted v_0 for each line species is averaged in the 1998, 2009, 2011, and 2015 spectra separately. Black points denote the average v_0 for the lines originating in the inner circumbinary ring.

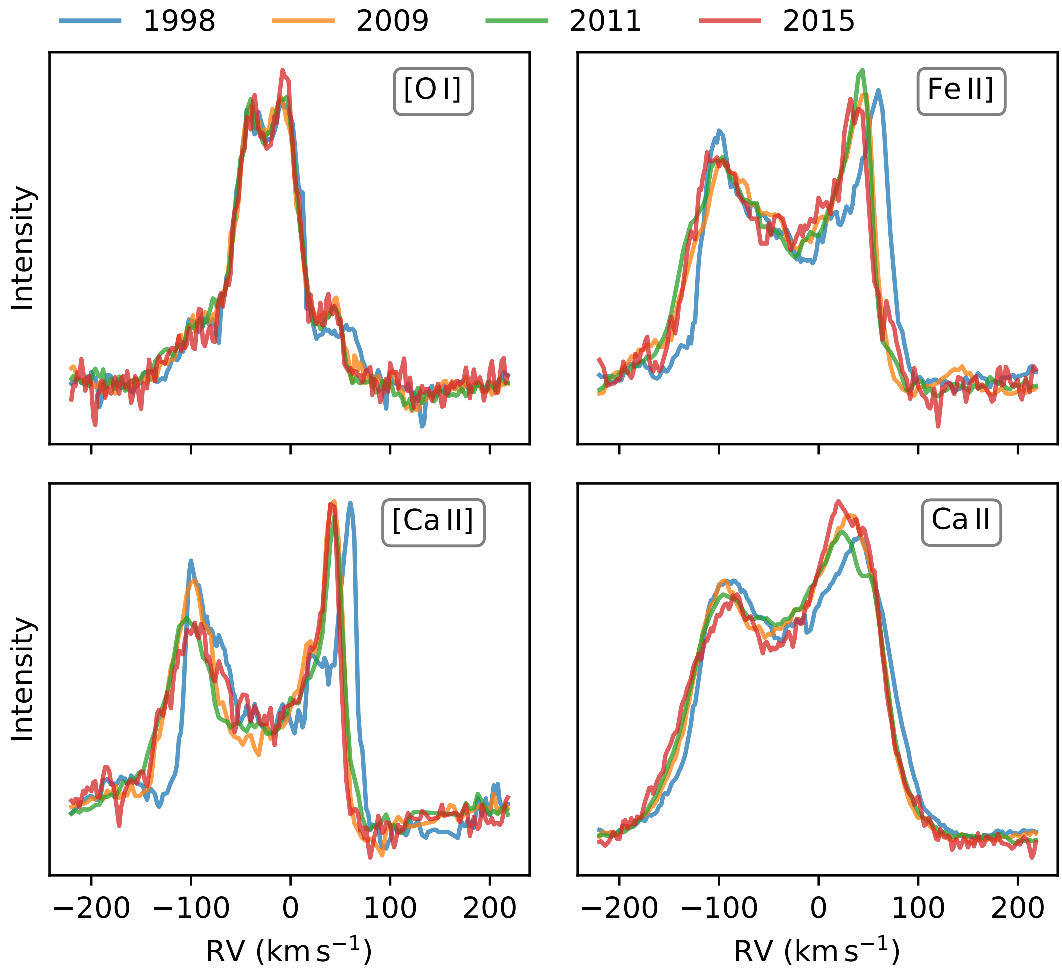

Figure 6.6: Summed circumbinary line profiles from FEROS, separating the spectra by year of observation. The Fe II] lines have had their polluting Gaussian components subtracted and the Ca II their polluting Paschen H I profiles subtracted before summation.

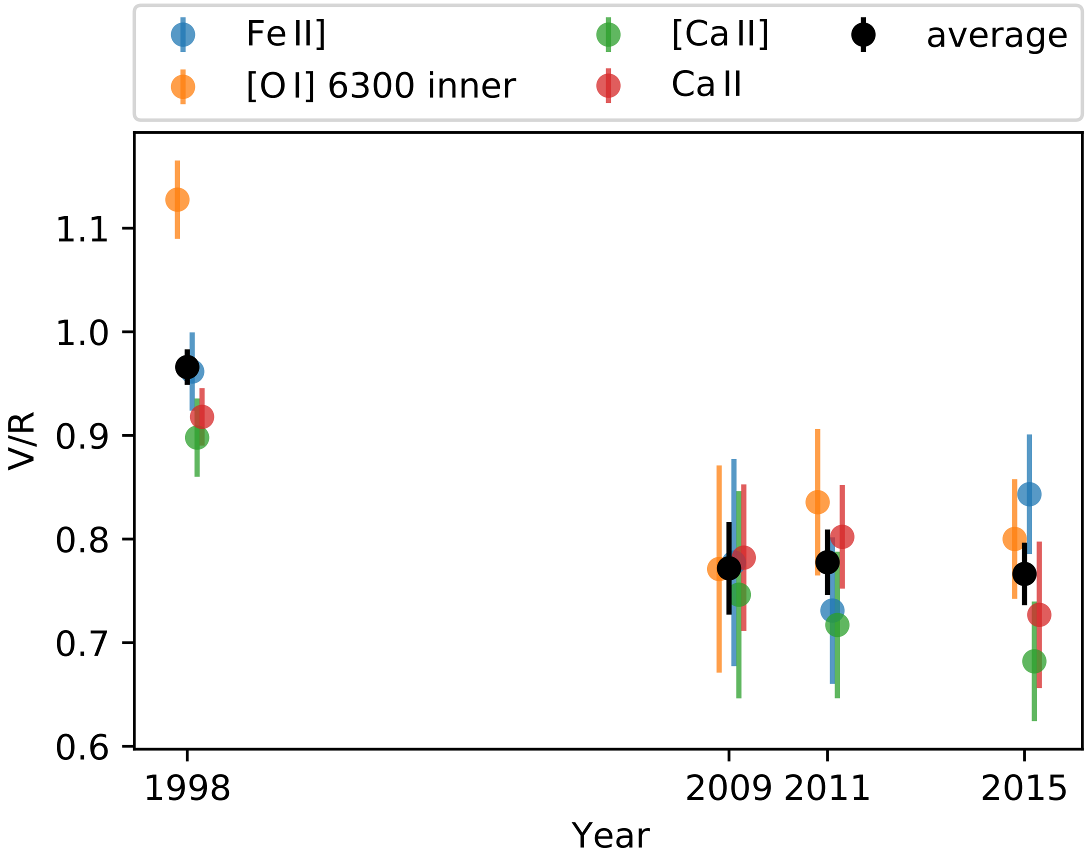

Figure 6.7: Same as Figure 6.5, except showing the evolution of the V/R of the double-peaked emission lines arising from the inner circumbinary ring, as observed by FEROS, in each year of observation. The black points denote the mean V/R values of all lines in a given year.

6.4.3 V/R variations

Figure 6.7 displays the V/R peak ratios for the emission lines that originate in the inner circumbinary ring, observed by FEROS, against observation year. The Fe II] and Ca II lines had the polluting Gaussian component and H I Paschen profiles, respectively, subtracted before calculating the V/R ratio. There is some slight variation in the V/R parameter for the lines with the values dropping over time for each line, indicating that the red peaks are getting stronger when compared to the blue peaks of the profiles. The varying V/R of the profiles over time may also be seen by eye in Figure 6.6.

Ring	$v_{\rm kep}\sin i$ (km s^{-1})	$v_{\rm kep}$ (km s^{-1})	R (AU)
Outer ring	27.3 ± 0.6	32^{+11}_{-4}	27^{+9}_{-10}
Inner ring	84.6 ± 1.0	98^{+33}_{-11}	$2.8^{+0.9}_{-1.1}$

Table 6.2: Measured projected orbital speeds ($v_{\rm kep}\sin i$), deprojected orbital speeds ($v_{\rm kep}$), and circumbinary ring radius (R). $v_{\rm kep}\sin i$ are the same values as in Table 6.1.

6.5 Discussion

For the higher $v_{\rm kep}\sin i$ lines listed in Table 6.1, their $v_{\rm kep}\sin i$ values agree with each other very well, therefore it can be inferred that these lines arise in the same radially thin circumbinary region about the binary. This is supported by Figure 6.4, which shows that all of the emission lines display remarkably similar circumbinary ring profiles throughout the FEROS observations. Therefore, in the upcoming analysis, the average values of $v_{\rm kep}\sin i$ will be considered for all lines in the upcoming calculations.

6.5.1 Radii of the circumbinary rings

In this analysis, the circumbinary disk inclination for the molecular ring of $60 \pm 20°$, which is informed by the disk studies of Borges Fernandes (2010) and Kraus et al. (2013), is used.

Table 6.2 lists the calculated deprojected orbital speeds and orbital radii of the circumbinary rings. They were calculated using Monte Carlo sampling, with 1 000 000 random Gaussian-distributed samples of $M_{\rm pr}$, $M_{\rm sec}$, i, and $v_{\rm kep}\sin i$ for both the inner and outer rings. $v_{\rm kep}\sin i$ are the average fitted Keplerian velocities to the ring profiles, and the values are taken from Table 6.1. For each sample, $v_{\rm kep}$ is calculated for each ring, and then the corresponding ring radius is calculated using the total enclosed mass of the binary and Equation 6.1. The median value of the parameter samples is taken as the best estimate value, and the difference of the median with the 84th and 16th percentiles is taken as the upper and lower uncertainties respectively. The closer ring has a radius of $R = 2.8^{+0.9}_{-1.1}$ AU from the binary, and the outer ring has $R = 27^{+9}_{-10}$ AU from the binary. As expected, the rings orbit slightly closer into the binary than as reported by Maravelias et al. (2018) due to the lower masses of the binary components reported in Chapter 4. These correspond to $\sim$4.7 and 45 semi-major axes of the binary, respectively. Marchiano et al. (2012) finds that the dust envelope begins at $\sim 230\,R_{\rm pr}$. Using $R_{\rm pr} = 27^{+9}_{-7}\,R_\odot$ from Chapter 4, this corresponds to the dust envelope radius of 29^{+10}_{-7} AU. This places the outer O I ring in a similar region to the inner edge of the system's dust envelope.

The σ parameters of the forbidden emission lines observed by FEROS shown in Table 6.1 indicate that the circumbinary emission originates in radially thin rings. The velocity resolution of FEROS is $\sigma_{\rm res} = c/R = 6.25\,{\rm km\,s^{-1}}$ and, with turbulent and thermal velocities, these can account for the majority of the measured σs of these lines. The permitted Ca II emission FEROS has a much larger σ than the forbidden emission lines. This may be due to the permitted emission originating in a more radially extended region than the forbidden emission, which require the correct conditions of density and temperature in order to be emitted. A very rough estimate can be made of the difference in radial width of the Ca II and forbidden emitting regions by comparing their relative σ values. σ is composed of multiple constituents, such that

$$\sigma^2 = \sigma^2_{\rm res} + \sigma^2_{\rm therm} + \sigma^2_{\rm turb} + \sigma^2_{\rm size}, \tag{6.4}$$

where $\sigma_{\rm res}$ is the spectral resolution of the observing instrument, $\sigma_{\rm therm}$ is the thermal broadening, $\sigma_{\rm turb}$ is broadening due to turbulence, and $\sigma_{\rm size}$ is broadening due to a finite radial width of the circumbinary rings. Assuming that $\sigma_{\rm therm} \approx \sigma_{\rm turb} \approx 1\,{\rm km\,s^{-1}}$, estimations can be made for $\sigma_{\rm size}$. If $\sigma_{\rm size}$ is then approximated as of the order of the orbital velocity difference between the inner and outer edge of a circumbinary ring, it can be shown that

$$\left(\frac{\sigma_{\rm size}}{\sin i}\right)^2 \approx \left(v^{\rm in}_{\rm kep} - v^{\rm out}_{\rm kep}\right)^2 = GM\,\frac{R_{\rm out} - R_{\rm in}}{R_{\rm in}R_{\rm out}} \approx GM\,\frac{\Delta R}{R^2}, \tag{6.5}$$

where $v^{\rm in}_{\rm kep}$ and $v^{\rm out}_{\rm kep}$ are Keplerian velocities of the inner and outer edges respectively, $R_{\rm in}$ and $R_{\rm out}$ are the radii of the inner and outer edges respectively, $\Delta R = R_{\rm out} - R_{\rm in}$, and R is the representative radius taken from the double-peaked Keplerian ring profile. ΔR is therefore the representative width of the ring. Using the average σ of the inner ring's forbidden emission (from the bottom line of Table 6.1) gives $\Delta R = 0.02 \pm 0.01$ AU, whereas using the σ of the permitted Ca II emission gives $\Delta R = 0.2 \pm 0.1$ AU. It must be noted that, since it originates from permitted transitions, the Ca II emission may suffer some self-absorption and re-emission which may also be a contributing factor to its larger σ. Additionally, this method only yields very rough estimates for the relative radial widths of the rings.

6.5.2 Limits on precession of the circumbinary ring's inclination

Test particles' orbits in circumbinary trajectories are expected to precess about the inner binary in inclination and longitude of ascending node, dependent on the mass ratio, eccentricity, and separation of the binary (Doolin & Blundell 2011). The same precession occurs in hydrodynamic circumbinary disk simulations; however, the amplitude of the disks' precession becomes damped over time and the inclination and longitude of ascending node reach a steady state (Martin & Lubow 2017, 2018, 2019; Smallwood et al. 2019).

For the thin circumbinary rings, precession in the inclination of their orbits to the line of sight would be observed as variations in the measured $v_{\text{kep}} \sin i$ and the splitting of the peaks of the emission line profiles as the inclination and longitude of ascending node of the ring varies around the binary. There are no signs any significant variations in the fitted $v_{\text{kep}} \sin i$ over the FEROS dataset. Given $v_{\text{kep}} \sin i = 84.6 \pm 1.0\,\text{km}\,\text{s}^{-1}$ for the inner ring, the changes to the inclination of the inner circumbinary ring's orbit to the line of sight may be limited to $\lesssim 7°$, assuming an inclination of $\sim$60° over the observational period.

6.5.3 An eccentric ring?

The changes in v_0 observed in the inner circumbinary ring, described in Section 6.4.2, between 1998 and 2015 data are unusual, since a circumbinary disk is expected to have a constant systemic velocity equal to that of the centre of mass of the system. The ring cannot be circumstellar, since its v_{kep} value and the individual masses of the binary components imply a ring radius that is greater than the orbital separation of the binary, by Equation 6.1. Therefore, the v_0 change cannot be a reflection of the binary orbit.

Presuming that the circumbinary ring cannot have a true bulk velocity difference to the centre of mass of the system, and the constant v_0 of the outer ring observed in [O I] implies that centre of mass velocity of the system is unchanged, a change in v_0

implies that circular symmetry of the inner circumbinary ring has been broken over the course of the FEROS observations. An axisymmetric ring orbiting the centre of mass will have the same central velocity at the centre of mass, and will lead to a symmetric and constant profile, which is clearly not observed.

Two effects may lead to a loss of circular symmetry in the circumbinary rings: either overdensities are present in the ring, or the circumbinary ring is eccentric. With only a few epochs of observation of the FEROS spectra, it is difficult to determine exactly which process is occurring in the circumbinary ring. However, eccentricities are expected to be excited in circumbinary disks due to interaction with the binary (Lubow & Artymowicz 2000), and hydrodynamic simulations of circumbinary disks consistently show that this is the case, and furthermore that their eccentricities may even be caused to oscillate (e.g. Papaloizou et al. 2001; Pierens & Nelson 2013; Dunhill et al. 2015; Lines et al. 2015, 2016; Fleming & Quinn 2017; Thun et al. 2017). The densities of these simulated eccentric disks are higher at apastron. Therefore, in GG Car, the varying v_0 and V/R of the inner circumbinary ring lines may indicate that the binary has pumped the eccentricity of the ring.

Figure 6.8, top panel, displays a simple model of what changes in line profiles may be expected if eccentricities are pumped in a thin circumbinary ring. For a range of eccentricities, the orbital velocity amplitude and argument of periastron are kept constant at $84.6\,\mathrm{km\,s^{-1}}$ and $180°$, respectively. The assumption is made that the material in the thin, eccentric ring emits equal intensity at each mean anomaly interval in its orbit. The higher velocity peak, at periastron, is less intense since the material spends less time at periastron due to the higher orbital speeds. Higher eccentricities cause the central velocity to shift away from 0 and for the V/R ratio to lower. Interestingly, the peak-to-peak splitting remains near constant for the different eccentricities. This mirrors the variations that are observed in the emission lines which arise in the inner circumbinary ring (Figure 6.6). Changes in the argument of periastron, ω, of an eccentric disk may also lead to the variations of v_0 and V/R observed in the inner ring. This is displayed in the bottom panel of Figure 6.8. Here, eccentricity is held constant at 0.1, and ω is varied from 0–270°.

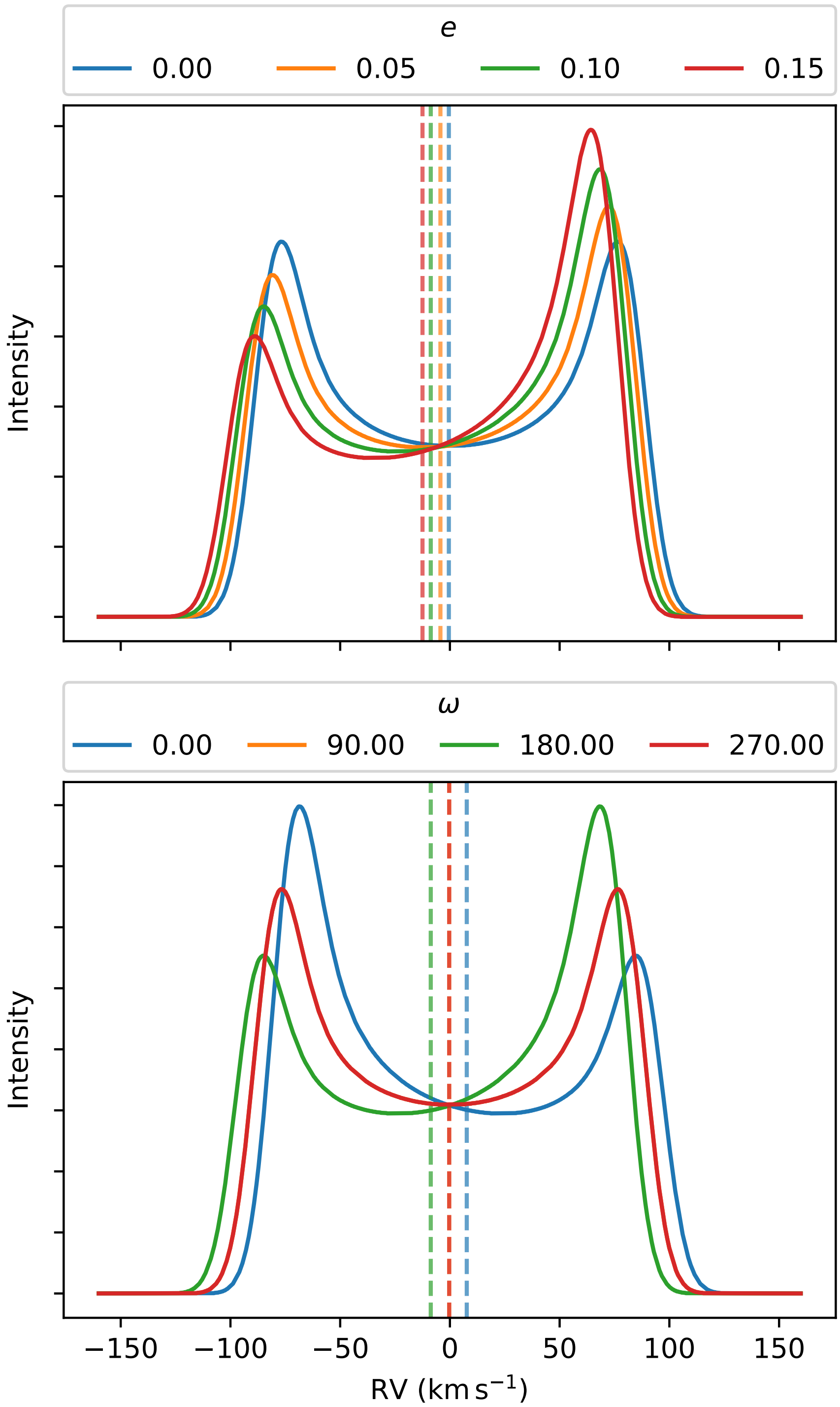

Figure 6.8: Effect of varying eccentricity, e (top panel), and argument of periastron, ω (bottom panel), of a circumbinary ring on the observed emission line profile. The amplitude of the rings are kept constant at $84.6\,\mathrm{km\,s^{-1}}$, and the profiles are convolved with a Gaussian of width $9.8\,\mathrm{km\,s^{-1}}$. ω in the top panel is kept constant at $180°$, and e in the bottom panel is kept constant at 0.1. Vertical dashed lines with a matching colour of a model indicate the mid-point between the two peaks of the given model. Note that the line profiles for $\omega = 90°$ and $\omega = 270°$ are identical.

Thun et al. (2017) finds a precession period of eccentric circumbinary orbits of

$$T_{\rm prec} = \frac{4}{3}\frac{(q+1)^2}{q}\left(\frac{R}{A}\right)^{7/2}\frac{(1-e_{\rm d}^2)^2}{\left(1+\frac{3}{2}e^2\right)}P, \tag{6.6}$$

where $T_{\rm prec}$ is the precession period, q is the binary mass ratio $M_{\rm sec}/M_{\rm pr}$, R is the circumbinary ring's semi-major axis, A is the binary semi-major axis, e is the binary eccentricity, $e_{\rm d}$ is the eccentricity of the orbiting material, and P is the binary orbital period. The eccentricity of the ring about GG Car is currently unknown, but entering the binary orbital parameters gives a precession period of ~ 1200 binary orbits if $e_{\rm d} \approx 0$ (which gives the longest precession timescale). The difference in time between the 1998 and 2015 observation periods corresponds to about 200 binary orbits. As a comparison, using Equation 6.6, the precession rate for the outer [O I] ring would be $\sim 6 \times 10^6$ binary orbits. It therefore follows that we would not be able to detect any significant dynamical changes in the outer ring over the FEROS observation period of $\sim$200 binary orbits. However, the FEROS observations do cover a significant portion of the expected precession period of the inner circumbinary ring.

6.5.4 Circumbinary ring simulation

To test whether the observed v_0 and V/R changes of the emission lines arising in the inner circumbinary ring could be due to the binary inducing eccentricity in the inner circumbinary ring, the binary and ring system is simulated using the smoothed particle hydrodynamic (SPH) code `PHANTOM` (Price et al. 2018). `PHANTOM` has been used widely in the literature to study the dynamics of circumbinary disks.

The binary stars are simulated as sink particles with the masses and orbital parameters reported in Chapter 4, and given in Table 3.4. The circumbinary ring is simulated as initially thin, circular and coplanar, with an initial radius of 2.8 AU from the centre of mass of the binary. The simulated ring has an initial radial width of 0.01 AU; it was found that the ring spreads radially slightly near the beginning of the simulation as a steady state was reached, and this initial width led to a steady-state radial width of $\sim$0.2 AU which roughly matches the inferred width of the Ca II emitting region (the extent of this radial spreading is dependent on the initial H/R value, and is discussed further in Appendix C.2.2). Due to the very thin extent of the ring, the choices of the initial surface density and temperature power laws choices bear negligible effect on the simulation. The ring has an initial mass of $5 \times 10^{-9}\, M_\odot$

Binary parameters	
M_{pr}	$24\,M_{\odot}$
M_{sec}	$7.2\,M_{\odot}$
a_{bin}	$0.61\,\mathrm{AU}$
e_{bin}	0.5
Ring parameters	
R_{in}	$2.8\,\mathrm{AU}$
R_{ref}	$2.805\,\mathrm{AU}$
R_{out}	$2.81\,\mathrm{AU}$
M_{disk}	$5 \times 10^{-9}\,M_{\odot}$
$H/R(R = R_{\mathrm{ref}})$	0.001
α_{SS}	0.005
N_{part}	100 000

Table 6.3: The "fiducial" parameters for the circumbinary ring simulation in PHANTOM.

distributed evenly between 100 000 SPH particles. The Shakura & Sunyaev (1973) viscosity, α_{SS} is set to 0.005; while this choice leads to a low artificial viscosity value of $\alpha_{\mathrm{AV}} = 0.044$, it is acceptable for this simulation since the gas does not experience any strong shocks and it has the benefit of avoiding artificial evolution of the ring (Meru & Bate 2010). In Appendix C.2.3 it is shown that large changes in α_{SS}, and therefore by extension α_{AV}, bear little effect on the simulation output leading us to conclude that this is a safe value for α_{SS} given the aim of the simulation and its initial conditions. The default β artificial viscosity value $\beta_{\mathrm{AV}} = 2$ is used. Table 6.3 displays the parameters of the simulation presented in this study. The evolution of the circumbinary ring is calculated over 4000 binary orbits.

Figure 6.9 displays a schematic of the simulation geometry. In this figure, the orbit of the primary and secondary stars in the x-y plane are displayed by the blue and orange ellipses, respectively. The orbit of the circumbinary ring is displayed by the green ellipse. All orbits are in the anti-clockwise direction. The eccentricity vector of each SPH particle in the ring is calculated and the mean of each component is taken, giving the eccentricity vector of the ring, $\boldsymbol{e}_{\mathrm{av}}$. The eccentricity of the ring, $e = |\boldsymbol{e}_{\mathrm{av}}|$. The argument of periastron of the ring, ω, is calculated as the angle between $\boldsymbol{e}_{\mathrm{av}}$ and the eccentricity vector of the primary star of the binary, $\mathbf{e}_{\mathrm{bin}}$, in the anti-clockwise (prograde) direction. The direction of $\mathbf{e}_{\mathrm{bin}}$ is denoted by the blue arrow and the direction of $\boldsymbol{e}_{\mathrm{av}}$ is denoted by the green arrow. Chapter 4 determined the argument of periastron of the primary star, $\omega_{\mathrm{bin}} = 339.87°$ to the plane of the sky; this allows us to define a direction towards Earth along which we can project velocities to calculate the radial velocities that would be observed from the Earth. The plane of the sky direction is denoted by the red arrow, and the direction to Earth is the black arrow in Figure 6.9.

Figure 6.10 displays the evolution of e and ω of the circumbinary ring over simulation time. The ring displays oscillations of e and ω, similar to those that have been observed in the previously mentioned studies of simulations of circumbinary disks. The eccentricity of the ring varies between $\sim 0-0.12$ with a period of ~ 1040 binary orbits. ω varies gradually from $\sim 100-250°$, but jumps back to $100°$ when $e \approx 0$. Lubow & Artymowicz (2000) predict the rate of change of eccentricity, $\dot{e}$, of a circumbinary disk about an unequal mass eccentric binary to grow as

$$\dot{e} = \frac{15}{16} e_{\rm bin}\, \mu(1-\mu)(1-2\mu) \left(\frac{a_{\rm bin}}{R}\right)^3 (1-e^2)^{-2} \sin\omega, \tag{6.7}$$

where $e_{\rm bin}$ is the eccentricity of the binary, $\mu = M_{\rm sec}/(M_{\rm pr} + M_{\rm sec})$, $a_{\rm bin}$ is the semi-major axis of the binary, R is the semi-major axis of the circumbinary ring's orbit.[1] The relationship in Equation 6.7 between $\dot{e}$ and ω is reproduced remarkably well in the simulation, as displayed in Figure 6.10: at minimum eccentricity, ω is undefined. As the disk first becomes eccentric, $\omega \approx 100°$, meaning $\sin\omega > 0$ and $\dot{e}$ is positive, leading the eccentricity to grow. As ω increases and passes $180°$, $\sin\omega$ becomes negative and e begins to decrease. ω continues to increase until $e \approx 0$, at which point ω is again undefined and the process starts again.

Emission line profiles which could be expected from the circumbinary ring are calculated by projecting the velocities of the SPH particles along what would be the line of sight to Earth, demonstrated in Figure 6.9, where the argument of periastron of the binary is $\omega_{\rm bin} = 339.87°$ to the plane of the sky. The projected velocities are multiplied by $\sin(60°)$ to account for the inclination of the disk. The radial velocities of the SPH particles are histogrammed and convolved with a Gaussian of width $6.25\,{\rm km\,s^{-1}}$, which is the resolution of FEROS. Figure 6.11 displays simulated line profiles corresponding to the times denoted by dashed vertical lines in Figure 6.10. The colour of the vertical line corresponds to the simulated profile in Figure 6.11.

[1] Note that Equation 6.7 is multiplied by -1 compared to the Equation 2 of Lubow & Artymowicz (2000); this is because we are measuring ω relative to the eccentricity vector of the primary, whereas Lubow & Artymowicz (2000) measure it from the eccentricity vector of the secondary. These are, by definition, $180°$ from each other, therefore $\sin(\omega + 180°) \rightarrow -\sin\omega$.

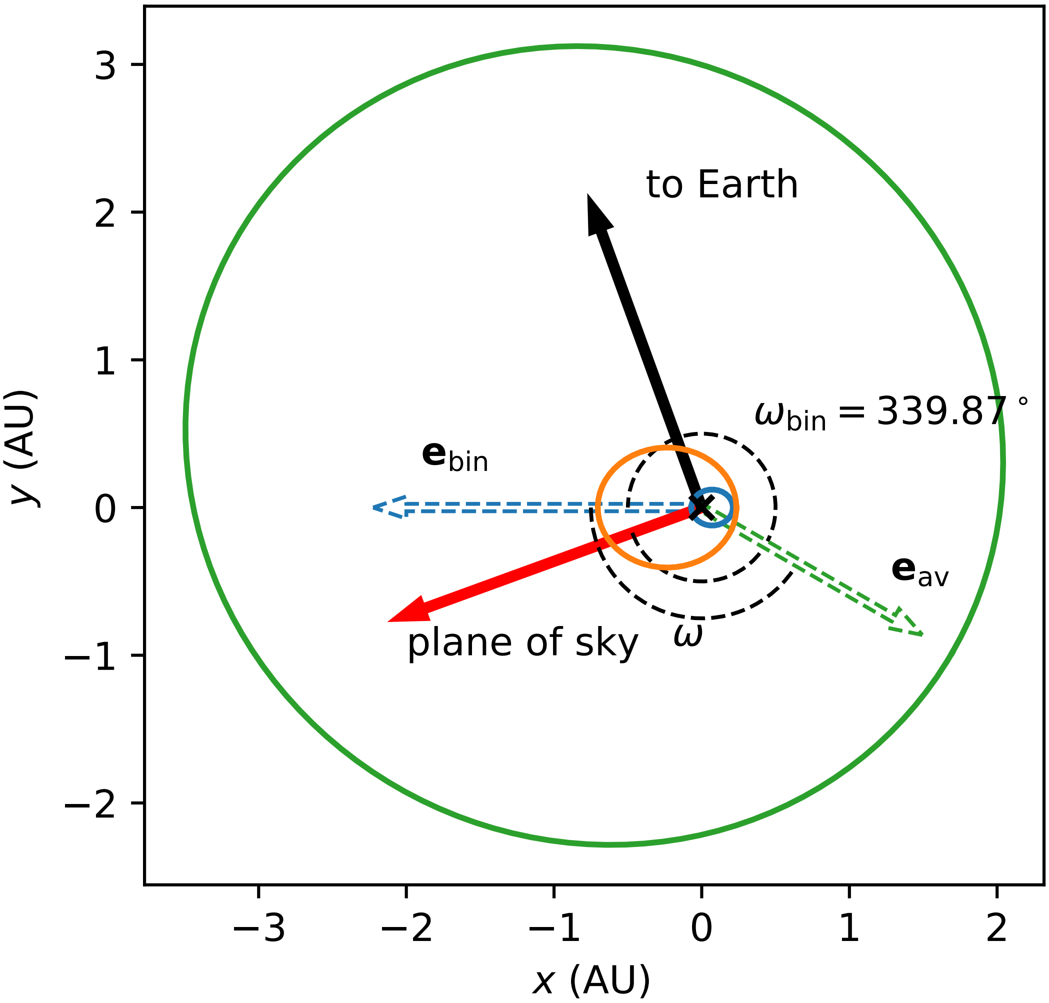

Figure 6.9: Schematic of the PHANTOM SPH simulation geometry in the x-y geometrical plane. The blue ellipse represents the orbit of the primary star, the orange ellipse the orbit of the secondary star, and the green ellipse the orbit of the circumbinary ring at a particular instant. All three of the orbits are anti-clockwise in this schematic. The eccentricity of the ring is exaggerated in this schematic. A black cross denotes the centre of mass at $(0, 0)$. A blue arrow denotes the direction of the primary star's eccentricity vector, $\mathbf{e}_{\rm bin}$, and the green arrow denotes the direction of the circumbinary ring's eccentricity vector, $\mathbf{e}_{\rm av}$, at this particular point in the simulation. The angle from $\mathbf{e}_{\rm bin}$ to $\mathbf{e}_{\rm av}$ in the anti-clockwise direction defines ω, the argument of periastron of the circumbinary ring. To project the velocities to the line-of-sight that would be seen from Earth, the argument of periastron of the primary star found in Chapter 4, $\omega_{\rm bin} = 339.87^\circ$, is utilised; this defines the angle between $\mathbf{e}_{\rm bin}$ and the plane of the sky. The plane of the sky direction is denoted by a red arrow, and the would-be line-of-sight to Earth is denoted by a black arrow.

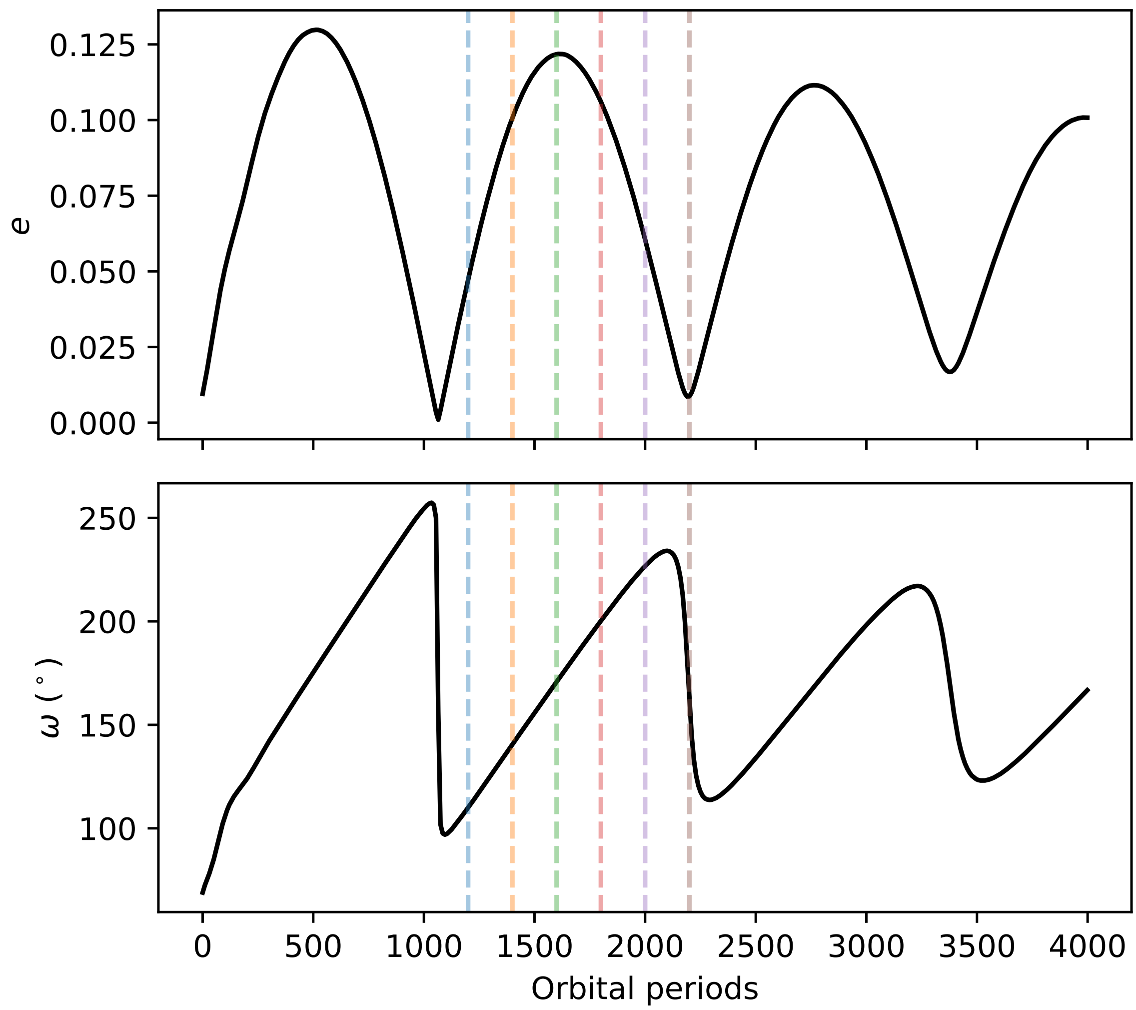

Figure 6.10: Eccentricity, e, and argument of periastron, ω, of the simulated circumbinary ring against time in units of binary orbital period. ω is measured relative to the binary's argument of periastron, which is defined to be 0°. Vertical lines denote the times of the simulated emission line profiles in Figure 6.11, with the colours of the lines matching the colours of the corresponding simulated profiles in that figure.

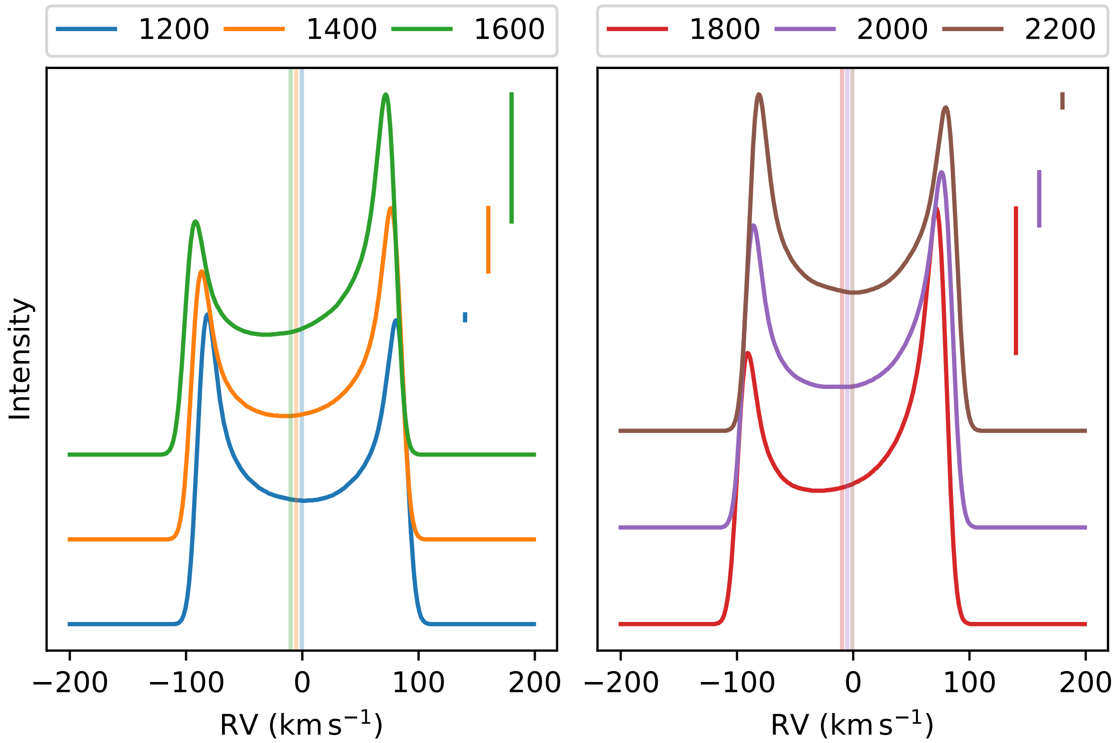

Figure 6.11: Simulated emission line profiles expected from the circumbinary ring at different times in the simulation. The simulation time of each profile is given in the legend, in units of binary orbital periods. These times are denoted by vertical lines in Figure 6.10, with the colors of the vertical emission lines matching its corresponding vertical line in that Figure. The velocities of the ring particles are projected such that these are the line profiles that would be observed from Earth defining the argument of periastron of the binary, $\omega = 339.87°$, relative to the plane of the sky and inclination 60°. Vertical lines to the right of the profiles indicate the difference in intensity between the red peak and the blue peak of a given profile. The lines are slightly vertically offset for clarity.

The second oscillation period is focused on to allow the simulation to reach a pseudo-steady state. The left panel shows the line profiles as the circumbinary ring becomes more eccentric, and the right panel shows the lines as the ring becomes less eccentric. The profiles are vertically offset for clarity. Vertical lines to the right of the profiles show the difference in intensity between the blueshifted peak and the redshifted peak of a given profile. The time spacing between the profiles presented is 200 binary orbits, which was chosen since this is roughly the time difference between the first and last FEROS observation.

Once projected along the line-of-sight that would be observed from Earth, the oscillations in eccentricity of the circumbinary ring lead to the blueshifted peak becoming less intense than the redshifted peak while the eccentricity increases, then while the eccentricity decreases the profile returns to a symmetric profile with peaks of equal intensity. The centre of the profile also shifts slightly towards negative RV while the eccentricity is increasing, returning to the centre as eccentricity decreases. The profile at 1200 binary orbital periods, in the left panel of Figure 6.11, is symmetric despite the ring being slightly eccentric at this time ($e \sim 0.046$); this is because $\omega \sim 110°$ at this time in the simulation, meaning that $\mathbf{e}_{\rm av}$ is along the line of sight to Earth, making the simulated line profile symmetric about $0\,{\rm km\,s^{-1}}$. The peak-to-peak splitting of the simulated profiles remains roughly constant throughout the oscillation cycle. The variability of the simulated emission lines in the case of increasing eccentricity closely resembles what is observed in the real circumbinary emission lines as observed by FEROS, and most clearly displayed in Figure 6.6; over the FEROS observations, the blueshifted peak of the inner circumbinary ring profiles becomes less intense compared to the redshifted peak, and the centre of the profile shifts slightly to the blue whilst the peak-to-peak splitting remains constant.

The variations in v_0 and $v_{\rm kep}\sin i$ of the simulated emission line profiles are quantified by fitting them in an identical manner to the real line profiles as described in Section 6.3. The fit results are displayed in Figure 6.12, along with the calculated V/R ratio, in the bottom panel. Figure 6.12 shows that it takes ∼500 binary orbits for the circumbinary ring to reach a pseudo-steady state. The simulated line profiles are noiseless, which leads to more precise parameters results from the fitting than the real spectra. Figure 6.12 shows that, using the assumption of an axisymmetric ring, the inferred systemic velocity v_0 varies between $\sim 0 - -10\,{\rm km\,s^{-1}}$ compared with the centre of mass of the system. $v_{\rm kep}\sin i$ displays slow, stochastic changes, with its value generally decreasing over the simulation time. V/R varies between ∼1 when the ring is circular, and ∼0.65 when the ring is most eccentric. This clearly demonstrates that the effects observed in the FEROS data, of decreasing v_0 and V/R but constant $v_{\rm kep}\sin i$, may be caused by eccentricity oscillations in the inner circumbinary ring.

Although the overall magnitudes of the v_0 and V/R changes, displayed in Figure 6.12, match that which are observed in the FEROS spectra (Figures 6.5 and 6.7), the FEROS data makes these changes in ∼200 binary orbits; for the simulated profiles, it takes ∼550 binary orbits for v_0 to change from $0\,{\rm km\,s^{-1}}$ to $-10\,{\rm km\,s^{-1}}$. In Appendix C.2.5 it is shown that, in agreement with previous work (e.g. Lubow & Artymowicz

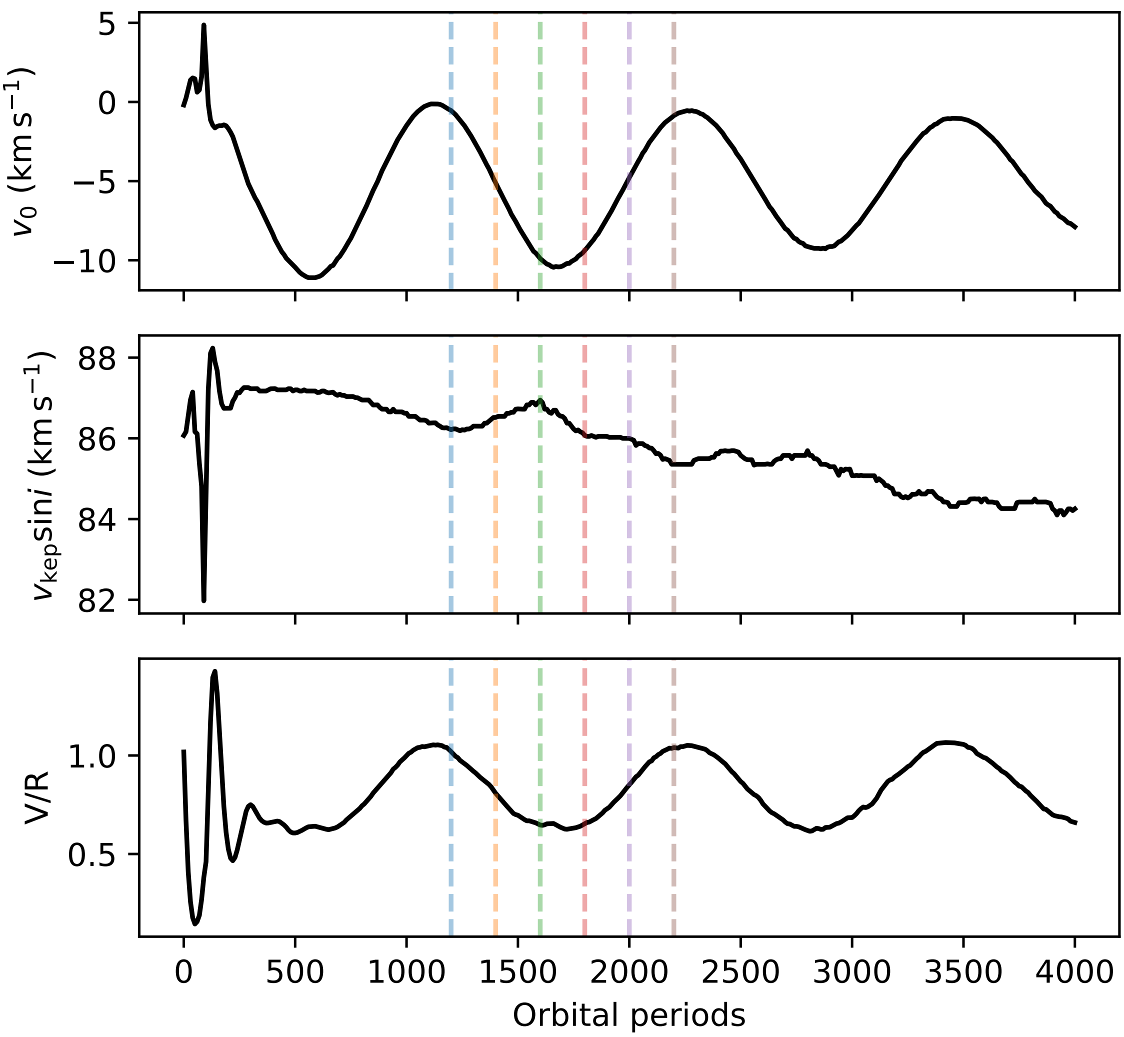

Figure 6.12: Results of fitting circular, symmetric ring profiles to the simulated line profiles in an identical way to the real spectra plotted against simulation time. v_0 is presented in the top panel, fitted $v_{\rm kep} \sin i$ is presented in the middle panel, and V/R ratio is presented in the bottom panel. Vertical lines correspond to the same profiles as shown in Figure 6.11, with the colors of the lines matching the color of the simulated profiles.

2000; Thun et al. 2017), the timescale of this eccentricity oscillation is strongly dependent on the simulated circumbinary ring's initial orbital radius and that the timescale of eccentricity oscillation is much reduced with even a marginally smaller simulated initial radius. Given the large fractional error of the observed circumbinary ring's radius, this leads to a correspondingly large range of allowed oscillation timescales. In Appendix C.2.5, it is found that the allowed circumbinary ring radii determined from the FEROS spectra may allow eccentricity oscillation periods in the range from $\sim$600 − 4000 binary orbital periods.

Similarly, there are considerable uncertainties associated with binary's parameters which would affect the simulation. Most notably are the mass ratio of the binary components ($\mu = 0.23 \pm 0.06$), separation ($a = 0.61 \pm 0.03\,\mathrm{AU}$) and the inclination of the binary and circumbinary orbit ($i = 60 \pm 20°$). According to Equation 6.6, the uncertain separation and mass ratio of the components will affect the timescale of the precession. The uncertain inclination, on the other hand, will affect the amplitude of the inferred v_0 variations as a lower inclination will diminish the radial velocity differences. The argument of periastron of the primary star is well constrained in Chapter 4 ($\omega_{\mathrm{bin}} = 339.87^{+3.10}_{-3.06}\,°$), and it is the argument of periastron which determines the axis of eccentricity oscillations. This therefore means that the overall pattern of the emission line profile changes and associated v_0 variability are captured to a good degree, even if the period of the variations or their amplitude are not fully reproduced.

In Appendix C.2 I additionally investigate the effect of varying the ring's mass, the ring's artificial viscosity, initial H/R, and simulation resolution compared to the "fiducial" simulation of Table 6.3. It is found that the ring's mass and artificial viscosity bears very little effect on the simulation results. A larger initial H/R value causes the ring to spread further radially before reaching a steady state, decreasing the radius of the inner edge of the ring and therefore also decreasing the oscillation time. Varying H/R does not affect the qualitative conclusions of this study. I therefore conclude that the SPH simulations are robust against the specific values of the various input parameters, with common behaviour which resembles the behaviour observed in GG Car existing across all plausible input ranges.

This shows that the variations observed in the emission line profiles originating in the inner circumbinary ring of GG Car could feasibly and plausibly be caused by the excitation of the eccentricity of the ring, and that eccentricity pumping can be expected to occur over the FEROS observation timescales given the binary's orbital solution and the radius of the inner circumbinary ring. Given this paradigm, it appears that FEROS observed GG Car as its ring was becoming more eccentric, observing just a part of an eccentricity pumping period. This scenario could be confirmed by further high-resolution observations of GG Car, which may observe the profiles becoming symmetrical and the v_0 of the lines returning to the systemic velocity of the system. Should a full cycle of symmetric emission line profiles, to negative v_0 and $V/R < 1$, and back to symmetry be observed within a period of $\sim 600 - 4000$ binary orbital periods ($50 - 300$ years), this would give very strong evidence for eccentricity oscillations occurring in the circumbinary ring of GG Car.

6.5.5 Other causes of variability

The loss of circular symmetry leading to variations in the circumbinary ring profiles could plausibly be caused by other means, such as dissipation of the ring leading to overdensities. Dissipation of circumbinary disks is expected due to strong illuminating radiation from the binary (Alexander 2012). Other potential causes of overdensities occurring in the ring could be interaction of the ring with the wind of the primary, or reaccretion of part of the ring back onto the binary in the interim time between the two observation periods.

Should the variations be due to overdensities, these could be expected to orbit the binary, leading to variations. At the inner ring's orbital radius, and with the masses of the binary, the orbital period of the ring is 310^{+140}_{-170} days (~ 10 binary orbital periods), therefore variations may be expected at this period if orbiting overdensities were present.

Given the relative constancy of the circumbinary ring profiles between 2009–2015, it follows that the variations would be more likely to be due to eccentricity oscillations than orbiting overdensities, due to the longer timescale of the former process. As mentioned in the previous section, more epochs of high-resolution observation would be able to more accurately determine the variations of the circumbinary ring, and to be able to discriminate definitively between a scenario of eccentricity oscillations or orbiting overdensities.

6.6 Conclusions

I have presented high resolution FEROS optical spectra of the B[e]SG binary GG Car, investigating its emission lines which arise from the circumbinary environments of the system. I find, in agreement with Maravelias et al. (2018), that there are two concentric circumbinary rings which are manifested in GG Car's atomic emission line profiles. I have discovered that semi-forbidden Fe II] and permitted Ca II emission are formed in the inner circumbinary ring along with [O I], [Ca II], and CO emission. This is the first reported observation of permitted transition lines being observed to exhibit the ring profiles typical of forbidden emission in B[e]SGs. The outer ring is only manifested in [O I] emission.

The inner ring has a projected orbital speed $v_{\rm kep} \sin i = 84.6 \pm 1.0\,{\rm km\,s^{-1}}$, and the outer ring has $v_{\rm kep} \sin i = 27.3 \pm 0.6\,{\rm km\,s^{-1}}$. Using the updated binary masses of Chapter 4, and a disk inclination of $60 \pm 20^{\circ}$, it is found that the radii of the circumbinary rings are $2.8^{+0.9}_{-1.1}$ AU and 27^{+9}_{-10} AU for the inner ring and outer ring respectively. Using the circumbinary disk lines, the systemic velocity of the system is determined to be $-23.2 \pm 0.4\,{\rm km\,s^{-1}}$.

There is no significant variability in the measured $v_{\rm kep} \sin i$ of the emission lines over $\sim$20 years of observations, indicating that the radii and inclination of the circumbinary rings are constant over this timescale. The width of the Gaussian used to convolve the disk profile for the permitted Ca II emission is significantly larger than for the forbidden emission lines; this implies that the emitting region of the Ca II emission may have a larger radial width than the forbidden emission.

The inferred systemic velocity, v_0, from the inner circumbinary ring becomes more blushifted over the FEROS observations, and the V/R ratio of the double peaked profiles drops. This indicates dynamical change of the ring's orbit and a breaking of circular symmetry. I have simulated the inner circumbinary ring using the SPH code `PHANTOM`, observing that the binary can be expected to excite oscillations of the ring's eccentricity over timescales similar to the FEROS observations. The variations observed in the inner circumbinary ring's emission lines observed by FEROS are consistent with the variations expected due to these eccentricity oscillations in the case that the observations were taken whilst the eccentricity is rising, given the orientation of the system.

Further high-resolution observations are needed to understand the cause of variability in the inner circumbinary ring of GG Car. If the ring profiles were to return to a symmetric profile with a timescale $600-4000$ binary orbital periods would give exceptional evidence to eccentricity oscillations occurring in the ring. On the other hand, cycles at $\sim$320 days may indicate that gaps in the circumbinary ring are present and their orbits about the binary cause the observed variability. It is predicted that the former scenario is more likely, given the relative lack of variability in the emission line profiles between 2009 and 2015.

It remains a mystery how these thin, circumbinary rings may be remarkably stable over the observation times given their proximity to the luminous primary star which hosts a powerful stellar wind. Further work needs to be done in order to understand the origin of these remarkable structures in B[e]SGs. I have shown that, for the B[e]SGs that are in binaries, the time-varying gravitational potential of the binary may lead to observable dynamical effects in their circumbinary rings.

Chapter 7

Conclusion

Abstract

In this conclusion chapter I discuss, in the context of this thesis, some further time-series analysis which may be undertaken to further understand the B[e]SG phenomenon. I present a preliminary photometric study with TESS and ASAS-SN time-series data to compare the phenomena reported in GG Car with other confirmed B[e]SGs of the Milky Way. I find very strong evidence for binarity in one of the B[e]SGs (CPD-57 2874), which shows an eclipsing binary lightcurve. This object has not been considered to be a binary in the literature. There are signatures of binarity for two more objects (CPD-52 9243 and MWC 137) which likewise have not been considered to be binaries. This increases the number of confirmed Galactic B[e]SGs which are confirmed or suspected binaries from 4/9 to 7/9. This has implications for the role that binarity plays in the displaying of the B[e]SG phenomenon. Furthermore, signatures of pulsations at timescales similar to the observed short-period variability of GG Car are detected in two of the confirmed B[e]SGs, indicating that this may be a more common feature in the class than previously thought. These findings indicate the power that time-series observations and analysis hold in the understanding of the B[e]SGs. I then provide a summary of this thesis, and leave the reader with some final words.

7.1 Future work: time-series studies of B[e] supergiants

The most vital future work to build on this thesis is to compare the unusual phenomena reported in GG Car to the other confirmed B[e]SGs to see if a consistent picture of the stellar class may be built. This thesis has shown the power of studying these objects with time-series observations, and therefore future studies of B[e]SGs should also use these methodologies to their fullest extent. This section takes a quick look at the time-series photometry of the Galactic B[e]SGs to place GG Car in the context of this population sample.

This preliminary study of the population sample of B[e]SGs focuses on the confirmed Galactic B[e]SGs listed in table 9 of Kraus (2019), of which there are 9 specimens. Only four of these B[e]SGs are noted to be “confirmed or suspected binaries”. I obtained TESS lightcurves of all 9 confirmed objects by reducing FFI data using `eleanor` (Feinstein et al. 2019) in the same manner as the lightcurve of GG Car presented in Chapter 3.2.2. The resulting lightcurves are presented in Figure 7.1. Good quality lightcurves were not obtained for AS 381 or MWC 349 due to systematic issues in their TESS sector data leading to unacceptable artefacts in the lightcurves (they both fall within Sectors 14 and 15); MWC 300 has not yet been observed by TESS, therefore the lightcurves of these objects are not presented in Figure 7.1. The lightcurves have all been normalised by their median values, and the x-axis shows the time in days from the first observation by TESS. The object of the lightcurve and TESS Sectors of the observations are given in the legend of each panel.

The lightcurves are diverse in this B[e]SG sample, but two of the objects show variability on similar timescales as the 1.583-day variability observed in GG Car and presented in Chapter 5. This variability is clearly seen in MWC 137 (which has a period of ∼2 days) and CPD-52 9243 (∼3 days). This type of variability on timescales of the order of days, which TESS has revealed, may be a commonality of the B[e]SG class, rather than being unique to GG Car. Variability such as this had previously been considered to be rare in the B[e]SG class (e.g. Zickgraf et al. 1986; Krtičková & Krtička 2018). Further study of this variability in these objects, which has not been noted before, is needed to understand the role that pulsations may have in the displaying of the B[e]SG phenomenon.

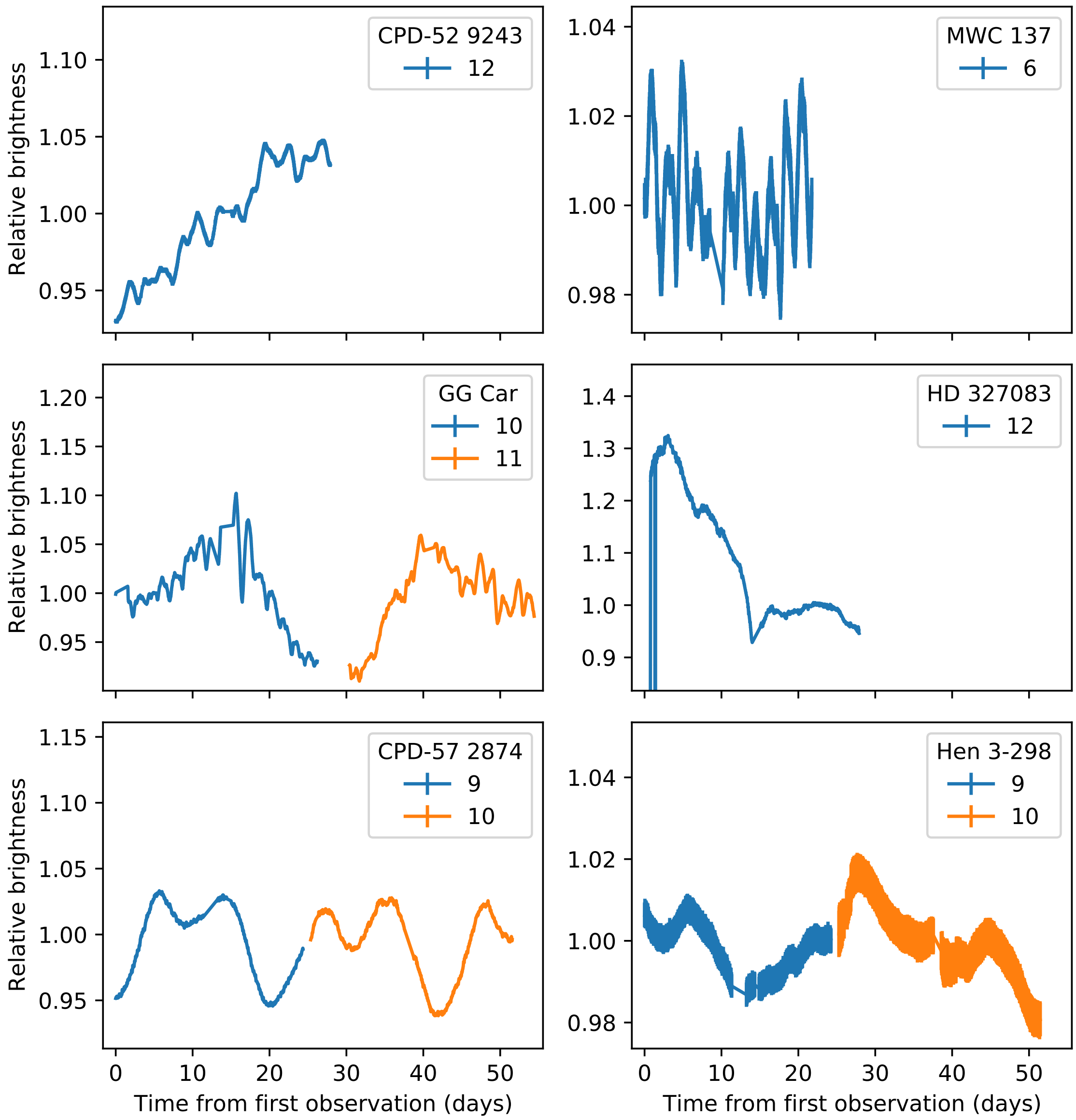

Figure 7.1: TESS lightcurves of the confirmed Galactic B[e]SGs, excluding MWC 300, AS 381 or MWC 349 due to contamination of the lightcurves for these sources. The object in each panel is given in the legend, along with the TESS sectors of its observation. The lightcurves were reduced using `eleanor` (Feinstein et al. 2019). The time of the first observation of the object by TESS is subtracted from the observation time.

Interestingly, CPD-57 2874 shows a longer, repeatable signal in its lightcurve with one deeper dip in brightness and one shallower dip. This is reminiscent of the β Lyrae-type eclipsing binary lightcurves, in which one star is overflowing its Roche lobe and an accretion disk forms around the secondary leading to a continuous lightcurve of two minima of different depths. To ensure that this is not a peculiarity of the TESS data in this Sector, I accessed the ASAS-SN photometry of CPD-57 2874 using the `Sky Patrol` functionality, which is available in both the V- and the g-bands. I utilise the CLEAN algorithm described in Appendix B.1 to calculate periodograms of the V- and g-band data separately, and calculate the geometric mean of the periodograms of the two wavelength bands similarly to the periodograms presented in Chapter 5, so that common periodicities are promoted and noise in the periodograms is suppressed. Figure 7.2, top panel, displays the resultant periodogram of the CPD-57 2874 photometry. The strongest peak is at frequency of 0.0464 days^{-1} which corresponds to a 21.559-day periodicity. The first, second, and third harmonics of this periodicity are also clearly visible in the periodogram. In the middle panel of Figure 7.2 the V-band data of CPD-57 2874 are folded by the 21.559-day period, and the bottom panel shows the g-band data folded by the same period. The same variability reminiscent of β Lyrae variables presents itself in the ASAS-SN data as in the TESS data.

Few published works have studied CPD-57 2874 in great detail, especially in time-series data. It was reported as a P Cygni type star by Carlson & Henize (1979). McGregor et al. (1988) noted the presence of forbidden emission lines, CO emission and measured its high luminosity. Domiciano de Souza et al. (2007, 2011) spatially resolved the dusty circumstellar environment with VLTI data. The system is not listed as a suspected or confirmed binary in Kraus (2019), and I find no reference to any potential binarity or confirmation of its singularity in the literature. There is no mention of any other causes of variability in the system. Given its lightcurve, and the lack of evidence to show that it is a single, I tentatively identify CPD-57 2874 as a suspected binary.

ASAS-SN photometry data were accessed and a similar analysis was undertaken for the other confirmed Galactic B[e]SGs. Another object which shows a clear periodicity in its photometry data is CPD-52 9243, with a period of 66.5 days. The periodogram of the photometry is displayed in the top panel of Figure 7.3, and the folded V-band photometry is shown in the middle panel and the folded g-band photometry is given in the bottom panel. This variability can be seen in the TESS data

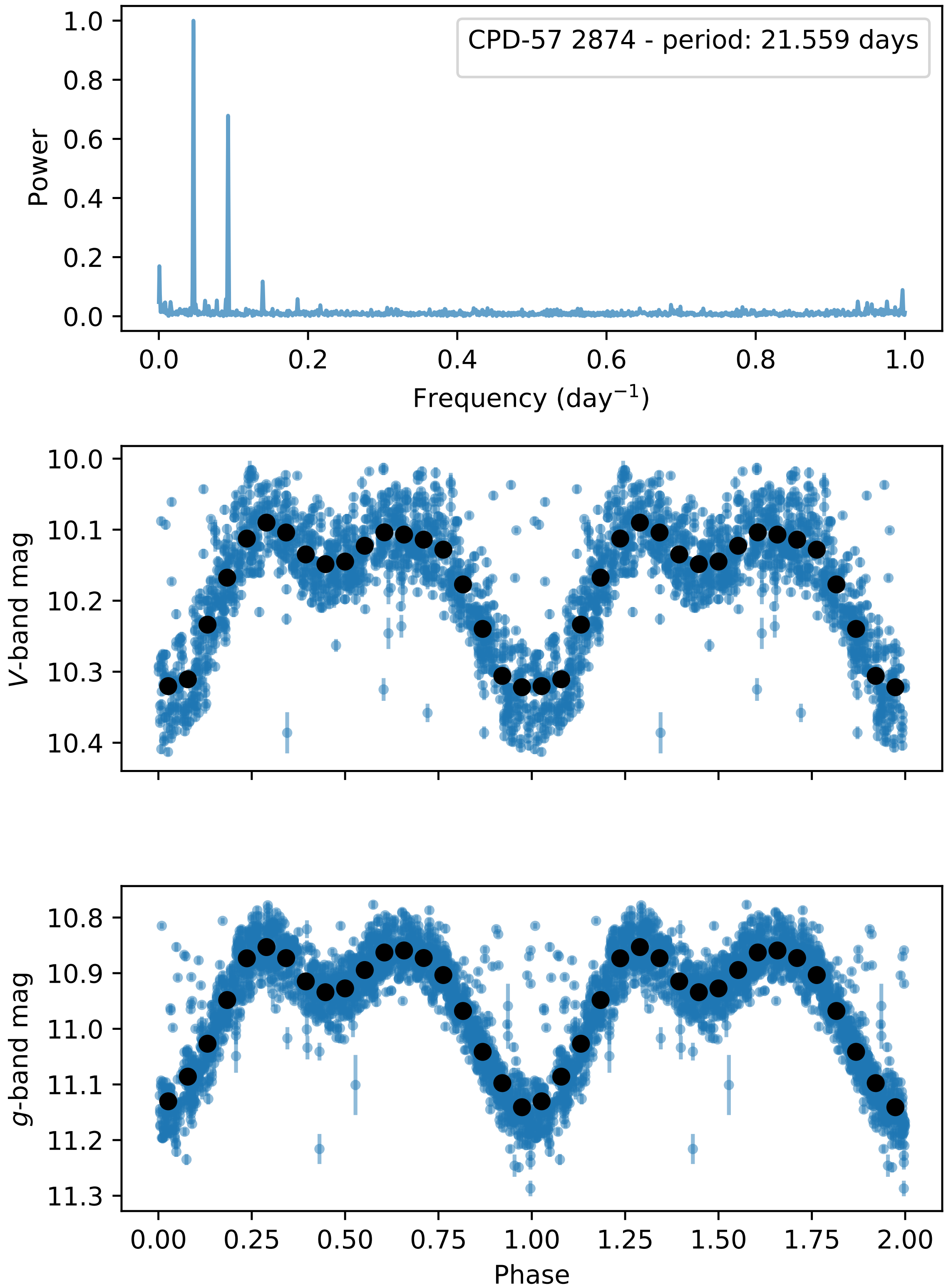

Figure 7.2: Top panel: Periodogram of the ASAS-SN data of CPD-57 2874. The period of the strongest peak is quoted in the legend. Middle panel: the V-band ASAS-SN data folded by the period quoted in the legend. Bottom panel: the g-band ASAS-SN data folded by the period quoted in the legend.

of Figure 7.1, as the object brightens during the Sector 12 observations. However, the short-period variability which is apparent in the TESS lightcurve is not detectable in the periodogram of the V- and g-band data. The lightcurve of CPD-52 9243 folded by its 66.5-day period resembles the lightcurve of GG Car over its orbital period, presented in Chapter 4. Cidale et al. (2012) studied the circumstellar environment of CPD-52 9243, and suggested that it may be a binary due to the presence of a detached CO ring. There are no other references to its binarity, and it has not been extensively observed with time-series data in the literature. Similarly to CPD-57 2874, it is not listed as a suspected binary in Kraus (2019). Further time-series data, especially spectroscopy, would be required to confirm its binarity status but these indications show that it may also be considered as a suspected binary.

HD 327083 is listed as a suspected binary in Kraus (2019) based on the spectroscopic observations of Miroshnichenko et al. (2003), who found anti-phased absorption but were unable to determine a period with their sparse observations. Wheelwright et al. (2012) found that CO was present in a disk which appeared to be circumbinary. Figure 7.4 shows the ASAS-SN photometry power spectrum of HD 327083 and the data folded by the strongest period of 107.991 days. This would most likely be the period of the binary's orbit, which has not yet been constrained in the literature.

The final B[e]SG to be investigated in this Conclusion chapter is MWC 137, which shows short-period variability in the TESS data of Figure 7.1. The power spectrum of its ASAS-SN photometry is displayed in Figure 7.5. Its power spectrum displays two clear peaks, one corresponding to a period of 1.933 days, which matches the variability which can be seen in its TESS lightcurve in Figure 7.1, and the other peak corresponding to 466.2 days. Figure 7.6 folds the V-band and g-band ASAS-SN data of MWC 137 by these two periods. Comparing this system to GG Car, the short-period variability could be interpreted as intrinsic variability of one of the stellar components, and the longer-period variability as a binary orbital period. Mehner et al. (2016) discovered a jet originating from the system, indicating the presence of an accretion disk. One of their proposed origins of the jet is the presence of a companion star which forms an accretion disk due to material from the primary overflowing its Roche lobe. Muratore et al. (2014) detected that the CO emission originating in the system is detached from the stellar surface, and Kraus et al. (2017) resolved its circumstellar environment and observed a double cone structure. The putative detection of a $\sim$466-day period further suggests evidence for the presence of a companion,

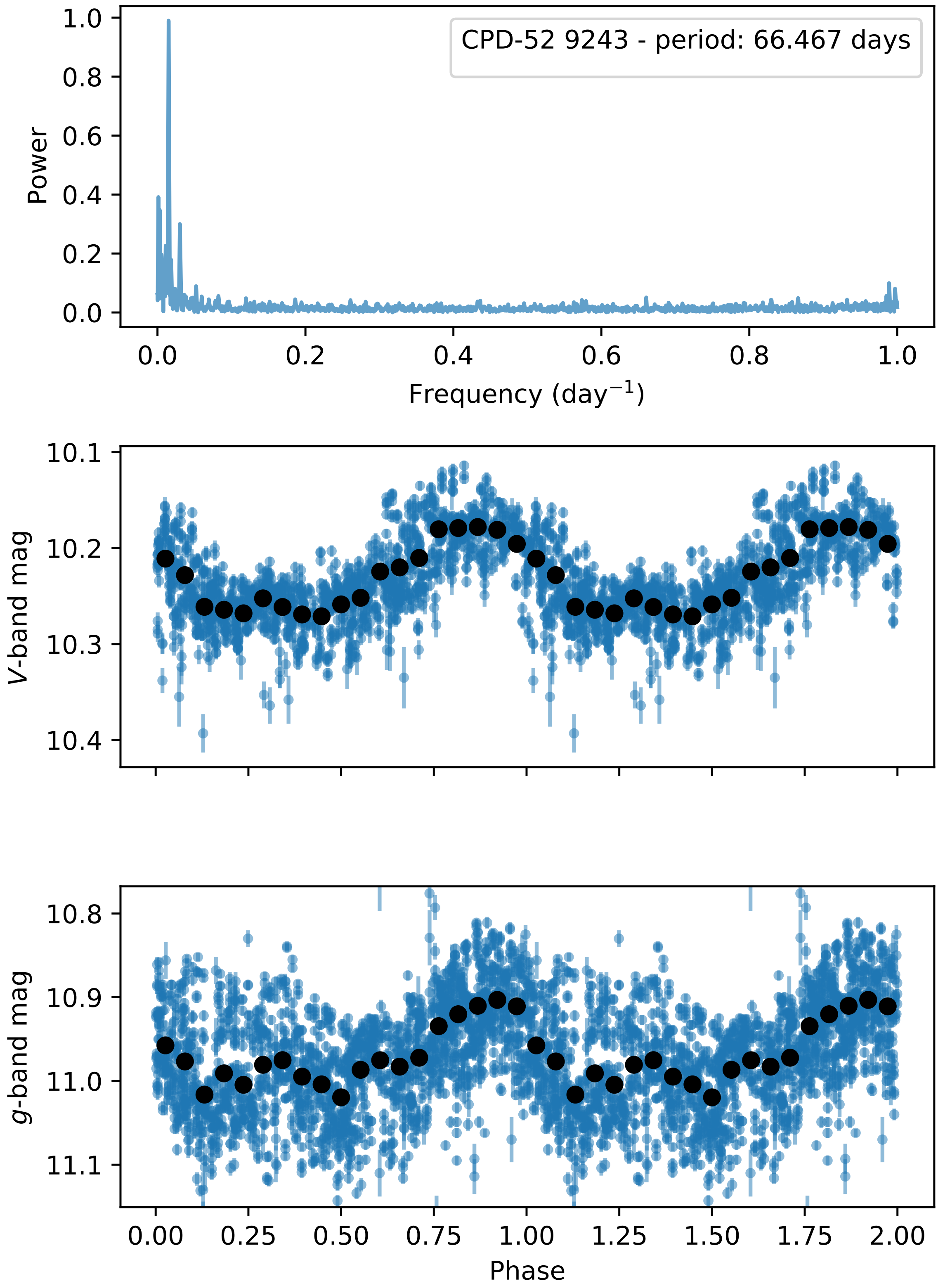

Figure 7.3: Same as Figure 7.2, except analysing the photometric data of CPD-52 9243. The photometry data are folded by the period of the strongest peak in the periodogram in the top panel.

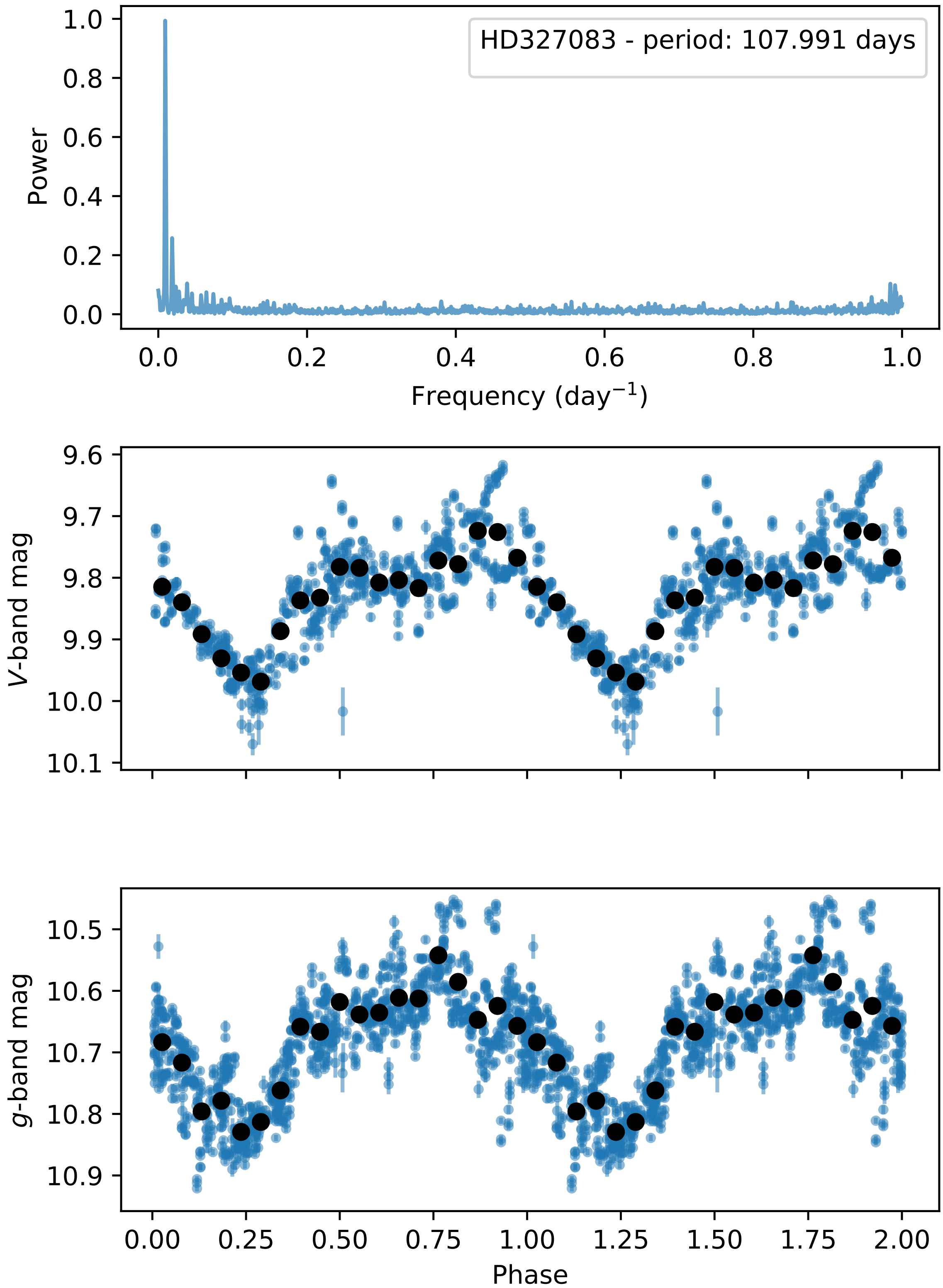

Figure 7.4: Same as Figure 7.2, except analysing the photometric data of HD 327083. The photometry data are folded by the period of the strongest peak in the periodogram in the top panel.

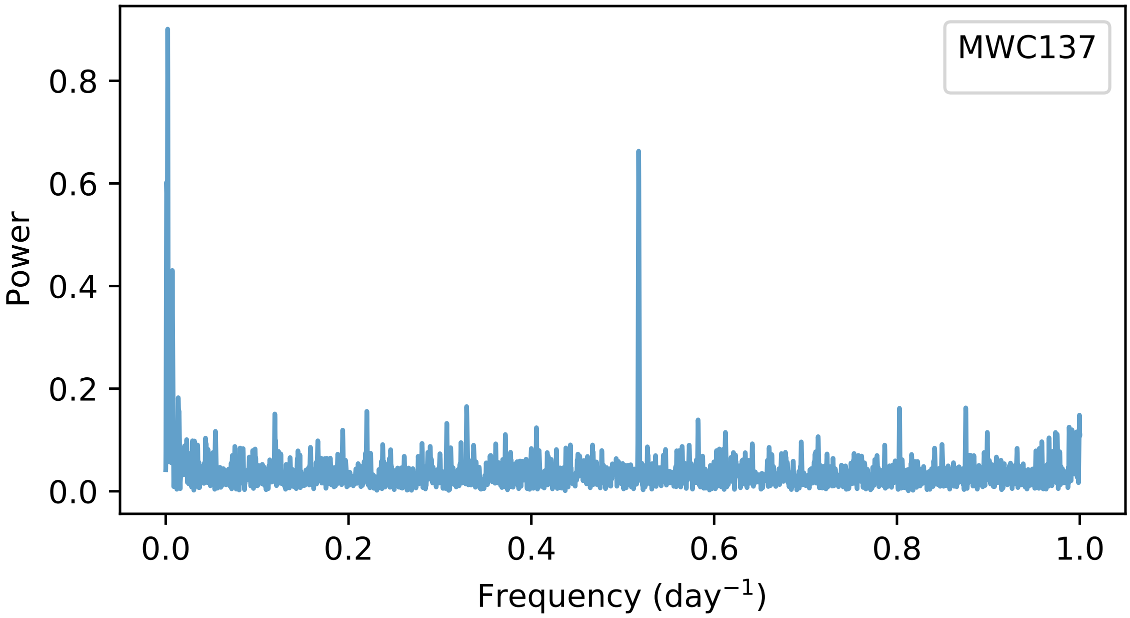

Figure 7.5: Periodogram of the ASAS-SN photometry of MWC 137, calculated in the same manner as the power spectrum in the top panel of Figure 7.2.

though more work would need to be done to confirm this. There is no mention of the observed ∼2 day period in the system in the published literature about MWC 137, which I detect very clearly in both the ASAS-SN and TESS data.

Nearly all of the other B[e]SG specimens whose ASAS-SN photometry were obtained do display variability in their lightcurves, but their variability is either stochastic or cyclical on longer timescales than the available ASAS-SN observation window thus far, therefore I do not present the variability of these objects in this conclusion chapter. Further study of this irregular variability, which is reminiscent of the S Doradus variability of the Luminous Blue Variables, would therefore be fruitful in the understanding of the B[e]SG phenomenon. This also goes against the commonly held view that B[e]SGs are not significantly variable (Lamers et al. 1998).

While further analysis would need to be undertaken beyond this preliminary look at the Galactic B[e]SGs, this study goes to show that time-series data have not been used to the fullest extent in understanding these elusive objects. Periodicities which may arise from binarity are detected in four objects presented, three of which are not currently considered to be potential binaries in the literature (CPD-57 2874, CPD-52

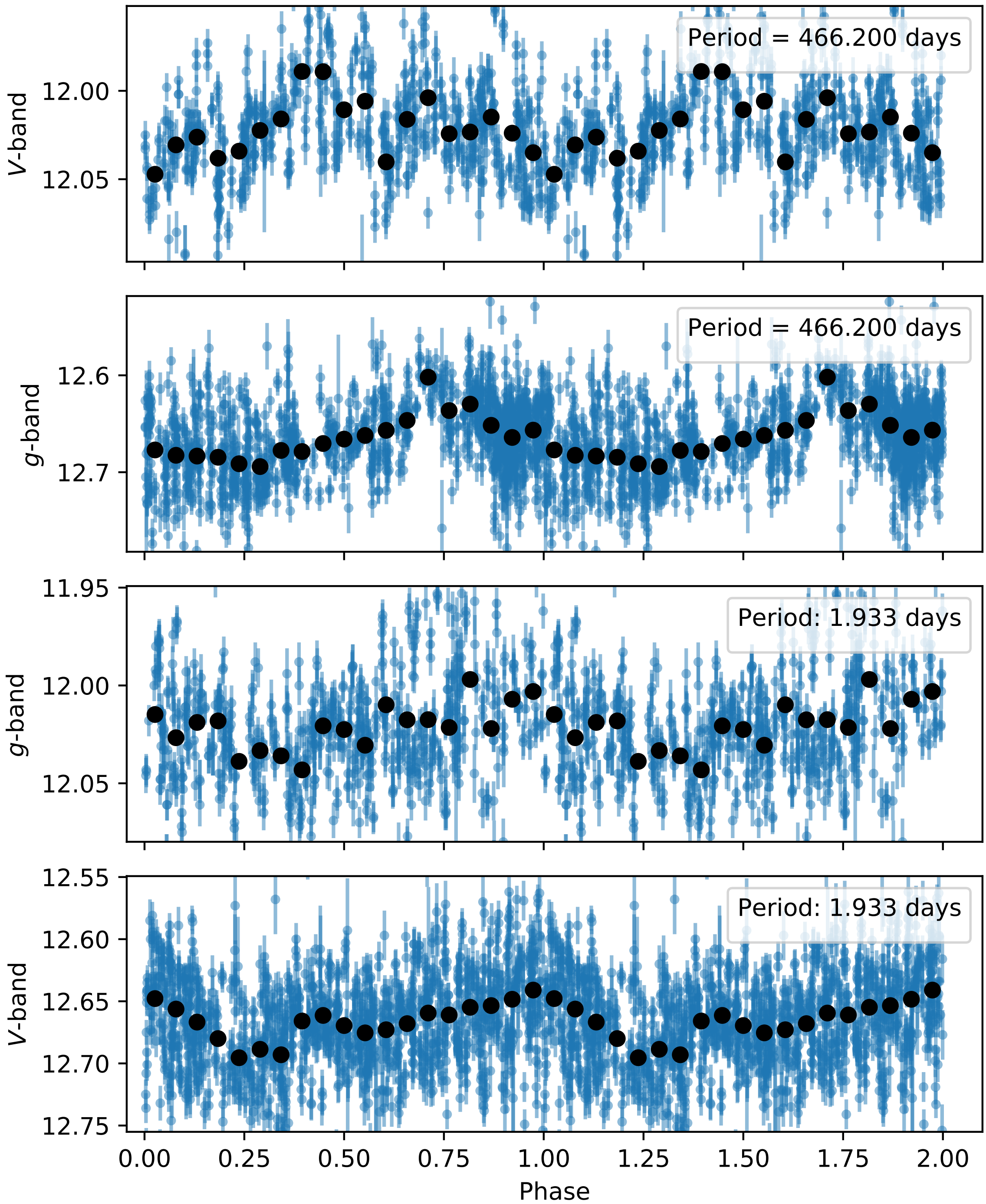

Figure 7.6: Folded g- and V-band ASAS-SN photometry of MWC 137 folded by the two strongest periodicities in the power spectrum of Figure 7.5. The period of the folding is given in the legend of each panel.

9243, and MWC 137). Spectroscopic searches for significant radial velocity variations at the observed photometric periodicities would be able to determine whether the objects are binaries. Should they be confirmed to be binaries in follow up studies, then the proportion of Galactic B[e]SGs which are "confirmed or suspected" binaries would increase from 4/9 to 7/9. Caution should be used in drawing firm conclusions from this due to the small sample size, but it is an indication that binarity and binary interaction may play a very important role in the displaying of the B[e]SG phenomenon, which has recently been somewhat downplayed in the literature. Further beneficial work would also be to determine the binarity status of the B[e]SGs of the Magellanic clouds, of which even less is known about their binarity than that of the Galactic sample. Furthermore, using precision *Gaia* parallaxes to constrain their distances, the B[e]SG status of the six Galactic candidates could be confirmed or refuted, potentially enlarging the population sample. The signs that variability on the order of ∼1–2 days may be rather common for the B[e]SG class, rather than the presumed rarity that it is now considered, may be an indication that asteroseismology and pulsations also play an important role in the displaying of the B[e] phenomena in these object. The longer-term and irregular variability of some of the systems should also be studied in greater detail.

7.2 Thesis summary

In Chapter 1 I introduce the rare B[e] supergiant (B[e]SG) stars and highlight their importance in the understanding of massive star evolution. I review the understanding of the B[e]SG phenomenon, with the current theories being that they are massive stars which have recently evolved off the main sequence with complex circumstellar environments consisting of warm dust and atomic rings, which lead to their displaying of the B[e] phenomenon of hybrid spectra and forbidden emission lines. I introduce some of the unanswered questions about B[e]SGs, such as at what stage are they in their evolution, how common is the phenomenon, how does material get lifted from the stellar surfaces and arranged in such unusual distributions, and to what extent is binarity involved in the B[e]SG phenomena. I also introduce concepts of circumbinary disks, since the disks of B[e]SGs which are confirmed binaries are almost all circumbinary, and their dynamical properties.

Chapter 2 concerns itself with my contributions to Professor Katherine Blundell's Global Jet Watch (GJW) project. I describe my improvements in finding emission line centres in the wavelength calibration frames, finding the polynomial order to fit the wavelengths, and using Telluric absorption in the one-dimensional spectra to correct the wavelengths. All of these improved the wavelength calibrations of the GJW project compared to previous versions. I describe the construction of the illumination calibration frames, and how the spectra are corrected for any slight misalignment between the calibration frames and the scientific frames. I describe how regridding the CCD frames to a finer mesh reduces noise features in the final one-dimensional spectrum, and how the novel method of using a fitted "gradient" method maximises the potential spectral resolution in the extraction of the one-dimensional spectrum.

Chapter 3 introduces the B[e]SG binary GG Carinae (GG Car), reviewing the literature published about the object and highlighting that its binary orbital solution has never before been satisfactorily determined. I introduce the available observations of GG Car, from spectroscopic observations from the GJW and FEROS, to photometric observations from ASAS, ASAS-SN, OMC, and TESS, and how these data were obtained. I determine the luminosity of the B[e]SG primary to be $L = 1.8^{+1.0}_{-0.7} \times 10^5\, L_\odot$ and constrain its mass to be $24 \pm 4\, M_\odot$. I identify the emission lines in GG Car's GJW spectra, and investigate the hydrogen Balmer lines in the FEROS spectra. I find that the Balmer series consists of strong emission and blueshifted absorption, with the emission becoming weaker throughout the Balmer series. I note that there are multiple ($\sim$3) blueshifted absorption components in the hydrogen and helium lines, indicating a complex wind profile. I also note the presence of double-peaked emission lines indicating the presence of its gaseous disk.

Chapter 4 studies the variability of GG Car at its 31-day orbital period. I show that there is one photometric maximum and one minimum per orbital period, with the variability's amplitude being somewhat stochastic. I show that the amplitude of the radial velocity (RV) variations of the system's emission lines are correlated to the energetics of the emission lines' atomic energy levels. I accurately determine the orbital solution of the binary, for the first time, using these emission lines which originate in the wind of the primary star and modelling the atmosphere of the B[e]SG primary using `CMFGEN`. I show that the binary is significantly eccentric with $e = 0.5 \pm 0.03$ and constrain the mass of the secondary to $7.2^{+3.0}_{-1.3}\, M_\odot$. With the knowledge of the correct orbital solution, I show that the system is brightest when the binary is at periastron and dimmest at apastron. The blueshifted absorption of the He I lines is likewise deepest at periastron and weakest at apastron. Having discounted other potential sources of the system's photometric variability, I show that its brightness variations at the binary orbital period may be explained by the secondary component accreting the wind of the primary, leading to variable accretion rates over the eccentric orbit. I suggest that the signs of interaction in the close binary, along with recent studies by other authors on the nature of classical Be stars, warrant the evolutionary history of GG Car to be reanalysed in a binary evolution scenario rather than the quasi-single stellar evolution used in previous works.

In Chapter 5, I investigate in detail short period variability in GG Car, of which there had hitherto been the faintest of hints in the object's published literature. Using Fourier analysis, I confirm the presence of a 1.583156 ± 0.0002-day variability in both the system's photometry and the RVs of its He I, Fe II and Si II emission lines. Similarly to their variations at the orbital period, the amplitudes of the RV variations are correlated to the enegetics of the emission lines. I show that the amplitude of the short period variability is modulated by the orbital phase of the binary in both photometry and spectroscopy, with greatest amplitudes just after periastron passage. I determine that the variability is most likely due to excitation of the $l = 2$ f-mode of the primary star which is excited by the strong tidal forces from the secondary felt at periastron. This demonstrates that an interaction of binarity and pulsations may lead to the system's presenting of the B[e] phenomenon.

In Chapter 6, I study the atomic emission lines which originate in the circumbinary disk of GG Car using high-resolution spectra from FEROS. Agreeing with previous studies, I observe two distinct circumbinary rings in the system. I reported permitted Ca II and semi-forbidden Fe II] emission arising in the inner circumbinary ring, along with the [Ca II] and [O I] emission. There are subtle changes in the central radial velocities and V/R ratios of the lines which originate in the inner circumbinary ring over the 15 years of FEROS observations. I show that these variations may be due to the ring being excited to higher eccentricities by the binary, and I run smoothed-particle hydrodynamic simulations of the system to show that the observed variations may be recreated on similar timescales given the orientation of the binary due to these excitations. This would be one of the first, if not the first, examples of eccentricity growth actively observed in circumbinary disks, though they have often been predicted in hydrodynamic simulations. This suggests that the B[e]SG class may provide useful objects to test circumbinary disk dynamics, such as precession and eccentricity growth.

Chapters 3, 4, 5 and 6 of this thesis therefore build one of the most comprehensive pictures of a B[e]SG specimen available, of which GG Car is one of only ~33 confirmed candidates. It is now one of the few B[e]SGs to have been extensively observed and analysed with time-series astronomical data. As demonstrated in the work of this thesis, the endeavour to understand a single object in this enigmatic class of star requires topics from across the stellar physics field to be consulted, from binarity to stellar winds, and from asteroseismology to circumbinary disk dynamics, from stellar evolution to accretion and binary interaction.

Section 7.1 again demonstrates the untapped power that time-series data holds in the understanding of the B[e]SG phenomenon, finding hints of binarity in three Galactic objects which had not previously been considered to be binaries. At least one more object with considerable variability on timescales of a few days is also found, whereas this type of variability was believed to be rare for the B[e]SG class.

7.3 Final words

The B[e]SGs are a poorly understood class of star, but are a vitally important part of massive stellar evolution to understand. While the ultimate origin of the B[e]SG phenomenon may remain elusive, I have presented a detailed case study of GG Carinae, measuring its stellar and orbital properties and detecting and explaining its variability. I have shown that, beyond massive stellar physics and evolution, these objects are also interesting test-cases to study circumbinary disk dynamics.

This thesis has demonstrated that analysing time-series data of the B[e]SGs may reveal profound insights into their nature and the displaying of their enigmatic phenomena. With time-series analysis, there are strong indications of binarity and further variability in the Galactic B[e]SGs, which otherwise have not been detected. The analysis of modern time-series data available from TESS, ASAS-SN, FEROS, Gaia, and the Global Jet Watch therefore presents a clear path to understand the processes and origin of these rare, unusual, and fascinating stars.

Appendices

Appendix A

Appendix to Chapter 4

A.1 Log-likelihood equation

Consider a situation where, given observations y at times x with uncertainty σ, we need to fit model parameters, θ, of a function $\bar{y} = f(x, \theta)$. There will be some amount of error in the measurements of y, such that

$$y_i = f(x_i, \theta) + b_i, \tag{A.1}$$

where i indicates the ith observation, and b_i is the error in the measurement. It is assumed that b_i is Gaussian distributed with standard deviation, σ_i. Given n observations, the probability of observing the values of y given θ, x, and σ, is given by

$$P(y|\theta, x, \sigma) = \prod_{i=1}^{n} \frac{e^{-(y_i - \bar{y}_i)^2/2\sigma_i^2}}{\sqrt{2\pi}\sigma_i}. \tag{A.2}$$

Equation A.2 assumes that the measurements and uncertainties of each observation are independent, and the uncertainties are Gaussian distributed.

When fitting a model, we are interested in finding out the probability distributions of the model parameters, θ, given the observations x, y, and σ. From Bayes' theorem, $P(\theta|y, x, \sigma) \propto P(\theta)P(y|\theta, x, \sigma)$, where $P(\theta)$ are the parameters' priors. We assume that the priors are uniform. Therefore,

$$\ln(P(\theta|y, x, \sigma)) \propto \sum_{i=1}^{n} \left[\ln(e^{-(y_i - \bar{y}_i)^2/2\sigma_i^2}) - \ln(\sqrt{2\pi}\sigma_i)\right] = \sum_{i=1}^{n} \left[-\frac{(y_i - \bar{y}_i)^2}{2\sigma_i^2} - \ln(\sqrt{2\pi}\sigma_i)\right], \tag{A.3}$$

and therefore,

$$\ln(P(\theta|y, x, \sigma)) \propto -\frac{1}{2}\sum_{i=1}^{n}\left[\frac{(y_i - \bar{y_i})^2}{\sigma_i^2} + \ln(2\pi\sigma_i^2)\right]. \tag{A.4}$$

Equation A.4 therefore gives the log-likelihood of the model parameters, θ, given the data x, y, and σ. Equations 4.2 and 4.5 are based on Equation A.4, and are used in Markov Chain Monte Carlo calculations in order to find the posterior probability distributions of model parameters.

A.2 Orbital solution fits

Table A.1 displays the results of the orbital solution fits for the RV variations at the orbital period for the individual emission lines that were studied, along with the wavelengths, energies of the lower atomic state (E_i) and higher atomic state (E_k) associated with the line transitions. The wavelengths and energies were accessed from the NIST Atomic Spectra Database.

Species and wavelength (Å)	K ($\mathrm{km\,s^{-1}}$)	ω ($^\circ$)	e	v_0 ($\mathrm{km\,s^{-1}}$)	M_0 ($^\circ$)	jitter ($\mathrm{km\,s^{-1}}$)	E_i (eV)	E_k (eV)
Fe II 6317.3871	$9.98^{+0.89}_{-0.79}$	$311^{+3.9}_{-5.1}$	$0.271^{+0.068}_{-0.074}$	$-5.1^{+0.48}_{-0.44}$	$36.7^{+0.86}_{-2.1}$	$9.73^{+0.34}_{-0.33}$	6.2224968	8.1845409
Fe II 6383.7302	$10.4^{+0.62}_{-0.62}$	296^{+11}_{-11}	$0.286^{+0.059}_{-0.061}$	$-3.6^{+0.4}_{-0.39}$	$22^{+9.9}_{-9.4}$	$9.69^{+0.27}_{-0.26}$	5.55260574	7.4942594
Fe II 6456.3796	$7.7^{+0.57}_{-0.57}$	335^{+27}_{-20}	$0.214^{+0.078}_{-0.074}$	$-23.8^{+0.45}_{-0.38}$	47.4^{+26}_{-18}	$8.83^{+0.3}_{-0.24}$	3.90341902	5.8232247
Fe II 6491.663	$12.3^{+1.3}_{-1.2}$	260^{+12}_{-11}	$0.457^{+0.08}_{-0.078}$	$0.666^{+0.62}_{-0.61}$	$359^{+9.2}_{-7.4}$	$15.5^{+0.44}_{-0.43}$	10.9088323	12.8182036
Fe II 7513.1762	$8.12^{+1}_{-0.93}$	276^{+97}_{-79}	$0.0975^{+0.17}_{-0.078}$	$0.968^{+0.64}_{-0.74}$	$18.9^{+1.5e+02}_{-38}$	$13.5^{+0.53}_{-0.43}$	9.6536142	11.3033834
Fe II 7711.4386	$6.78^{+0.79}_{-0.66}$	258^{+15}_{-15}	$0.392^{+0.077}_{-0.078}$	$-24.8^{+0.45}_{-0.35}$	350^{+11}_{-13}	$7.88^{+0.41}_{-0.26}$	5.51071386	7.1180674
H alpha - 6562.819	$18.9^{+2}_{-1.9}$	262^{+19}_{-21}	$0.257^{+0.096}_{-0.12}$	$20.6^{+1.5}_{-1.2}$	345^{+19}_{-23}	$17.9^{+1.1}_{-1}$	10.1988357	12.0875051
He I 5875.5987	$41^{+1.9}_{-1.8}$	12.3^{+15}_{-13}	$0.247^{+0.045}_{-0.05}$	$62.3^{+1.4}_{-1.2}$	73.7^{+14}_{-12}	$28.9^{+0.95}_{-0.84}$	20.96408703	23.07365663
He I 6678.1517	$46^{+2.8}_{-2.5}$	$313^{+7.2}_{-6}$	$0.445^{+0.048}_{-0.057}$	$77.3^{+1.5}_{-1.6}$	$27.5^{+4.8}_{-4.2}$	$29.3^{+0.9}_{-0.99}$	21.21802284	23.07407493
He I 7065.17714	$32.8^{+4.2}_{-3.9}$	336^{+34}_{-62}	$0.179^{+0.16}_{-0.13}$	$86.8^{+3.1}_{-3.1}$	29.5^{+42}_{-37}	$50.1^{+2.1}_{-2}$	20.96408703	22.71846655
Si II 5957.56	$16.4^{+2.8}_{-2.6}$	298^{+17}_{-18}	$0.431^{+0.1}_{-0.15}$	$-86.2^{+1}_{-1.1}$	37.2^{+12}_{-12}	$23.6^{+0.84}_{-0.8}$	10.066443	12.146991
Si II 5978.93	$24.9^{+1.6}_{-1.6}$	$302^{+7.2}_{-7.2}$	$0.501^{+0.047}_{-0.049}$	$-48.8^{+0.84}_{-0.85}$	$27.1^{+4.6}_{-4.2}$	$20.9^{+0.64}_{-0.6}$	10.07388	12.146991
Si II 6347.11	$25^{+0.98}_{-0.99}$	$333^{+8}_{-7.4}$	$0.311^{+0.034}_{-0.032}$	$-41.7^{+0.57}_{-0.62}$	$49.4^{+6.8}_{-6.4}$	$13.8^{+0.46}_{-0.4}$	8.121023	10.07388
Si II 6371.37	$24^{+1.6}_{-1.5}$	$287^{+9.3}_{-8.3}$	$0.462^{+0.05}_{-0.045}$	$-62.8^{+0.83}_{-1}$	$22^{+6.5}_{-5.4}$	$17.2^{+0.76}_{-0.8}$	8.121023	10.066443

Table A.1: The line identifications and orbital solutions fitted to the 31-day RV variations for each emission line used in this study, along with the energy of the lower atomic state, E_i, and energy of the upper atomic state, E_k, of the lines. Wavelengths and energies were accessed from the NIST Atomic Spectra Database.

A.3 Determining v_∞

The terminal wind velocity, v_∞, is used in the `CMFGEN` simulation of GG Car's atmosphere in order to determine the line-emissivity kernels. As B[e]SGs have non-spherical winds, but instead host both a fast, polar wind and a slow equatorial wind, the one-dimensional code is used to simulate the equatorial wind since the lines studied are expected to form in that component.

The first determination of v_∞ comes from the half-width-at-zero-intensity (HWZI) of the Si II 6347 line in the FEROS spectra. This line is the cleanest of all the lines used in this study, having just one major component and no absorptions, unlike the He I and H-alpha lines. Si II 6371, unfortunately, suffers some mild blending which slightly affects the width determination of the line. The HWZI for each FEROS spectrum was determined by taking a median-filter of the Si II line in order to get a smoothed line profile. The noise of the spectrum was then taken as the mean of the absolute differences between the spectrum and the smoothed spectrum. The line is defined as being at zero-intensity when the smoothed spectrum dips below the level of the continuum plus the noise. Figure A.1 displays an example of determining the HWZI of an Si II line. The HWZI of the Si II 6347 line is calculated in all of the available FEROS spectra. The width is variable across the FEROS dataset, indicating wind fluctuations, but a median HWZI of $264.67\,\mathrm{km\,s^{-1}}$ is found with a standard deviation of $21\,\mathrm{km\,s^{-1}}$. This width is comparable to the widths of the He I and H I Balmer lines.

The second determination of v_∞ comes from the position of the bluemost edge of the middle absorption component in the Hydrogen Balmer series and He I lines in the FEROS spectra. Figure A.2 displays three Balmer Hydrogen lines and the He I 5875 line in a FEROS spectrum of GG Car. Generally these lines show three distinct absorption components, with the less blueshifted two often blended. Their bluemost edges are around ~ -160, ~ -290 and $\sim -550\,\mathrm{km\,s^{-1}}$. The absorption around $-160\,\mathrm{km\,s^{-1}}$ matches the H-alpha absorption visible in the GJW spectra, shown in Figure 4.4, and shows little sign of RV variability. I focus on the component around $-290\,\mathrm{km\,s^{-1}}$, since this is similar to the Si II HWZI. As with the Si II 6347 HWZI, the exact RV varies slightly over the FEROS observations. This will be due to both variations in the wind conditions and any residual motion of the wind when it was ejected from the B[e]SG primary. Since the systemic velocity is $\sim -22\,\mathrm{km\,s^{-1}}$,

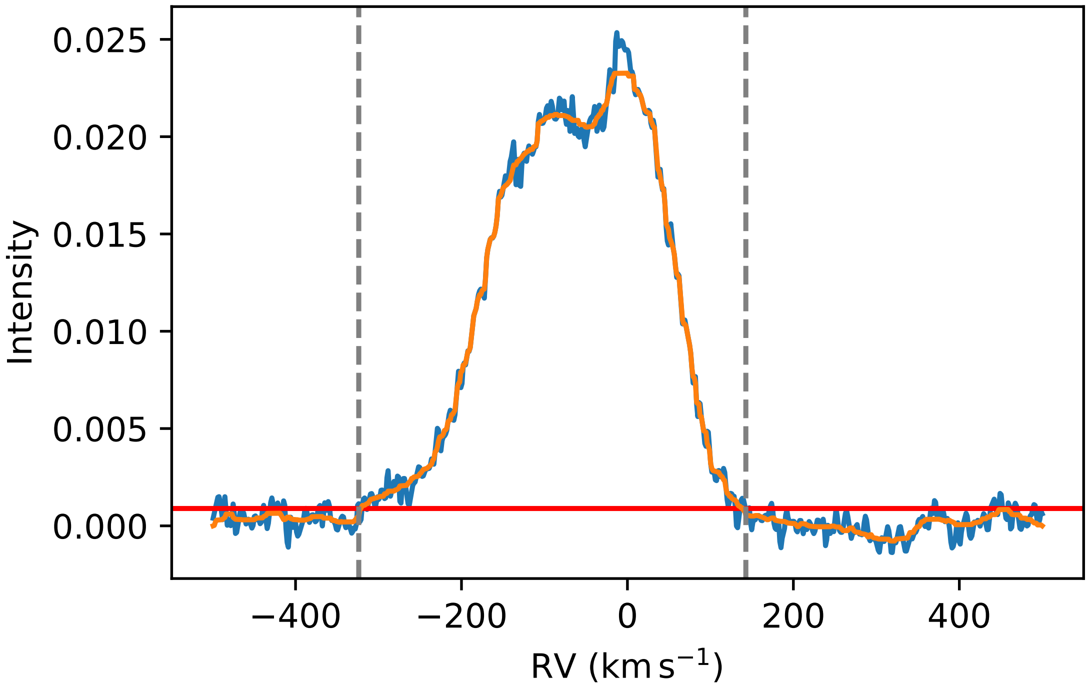

Figure A.1: Determination of the HWZI of an Si II line in FEROS. The original spectrum is in blue, and the smoothed spectrum is in orange. A red line indicates where zero intensity is defined, and dashed grey lines indicate where the smoothed spectrum drops below this level. The HWZI is half the distance between the two dashed lines.

average speed of this wind component is $\sim -265\,\mathrm{km\,s^{-1}}$.

Therefore, v_∞ in the `CMFGEN` simulation is set to be $265\,\mathrm{km\,s^{-1}}$. Since this is observed to be the characteristic HWZI of the Si II 6347 line and due to the blue-most edge of the He I and H I Balmer absorptions having this same RV, this gives evidence that these lines form in the same wind component. This $265\,\mathrm{km\,s^{-1}}$ is an estimate of the average v_∞ of this wind component, even though it is observed to vary slightly over the FEROS dataset.

A.4 Accretion model

In the two-dimensional wind-accretion model described in Section 4.4.3.3, the position of the two binary components are calculated using Kepler's laws and the binary orbital parameters measured in Section 4.3. The primary emits a radial wind from its equator with speed v_{wind} from the reference frame of the primary, which is modelled as a discrete ring being ejected at every timestep, dt. The centre of the ring travels with a bulk velocity equal to the velocity of the primary at ejection, $\bar{v}_{\mathrm{bulk}}$. This makes the center of the "wind ring"

$$\bar{x}_{\mathrm{ring}} = \bar{x_0} + \bar{v}_{\mathrm{bulk}}\, t_{\mathrm{ring}}, \tag{A.5}$$

where $\bar{x_0}$ is the location of the primary when the ring was ejected and t_{ring} is the life time of the ring since emission. The radius of the ring is

$$r_{\mathrm{ring}} = R_* + v_{\mathrm{wind}}\, t_{\mathrm{ring}}, \tag{A.6}$$

where R_*, the stellar radius, is the radius at which the ring is ejected.

Matter within the ring is counted as accreted by the secondary when the expanding ring passes within the Roche lobe of the secondary. This occurs when

$$r_{\mathrm{ring}} > |\bar{x}_{\mathrm{ring}} - \bar{x}_{\mathrm{comp}}| - r_{\mathrm{roche}}, \tag{A.7}$$

where $\bar{x}_{\mathrm{comp}}$ is the position of the companion at the timestep, and r_{roche} is the radius of the secondary's Roche lobe, calculated using Equation 4.9 and the instantaneous separation of the components in their orbit. As it is assumed the wind is radial, at accretion the wind will be travelling directly away from $\bar{x}_{\mathrm{ring}}$ with a magnitude v_{wind};

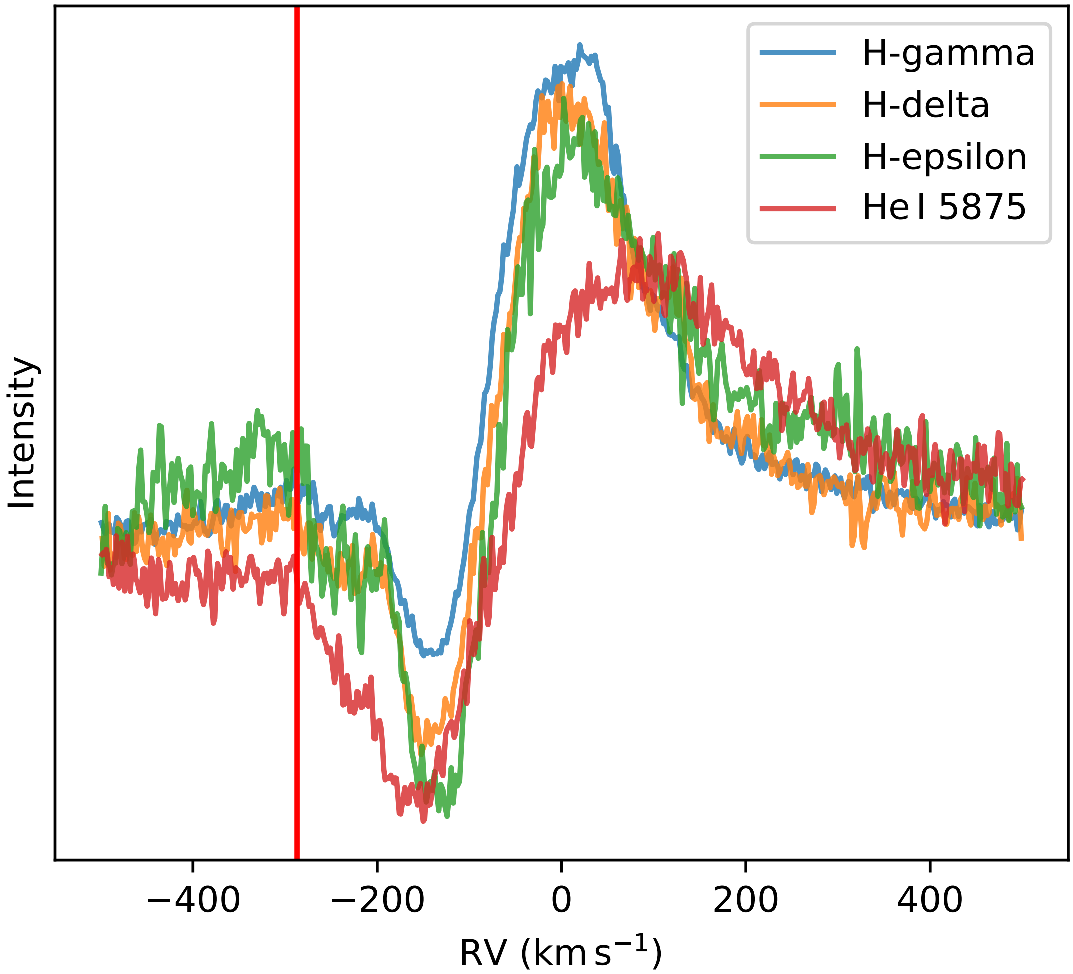

Figure A.2: Balmer H I complexes and He I 5875 in an example FEROS spectrum of GG Car. The spectrum has been continuum subtracted, then each line normalised by the standard deviation of the spectrum in the velocity range. A vertical red line is placed at $-287\,\mathrm{km\,s^{-1}}$.

this velocity vector is then $\bar{v}_{\text{ring}}$. The velocity difference between the wind and the secondary is

$$v_{\text{diff}} = |\bar{v}_{\text{comp}} - \bar{v}_{\text{ring}}|, \tag{A.8}$$

where $\bar{v}_{\text{comp}}$ is the velocity of the companion at accretion.

To determine the amount of mass accreted per ring, a first-order weighting from first principles is built to be applied when the radius of the ring passes the Roche radius of the secondary. Since it is assumed that the wind of the primary is concentrated in a thin disk in the orbital plane, a two-dimensional problem of a mass of accretion radius R_A travelling through a medium of mass per unit area ρ at velocity v is considered. The mass accretion rate, $\dot{M}$, will be equal to

$$\dot{M} = 2\, R_A\, \rho\, v. \tag{A.9}$$

The accretion radius R_A is the critical impact parameter at which a particle travelling with speed v toward the accretor will be accreted. R_A can be found by equating the gravitational energy of the particle with its kinetic energy, and is given by

$$R_A = \frac{2\, G\, M}{v^2}. \tag{A.10}$$

Assuming the wind is composed of many infinitesimally thin rings each of mass m, radius r, and thickness dr, the mass of the ring per unit area is

$$\rho = \frac{m}{2\pi r\, dr}. \tag{A.11}$$

Combining Equations A.9, A.10, and A.11, it is found that the accretion rate can be described by the proportionality

$$\dot{M} \propto \frac{1}{rv}. \tag{A.12}$$

This gives the weighting which is quoted in Equation 4.11.

Figure A.3 compares how $\dot{m}$, the modelled accretion rate described in Section 4.4.3.3, varies by changing the input eccentricity, e, or wind velocity, v_{wind}. All parameters, other than those indicated in the legend, are kept constant in these calculations compared to the calculation in Section 4.4.3.3. Unsurprisingly, lower e leads to a more uniform accretion rate through the orbital period, culminating in a constant $\dot{m}$ for $e = 0$. Higher eccentricities lead to more "pulsed" accretion profiles, with relatively more accretion occurring right at periastron.

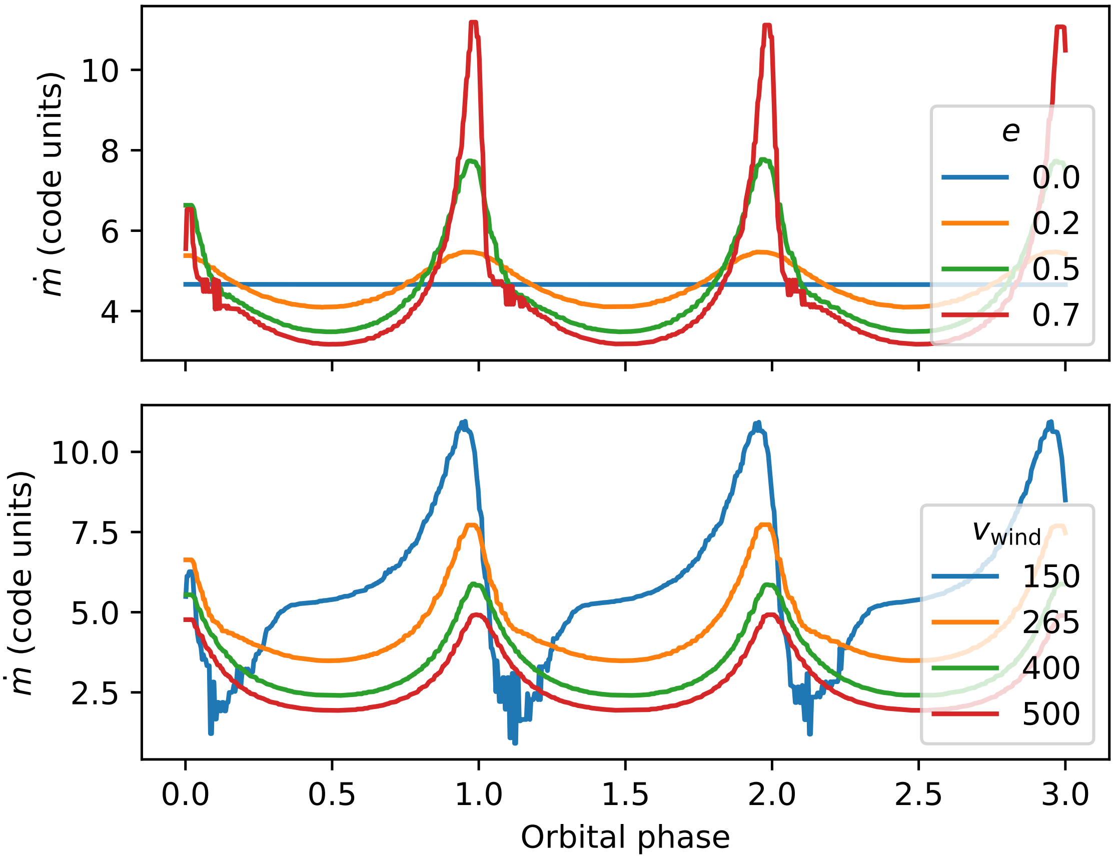

Figure A.3: Variations in the modelled accretion rate, $\dot{m}$ over the orbital period after varying the eccentricity e (top panel) and wind velocity v_{wind} (bottom panel). All other calculation parameters are kept constant as described in Section 4.4.3.3.

On the other hand, lowering $v_{\rm inf}$ below the $265\,{\rm km\,s^{-1}}$ assumed for the calculation in Section 4.4.3.3 leads to an irregular profile of the accretion rate, with the rate peaking before periastron and then falling dramatically after periastron. Increasing the wind speed above $265\,{\rm km\,s^{-1}}$ does not significantly affect the accretion signature, except $\dot{m}$ becomes more symmetric around periastron with the peak rate occurring at periastron.

These show that the accretion model is sensitive to the chosen e and $v_{\rm wind}$. The eccentricity of the model with $e = 0.5$ is the closest match to the V-band photometric variations observed, but any eccentricity between $\sim 0.2 - 0.7$ would be acceptable. Likewise, below the chosen $v_{\rm wind}$ of $265\,{\rm km\,s^{-1}}$ the calculated $\dot{m}$ does not resemble the V-band photometric variations observed. However, the calculation is robust with higher $v_{\rm wind}$.

Appendix B

Appendix to Chapter 5

B.1 CLEAN Fourier analysis

I use the one-dimensional CLEAN algorithm of Roberts et al. (1987) in order to calculate the power spectra in this thesis. The full details are in that paper, but here I will briefly restate its principles and the implementation of the algorithm.

When observing a signal in astronomy we are measuring an underlying function $f(t)$, sampled at a finite number N of discrete times, t_r. We therefore have a set of data

$$f_r,\ t_r \equiv f(t_r),\ t_r, \tag{B.1}$$

where $r = 1, 2, ..., N$. This is equivalent to multiplying $f(t)$ by a sampling function, $s(t)$, composing of Dirac delta functions, so therefore the sampled function is

$$f_s(t) \equiv f(t)s(t) = \frac{1}{N}\sum_{r=1}^{N} f(t)\delta(t - t_r) = \frac{1}{N}\sum_{r=1}^{N} f_r\delta(t - t_r). \tag{B.2}$$

From Fourier theory, the Fourier transform of the sampled signal $\mathrm{FT}[f_s] \equiv D(\nu)$ is the convolution of the fourier transform of the underlying signal $\mathrm{FT}[f(t)] \equiv F(\nu)$ and the Fourier transform of the sampling function $\mathrm{FT}[s(t)] \equiv W(\nu)$, such that

$$D(\nu) = F(\nu) * W(\nu) \equiv \int_{-\infty}^{\infty} d\nu' F(\nu')W(\nu - \nu'). \tag{B.3}$$

The observable functions $D(\nu)$ and $W(\nu)$ are the "dirty spectrum" and the "spectral window function" respectively. We calculate $D(\nu)$ and $W(\nu)$ from the data, since their integrals collapse to discrete Fourier transforms

$$D(\nu) = \int_{-\infty}^{\infty} f_s(t)e^{-2\pi i\nu t}\,\mathrm{d}t = \frac{1}{N}\sum_{r=1}^{N} f_r e^{-2\pi i\nu t_r} \tag{B.4}$$

and

$$W(\nu) = \int_{-\infty}^{\infty} s(t)e^{-2\pi i\nu t}\,\mathrm{d}t = \frac{1}{N}\sum_{r=1}^{N} e^{-2\pi i\nu t_r}. \tag{B.5}$$

Therefore, the aim of the CLEAN algorithm is to deconvolve the window function $W(\nu)$ from $D(\nu)$, in order to uncover the underlying power spectrum $F(\nu)$. It does this by iteratively building a new "cleaned" power spectrum using the most significant peak of the residual "dirty" spectrum, then subtracting the spectral window function from the residual spectrum, and repeating the process. The CLEAN algorithm of Roberts et al. (1987) to do this is as follows:

1. The user chooses the maximum frequency to calculate, $\nu_{\max}$ and the frequency increment, $\Delta\nu$. The dirty spectrum, D, will then be calculated for m positive frequencies, therefore $2m+1$ equally spaced points in the range $(-\nu_{\max},\,\nu_{\max})$,

$$\nu_j = \left(\frac{j}{m}\right)\nu_{\max}, \tag{B.6}$$

   where $j = -m, ..., m$.

2. Generate the "dirty" fourier power spectrum D_j value at each frequency value, ν_j where

$$D_j = \frac{1}{N}\sum_{r=0}^{N} y_r e^{-2\pi i\nu_j t_r}, \tag{B.7}$$

   where y_r is the observation r at time t_r, and N is the number of observations.

3. Next the spectral window, W, is generated for the frequency interval $(-2\nu_{\max}, 2\nu_{\max})$ with the spacing $\Delta\nu$. There will be $4m+1$ points in the spectral window. W is calculated at each frequency ν_j, by

$$W_j = \frac{1}{N}\sum_{r=0}^{N} e^{-2\pi i\nu_j t_r}, j = -2m, ..., 2m \tag{B.8}$$

4. Then the clean iterations are started, with gain G and number of iterations N_{iter}. We begin a new spectrum, C, which will be the "cleaned" Fourier spectrum. Before the iterations, it is an array of zeroes, the same size as the dirty spectrum, D.

5. For each CLEAN iteration k, where k runs from 0 to $N_{\mathrm{iter}} - 1$, we find the frequency ν_{peak} where the absolute value of the residual spectrum R^k is maximal in the positive frequency range (i.e. ν_{peak} must be positive). We call this maximum value of the residual spectrum A_{max}, and it occurs when $j = I_k$. Note that when $k = 0$, $R^0 \equiv D$. We then take the value of W at the frequency $2\nu_{\mathrm{peak}}$, which we call W_{peak}. We calculate the amplitude of the residual peak, corrected for the PSF contribution at the negative frequency peak

$$A_{\mathrm{max}}^{\mathrm{corr}} = \frac{A_{\mathrm{max}} - \bar{A}_{\mathrm{max}} W_{\mathrm{peak}}}{1- \mid W_{\mathrm{peak}} \mid^2}, \tag{B.9}$$

where $\bar{A}_{\mathrm{max}}$ is the complex conjugate of A_{max}. $A_{\mathrm{max}}^{\mathrm{corr}}$ is then added onto the cleaned spectrum C at index I_k, where $\nu = \nu_{\mathrm{peak}}$, so that

$$C_{I_k}^{k+1} = C_{I_k}^{k} + G \times A_{\mathrm{max}}^{\mathrm{corr}}. \tag{B.10}$$

$$C_{-I_k}^{k+1} = C_{-I_k}^{k} + G \times \bar{A}_{\mathrm{max}}^{\mathrm{corr}}. \tag{B.11}$$

6. We then need to subtract this peak from the residual dirty spectrum, using the contributions of the negative and positive PSF:

$$R_j^{k+1} = R_j^k - G \times \left(A_{\mathrm{max}}^{\mathrm{corr}} W_{j-I_k} + \bar{A}_{\mathrm{max}}^{\mathrm{corr}} W_{j+I_k} \right), \tag{B.12}$$

where $\bar{A}_{\mathrm{max}}^{\mathrm{corr}}$ is the complex conjugate of $A_{\mathrm{max}}^{\mathrm{corr}}$.

7. We then go back to step 5 and repeat the process N_{iter} times.

8. After N_{iter} CLEAN iterations, we then construct the "CLEAN beam", B_j, which is a gaussian of the values of W

$$B_j = e^{\frac{-\nu_j^2}{2\sigma^2}}. \tag{B.13}$$

In practice, B_j only needs to calculated out to 5 FWHM of the gaussian.

9. The CLEAN spectrum is then convolved with the CLEAN beam

$$C = 2C^{N_{\mathrm{iter}}-1} * B, \tag{B.14}$$

the factor of 2 is due to the power in both the real and imaginary parts.

Line	K (km s^{-1})
Fe II 6317.3871	$3.26^{+0.88}_{-0.86}$
Fe II 6456.3796	$3.49^{+0.97}_{-0.7}$
Fe II 7711.4386	$4.06^{+0.75}_{-0.78}$
He I 5875.5987	$20.8^{+2}_{-1.8}$
He I 6678.1517	$20.1^{+2.2}_{-1.9}$
He I 7065.17714	$14.9^{+7.3}_{-5}$
Si II 6347.11	$5.51^{+1}_{-0.9}$
Si II 6371.37	$5.57^{+1.8}_{-1.3}$

Table B.1: Amplitudes, K, of the 1.583-day RV variations for each emission line which displays variations at this period.

10. We then re-add the remaining parts of the "dirty spectrum"

$$C_j = C_j + R_j^{N_{\rm iter}-1} \tag{B.15}$$

11. The final CLEAN spectrum, S, is then constructed with the absolute values of $C^{N_{\rm iter}-1}$, where $j >= 0$

$$S_j = \mid C_j \mid \text{ where } j > 0 \tag{B.16}$$

B.2 Amplitudes of short-period spectroscopic radial velocity variations

To determine the RV variability of the emission lines, Keplerian orbital RV solutions are fitted to the RV data for each line separately at both the orbital and 1.583-day periods simultaneously, fitting for the amplitude K, the eccentricity e, the argument of periapsis ω, and the phase of periastron M_0 for each period. Jitter, j, is also fitted for, and is modelled as a correction of the RV uncertainties. The systemic velocity v_0 is fit separately for each line. The fits at the orbital period are discussed in Chapter 4, and are used to determine the orbital solution of the binary. It is shown in Section 5.3 that the 1.583-day period cannot be an orbital period of a hidden inner binary; however, modelling the RV variations with a Keplerian solution is useful for fitting an amplitude to a repeating signal of an arbitrary shape in noisy data. The amplitudes found between the line species can then be compared.

The RV variations for each emission line are fit separately by maximising the log-likelihood function, using the Monte Carlo Markov Chain algorithm `emcee` (Foreman-

Mackey et al. 2012). The log-likelihood for a set of parameters, θ, given N RV data points, D, with uncertainty σ is given by

$$\begin{aligned}\ln P(\theta \mid D,\, \sigma) = -\frac{1}{2}\sum_{i=0}^{N}\Bigg[&\frac{\left(D_i - v_{\mathrm{kep}}(\theta_{\mathrm{orb}}) - v_{\mathrm{kep}}(\theta_{1.583}) - v_0\right)^2}{\sigma_i^2 + j^2} \\ &+\ln\left(2\pi(\sigma_i^2 + j^2)\right)\Bigg]\,,\end{aligned} \tag{B.17}$$

where θ_{orb} and $\theta_{1.583}$ are the orbital parameters for the long- and the short- period respectively, and v_{kep} is the Keplerian velocity calculated for a set of orbital parameters. The fitted parameters, θ, encode θ_{orb}, $\theta_{1.583}$, v_0, and j. The uncertainties, σ, are taken from the least-squares fitting algorithm of the Gaussian fitting routines. Table B.1 lists the fitted amplitudes for all emission lines in this study at the 1.583-day period. The fitted parameters at the orbital period are listed in Chapter 4, appendix B.

Although it is not implied that the 1.583-day period is in any way due to an orbital effect, fitting Keplerian RV solutions is a convenient method to fit an arbitrarily shaped, periodic signal in this context, which allows for effective extraction of mutually comparable amplitudes. All parameters encoded in $\theta_{1.583}$ other than K are ignored, as they are fitted for convenience only and will have no physical significance.

B.3 Calculation of phase-amplitude figures

Figure B.1 demonstrates how the short-period amplitude versus orbital phase for the V-band photometric data, shown in Figure 5.8, was calculated. The V-band data had the photometric variations at the orbital period subtracted, then were binned by a sliding window in orbital phase, of phase width 0.25. The data within a window are then folded by the 1.583-day short period, and a sinusoid is fitted and the amplitude extracted. Each panel shows the photometric data in blue and the sinusoid fits as black in each of the phase windows.

The amplitudes of the 1.583-day variations vary significantly with orbital phase. The phase of the sinusoidal variations do not change significantly given the uncertainties of the fitted parameters.

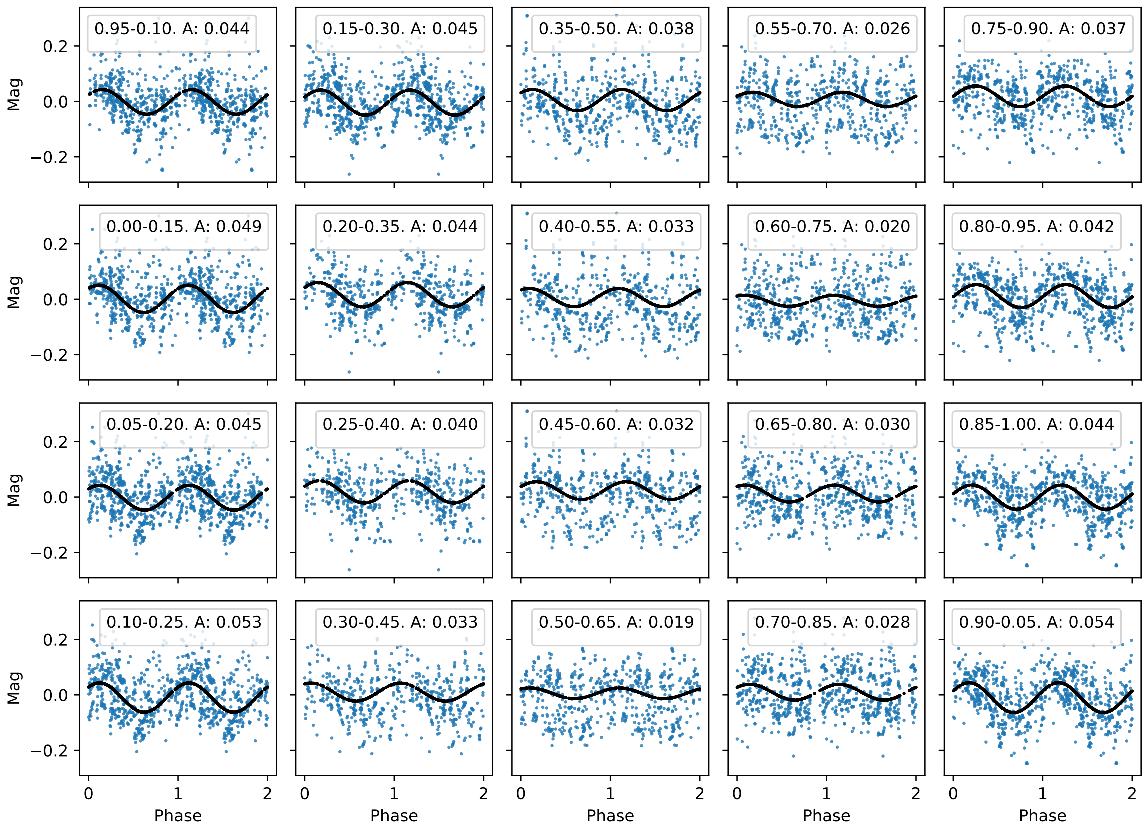

Figure B.1: Demonstration of how the short-period amplitude versus orbital phase for the V-band photometric data, shown in Figure 5.8, was calculated. Each panel shows the V-band data, with the 31-day orbital variance subtracted, in an orbital phase window of width 0.15 folded by the 1.583-day period. A black line shows the sinusoid fitted to the data in that phase window. The legend in each panel says the start phase, the end phase, and the amplitude of the fitted sinuosoid. The phase of the windows increases first down the columns in the figure, and then along the rows.

Appendix C

Appendix to Chapter 6

C.1 Long term change in $v_{\rm kep} \sin i$

Figure C.1 shows the fitted $v_{\rm kep} \sin i$ values for the inner circumbinary ring in GG Car in each year it was observed by FEROS. There is no significant change in the average $v_{\rm kep} \sin i$ measured, however the value for the [O I] line is lower in the later observations. This may be due to the inner [O I] ring becoming dominated by noise in the later spectra.

C.2 Effects of varying PHANTOM simulation parameters

I tested varying different input parameters of the inner circumbinary ring of the PHANTOM SPH simulations to observe their effects on the simulation output and test the robustness of the conclusions. The circumbinary ring's mass, initial radius, initial H/R, Shakura & Sunyaev (1973) viscosity $\alpha_{\rm SS}$, and the resolution of the simulation were varied.

C.2.1 Ring mass

Figure C.2 displays the effect of varying the initial mass of the inner circumbinary ring in the simulations between $5 \times 10^{-9}\,M_{\odot}$ and $5 \times 10^{-3}\,M_{\odot}$. A low mass was chosen since the disks of B[e]SGs are believed to be second-generation formed of material accumulated from mass-loss from the stellar surface, and would therefore have significantly lower masses than the binary components. The behaviour of the ring is near

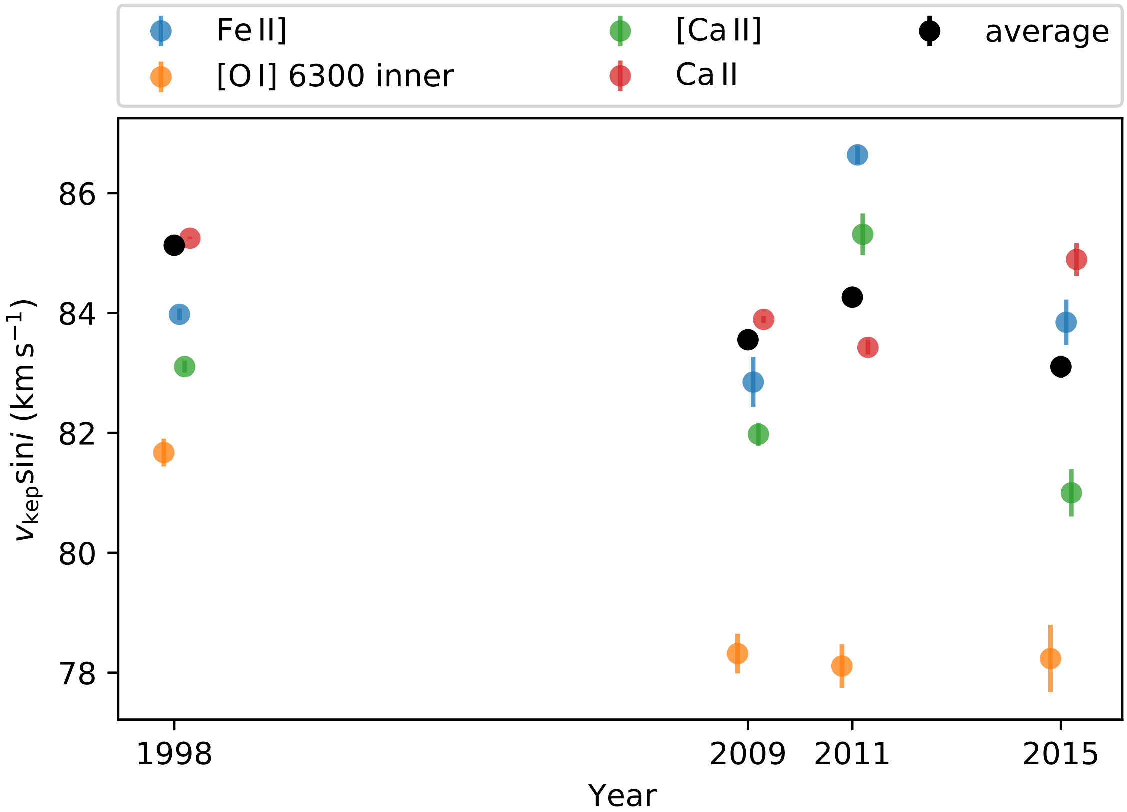

Figure C.1: Same as Figure 6.5, except showing the change in $v_{\rm kep} \sin i$ in the inner ring profilesin the FEROS observations.

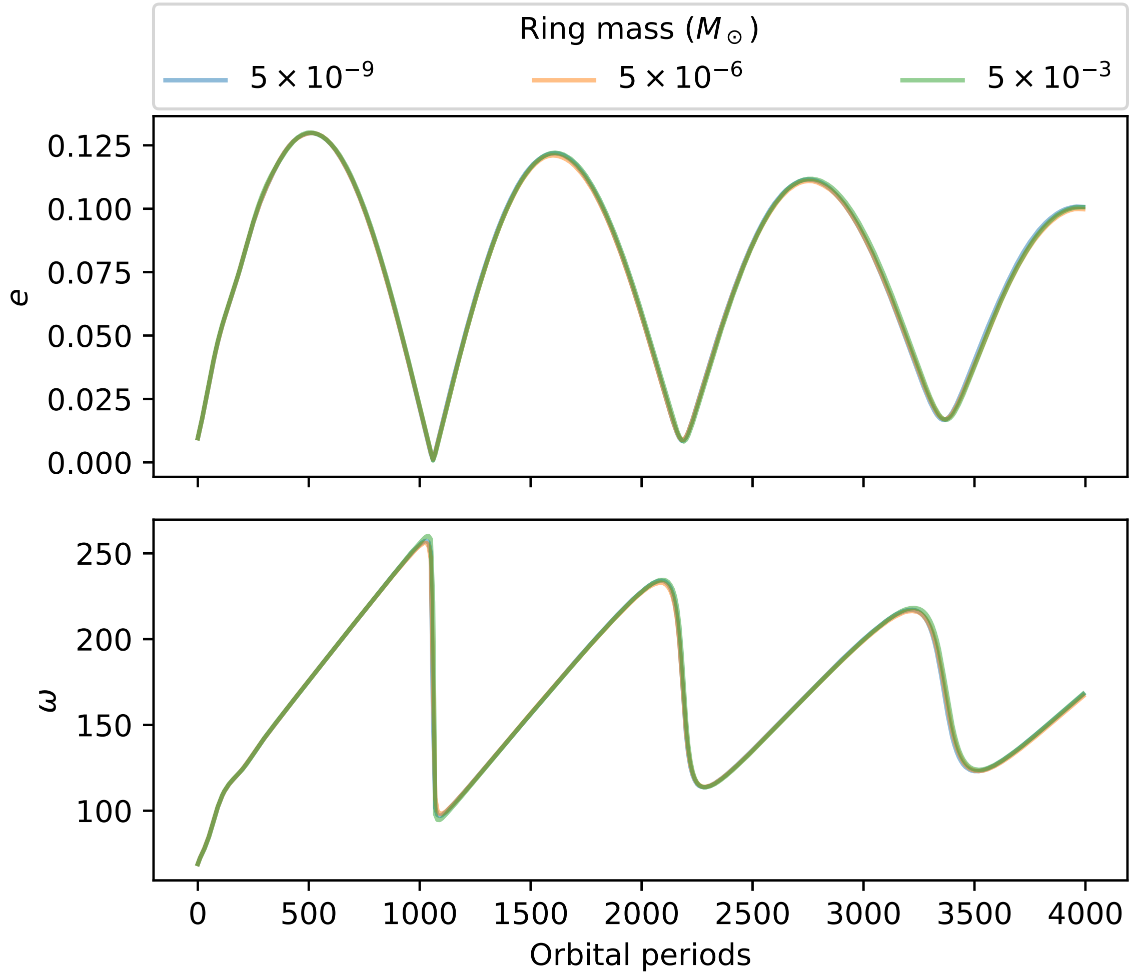

Figure C.2: Effect of varying the initial mass of the inner circumbinary ring on the oscillations of eccentricity, e, and argument of periastron, ω, of the ring.

identical for each input mass, since their masses are insignificant compared to the mass of the binary components. The variation of this input parameter therefore has no significant effect on the conclusions that are drawn from the SPH simulations.

C.2.2 H/R

Figure C.3 displays the effect of varying the initial H/R of the inner circumbinary ring. Increasing the H/R of the ring causes it to initially be more vertically extended; therefore, having a higher H/R value causes the ring to expand radially as it reaches equilibrium. The distribution of the surface density of the ring, Σ, against radius, R, is given in Figure C.4; these distributions are calculated for the snapshots at the second eccentricity minimum of the circumbinary ring, such that the rings are roughly circular.

For a high enough value, this causes the ring to resemble more a typical circumbinary disk, rather than the thin rings observed around B[e]SGs. Being more radially extended and with inner edges that are closer to the binary centre of mass, the rings with larger initial H/R are able to couple more efficiently with the binary which causes their oscillations to have a shorter period. The oscillations in the extended ring becomes more rapidly damped than the narrow rings over the simulation time, matching the similar finding in Martin & Lubow (2018).

Within the simulated times, varying the H/R parameter has little effect on the simulated line profiles over an oscillation period, therefore the conclusions in Section 6.5.4 referring to the varing V/R and v_0 of the emission lines do not strongly depend on the initial H/R chosen. From the emission line profiles it can be determined that the rings are radially thin, and therefore a smaller initial H/R parameter is preferred.

C.2.3 $\alpha_{\rm SS}$

Figure C.5 displays the effect of varying the Shakura & Sunyaev (1973) viscosity parameter, $\alpha_{\rm SS}$, on the eccentricity oscillations in the `PHANTOM` simulations. Varying $\alpha_{\rm SS}$ varies the artificial viscosity parameter, $\alpha_{\rm AV}$. There is very little effect on the simulation results for large changes of α using the fiducial simulation parameters.

As mentioned in the main text in Section 6.5.4, the fiducial choice of $\alpha_{\rm SS}$ leads to a low $\alpha_{\rm AV}$, though one which is acceptable given the simulation's aims and initial conditions. The low $\alpha_{\rm AV}$ value will also have the benefit of preventing artificial evolution of the ring. Increasing $\alpha_{\rm SS}$ to 0.05 gives a more typical value to the artificial viscosity ($\alpha_{\rm AV} = 0.44$) and, as can be seen in Figure C.5, there is minimal effect on the oscillations of e and ω through the simulation time. If the viscosity is increased further such that $\alpha_{\rm SS} = 0.1$, this makes the artificial viscosity relatively large ($\alpha_{\rm AV} = 0.88$) and close to the maximum allowed value of 1. As before, the simulation is not significantly affected, though the oscillations begin to diverge towards the end of the simulation.

This is interpreted as meaning the absolute value of the viscosity, and thereby simulation artificial viscosity, has minimal effect on the simulation results, and that

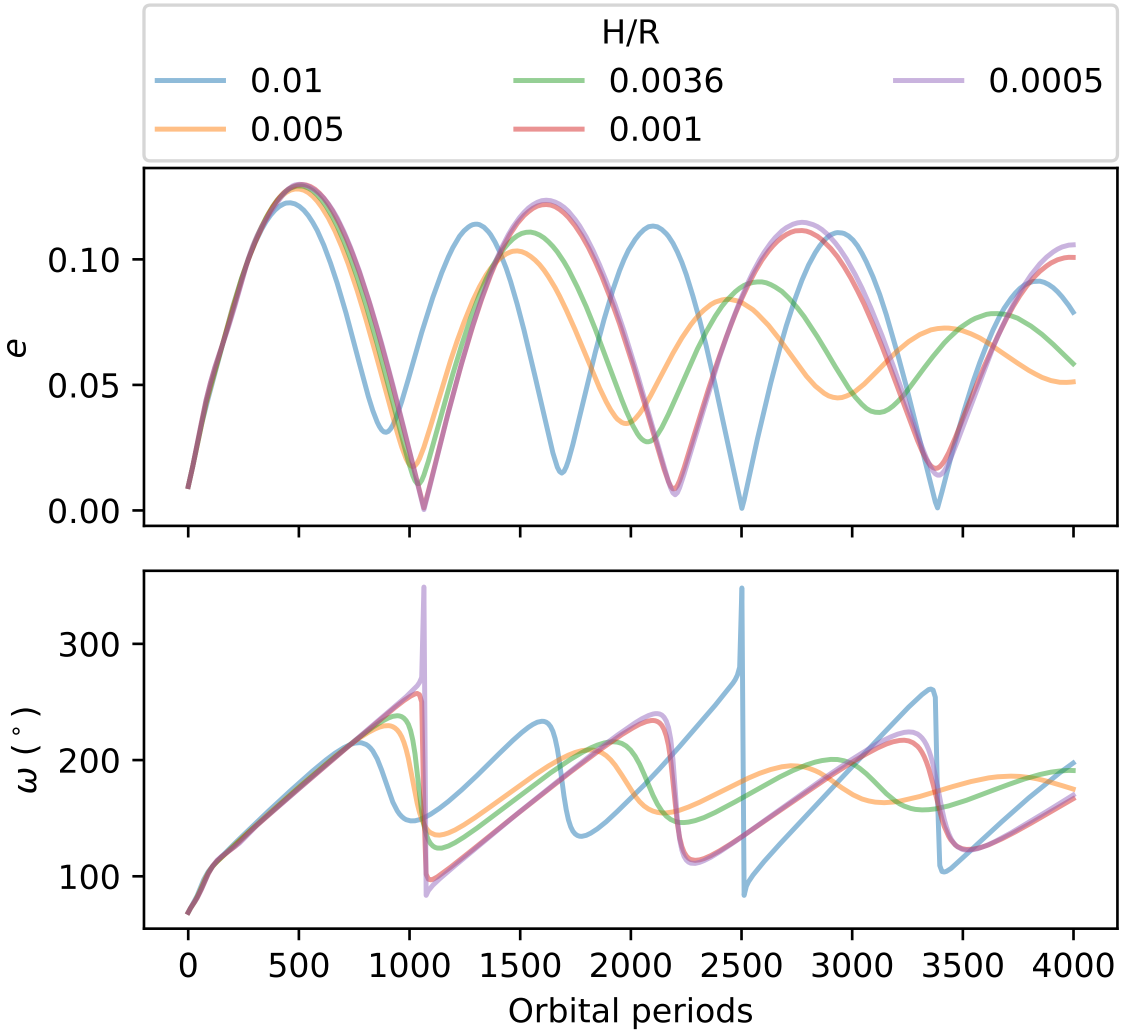

Figure C.3: Effect of varying the initial H/R of the inner circumbinary ring on the oscillations of eccentricity, e, and argument of periastron, ω, of the ring.

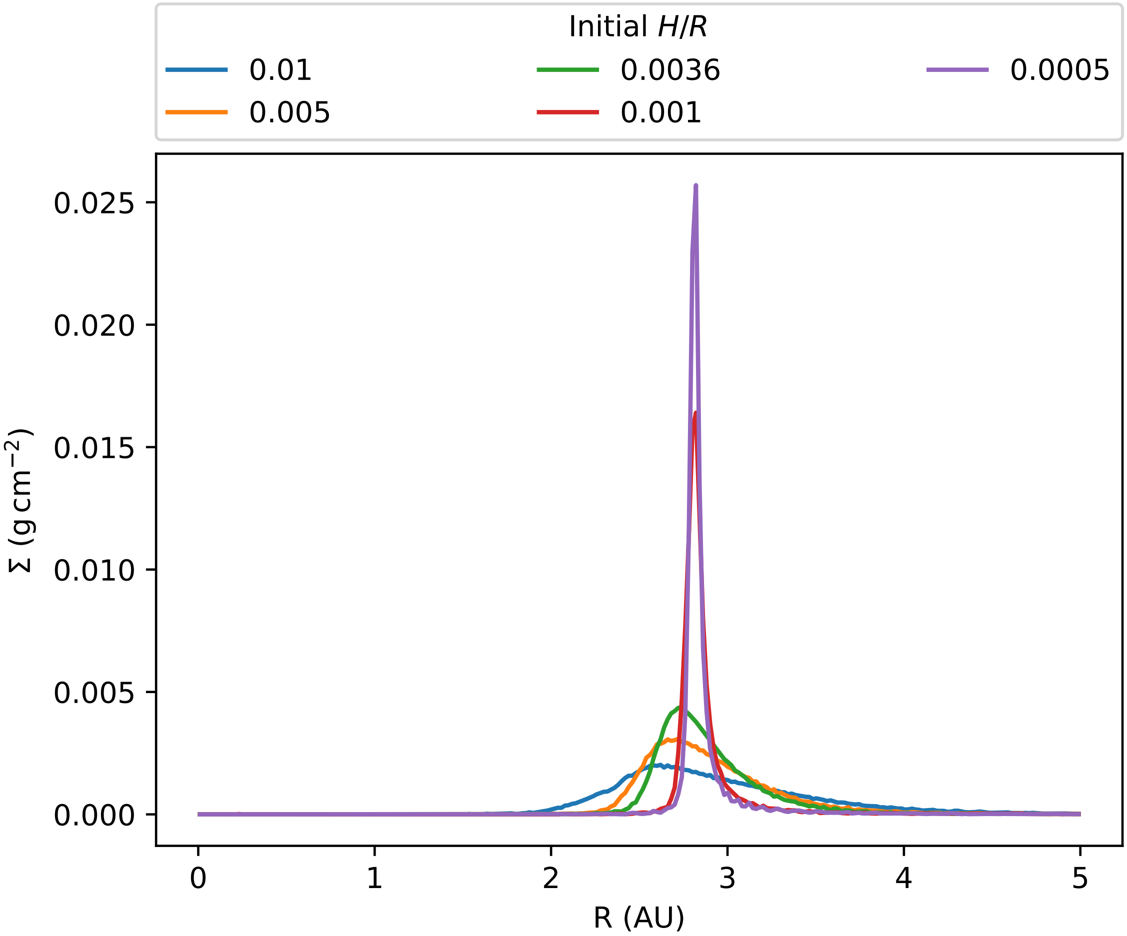

Figure C.4: Surface density, Σ, of the circumbinary ring against radius, R, in the PHANTOM simulations for varying initial H/R values at the ring's second eccentricity minimum. These Σ distributions are calculated for the snapshots where the eccentricity of the ring is at its second minimum in Figure C.3 (i.e. at 2200 binary orbital periods for $H/R = 0.0005$ and 0.001; 2060 for $H/R = 0.0036$; 1980 for $H/R = 0.005$; and 1690 for $H/R = 0.01$). This is so that the rings are studied at similar times in their evolution after they have reached a pseudo-steady state, and when they are roughly circular.

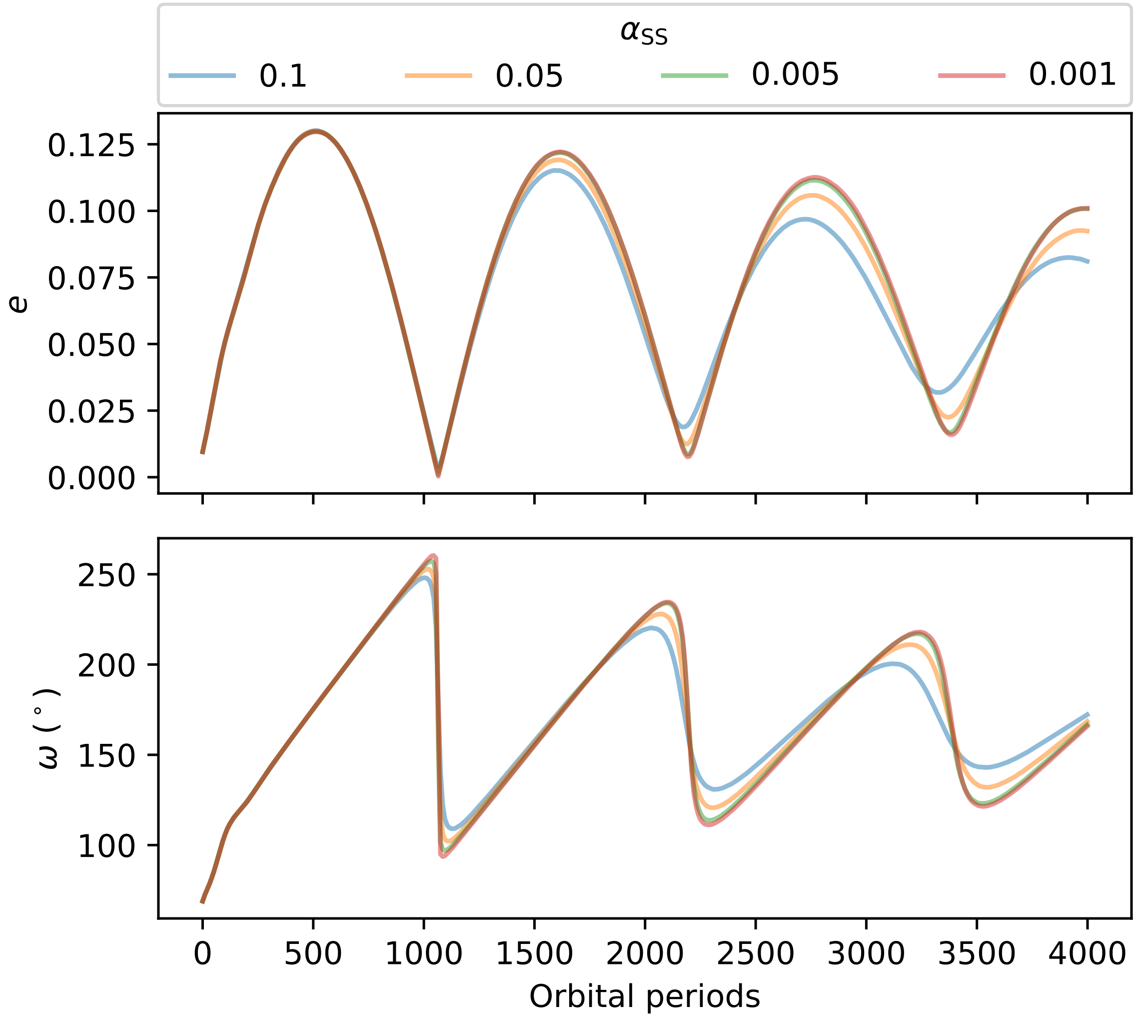

Figure C.5: Effect of varying the simulated viscosity in the circumbinary ring, α_{SS}, on its oscillations of eccentricity, e, and argument of periastron, ω.

the simulation is robust against large changes in α_{SS} and α_{AV}. The stated conclusions on the behaviour of the circumbinary ring in GG Car are therefore valid across the investigated ranges of viscosity.

C.2.4 Resolution

Figure C.6 demonstrates the effect of changing the resolution of the SPH simulations on the oscillations of e and ω. The number of SPH particles, $N_{\rm part}$, which simulate the circumbinary ring was varied between 50 000 and 150 000 particles. Fewer particles allow faster computation time, but at the expense of less physically well-resolved and robust simulations. Decreasing the number of SPH particles below 100 000 causes unacceptably different simulation results. On the other hand, increasing the number of particles above 100 000 does not significantly change the simulation results within the simulation time-frame but makes the calculation time much longer. Therefore, $N_{\rm part} = 100\,000$ was chosen for testing across all parameter space, since the simulations are accurate within the simulation time-frame and are calculated within a reasonable calculation time.

Towards the end of the simulation time, however, there is some small divergence between the 150 000 and 100 000 $N_{\rm part}$ runs. This does not affect the conclusions here, but if the simulation were to be run for a longer simulation time then a higher simulation resolution would be appropriate.

C.2.5 Initial ring radius

In order to check the dependence of the simulation on the initial orbital radius of the circumbinary ring, the semi-major axis of the ring, R, was varied between 2 AU and 4 AU in steps of 0.2 AU. The 2 – 4 AU range was chosen since this roughly corresponds with the limits given by the uncertainties of the radius of the inner ring. The effect of R on the variations of e and ω for selected models is shown in Figure C.7. For clarity, I do not plot the evolution of e and ω for every model that was calculated.

As expected from previous studies (e.g. Thun et al. 2017), there is a strong dependence of the oscillation timescale on the initial circumbinary orbital radius. However, the closer in rings with initial radius of 2 and 2.2 AU do not undergo oscillations in

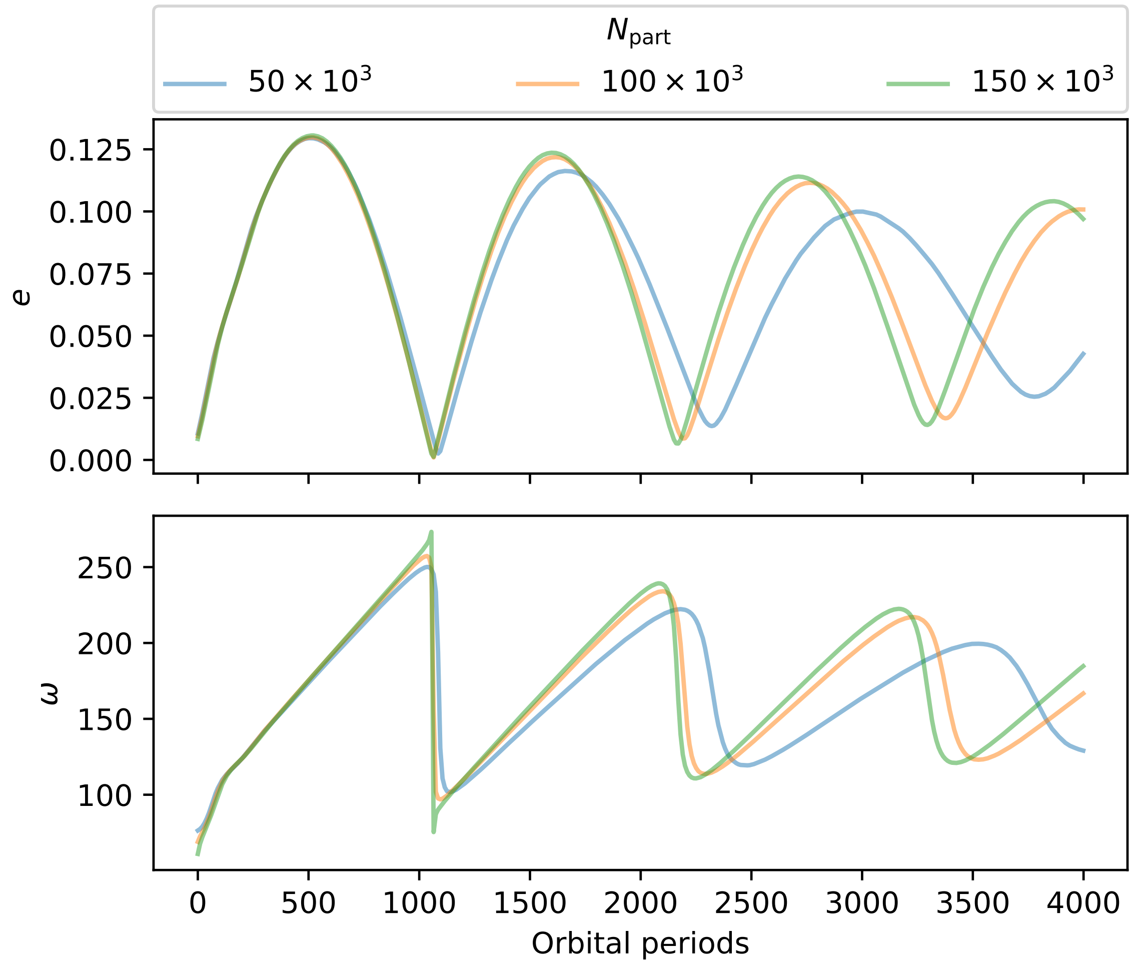

Figure C.6: Effect of varying the resolution of the simulation on the oscillations of eccentricity, e, and argument of periastron, ω, of the ring. The number of SPH particles in the simulation is shown in the legend.

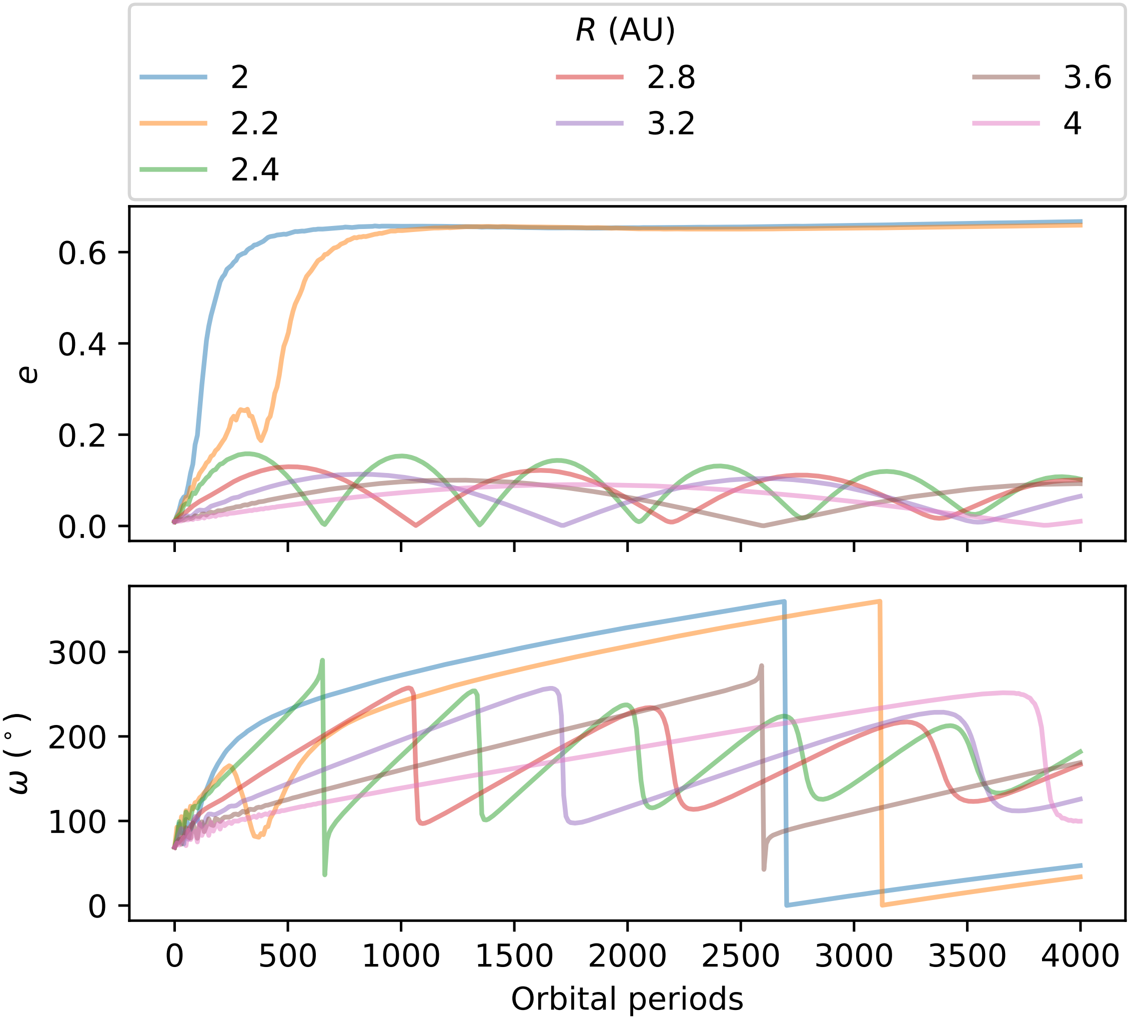

Figure C.7: Effect of varying the initial orbital radius of the inner circumbinary ring, R, on the oscillations of eccentricity, e, and argument of periastron, ω, of the ring in the `PHANTOM` simulation.

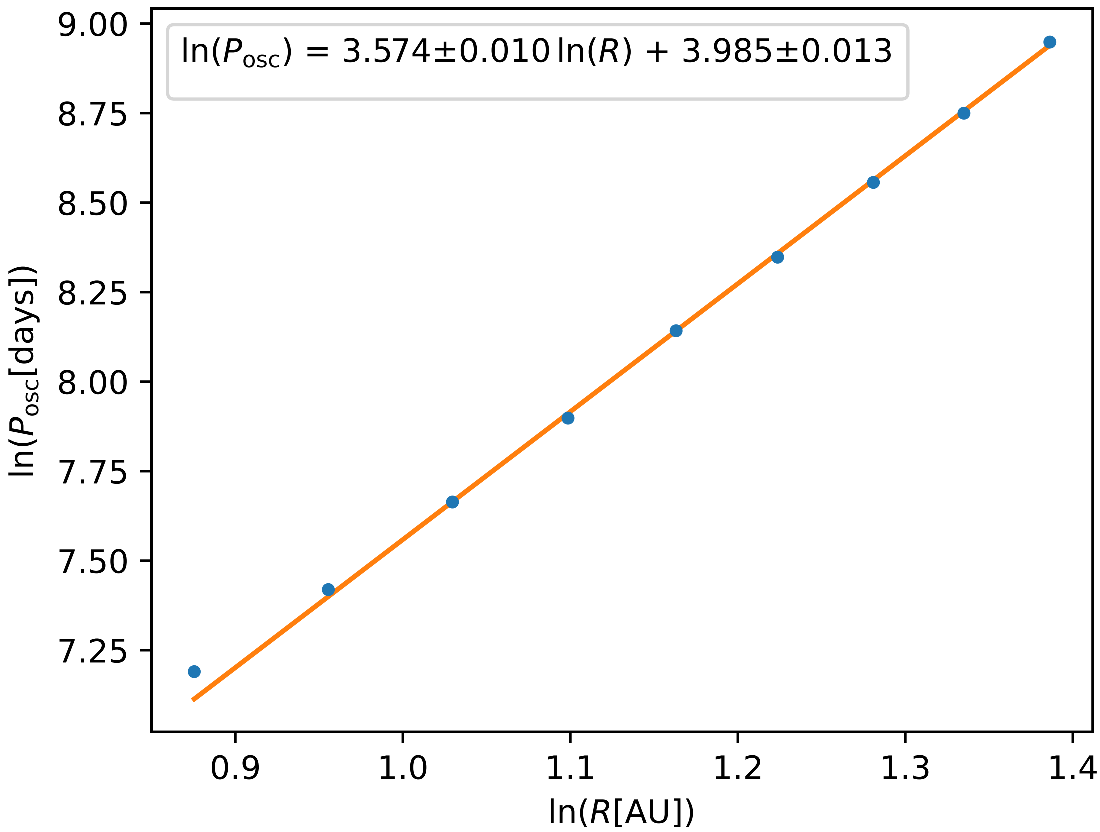

Figure C.8: Relationship between the initial circumbinary ring radius, R, and the period of eccentricity oscillation in the ring, $P_{\rm osc}$. A linear relationship is fitted to the natural logarithms of the two parameters, and the resulting linear coefficients are given in the legend.

eccentricity, but are instead excited up to high eccentricities of ∼0.6, after which the eccentricity remains constant whilst the argument of periastron precesses.

For the simulations where the circumbinary ring displayed oscillations in eccentricity (i.e. simulations with $R > 2.2\,$AU), I plot the natural logarithm of the period of oscillation, $P_{\rm osc}$, against the natural logarithm of R in Figure C.8. In this instance, $P_{\rm osc}$ is defined as the simulation time where the circumbinary ring reaches its first eccentricity minimum. There is a linear relationship between the two parameters in log space, and fitting a linear relationship gives a gradient of 3.574 ± 0.01, indicating that $P_{\rm osc} \propto R^{3.574}$. The simulations therefore agree very well with the findings of Thun et al. (2017), who find that the circumbinary disk precession timescale $P_{\rm prec} \propto R^{7/2}$ (Equation 6.6).

Bibliography

Aerts, C., Lefever, K., Baglin, A., et al. 2010, A&A, 513, L11

Aerts, C., Símon-Díaz, S., Bloemen, S., et al. 2017, A&A, 602, A32

Akashi, M., Sabach, E., Yogev, O., & Soker, N. 2015, MNRAS, 453, 2115

Alexander, R. 2012, ApJ, 757, L29

Allen, D. & Swings, J. 1976, A&A, 47, 293

Allen, D. A. 1973, MNRAS, 161, 145

Antoniadis, J. 2014, ApJ, 797, L24

Aret, A., Kraus, M., Muratore, M. F., & Borges Fernandes, M. 2012, MNRAS, 423, 284

Barbier, R. & Swings, J. P. 1982, in Be stars, ed. M. Jaschek & H.-G. Groth, Vol. 98 (Dordrecht, Reidel Publishing Company), 103–106

Beals, C. S. 1953, Publications of the Dominion Astrophysical Observatory, 9, 1

Benacquista, M. 2013, Undergraduate Lecture Notes in Physics, 262

Bertaux, J. L., Lallement, R., Ferron, S., Boonne, C., & Bodichon, R. 2014, A&A, 564, A46

Bertelli, G., Bressan, A., Chiosi, C., Fagotto, F., & Nasi, E. 1994, A&AS, 106, 275

Blundell, K. M., Bowler, M. G., & Schmidtobreick, L. 2007, A&A, 474, 903

Bodensteiner, J., Shenar, T., & Sana, H. 2020, A&A, 641, A42

Bonačić Marinović, A. A., Glebbeek, E., & Pols, O. R. 2008, A&A, 480, 797

Borges Fernandes, M. 2010, RevMexAA (Serie de Conferencias), 38, 98

Bowman, D. M., Burssens, S., Pedersen, M. G., et al. 2019, Nature Astronomy, 3, 760

Brandi, E., Gosset, E., & Swings, J.-P. 1987, A&A, 175, 151

Brown, A. G. A., Vallenari, A., Prusti, T., et al. 2018, A&A, 616, A1

Cannon, A. J. 1916, Annals of Harvard College Observatory, 76, 19

Carlson, E. D. & Henize, K. G. 1979, Vistas in Astronomy, 23, 213

Castor, J. I., Abbott, D. C., & Klein, R. I. 1975, ApJ, 195, 157

Chapellier, E., Le Contel, J. M., Le Contel, D., Sareyan, J. P., & Valtier, J. C. 1995, A&A, 304, 406

Chapellier, E. & Valtier, J. C. 1992, A&A, 257, 587

Chiţă, S. M., Langer, N., van Marle, A. J., García-Segura, G., & Heger, A. 2008, A&A, 488, L37

Cidale, L. S., Borges Fernandes, M., Andruchow, I., et al. 2012, A&A, 548, A72

Conti, P. S. 1975, in IAU Symposium No. 70: Be and Shell Stars, ed. A. Slettebak (Bass River, Massachusetts: Dordrecht, Reidel Publ. Comp.), 447

Damiani, F., Klutsch, A., Jeffries, R. D., et al. 2017, A&A, 603, A81

Davis, P. J., Siess, L., & Deschamps, R. 2013, A&A, 556, A4

De Cat, P., Telting, J., Aerts, C., & Mathias, P. 2000, A&A, 359, 539

De Wit, W. J., Oudmaijer, R. D., & Vink, J. S. 2014, Advances in Astronomy, 2014

Demircan, O. & Kahraman, G. 1991, Astrophysics and Space Science, 181, 313

Dermine, T., Izzard, R. G., Jorissen, A., & Van Winckel, H. 2013, A&A, 551, A50

Domiciano de Souza, A., Bendjoya, P., Niccolini, G., et al. 2011, A&A, 525, A22

Domiciano de Souza, A., Driebe, T., Chesneau, O., et al. 2007, A&A, 464, 81

Doolin, S. & Blundell, K. M. 2011, MNRAS, 418, 2656

Dukes, R. J. 1974, ApJ, 192, 81

Dunhill, A. C., Cuadra, J., & Dougados, C. 2015, MNRAS, 448, 3545

Eggleton, P. P. 1983, ApJ, 268, 368

Eker, Z., Soydugan, F., Soydugan, E., et al. 2015, Astron. J., 149, 131

Ekström, S., Georgy, C., Eggenberger, P., et al. 2012, A&A, 537, A146

El-Badry, K. & Quataert, E. 2021, MNRAS, 502, 3436

Ertel, S., Kamath, D., Hillen, M., et al. 2019, Astron. J., 157, 110

Evans, P. A., Osborne, J. P., Beardmore, A. P., et al. 2013, The Astrophysical Journal Supplement Series, 210, 8

Farago, F. & Laskar, J. 2010, MNRAS, 401, 1189

Farrell, E. J., Groh, J. H., Meynet, G., et al. 2019, A&A, 621, A22

Feinstein, A., Marraco, H. G., & Muzzio, J. C. 1973, A&AS, 12, 331

Feinstein, A. D., Montet, B. T., Foreman-Mackey, D., et al. 2019, PASP, 131, 094502

Finley, J. P., Belloni, T., & Cassinelli, J. P. 1992, A&A, 263, L25

Fitch, W. S. 1967, ApJ, 148, 481

Fitch, W. S. 1969, ApJ, 158, 269

Fleming, D. P. & Quinn, T. R. 2017, MNRAS, 464, 3343

Flower, P. J. 1996, ApJ, 469, 355

Foreman-Mackey, D., Hogg, D. W., Lang, D., & Goodman, J. 2012, PASP, 125, 306

Fuller, J. 2017, MNRAS, 472, 1538

Fuller, J., Kurtz, D. W., Handler, G., & Rappaport, S. 2020, MNRAS, 498, 5730

Gallart, C., Zoccali, M., & Aparicio, A. 2005, Annual Review of Astronomy and Astrophysics, 43, 387

Geisel, S. L. 1970, ApJ, 161, L105

Gnedin, Y. N., Kiselev, N. N., Pogodin, M. A., Rozenbush, A. E., & Rozenbush, V. K. 1992, Soviet Astronomy Letters, 18, 182

Goossens, M., Lampens, P., de Maerschalck, D., & Schrooten, M. 1984, A&A, 140, 223

Gosset, E., Hutsemekers, D., Surdej, J., & Swings, J.-P. 1985, A&A, 153, 71

Gosset, E., Surdej, J., & Swings, J.-P. 1984, A&AS, 55, 411

Götberg, Y., de Mink, S. E., Groh, J. H., et al. 2018, A&A, 615, A78

Gough, D. O. 1993, in Astrophysical fluid dynamics, Les Houches, Session XLVII, ed. J.-P. Zahn & J. Zinn-Justin (Amsterdam: Elsevier), 339–560

Grant, D., Blundell, K., & Matthews, J. 2020, MNRAS, 494, 17

Greenstein, N. K. 1938, Harvard College Observatory Bulletin, 908, 25

Griffiths, S. C., Hicks, R. B., & Milone, E. F. 1988, Journal of the Royal Astronomical Society of Canada, 82, 1

Gummersbach, C. & Wolf, B. 1995, A&A, 302, 409

Handler, G., Kurtz, D. W., Rappaport, S. A., et al. 2020, Nature Astronomy, 4, 684

Hanes, R. J., McSwain, M. V., & Povich, M. S. 2018, Astron. J., 155, 190

Haucke, M., Cidale, L. S., Venero, R. O. J., et al. 2018, A&A, 614, A91

Herbst, W. 1976, ApJ, 208, 923

Hernandez, C. A., Sahade, J., Lopez, L., & Thackeray, A. D. 1981, PASP, 93, 747

Hillier, D. J. & Lanz, T. 2001, in Spectroscopic Challenges of Photoionized Plasmas, ed. G. Ferland & D. Wolf Savin (ASP Conf. Ser.), 343

Hillier, D. J. & Miller, D. L. 1998, ApJ, 496, 407

Hoffleit, D. 1933, Harvard College Observatory Bulletin, 892, 19

Huang, W., Gies, D. R., & Mcswain, M. V. 2010, ApJ, 722, 605

Hur, H., Sung, H., & Bessell, M. S. 2012, Astron. J., 143, 41

Iben, Icko, J. & Livio, M. 1993, PASP, 105, 1373

Jayasinghe, T., Stanek, K. Z., Kochanek, C. S., et al. 2019, MNRAS, 489, 4705

Kanodia, S. & Wright, J. 2018, Research Notes of the AAS, 2, 4

Kaufer, A., Stahl, O., Tubbesing, S., et al. 1999, The Messenger, 95, 8

Kennicutt, R. C. 2005, Proceedings of the International Astronomical Union, 1, 3

Khokhlov, S. A., Miroshnichenko, A. S., Zharikov, S. V., et al. 2018, ApJ, 856, 158

Klement, R., Carciofi, A. C., Rivinius, T., et al. 2019, ApJ, 885, 147

Kochanek, C. S., Shappee, B. J., Stanek, K. Z., et al. 2017, PASP, 129, 104502

Koenigsberger, G., Georgiev, L., Moreno, E., et al. 2006, A&A, 458, 513

Koljonen, K. I. I. & Tomsick, J. A. 2020, A&A, 639, A13

Kraus, M. 2009, A&A, 494, 253

Kraus, M. 2016, Boletín de la Asociación Argentina de Astronomía, 58, 70

Kraus, M. 2017, in The B[e] Phenomenon: Forty Years of Studies, ed. A. S. Miroshnichenko, S. Zharikov, & D. Korcakova, Vol. 508 (ASP Conf. Ser.), 219–228

Kraus, M. 2019, Galaxies, 7, 83

Kraus, M., Borges Fernandes, M., & de Araújo, F. X. 2010, A&A, 517, A30

Kraus, M., Borges Fernandes, M., Kubát, J., & de Araújo, F. X. 2008, A&A, 487, 697

Kraus, M., Cidale, L. S., Arias, M. L., et al. 2016a, A&A, 593, A112

Kraus, M., Cidale, L. S., Arias, M. L., Oksala, M. E., & Borges Fernandes, M. 2014, ApJ, 780, L10

Kraus, M., Cidale, L. S., Liimets, T., et al. 2016b, The B[e] Phenomenon: Forty Years of Studies. ASP Conference Series, 508, 381

Kraus, M., Haucke, M., Cidale, L. S., et al. 2015a, A&A, 581, A75

Kraus, M., Liimets, T., Cappa, C. E., et al. 2017, Astron. J., 154, 186

Kraus, M., Oksala, M. E., Cidale, L. S., et al. 2015b, ApJ, 800, L20

Kraus, M., Oksala, M. E., Nickeler, D. H., et al. 2013, A&A, 549, A28

Krtičková, I. & Krtička, J. 2018, MNRAS, 477, 236

Kruytbosch. 1930, Bull. Astron. Inst. Netherlands, 6, 11

Kudritzki, R.-P. & Puls, J. 2000, Annual Review of Astronomy and Astrophysics, 38, 613

Kumar, P., Ao, C. O., & Quataert, E. J. 1995, ApJ, 449, 294

Kurfürst, P., Feldmeier, A., & Krtička, J. 2014, A&A, 569, A23

Kurfürst, P., Feldmeier, A., & Krtička, J. 2018, A&A, 613, A75

Kurtz, D. W., Handler, G., Rappaport, S. A., et al. 2020, MNRAS, 494, 5118

Lajoie, C.-P. & Sills, A. 2011a, ApJ, 726, 66

Lajoie, C.-P. & Sills, A. 2011b, ApJ, 726, 67

Lamers, H. 1986, A&A, 159, 90

Lamers, H. J., Zickgraf, F. J., De Winter, D., Houziaux, L., & Zorec, J. 1998, A&A, 340, 117

Langer, N. & Heger, A. 1997, B[e] stars, 235

Larson, R. B. 1974, MNRAS, 169, 229

Larson, R. B. 2010, Reports on Progress in Physics, 73, 014901

Levato, H., Miroshnichenko, A. S., & Saffe, C. 2014, A&A, 568, A28

Lines, S., Leinhardt, Z. M., Baruteau, C., Paardekooper, S.-J., & Carter, P. J. 2015, A&A, 582, A5

Lines, S., Leinhardt, Z. M., Baruteau, C., Paardekooper, S.-J., & Carter, P. J. 2016, A&A, 590, A62

Lomb, N. R. 1976, Astrophysics and Space Science, 39, 447

Lopes, D., Damineli, A., & De Freitas Pachecho, J. 1992, A&A, 261, 482

Lubow, S. H. & Artymowicz, P. 2000, Protostars and planets IV, 731

Luri, X., Brown, A. G. A., Sarro, L. M., et al. 2018, A&A, 616, A9

Majaess, D., Turner, D., Dékány, I., Minniti, D., & Gieren, W. 2016, A&A, 593, A124

Maravelias, G., Kraus, M., Cidale, L. S., et al. 2018, MNRAS, 480, 320

Marchiano, P., Brandi, E., Muratore, M. F., et al. 2012, A&A, 540, A91

Martin, R. G. & Lubow, S. H. 2017, ApJ, 835, L28

Martin, R. G. & Lubow, S. H. 2018, MNRAS, 479, 1297

Martin, R. G. & Lubow, S. H. 2019, MNRAS, 490, 1332

Mas-Hesse, J. M., Giménez, A., Culhane, J. L., et al. 2003, A&A, 411, L261

McGregor, P. J., Hyland, A. R., & Hillier, D. J. 1988, ApJ, 324, 1071

Mehner, A., de Wit, W. J., Groh, J. H., et al. 2016, A&A, 585, A81

Meru, F. & Bate, M. R. 2010, MNRAS, 406, 2279

Meynet, G. & Maeder, A. 2000, A&A, 361, 101

Millour, F., Meilland, A., Chesneau, O., et al. 2011, A&A, 526, A107

Miroshnichenko, A. S. 2007, ApJ, 667, 497

Miroshnichenko, A. S., Levato, H., Bjorkman, K. S., & Grosso, M. 2003, A&A, 406, 673

Moe, M. & Di Stefano, R. 2017, The Astrophysical Journal Supplement Series, 230, 15

Moreno, E., Koenigsberger, G., & Harrington, D. M. 2011, A&A, 528, A48

Morris, P. W., Eenens, P. R. J., Hanson, M. M., Conti, P. S., & Blum, R. D. 1996, ApJ, 470, 597

Muratore, M. F., Kraus, M., Oksala, M. E., et al. 2014, Astron. J., 149, 13

Oksala, M. E., Kraus, M., Cidale, L. S., Muratore, M. F., & Borges Fernandes, M. 2013, A&A, 558, A17

Oudmaijer, R. D., Proga, D., Drew, J. E., & De Winter, D. 1998, MNRAS, 300, 170

Pablo, H., Richardson, N. D., Fuller, J., et al. 2017, MNRAS, 467, 2494

Papaloizou, J. C. B., Nelson, R. P., & Masset, F. 2001, A&A, 366, 263

Patriarchi, P., Morbidelli, L., & Perinotto, M. 2003, A&A, 410, 905

Pereyra, A., de Araújo, F. X., Magalhães, A. M., Borges Fernandes, M., & Domiciano de Souza, A. D. d. S. 2009, A&A, 508, 1337

Pickering, E. C. & Fleming, W. P. 1896, ApJ, 4, 142

Pierens, A. & Nelson, R. P. 2013, A&A, 556, A134

Pittard, J. M., Stevens, I. R., Corcoran, M. F., & Ishibashi, K. 1998, MNRAS, 299, L5

Podsiadlowski, P., Morris, T. S., & Ivanova, N. 2006, in Stars with the B[e] Phenomenon, ed. M. Kraus & A. S. Miroshnichenko, Vol. 355 (ASP Conf. Ser.), 259

Pojmański, G. 2004, Astron. Nachr., 325, 553

Pojmański, G. & Maciejewski, G. 2002, Acta Astron., 52, 397

Polfliet, R. & Smeyers, P. 1990, A&A, 237, 110

Porter, A., Blundell, K., & Lee, S. 2021a, MNRAS, submitted

Porter, A., Blundell, K., Podsiadlowski, P., & Lee, S. 2021b, MNRAS, 503, 4802

Porter, A., Grant, D., Blundell, K., & Lee, S. 2021c, MNRAS, 501, 5554

Porter, J. & Rivinius, T. 2003, PASP, 115, 1153

Preibisch, T., Zeidler, P., Ratzka, T., Roccatagliata, V., & Petr-Gotzens, M. G. 2014, A&A, 572, A116

Price, D. J., Wurster, J., Tricco, T. S., et al. 2018, Publications of the Astronomical Society of Australia, 35, e031

Price-Whelan, A. M., Sipőcz, B. M., Günther, H. M., et al. 2018, Astron. J., 156, 123

Prusti, T., de Bruijne, J. H. J., Brown, A. G. A., et al. 2016, A&A, 595, A1

Puls, J., Kudritzki, R. P., Herrero, A., et al. 1996, A&A, 305, 171

Raguzova, N. V. & Popov, S. B. 2005, Astronomical & Astrophysical Transactions, 24, 151

Reig, P. 2011, Astrophysics and Space Science, 332, 1

Rezzolla, L., Most, E. R., & Weih, L. R. 2018, ApJ, 852, L25

Ricker, G. R., Winn, J. N., Vanderspek, R., et al. 2014, J. Astron. Telesc. Instrum. Syst., 1, 014003

Roberts, D. H., Lehar, J., & Dreher, J. W. 1987, Astron. J., 93, 968

Robitaille, T. P., Tollerud, E. J., Greenfield, P., et al. 2013, A&A, 558, A33

Roy, A. 2005, Orbital Motion, 4th edn. (IOP Publishing)

Saio, H., Georgy, C., & Meynet, G. 2013, MNRAS, 433, 1246

Salpeter, E. E. 1955, ApJ, 121, 161

Sana, H., de Mink, S. E., de Koter, A., et al. 2012, Science, 337, 444

Sana, H., Gosset, E., Nazé, Y., Rauw, G., & Linder, N. 2008, MNRAS, 386, 447

Savitzky, A. & Golay, M. J. E. 1964, Analytical Chemistry, 36, 1627

Scannapieco, C., Tissera, P. B., White, S. D. M., & Springel, V. 2008, MNRAS, 389, 1137

Scargle, J. D. 1982, ApJ, 263, 835

Sepinsky, J. F., Kalogera, B. Willems, V., & Rasio, F. A. 2007, ApJ, 667, 1170

Sepinsky, J. F., Willems, B., Kalogera, V., & Rasio, F. A. 2009, ApJ, 702, 1387

Sepinsky, J. F., Willems, B., Kalogera, V., & Rasio, F. A. 2010, ApJ, 724, 546

Shakura, N. I. & Sunyaev, R. A. 1973, A&A, 24, 337

Shao, Y. & Li, X.-D. 2014, ApJ, 796, 37

Shappee, B. J., Prieto, J. L., Grupe, D., et al. 2014, ApJ, 788, 48

Smak, J. 1969, Acta Astron., 19, 210

Smak, J. 1981, Acta Astron., 31, 395

Smallwood, J. L., Lubow, S. H., Franchini, A., & Martin, R. G. 2019, MNRAS, 486, 2919

Smith, R. G. 1987, MNRAS, 227, 943

Soker, N. 2000, A&A, 357, 557

Spina, L., Randich, S., Magrini, L., et al. 2017, A&A, 601, A70

Swings, J. 1974, A&A, 34, 333

Tapia, M., Roth, M., Marraco, H., & Ruiz, M. T. 1988, MNRAS, 232, 661

Thackeray, A. D. 1950, MNRAS, 110, 524

Thun, D., Kley, W., & Picogna, G. 2017, A&A, 604, A102

Torres, A. F., Cidale, L. S., Kraus, M., et al. 2018, A&A, 612, A113

Torres, G. 2010, Astron. J., 140, 1158

van den Heuvel, E. P. J. 1976, in Structure and Evolution of Close Binary Systems, ed. P. Eggleton, S. Mitton, & J. Whelan (Dordrecht, Reidel Publ. Comp.), 35

van den Heuvel, E. P. J. 2018, Proceedings of the International Astronomical Union, 14, 1

van Leeuwen, F., van Genderen, A. M., & Zegelaar, I. 1998, A&AS, 128, 117

VanderPlas, J. T. 2018, The Astrophysical Journal Supplement Series, 236, 16

Verbunt, F. & van den Heuvel, E. P. J. 1995, X-ray Binaries, 494

Virtanen, P., Gommers, R., Oliphant, T. E., et al. 2020, Nature Methods, 17, 261

Waelkens, C., Lamers, H. J. G. L. M., Waters, L. B. F. M., et al. 1991, A&A, 242, 433

Waelkens, C., Van Winckel, H., Waters, L. B. F. M., & Bakker, E. J. 1996, A&A, 314, L17

Walter, R., Lutovinov, A. A., Bozzo, E., & Tsygankov, S. S. 2015, The Astronomy and Astrophysics Review, 23, 2

Wang, Y., Weigelt, G., Kreplin, A., et al. 2012, A&A, 545, L10

Wellstein, S., Langer, N., & Braun, H. 2001, A&A, 369, 939

Wheelwright, H. E., de Wit, W. J., Oudmaijer, R. D., & Vink, J. S. 2012, A&A, 538, A6

Willems, B. & Aerts, C. 2002, A&A, 384, 441

Wilson, R. E. 1990, ApJ, 356, 613

Yadav, A. P. & Glatzel, W. 2016, MNRAS, 457, 4330

Yadav, A. P. & Glatzel, W. 2017, MNRAS, 471, 3245

Zahn, J. 1977, A&A, 57, 383

Zanazzi, J. J. & Lai, D. 2018, MNRAS, 473, 603

Zickgraf, F.-J. 1999, in The Be Phenomenon in Early-Type Stars, ed. M. A. Smith, H. F. Henrichs, & J. Fabregat, Vol. 175 (ASP Conf. Ser.), 26–36

Zickgraf, F. J. 2006, in Stars with the B[e] Phenomenon, ed. M. Kraus & A. S. Miroshnichenko, Vol. 355 (ASP Conf. Ser.), 135

Zickgraf, F. J., Humphreys, R. M., Lamers, H. J., et al. 1996, A&A, 315, 510

Zickgraf, F.-J., Wolf, B., Stahl, O., & Humphreys, R. M. 1989, A&A, 220, 206

Zickgraf, F.-J., Wolf, B., Stahl, O., Leitherer, C., & Appenzeller, I. 1986, A&A, 163, 119

Zickgraf, F.-J., Wolf, B., Stahl, O., Leitherer, C., & Klare, G. 1985, A&A, 143, 421